# CONTROLLING FORCE AND DISPLACEMENT: INSTRUMENTATION DESIGN AND APPLICATION IN THERMAL ACTUATION AND NANO-INDENTATION

By

Chunjie Fan

A dissertation submitted to the faculty of
The University of North Carolina at Charlotte
in partial fulfillment of the requirements
for the degree of Doctor of Philosophy in
Mechanical Engineering

Charlotte

2021

Approved by:

Dr. Stuart T. Smith

Dr. Joshua A. Tarbutton

Dr. Jimmie A. Miller

Dr. Qiuming Wei

Dr. Thomas J. Suleski

# ABSTRACT

CHUNJIE FAN. Controlling force and displacement: Instrumentation design and application in thermal actuation and nanoindentation. (Under the direction of DR. STUART T. SMITH)

The motivation of this research is to build systems that precisely control displacement in the presence of external load (both linear and rotation force). To achieve this, two experimental platforms have been created. Those instruments incorporate actuation stages, rotary apparatus, and rotary encoder and displacement sensors. During experiments the temperature of the stage and the environment are recorded. Characterization of these processes necessarily requires generation and monitoring of forces and measurements of displacement, rotation, and environmental temperature. The actuator methods include thermal expansion and piezoelectrical actuation, and the displacement sensing includes optical knife-edge and capacitive gage sensors.

A thermally actuated, single-axis, bidirectional translation stage is designed and constructed. To increase the temperature of the thermal actuator, induction heating is used while air-water-mist cooling is used to decrease the temperature. An automated control strategy comprising PID closed loop control (for heating) and On/Off switching between air and mist control (for cooling) is described. Future work on thermal actuators includes an investigation of the feasibility of manufacturing and implementation of a compact system that can be integrated into systems scaled between MEMS devices and devices smaller than 25 mm. With a decrease in the overall dimensions of the actuator, it is expected that the dynamic properties will improve while continuing to support loads in excess of 1000 N for displacement control.

A second study seeks to determine whether there exist torsional forces during indentation measurements. To precisely measure torsional forces produced by rotations within the indent

region, an air bearing is employed since there is little rotational resistance other than inertia of the bearing itself. The general design combines an air bearing and an indentation system. The air bearing system is mounted on the x/y moving table of a Moore measuring machine while the indentation apparatus is mounted on the vertical carriage in place of the spindle stage. A coarse and fine adjustment mechanism is assembled onto the air bearing spindle to align the tip of the nano-indenter to within 1 μm of its axis of rotation. The indentation system consists of an alignment sensor that will provide feedback for the indenter adjustment. Two flexure structures with two capacitance gauges, and a PZT (Lead-Zirconate-Titanate) linear actuator are built for the actuation and load-cell stages. The specimen is glued on the bottom of the load-cell stage. Rotation is measured using an A-B quadrature encoder affixed to the spindle of the air bearing and capable of resolving rotation to 0.0002 μrads. The indentation depth control and data capture are completed using a National Instruments myRIO Data Acquisition device. The actuation stage has a displacement range of 16 μm and this is used to generate a penetration force between a sample and a indenter tip and this force pass through, and is measured by the load-cell stage. Numeric experiments have been performed with penetration depths from 200 nm to 2000 nm and with penetration forces between 20 mN to 200 mN. After indentation, rotations were not detected for this research for Si (hardness ~ 12.5 GPa), Fe, large grain sized Fe, NiP, Cu, large grain sized Cu, Al, and Carbon Fiber Reinforced Polymer (CFRP) (hardness ~ 0.1 GPa).

# ACKNOWLEDGEMENTS

I would like to thank a lot of people who made my Ph.D. dissertation possible. First and most important, I would like to thank my adviser Dr. Stuart Smith for his help, patience, kindness, and direction on the precision instrumentation design, development and optimization. Without him, I wouldn't have been able to complete this project in high quality. His knowledge on precision instrumentation design and metrology as well as physics always encourages me to learn smart and work hard.

I would also thanks Dr. Joshua Tarbutton and Dr. Jimmie Miller in serving as my dissertation committee member and his advice for the thermal actuator design and advice for the presentation. I would also like to thank Dr. Jimmie Miller for lending various measurement instruments and for training me to use atomic force microscope. I would also like to thank Mr. Brian Dutterer for manufacturing some parts for those projects. I would like to thank Dr. Chris Evans to lend me Nickel Phosphorus samples. I would like to thank Dr. Youxing Chen and his student Liuqing Yang to lend me pure copper samples and to train me for using scan electron microscope. I would also like to thank Mr. Greg Caskey for helping me set up the autocollimator and do the measurement of the tilt measurement for the linear flexure-based actuation stage. I would also like to thank Dr. Kumar Arumugam, Jesse Groover, Michael Erikson, Ameya Parab, Elias Gilbert, Ezron Manco and Mr. Geoffrey Heacock for manufacturing some parts for those projects. The authors acknowledge the helpful contributions and air bearing donation from David Arneson (Professional Instrument Company). I want to thank Dr. Todd Noste for help me to calibrate the Lion$^{TM}$ ultra-precision capacitance gauges. I want to thank Dr. Brigid Mullany to train me using Zegage profilometer. I would like to thank Dr. Nicolas Sizemore for helping me to do surface measurement of the capacitive gauge sensors. I would like to thank Dr. Jeffery Thousand

and Mr. Scott Williams to help me finish the 3D Microfabrication of the rotational mechanism using Nano-scribe high-resolution 3D printer.

Lastly, I want to thank and bless all of those who supported me in any respect during the completion of the project.

TABLE OF CONTENTS

# LIST OF TABLES

# LIST OF FIGURES

# CHAPTER 1: INTRODUCTION

Precision engineering relies on instruments and machines that comprise actuators and sensors [1-17]. In general, actuators drive motion, and sensors detect the change of signals to measure and to control the movement.

The motivation of this dissertation is controlling force and displacement for instrumentation design and application in thermal actuation and nano-indentation. Based on the type of actuation, (Huber, 1997) [5] mapped and plotted the mechanical driving force and displacement (stress and strain). Different actuation methods have different merits based on the power density and bandwidth.

Piezoelectric actuators exhibit limited strain capabilities based on the maximum tolerable external electric field. These actuators, typically exhibiting a maximum strain of around 0.1%, have a range of displacements dependent upon their physical size, and are capable of supporting loads producing compressive stresses up to around 200 MPa. Because of their high losses, a major drawback of piezoelectric actuators is the required heat dissipation if the actuator is to provide substantial mechanical work or power. The limited thermal conductivity of piezoelectric ceramics, heat removal is further complicated. For the actuator to maintain its piezoelectric behavior, the operating temperature needs to be limited to below the Curie temperature. Thermal actuators use temperature change as their relative mechanism to provide force and motion. They can exhibit higher strain than piezoelectric materials, are relatively simple devices, and can operate in a range of environments, and also have relatively high time constant comparing with ceramic.

Micro-electrical mechanical system (MEMS) thermal actuators using resisting heating are widely used for linear or rotary mechanism for precision miniature instruments and machines [7-9]. Large scale thermal actuator in 30 mm major dimension has been studied [17], however, thermal actuators with high preload capability are rarely seen for precision instruments and applications. For the study presented in this thesis, a single degree of thermal actuator with 200 μm range and 1 kN preload force has been designed and built. Induction heater is used as the heating source, and air or mist cooler is used as the cooling source. By controlling the heating and cooling processes, the displacement of the actuator will be controlled and measured using an optical knife-edge sensor. The heating power for the thermal actuator in the final prototype was produced using an induction coil controlled using a closed loop PID duty cycle (PWM) controller signal via a motor driver powered by either 240 or 480 W power sources. The motor driver, in turn, provided the power to a zero-volt switching circuit (ZVS) that provides an alternating current (AC) to the induction coils. The induction coils then produced a fluctuating magnetic field that induced eddy currents inside the thermal actuator tube located within these coils. To have a fast retract response, a cooling system with air/mist cooler was designed. The time constant of the heating system is around 50 seconds, and the time constant of cooling system is around 14 seconds. The steady state root-mean-square (RMS) controller error is around 15 nm under an actuator preload of 1000 N. The applications of this research include precision actuators, machines, tilt adjustment structure for telescopes, and injection molding process for plastic, polymer, and glass materials.

The contribution of the nanoindentation instrument is to create a new method to measure torsion effects during nano-indentation. A novel nano-indentation machine with rotary function is designed and built. This novel nanoindentation instrument has a piezo actuation stage, load-cell

stage, and rotary stage with rotary air-bearing. The actuation stage supplies the driven displacement to push the indenter to the sample surface. The load-cell will measure the force between the actuation stage and the indenter, which is coaxial with the rotary stage. The point of contact is estimated when the load-cell begins to vary corresponding to a force between the indenter and the sample surface. The actuation stage has a16 µm range and the load-cell stage has a range of 10 µm (1 N). The tilt angle of the actuation stage during translation is less than 0.05 arc sec in this 16 µm range. The rotary encoder has a 0.05 arc sec rotary resolution, the stability of the rotary air-bearing is ~ 0.004 µrad in 10 minutes. The stability test shows the actuation stage has 3 nm variance, and the load-cell stage has 5 nm variance in 10 minutes. The load-cell has a stiffness of ~100 kN/m, and the frame has a stiffness around 5000 kN/m. Temperature sensors are used to measure the environment and the instrument.

Because the thermal actuator and indenter developments resulted in separate machines, these are discussed separately. The design, the performance, the experimental evaluation and the results of the thermal actuator are discussed in chapter 2. Chapters 3 through 6 separately present: the conceptual design of the instrument, design manufacture and implementation of capacitance displacement sensing, system characterization, and measurement results. A final chapter concludes the findings of these studies and suggests for future initiatives for advancing these two technologies.

# CHAPTER 2: THERMALLY ACTUATED, LINEAR TRANSLATION STAGE

The objective of this study is to optimize a novel, thermally actuated, single degree of freedom flexure-based translation stage with 100 μm or 200 μm range and capable of operation in the presence of preloads up to 1000 N. The displacement of the thermal actuator (an aluminum tube) is based on the thermal expansion and contraction of the thermal actuator tube. The first design is using joule heating nichrome wire to radiate energy for the actuator. The optimized design uses induction heating to replace the nichrome wire radiation heating. The induced eddy current from the induction heater increases the temperature of the thermal actuator tube, which provides the expansion force and converted it into a forward motion of the translation stage. In contrast, the contraction is from the decreasing of the temperature using the cooling air and mist flowing through the inner of the tube. The control system includes a PID controller for heating up and maintaining the position during steady state, and on/off controller for cooling down. An optical knife-edge sensor is a calibrated as displacement sensor. Testing verifies that the system meets the same procedures and results with 0 N, 500 N and 1000 N preloaded from a compression spring. The step used for forward and backward displacements is 20 micrometers. The displacement range of the actuator is 100 micrometers for a 240 W power source and 200 micrometers for a 480 W power source. And the stage can retain a constant position with a variation of ±50 nm for 240 W power supply and ±70 nm for 480 W power supply. The time constant of this thermal actuator is around 50 seconds for heating up process, 10 seconds for cooling down process. Thermodynamics of this model is analysis in the section 2.7.

## 2.1 INTRODUCTION AND LITERATURE REVIEW

Different performance actuators are reviewed in this list: such as electromechanical actuator (Lorentz, reluctance, and inductance), piezoelectric actuator, fluid pressure actuator, and

thermal expansion and contraction actuator [1-4]. Most reviews explain the performance of actuating stages in terms of their work density (products of force and travel range, divided by the volume of the actuator), work (products of force and displacement), power density (products of force and velocity, divided by volume), strain, response time, and resolution. Huber et al., 1997, [5] review a broad range of actuators and provide performance parameter maps (or Ashby plots) that help visualize the relative merits of different actuators. And in Huber et al.'s paper, thermal actuators are in the region that provide large stresses (force) but are slow in frequency response while the specific actuation stress (ratio between stress and density) of thermal expansion is the highest among all actuator types [5]. Because of this high force capability, thermal actuators can have a high-power density that is competitive with piezoelectric and voice coil actuators, although, in comparison with the latter two types, thermal actuators do not translate to high dynamic bandwidth of large dimensions or sizes. Since the performance of many actuator types often depends upon the physical dimensions or sizes, scaling effects (not considered in the Huber et al. review) are considered in a review [6] based on similar performance considerations with an emphasis on precision. The following Figure 1 shows how a thermal actuator system works.

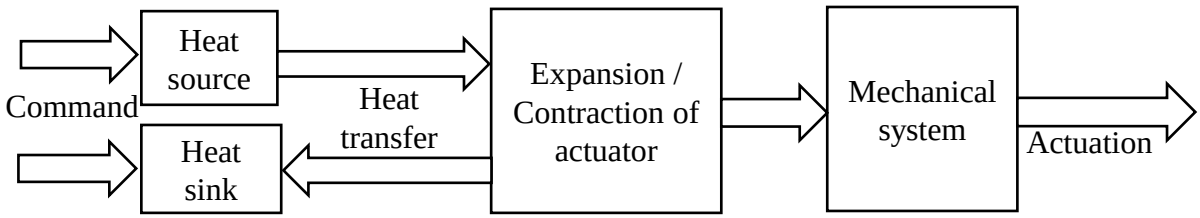


Figure 1. A thermal actuator system.

Precision motion control of thermal actuators is not common with only a few publications. Thermal actuation can be simply explained: passing a current through a wire, bar, or MEMS beam creates resistive heating which increases its length. Because dynamic bandwidth tends to increase

with reduced size, MEMS thermal actuators have recently been produced for precision control with resolutions of 1 nm in displacement, and 12 nN in load [7-9]. Two studies of larger sized actuators used in precision motion have been published. Snyder, 1993, presented a thermally actuated actuator for tilt control of optical mirrors [10]. This actuator comprised a simple notch-type flexure that is initially deflected and held in place using a Nickel Chromium Iron wire (10 mm long, 0.13 mm diameter). By monitoring the electrical resistance, rotations of up to 1 milli-radian were possible with a resolution of 20 μrad. In a study to explore the limiting accuracy of an optical interferometer, Lawall and Kessler, 2000, wound a copper wire around a 106 mm long thin aluminum tube to provide smooth motion control of an optical flat mirror [11]. This actuator was capable of providing smooth and continuous motion of a mirror from which it was demonstrated that residual errors of the interferometer could be reduced to 10 pm levels.

The dynamic response of a thermal actuator (i.e., the rate of heat transfer in and out of the device) is related to its time constant. For an ideal lumped model, the time constant is proportional to the thermal diffusivity (most metals are between $10^{-4}$ to $10^{-6}$ $m^2 \cdot s^{-1}$) and inversely with the square of the length of the path for heat flow. In practice, the time constant of thermal actuators is influenced by physical dimensions, power input, material, and heat transfer characteristics of the actuator. Estimates for the time constants of thermal actuators in this review are listed in Table 1 with the dimensions of the actuator. From this table, the general trend is the smaller the size, the smaller the time constant.

However, the optimized design of thermal actuators is sparsely reported in the available literature indicating that optimization has not been aggressively pursued. Consequently, mapping

of the few available papers covered in this review, shows an increase in the response with reduction of size, albeit with considerable scatter in this trend.

Table 1. Dimensions and open-loop time constant ($\tau$) of thermal actuators reported in research literature.

| Dimensions | $\tau$ | Reference |
|---|---|---|
| 195 μm long, 60 μm wide, 20 μm thick, poly-Si comb | 0.16 ms | [12] |
| 300 μm long, 17 μm wide, 5 μm thick, polysilicon cantilever | 0.24 ms | [13, 14] |
| 600 to 1400 μm long, 6 μm wide, 3 μm thick, Al-Si bimorph | 0.5 to 3.8 ms | [15] |
| 1.8 mm long, 0.6 mm wide, 0.1 mm thick, Silicon cantilever | 20 ms | [16] |
| 10 mm long, 0.13 mm diameter mixed alloy wire | 0.87 s | [10] |
| 30 mm long, 10 mm wide, 10 mm thick, 42CrMo4-steel bar | 49.81 s | [17] |
| 120 mm long, 10.5 mm diameter, 1.7 mm wall-thick Al tube | 50.87 s | This paper |

There are a number of benefits to using thermal actuators. Over a large range of temperatures, the thermal expansion coefficients of metals are relatively constant (typically increasing with temperature for metals and alloys) [5]. Hence thermal actuators can, in principle, operate over a correspondingly large temperature range. The large actuation temperature range produces high strain (0.2 percent in this study) that is significantly larger than the piezoelectric actuators (typically around 0.1 percent). Thermal actuators can tolerate a higher temperature environment compared with piezoelectric actuators so that they can be used for molding processes like optical lens manufacturing. Other attributes are simplicity of construction compared with other actuation methods, the materials of the actuator can withstand large radiation doses, and components can be robust at high pressure and gravity loads. Among other applications, such a combination of attributes is considered favorable for extreme environmental requirements, specifically for future space exploration [18].

Thermal energy can be achieved by resistive heating, conduction, and radiation from a heat source. For resistive heating of metals, electrical current can be produced by applying a voltage

across the actuator or by induced eddy currents from an induction coil, this latter method being chosen for this study. Induction heating, as a source of fast heating, is already widely used in the manufacturing industry for surface hardening, melting, quenching, and shrink fit assembly [19, 20], and in the semiconductor industry for crystallizing silicon or germanium [21, 22]. The thermal actuator in this present study uses induction heating and air mist cooling to control a bidirectional displacement (Section 2.2). The induction heater comprises a wire wound around the outside of a cylindrical tube actuator and mist flowing through the inside of this tube. To prevent overheating, the wire used for the induction coil is a hollow copper tube through which there is a flow of cooling water (room temperature in this case).

In conclusion, this paper introduces a thermal model for induction heater and air-mist cooler (Section 2.4). Based on experimental evaluation, unknown input parameters for the model are obtained, such as the heat transfer coefficient, the maximum displacements, and other limitations. Dynamic response is more difficult to determine theoretically and was determined experimentally (Section 2.6).

It is demonstrated that a higher wattage power supply to feed the zero-voltage switching circuit improved the dynamic response (Section 2.6.6). Using the available higher wattage power supply, a trade-off was observed between the higher input power with larger displacement range and the corresponding increase in the controller's steady state RMS error. This increase in steady state error is believed to be due to an inability to extract the heat from the actuator and also an increase in the temperature of the main cooling system's storage capacity (Section 2.7). Other obstacles, such as thermal barriers, thermal limitations of material construction, and controller strategies, are also observed and noted.

In summation, the physical characteristics of the actuator and operating system, the thermal model of the actuator, the operating conditions of the actuator including load, displacement range, and the controller response including resolution and steady state RMS error are presented using two different wattage power supplies in this study (Section 2.8). At the higher heating power, some components of the design became close to failure (the hot glue used for sealing the cooling water through the induction coil begins to melt when the temperature of the induction coil is above 80 Degree Celsius) and therefore the achievable limits of performance with unrestricted heating and cooling power have not been explored.

## 2.2 THEORY OF INDUCTION HEATING

For the purposes of this section, Table 2 lists the values for modeling the expansion tube of the thermal actuator.

Table 2. Material Properties and geometric parameters of the Al actuator tube.

| Properties | Value | Unit |
|---|---|---|
| Thermal expansion (ΔL) | ~200 | μm |
| Coefficient of thermal expansion (α) | $23 \cdot 10^{-6}$ | $°C^{-1}$ |
| Length of the actuator (L) | 120 | mm |
| Young's modulus (E) | $69 \cdot 10^{9}$ | $N \cdot m^{-2}$ |
| Preload force (F) | 1000 | N |
| Outer radius of the actuator (b) | 5.1435 | mm |
| Inner radius of the actuator (a) | 3.4163 | mm |
| Radius of the induction coil ($r_0$) | 8.6485 | mm |
| Permeability (μ) | $1.2567 \cdot 10^{-6}$ | $H \cdot m^{-1}$ |
| Electrical conductivity (σ) | $2.8571 \cdot 10^{7}$ | $Siemens \cdot m^{-1}$ |
| Sinusoidal current ($i_0$) | ~44 | A |
| Thermal conductivity | 203 | $W \cdot (m \cdot K)^{-1}$ |
| Density (ρ) | 2.70 | $g \cdot cm^{-3}$ |

The change in length of the actuator tube varies with temperature changes so that: $\Delta L = \alpha L \Delta T$. Where $\alpha$ is thermal expansion coefficients and it is relatively constant over the range of the temperatures used in this study, $L$ is the length of the tube, $\Delta T$ is the temperature

changes of the actuator between average original temperature and the average working temperature. For an actuator, the axial deformation of the actuator under preload is $\delta = FL/EA_{cylinder}$ , where $A_{cylinder} = \pi(b^2 - a^2)$.

The induction heater comprises a tubular induction coil wound around the outside of the actuator tube, and cooling air or mist flowing through the inner diameter of the actuator tube (Figure 2). The wire for alternating current going through in the induction heater is a hollow copper coil to enable a flow of cooling water through the hole to maintain the coil at a desired temperature. Currents for resistive heating can be produced by applying a voltage across the actuator or by eddy currents from an induction coil, this latter method being chosen for this study.

The current flow along the induction coil will generate a varying magnetic field. And when this changing magnetic field is passing through any conductive object, eddy currents will be induced in the conductive object and thereby generating heat.

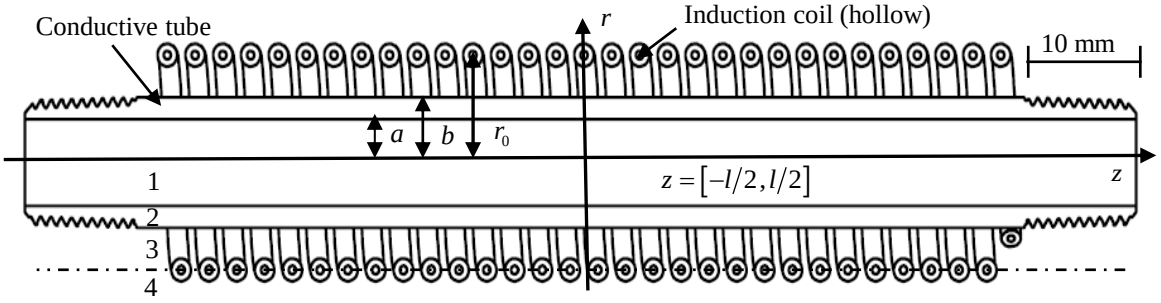


Figure 2. The actuator tube surrounded by the induction coils.

This section describes how to calculate the eddy current by solving Maxwell's electromagnetic equations in a cylindrical conductive tube of finite length. Bessel functions are

used to express the electromagnetic field and the induced current inside the conductive tube. Based on the paper from Dodd and Deeds [12-13], the magnetic vector potential $A$ satisfies the equation

$$\nabla^2 A = -\mu i_0 + \mu\sigma(\partial A/\partial t) + \mu\nabla\left(1/\mu\right)\times\left(\nabla\times A\right). \tag{2.1}$$

Where $\mu$ is the permeability of the conductor, $i_0$ is the current passing through the induction coil that are, in turn, a sinusoidal function of time, $i_0 = i_0^{'} e^{j\omega t}$, $i_0^{'}$ is the amplitude of the sinusoidal current, $\sigma$ is the electrical conductivity of the tube. Figure 2 shows how the induction coils are surrounding the actuator tube. The inner diameter of the tube can be expressed as $a$, the outer diameter is $b$. Because the vector potential is a radial function [12-13], $A(r,z) = R(r)Z(z)$, the governing equation can be expressed in polar coordinates by

$$\frac{1}{R(r)}\frac{\partial^2 R(r)}{\partial r^2} + \frac{1}{rR(r)}\frac{\partial R(r)}{\partial r} + \frac{1}{Z(z)}\frac{\partial^2 Z(z)}{\partial z^2} - \frac{1}{r^2} - j\omega\mu\sigma_i = 0. \tag{2.2}$$

Setting $(\partial^2 Z(z)/\partial z^2)/Z(z) = -\alpha^2$ leads to an independent solution for the area of the conductive tube

$$Z(z) = A\sin\alpha(z - z_0) + B\cos(z - z_0), \tag{2.3}$$

$$R(r) = CI_1[(\alpha^2 + j\omega\mu\sigma_i)^{1/2} r] + DK_1[(\alpha^2 + j\omega\mu\sigma_i)^{1/2} r], \tag{2.4}$$

Where $z_0$ is the position of each coil in the $z$ axis. The solutions in each region can be determined from the following equations:

$$
\begin{aligned}
A^{(1)}(r, z-z_0) &= \int_0^{\infty} C_1(\alpha) I_1[(\alpha^2 + j\omega\mu\sigma_1)^{1/2} r]\cos\alpha(z-z_0)d\alpha \\
A^{(2)}(r, z-z_0) &= \int_0^{\infty} \left\{C_2(\alpha) I_1[(\alpha^2 + j\omega\mu\sigma_2)^{1/2} r] + D_2(\alpha) K_1[(\alpha^2 + j\omega\mu\sigma_2)^{1/2} r]\right\}\cos\alpha(z-z_0)d\alpha \\
A^{(3)}(r, z-z_0) &= \int_0^{\infty} [C_3(\alpha) I_1(\alpha r) + D_3(\alpha) K_1(\alpha r)]\cos\alpha(z-z_0)d\alpha \\
A^{(4)}(r, z-z_0) &= \int_0^{\infty} D_4(\alpha) K_1(\alpha r)\cos\alpha(z-z_0)d\alpha
\end{aligned}
\tag{2.5}
$$

The boundary conditions for this geometry:

$$
\begin{aligned}
&A^{(1)}(a, z-z_0) = A^{(2)}(a, z-z_0) \\
&\frac{\partial A^{(1)}(r, z-z_0)}{\partial r}\Big|_{r=a} = \frac{\partial A^{(2)}(r, z-z_0)}{\partial r}\Big|_{r=a} \\
&A^{(2)}(b, z-z_0) = A^{(3)}(b, z-z_0) \\
&\frac{\partial A^{(2)}(r, z-z_0)}{\partial r}\Big|_{r=b} = \frac{\partial A^{(3)}(r, z-z_0)}{\partial r}\Big|_{r=b} \\
&A^{(3)}(r_0, z-z_0) = A^{(4)}(r_0, z-z_0) \\
&\frac{\partial A^{(3)}(r, z-z_0)}{\partial r}\Big|_{r=r_0} = \frac{\partial A^{(4)}(r, z-z_0)}{\partial r}\Big|_{r=r_0} + \mu I\delta(z-z_0)
\end{aligned}
\tag{2.6}
$$

Solve these above equations

$$
\begin{aligned}
A^{(2)}(r, z-z_0) &= \frac{\mu I}{\pi}\int_0^{\infty} \frac{r_0 K_1(\alpha r_0)}{bD}\left\{\begin{matrix}[\alpha_2 I_1(\alpha_1 a) I_0(\alpha_2 a) - \alpha_1 I_1(\alpha_2 a) I_0(\alpha_1 a)] K_1(\alpha_2 r) + \\ [\alpha_2 K_0(\alpha_2 a) I_1(\alpha_1 a) + \alpha_1 K_1(\alpha_2 a) I_0(\alpha_1 a)] I_1(\alpha_2 r)\end{matrix}\right\}\cos\alpha(z-z_0)d\alpha \\
D &= \left(\begin{matrix}[\alpha_2 K_0(\alpha_2 b) K_1(\alpha b) - \alpha K_0(\alpha b) K_1(\alpha_2 b)][\alpha_1 I_1(\alpha_2 a) I_0(\alpha_1 a) - \alpha_2 I_1(\alpha_1 a) I_0(\alpha_2 a)] + \\ [\alpha_2 K_0(\alpha_2 a) I_1(\alpha_1 a) - \alpha_1 K_1(\alpha_2 a) I_0(\alpha_1 a)][\alpha I_1(\alpha_2 b) K_0(\alpha b) + \alpha_2 I_0(\alpha_2 b) K_1(\alpha b)]\end{matrix}\right)
\end{aligned}
\tag{2.7}
$$

From the equation above, set $z_0$ equals 0, the induced eddy current density can be calculated into

$$
J(r, z) = -j\omega\sigma A(r, z). \tag{2.8}
$$

With the given constant current $I$ (1 A), the higher the frequency of the induction heater, the higher the induced eddy current will be (Figure 3).

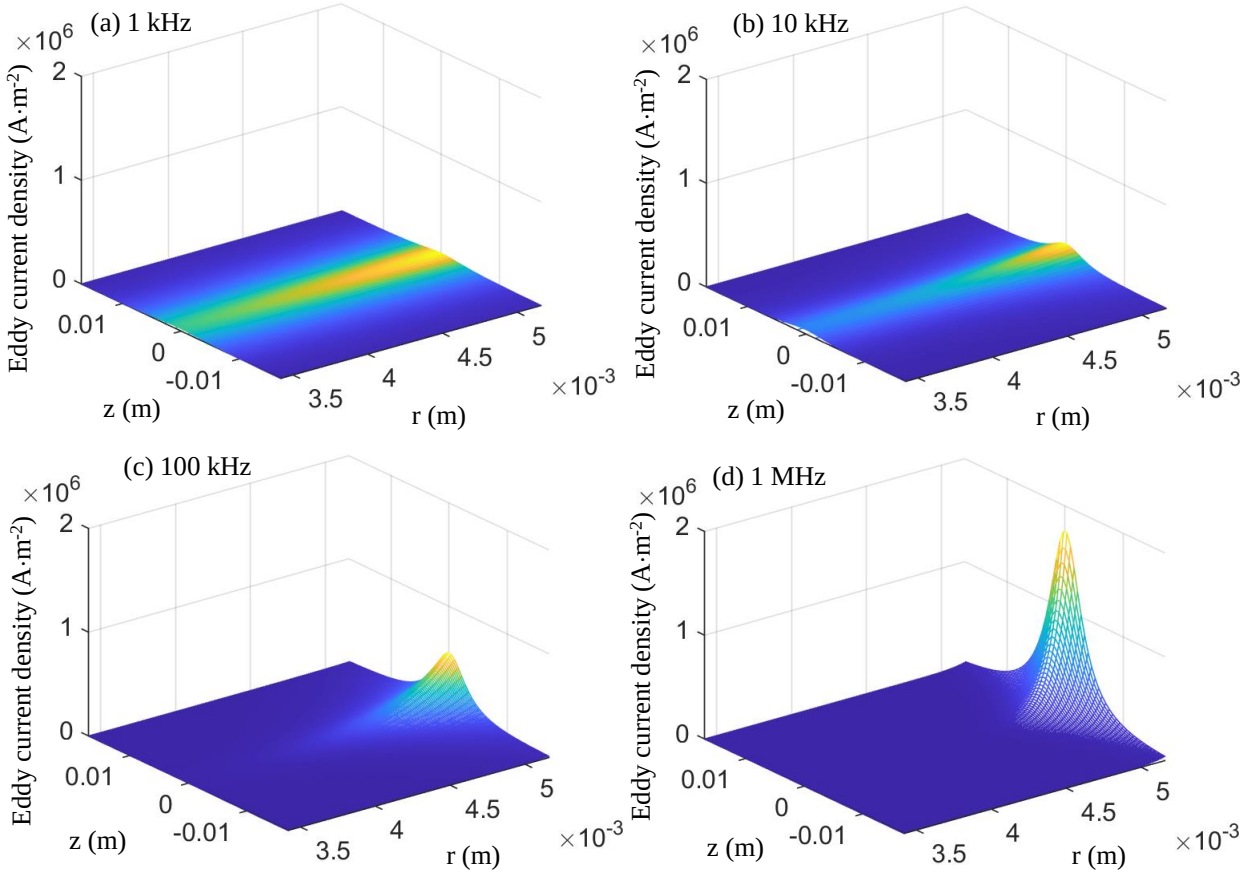


Figure 3. Frequency responds eddy current density.

Figure 3 shows that the eddy current (1 A) is increasing as the frequency increases (1 kHz, 10 kHz, 100 kHz, and 1 MHz). The surface fitting of the induced eddy current density is as follows:

$$J(r,z) = a_1 \mathrm{e}^{(b_1 r - c_1|z|)} \tag{2.9}$$

The unit area eddy current inside the actuator tube is

$$di = J(r,z)dA = J(r,z)drdz \tag{2.10}$$

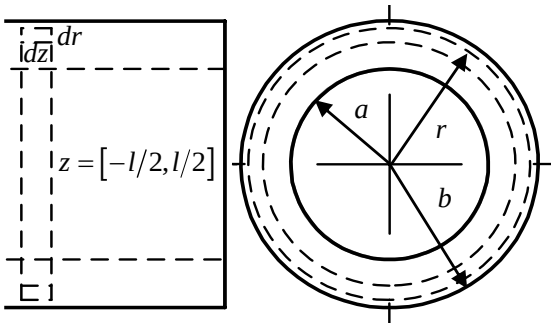


Figure 4. Elemental current analysis in actuator tube.

Equation (2.10) can be integrated to compute the total induced eddy current around the actuator for a single turn coil. Integrating first from the inside radii of the actuator to the outside radii, then from the symmetric $z = 0$ to the overall half-length of the actuator, one of the induced eddy currents can be calculated in Equation (2.11), and the induced eddy current from 1 A resonant current is plotting in Figure 5.

$$i = \int_{-l/2}^{l/2} \int_{a}^{b} J(r,z)drdz = 2\int_{0}^{l/2} \int_{a}^{b} J(r,z)drdz. \tag{2.11}$$

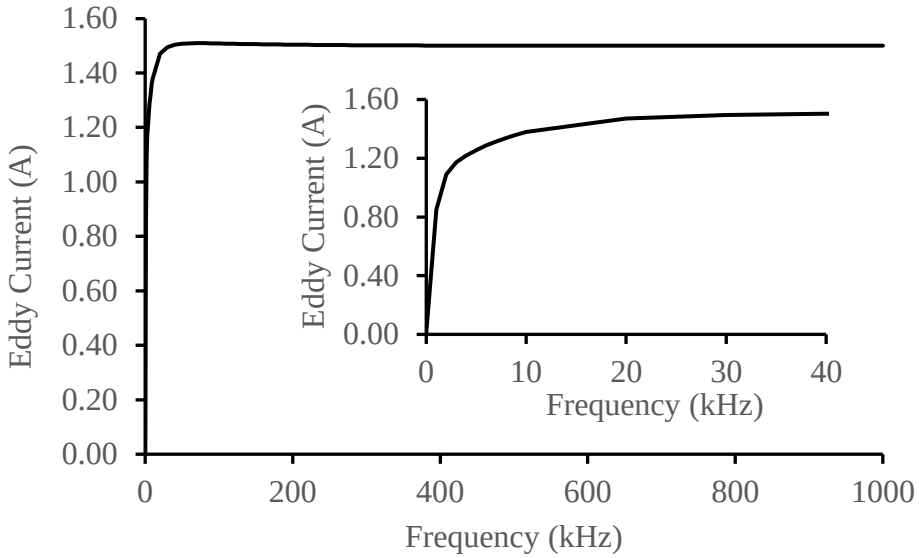


Figure 5. Induced eddy current increases with frequency increases, 1 A resonant current.

Considering Figure 4, each elemental area in the cross-section of the actuator tube will contain an elemental current $di$ that will traverse circumferentially around the tube axis for which the resistance $dR$ is

$$dR = 2\pi\rho r / (drdz). \tag{2.12}$$

For each element, the power generated by a single induction coil in the form of heat is

$$d\dot{Q}_{gain} = (di)^2 dR = 2\pi\rho r J(r,z)^2 drdz. \tag{2.13}$$

The heating power generated inside the tube by $N$ coils can be computed from the following equation

$$\dot{Q}_{gain} = N\int_{-l/2}^{l/2}\int_{a}^{b} 2\pi\rho r J(r,z)^2 drdz. \tag{2.14}$$

From the computing of Equation (2.14), the heating power induced from a single induction coil is can be calculated when the parameters $N, l, a, b$ are given. The total heating power from N coils using a known current at resonant frequency will be plotted out. A least-square fit (R-square) of the eddy current density generated by N coils is:

$$J_{fit,Ncoils}(r,z) = a_n e^{(b_n r)} \Big/ \left(1 + e^{\left(c_n(|z|-d_n)\right)}\right). \tag{2.15}$$

Figure 5 shows the higher the excitation frequency of the induction coil, the higher the induced eddy current. Beyond an induction coil excitation frequency of around 30 kHz, the induced eddy current amplitude increases relatively slowly. Meanwhile, as can be seen from Figure

3, the skin depth $\delta \approx \sqrt{2/\omega\sigma\mu}$ decreases as the frequency increases, and this localization of the eddy currents causes the heat generation to steadily increase. As a general rule, higher frequency is more efficient. However, the efficiency gain becomes less significant when the frequency is beyond the threshold frequency, 300 kHz. As shown in Figure 6, there is a rapid increase in the power before a frequency of 300 kHz (above this value, gain is linear). As the frequency increases, the skin depth decreases leading to a significant radial temperature gradient in the actuator tube. In this experimental, the alternating current through the hollow copper wire coil will be tried in the range of 200 kHz to 400 kHz.

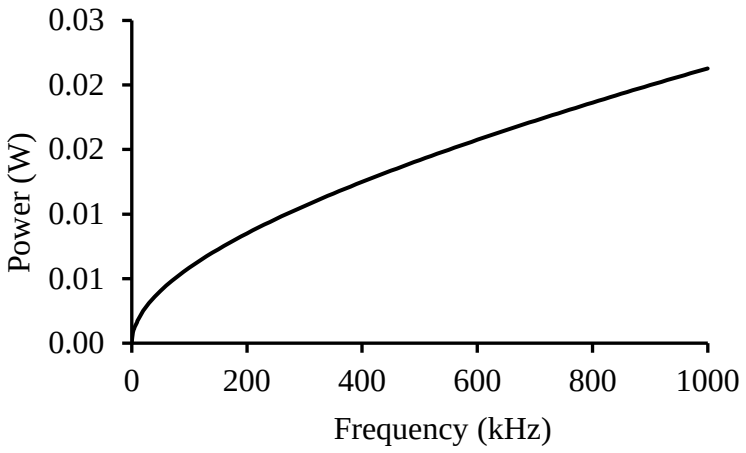


Figure 6. The induced heating power as a function of excitation frequency.

## 2.3 FIRST DESIGN AND PROTOTYPE

The original design of a thermal actuator used a nichrome heating element for conductive and radiative heating of the actuator tube, see Figure 7.

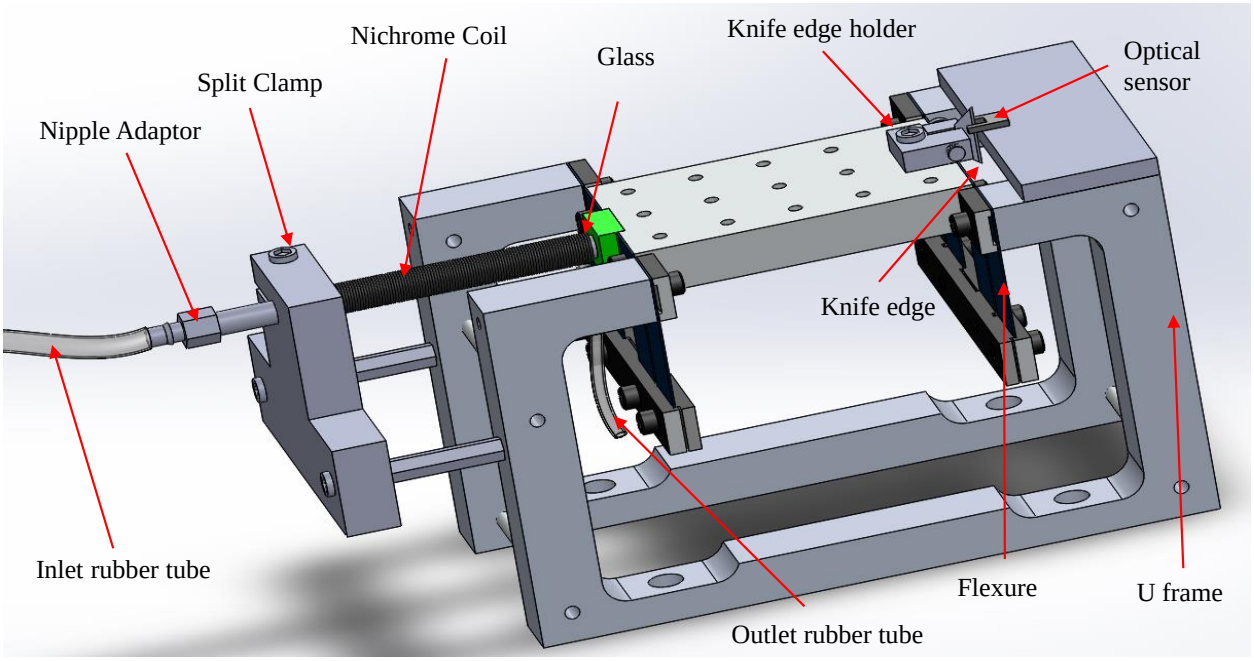


Figure 7. Original design of the thermally actuated translation stage.

A flexure-based stage was used in the original design of the thermally actuated translation stage. The first prototype is made of a monolithic Aluminum structure. And the overall design of the flexure system can be divided into 4 basic sections: heating system (Nichrome wire joule heating), Cooling System (pumped water cooling), flexure support structure (flexure-based translation stage and U frame), and knife-edge optical sensor (Figure 7). The performances of the thermal actuator, and optical displacement sensor are evaluated in this section. The finite element analysis (FEA) is used to estimate the deformation of the computer-aid design (CAD) modeled flexure support structure. The control system is explained in section 2.3.7.

### 2.3.1 HEATING SYSTEM

The heating system consists of Ni-Cr wire of 1.6 mm diameter wound around an Aluminum tube, as showing in Figure 8. The aluminum tube of length 150 mm was used to get the required displacement of the flexure. The inner diameter and outer diameter of the aluminum tube is 0.305

inches and 3/8 inches respectively. The wire was coiled around an aluminum tube so that the heating could be radiated toward the tube actuator. A split clamp was used to hold the aluminum at one end and to restrict the expansion of aluminum to just one side. The other end of the aluminum tube is connected to the flexure block through a multi layered sandwiched glass insulator with air in between the layers for better insulation.

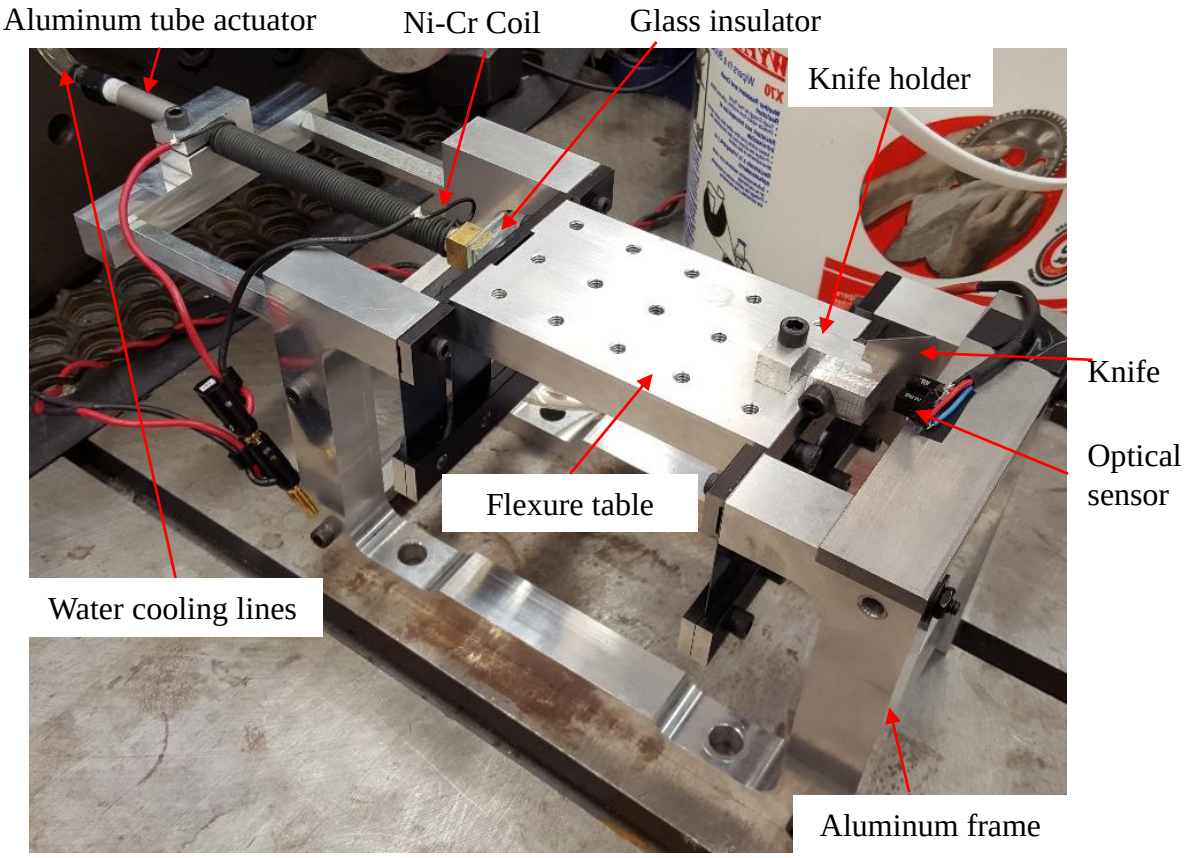


Figure 8. The heating system consists of Ni-Cr wire of 1.6 mm diameter wound around an Aluminum tube.

### 2.3.2 COOLING SYSTEM

The tube actuator was threaded on one side for attaching a nipple adaptor for the rubber tubing, which was used for passing cooling water through it as shown in Figure 9. The cooling water supply was pumped by a DC motor through high temperature resistant rubber inlet to the

hollow Aluminum tube to control its temperature. And the flow rate of the water was controlled by the voltage of the motor, which was in turn controlled by the motor driver in the Control system block in section 2.3.7.

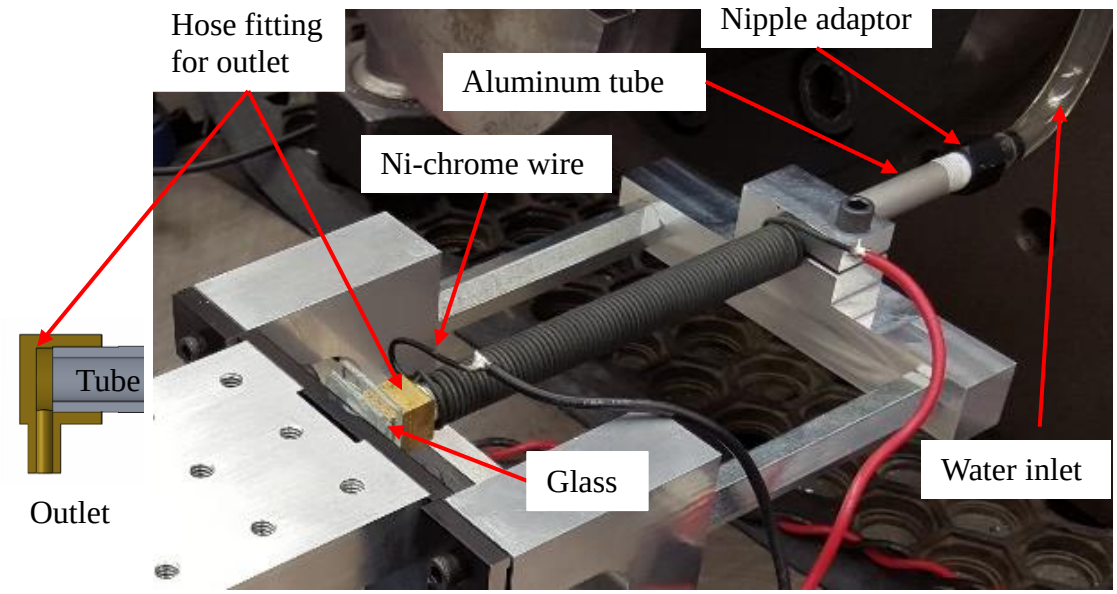


Figure 9. A nipple adaptor is threaded on one side of the tube used for passing cooling water into, another end is threaded on hose fitting for the outlet.

### 2.3.3 THERMAL EVALUATION

After the model was assembled, the actual working state of each component was verified. The heating system was run independently to find out the maximum temperature that could be reached by the original aluminum rod actuator, the time required and the expansion of rod due to this heating. A FLIR thermal camera was used to measure the temperature of the nichrome wire as shown in Figure 10, and A LM35 temperature sensor was attached to the hose fitting of the thermal actuator. By applying a 3.5 A current through the Ni-Cr wire, it was found that the wire temperature reached 140 degree C after heating for 120 seconds, after which this temperature remains constant. Several tests were conducted to validate the claims of the original model for 100

um range and this was found that this displacement can be achieved with a response time of around 40 seconds.

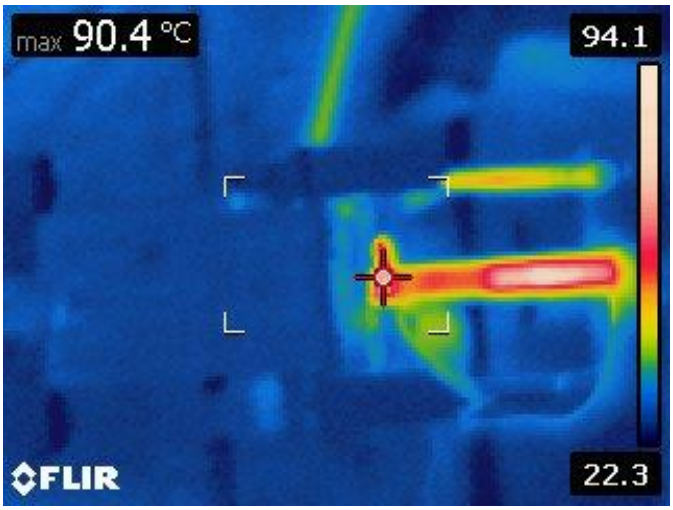


Figure 10. A FLIR thermal camera was used to measure the temperature of the nichrome wire.

### 2.3.4 OPTICAL SENSOR EVALUATION

A RPI0352E optical knife-edge sensor, a circuit board, and an aluminum hex bar optical sensor mount are assembled together. A complete Solidworks model of the opto-sensor design is showing in Figure 11.

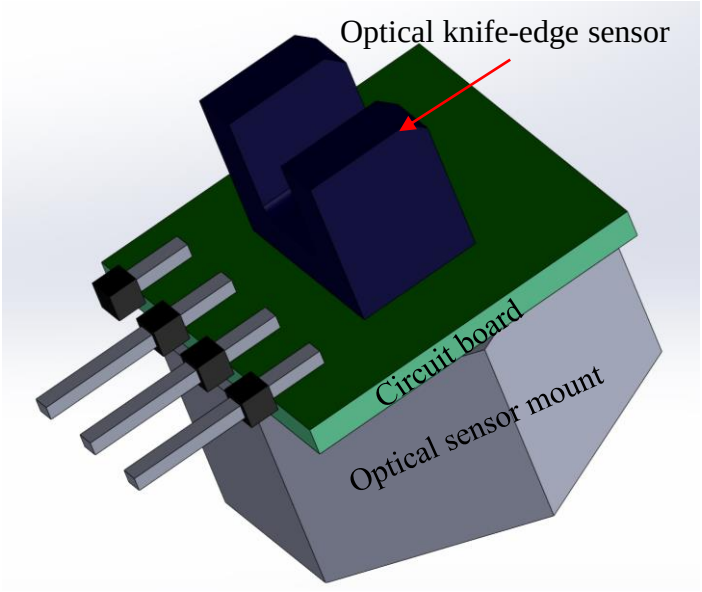


Figure 11. Solidworks model of the optical knife-edge sensor (Rohm RPI0352E).

The RPI0352E is a compact trans-missive sensor that includes an infrared emitter (pin 8 and pin 1) and a phototransistor detector (pin 4 and pin 5), located face-to-face in a surface mount package. A 2 kΩ resistor is used to control the current flow of the emitter so that it will has relative high infrared light intensity without overheating flow. A potentiometer is used for the detector end so that the voltage range is between 0 to 5 V while the infrared beam were fully blocked or not blocked by the knife-edge. Figure 12 shows the circuit of the optical knife-edge sensor (left) and how the knife-edge sensor is working (right). Based on the percentage of the beam (intensity of the light) transfer to the detector, the voltage will be different. Then the movement of the knife-edge along the beam path, will be recorded as a voltage.

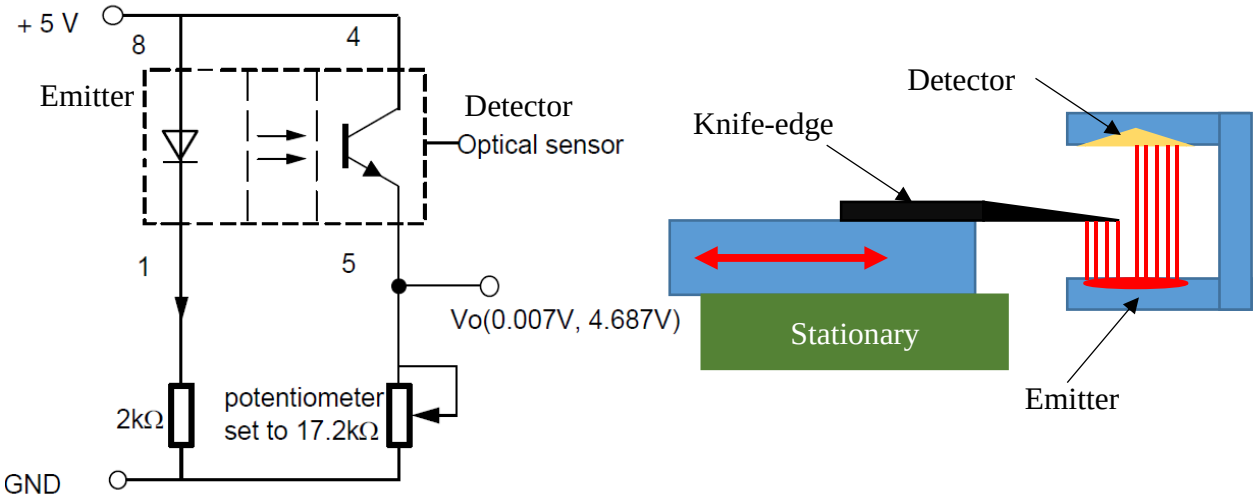


Figure 12. The circuit of the optical knife-edge sensor (left) and how the knife-edge sensor is working when the beam was fully blocked or not blocked by the knife-edge (right).

The optical knife-edge sensor will be evaluated by comparison method with a known reference displacement equipment. For instance, an Aerotech ABL 10100-LT positioning stage was used as the known displacement/positioning system. This stage has a manufacturer claimed positioning uncertainty of +/- 0.2 $\mu$m and a displacement measurement resolution of 0.5 nm. Figure 13 below shows all of the equipment that was used for this evaluation.

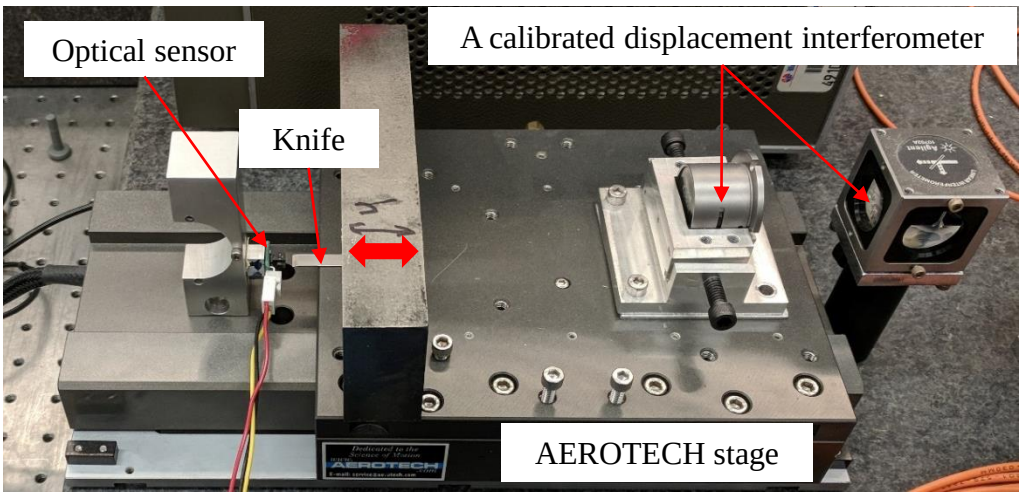


Figure 13. The optical displacement interferometry equipment and the AEROTECH stage are used for evaluation of knife-edge sensor.

The maximum range of the optical sensor mounted on a micrometer gauge for test purposes was found out to be 1000 µm (Figure 14 top). In this range, the sensor showed linear behavior between 300 µm and 500 µm (Figure 14 bottom). Hence this range (200 µm) of the optical sensor was taken as the working range of the sensor. The voltage response of the sensor with change in displacement is shown in Figure 14.

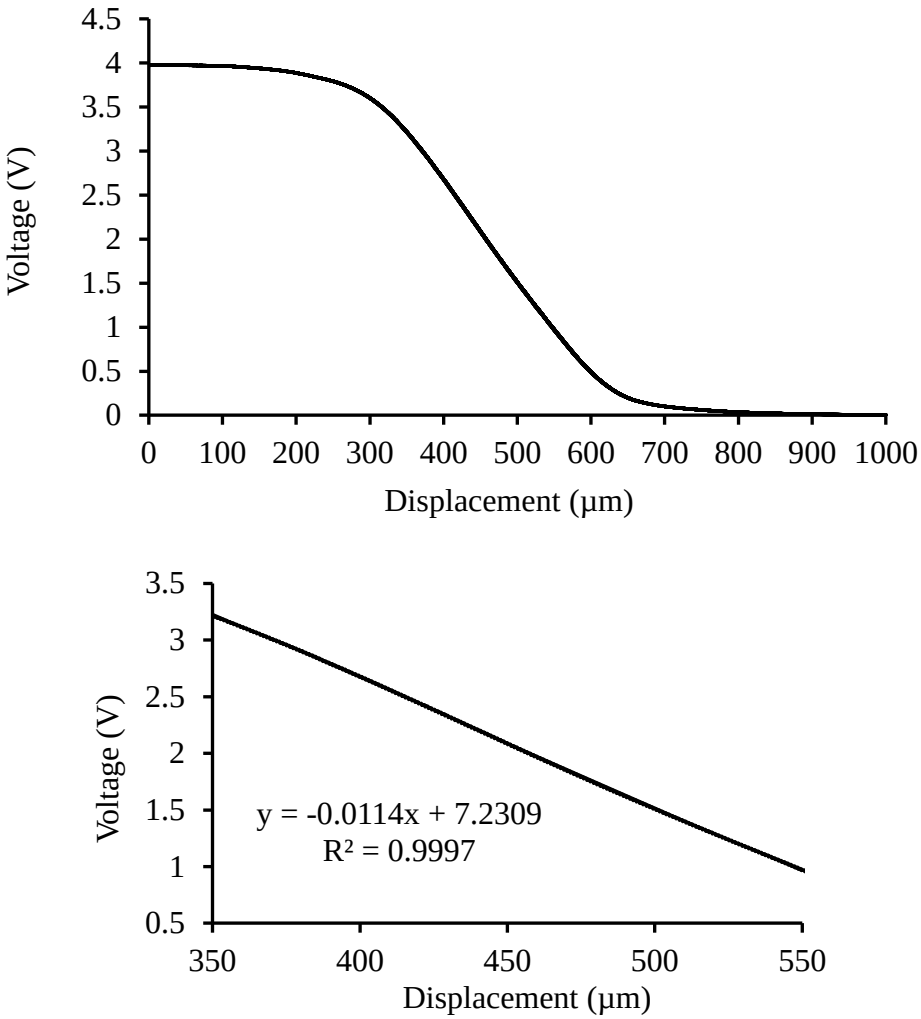


Figure 14. Top: Voltage v/s Position response of IR optical sensor for complete range. Bottom: Voltage v/s Position response of IR optical sensor for linear range.

### 2.3.5 FLEXURE TRANSLATION STAGE EVALUATION

The flexure translation stage includes U frame stage mount, translation stage, leaf springs, and fasten screws, in Figure 15. The stage mount was made from two milled aluminum U frames, which were used to fasten the translation stage together with the leaf springs. The flexure-based translation stage, which was the element that translates in the desired linear motion, is also machined from a solid aluminum block. Several holes in uniform fashion are bored into the stage for attaching the required mechanism on top of the block. The spring system is made of thin leaves of spring steel with clamp, which was used to constraint the translation stage in one degree of freedom.

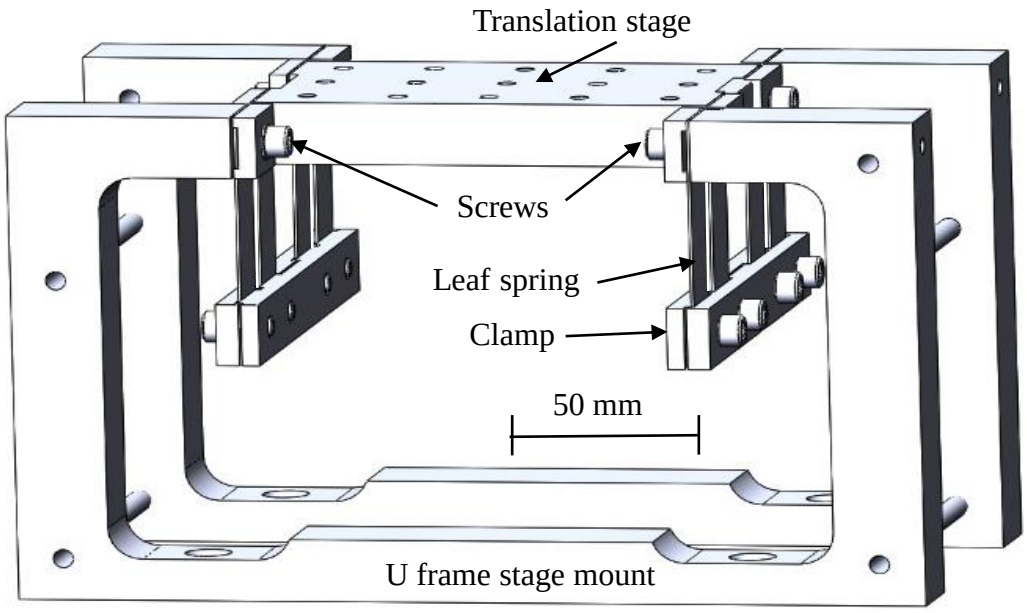


Figure 15. A CAD model of the flexure-based translation stage.

The leaf springs are manufactured from hardened steel sheet, and the total stiffness of the flexure structure [25] is calculated as $K = 24EI/L^3$, where $E$ is the young's modulus, $I$ is the second moment of area about the neutral axis of the leaf spring, and $L$ is the length of each leaf

spring (Table 1). Figure 15 shows the solid model of the translation stage comprising a single degree of freedom linear, folded, double compound flexure stage, a variant of the design in [26].

There was a possibility that the flexure block may deviate from the intended linear path due to the line of action of the actuator and the spring not exactly aligned. The original flexure stage was tested for this deviation using a laser interferometer by mounting it on a Monarch CNC Milling Machine bed in the Metrology Lab of Duke Centennial Hall Room 126. For the straightness measurement, an actuator rod, connected with the spindle (rotation locked) of the milling machine, will give a driven force to the translation stage so that the stage will moves forward or backward. The polarized beam splitter (PBS interferometer), a retroreflector, and a mounting fixture was assembled, and they were fixed together with the U frame structure by using epoxy, metal block and C clamp. Another retroreflector was fixed together with the moving translation stage. When the actuator gives a 100 μm forward or backward movement, the laser interferometer records the straightness error along this range. Figure 16 shows the set-up of the straightness measurement of the translation stage, and the right side of the picture is the carton explanation of how the system works.

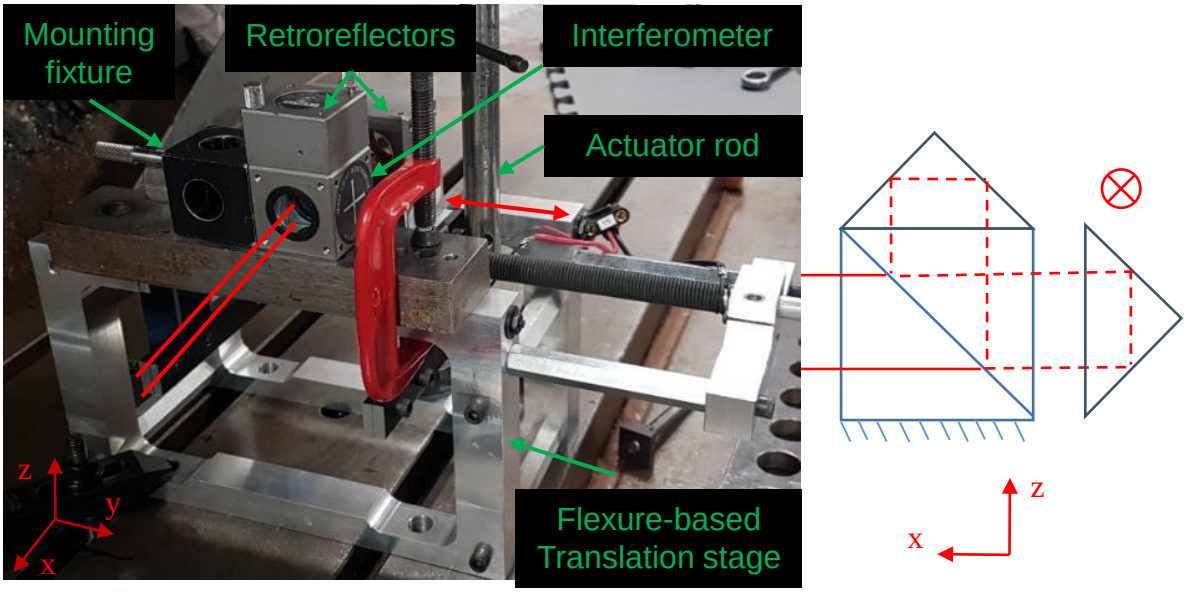


Figure 16. Straightness error measurement using a polarized beam splitter as the interferometer.

The angular interferometer was glued with the U frame, and the angular retroreflector was glued with the stage. When the actuator rod drives the stage forward or backward, the angular error of the y axis (pitch), and z axis (yaw) will be measured from the laser interferometer. Figure 17 and Figure 18 show the setting up for the pitch and yaw characterization.

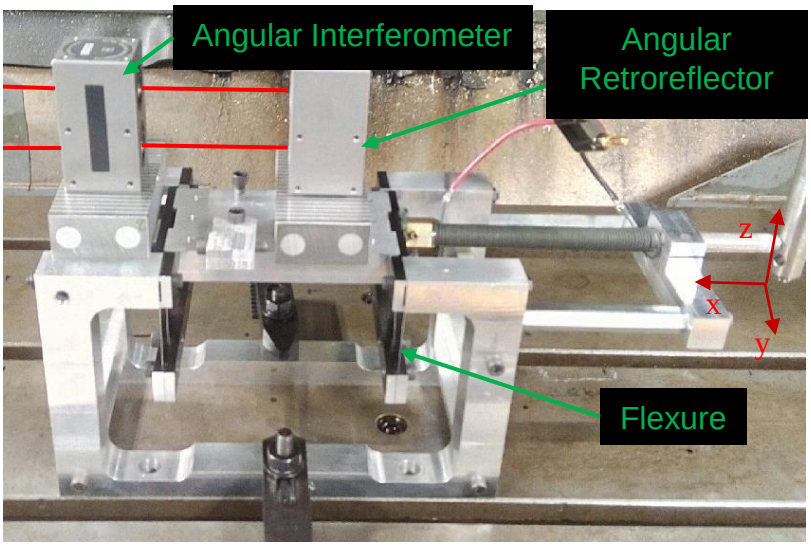


Figure 17. Pitch error measurement flexure-based translation stage.

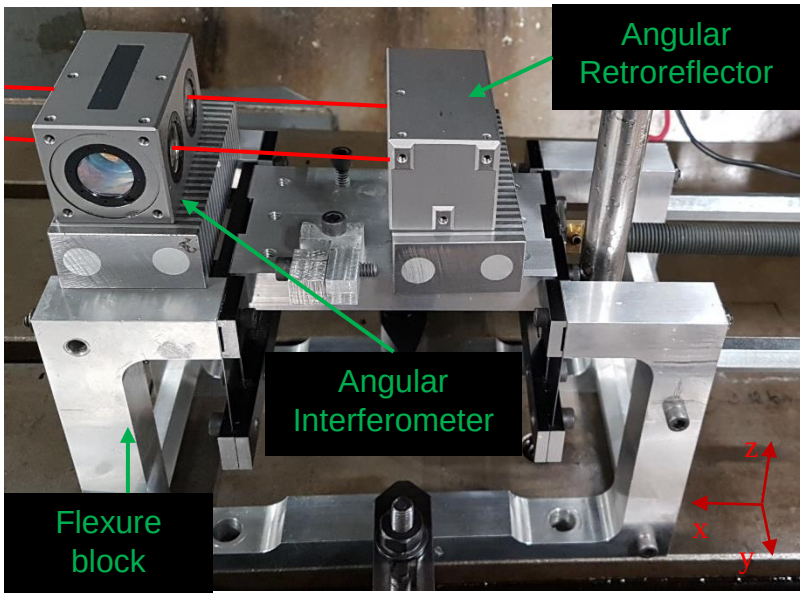


Figure 18. Yaw error measurement flexure-based translation stage.

From this test, the mean straightness error was found to be 0.122 µm, the mean pitch error was found to be 0.54 arc-sec and a mean yaw error of 0.62 arc-sec over a range of 100 µm.

### 2.3.6 CAD MODEL SIMULATION

The CAD model of the original design was analyzed for the new desired goal of 1000 N load capacity. The analysis was done using SOLIDWORKS. The results of the analysis are shown in Figure 19.

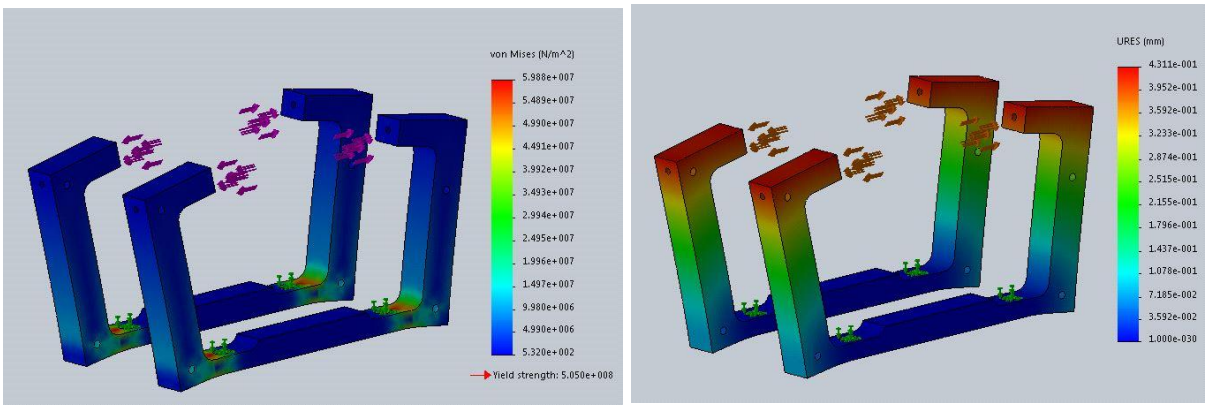


Figure 19. FEA von Mises and Deflection Analysis of Original Base structure

The maximum displacement was found to be 400 µm on one side and 800 µm on both sides, which is unacceptable in comparison to the desired range of the flexure of 100 µm. Hence, the original frame clearly cannot support the proposed load of 1000 N load without also undergoing significant deformation.

### 2.3.7 CONTROL SYSTEM

Figure 20 shows the block diagram of the control system. The control system block includes PID controller using LabVIEW, myRIO, pump, power amplifiers, flexure-based actuator stage, optical knife-edge displacement sensor, and external ADC. The linear displacement of the flexure block was measured by means of an optical knife-edge sensor. The sensor was mounted on to the base structure. The knife-edge was mounted on the flexure block by means of a knife-edge holder made of 6061 aluminums, which holds the blade in the passage between the block, which was tightened by a screw. The sensor has a response of change in voltage with respect to the change in intensity of light passing though the sensor. This intensity of light was controlled by the penetration of knife-edge due to translation of moving block into the sensor area resulting in voltage change proportional to the displacement of the flexure black relative to the frame. The output voltage of the optical sensor was connected to the myRIO, which has an ADC card, that converts the analog signal from the knife-edge sensor into a bit value that was calibrated and converted into a displacement.

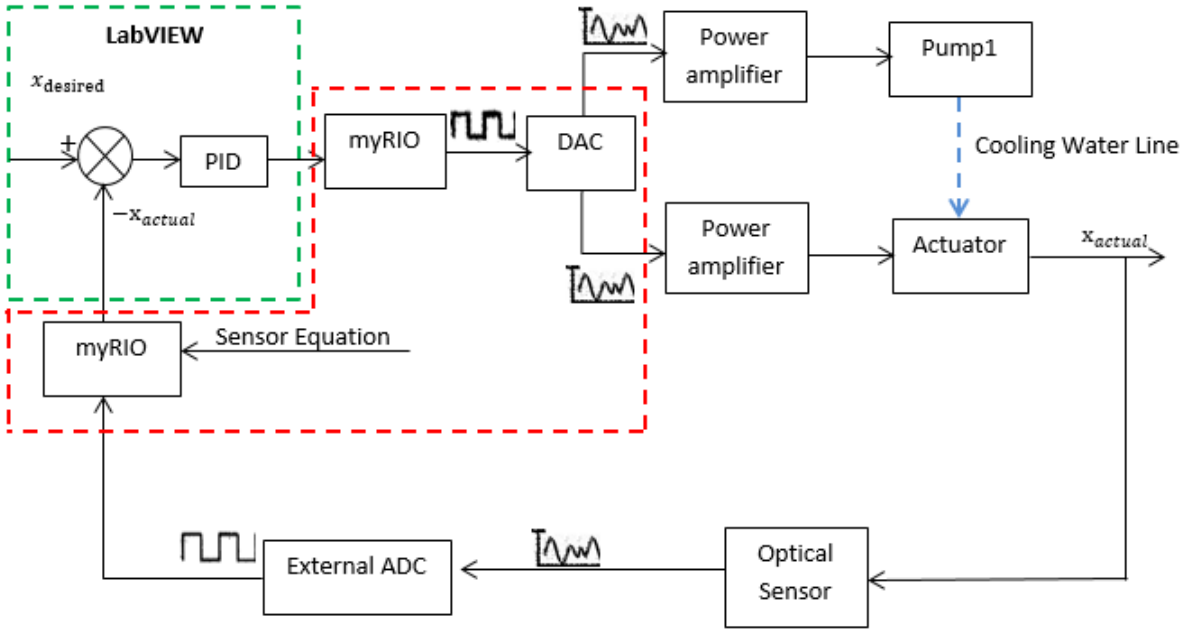


Figure 20. Block diagram of the control system.

LabVIEW has a built-in PID algorithm, that receives the error between the desired position and current position of the flexure from the optical sensor. The output of the PID is then sent to the Digital to Analog converter, which converts digital signals to analog. Closed loop controller is used for minimizing the position error by adjusting the current of the heating power amplifier and the current for control the flow of the pump1. When the actual measured position is smaller than the desired position, the current of the amplifier for the heating will increase, and the current for the pump1 will decrease. When the actual position is larger than the desired position, heating current will decrease, and the cooling current will increase.

## 2.4 SECOND DESIGN

It was found that the original design of the U frame structure was not compliant. For instance, there was risk of lost motion as the aluminum rod is expanding. Hence, a stiffer frame is designed and is described in section 2.4.1.

A spring preload structure was designed and coaxial aligned with the actuator. This new design includes a knob and a compression spring preload structure. More details will be explained in section 2.4.2.

As the temperature of the actuator increased, the heat could transfer to the nearby frame and stage since of thermal conductivity, and this will cause non-uniformed deformations to the system. A new cooling system for maintaining the temperature of the frame and stage is designed and is described in section 2.4.3.

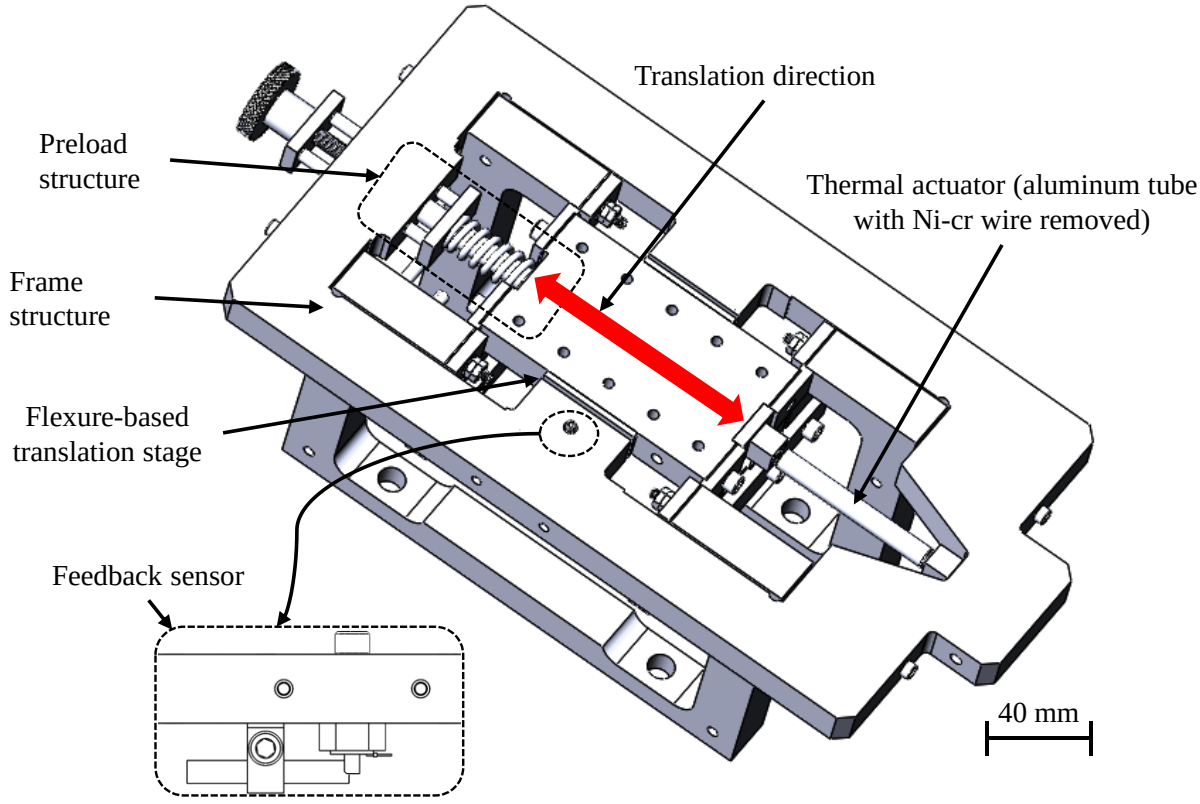


Figure 21. Solid model of the translation stage showing the thermal actuator without induction coil. Inset view shows knife-edge displacement sensor located on the underside of the stage.

Figure 21 shows the solid model of this thermal actuator. The overall final design includes frame structure, flexure-based translation stage, preload structure, feedback sensor, heating system, cooling system (with thermal isolation) and control system.

### 2.4.1 DESIGN OF THE NEW FRAME

To increase the frame stiffness, a monolithic design was selected its detailed designs for the holes are labeling in the Figure 22 and their functions are discussed in section 2.4.2 and 2.4.3 as well.

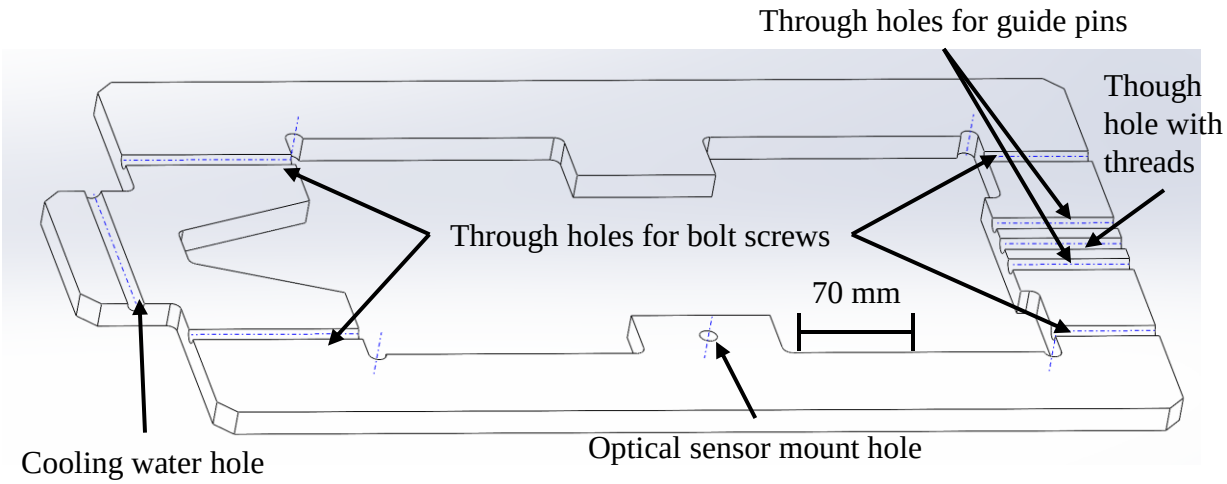


Figure 22. CAD Cross section view model of outer frame.

The material of the frame was to be decided between steel and aluminum. Therefore, for both materials the frame were simulated in SOLIDWORKS under 1000 N load assuming that the base structure is rigid body. The FEA deflection analysis of aluminum (Figure 23 left) & steel (Figure 23 right) frames is shown below:

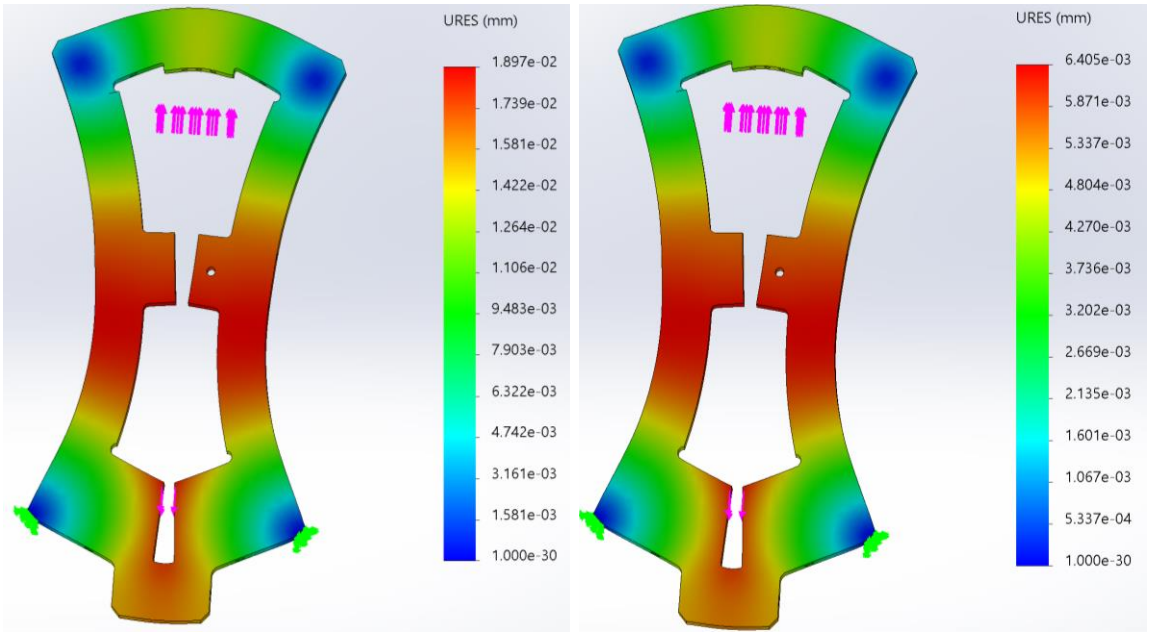


Figure 23. Left: FEA Deflection Analysis of Aluminum frame shows a maximum deformation of 19 µm. Right: FEA Deflection Analysis of Steel frame shows a maximum deformation of 6 µm.

As the steel frame with a low deflection of 6.4 µm, showed result that is more promising than the aluminum deflection of 19 µm. In this design, steel was selected as a frame material with the only downside being the increase in the weight of the block.

The deformation of the main frame and stage mount structure (two ‘U’ shaped frames) were taken into consideration as they contributes the main deflection of the system. For that, assembly of the stage mount structure and the reinforcing frame was assembled and simulated together as well. The FEA stress and the deflection analysis of the assembled CAD model was analyzed under 1000 using SOLIDWORKS. The results in Figure 24 show that there is no stress concentration inside the structure, and the total deflection was found to be 6 µm or 3% of the maximum actuator expansion range of 200 µm.

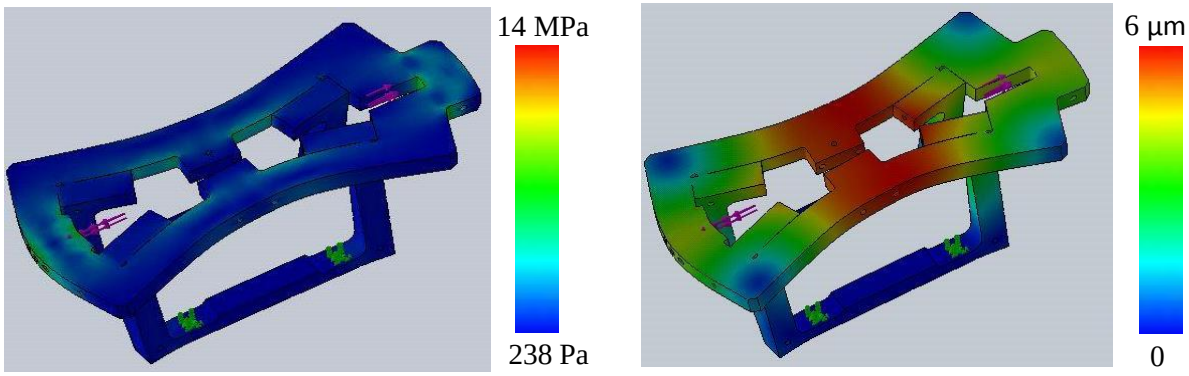


Figure 24. FEA analysis of the assembled frame and U frame structure: Left) FEA von mises stress shows a 14 MPa maximum stress at the load area. Right) FEA deflection analysis shows 6 µm maximum deformation at the center area of the frame.

### 2.4.2 DESIGN OF THE PRELOAD STRUCTURE

A spring was guided using a rod attached to the frame so that the spring action is colinear with both the frame and the moving block as shown in Figure 25. The spring was compressed using a screw, which is present at the outer end of the frame. This knob is in contact with a plate, which transfers the linear motion of the knob from the outer end of the frame to the inside spring end of the frame by two guide pins. This block has two 'blind' holes (cavity) to accommodate the guide pins. On the opposite end, i.e. on the inner side of the frame is a dimensionally similar plate with identical holes for transferring the guide pins' motion to the spring except. On the inner-frame plate we have a 'through' central hole so that the guiding rod for the spring can pass through the plate. The knob moves inside or outside the frame per direction of rotation. This linear motion of the knob pushes the guide plates, compressing the spring. Hence, by tightening the knob the preload acting on the spring can be used to creating variable loads.

Even though the above deformation values are negligible for the original frame, it was difficult to predict the error motion of the flexure block at the design stage. Hence two holes were

drilled on the frame's central section, so that four oval guide pins can be inserted to guide the flexure block. This arrangement reduced the possibility for yawing error motion of the flexure.

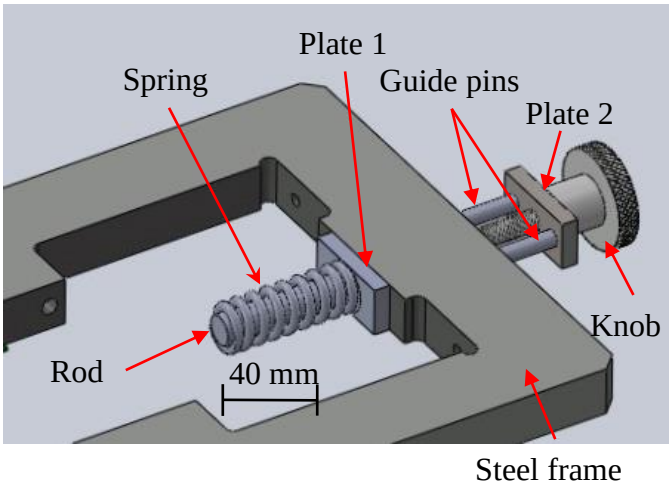


Figure 25. CAD Model of Spring, two blocks and guide pins assembly.

In addition, a compression spring was introduced on the actuation (output) side of the flexure connecting the flexure block and reinforcing frame. The stiffness of the spring was selected as 294.81 lbs. /in. (51.62 N/mm). The required loading of the spring was 225 lb (1000 N), requiring a compression distance of 0.76 in (19.3 mm).

### 2.4.3 DESIGN OF THE COOLING SYSTEM

In the new monolithic design, the outside frame is in direct contact with the actuator (Aluminum rod) through the hose fitting. This induces a possibility of change in the dimensions of the frame as well as thermal fatigue. To avoid this, a hole was drilled through the frame (see Figure 26) close to the contact point with the actuator as shown in Figure 26a so that cooling water can pass through this hole to maintain the frame at a constant temperature. In order to incorporate cooling system, two 0.25" holes 0.375" deep were drilled from the bottom side of flexure stage as well (Figure 26b). Further, to connect these holes together, a horizontal 0.25" hole was drilled

from one side. Figure 26 shows that two holes in the frame and the stage were drilled so that cooling water could be pumped through to maintain the frame and stage at a constant temperature to avoid any thermal deformation. During the experimental test, the temperatures of the frame and the stage were recorded. Figure 27 shows that the temperature sensors mounted on the frame and the flexure block.

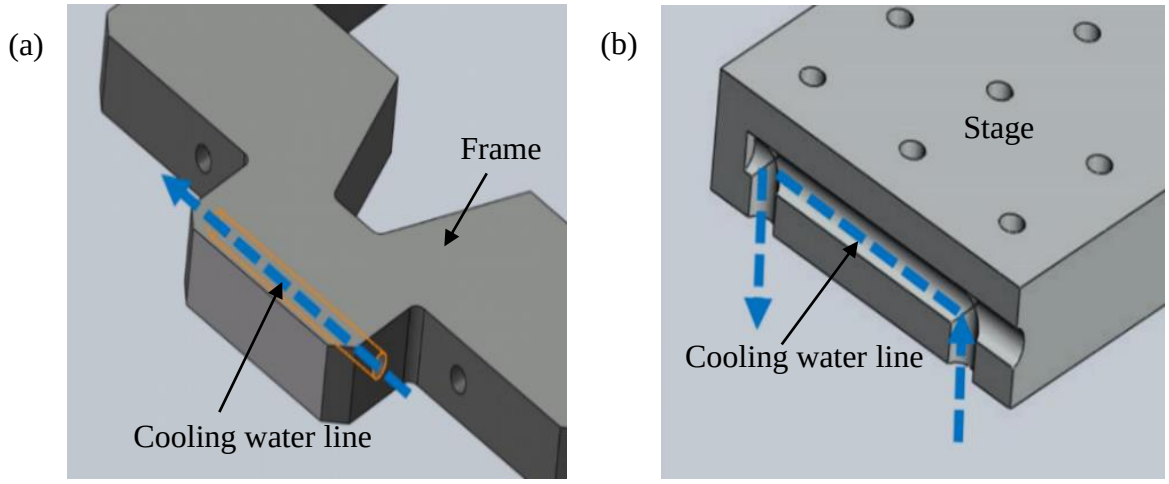


Figure 26. Holes on frame and flexure block: (a) Cooling water line inside the frame (b) Cooling water line inside the translation stage.

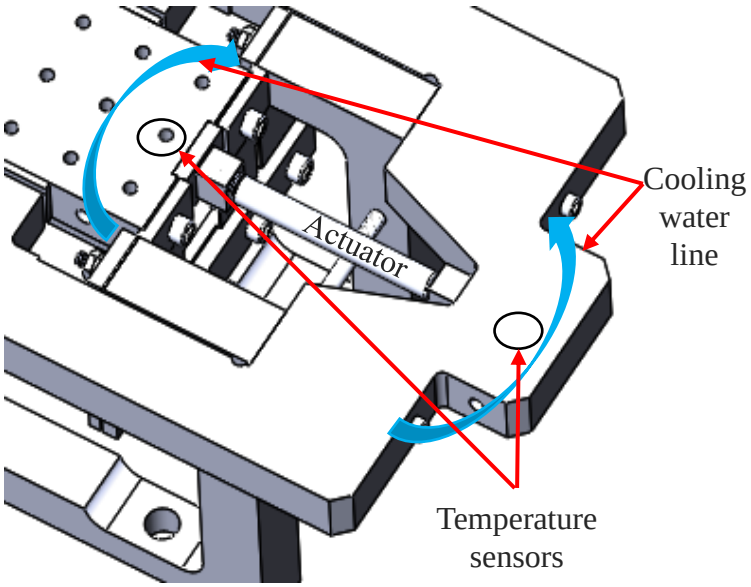


Figure 27. Thermal isolation by mounting temperature sensors at bottom of frame and table.

## 2.5 MANUFACTURING OF SECOND DESIGN

The manufacturing for the second design include the made of steel frame, preload structure, knife holder and optical sensor by using Hass CNC machine and Lath.

### 2.5.1 STEEL FRAME

Manufacturing of the reinforcing frame used a Hass CNC machine from a stock 1018 steel plate having dimensions of 0.75”x8”x24” and cut to approximately 15” in length for the milling operation. The profile of the part was milled using a pocketing tool path with a 0.75” carbide end mill and a finishing pass was made with a 0.25” ball end mill. A vertical through-hole was drilled on the CNC set-up for mounting of the optical sensor. The inner profile was enlarged by 0.05” from the initial cut profile on a Bridgeport conventional milling machine using a 0.75” HSS end mill. Holes were drilled on the Bridgeport using a 0.25” extended drill bit, a standard 0.25” drill bit. Tapped holes were made using 5/16-24 relieved tap and a 1/4-20 HSS tap. Figure 28 show the manufactured steel frame structure.

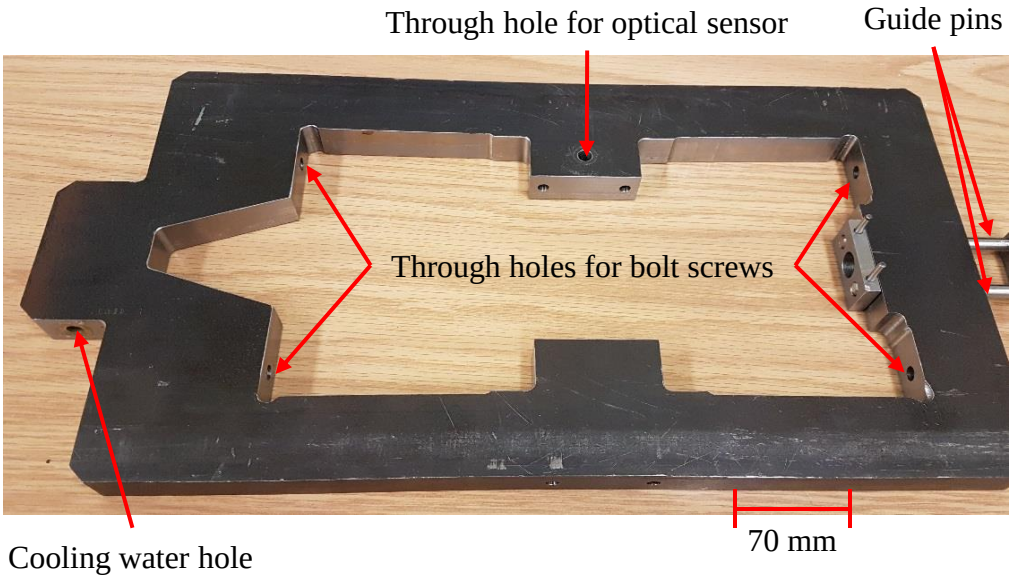


Figure 28. Steel frame structure made.

### 2.5.2 PRELOAD STRUCTURE

Both plates were manufactured on the Bridgeport conventional milling machine from 0.25”x0.75” high-tolerance mild steel bar stock. Cutting tools used were a 0.75” HSS end mill and specific drills for clearance specifications per part drawings. Dowel pins (guide pins) with 0.25” OD were prepared and clamped using a collet block, allowing for a 1/8” hole to be drilled and reamed at both ends at the holes. The assembly was pressed together using 1/8”x1.25” dowel pins connecting the guide plates to the guide pins. And Figure 29 shows the assembled preload structure using knob, guide plates, guide pines, compression spring, and spring guide rod.

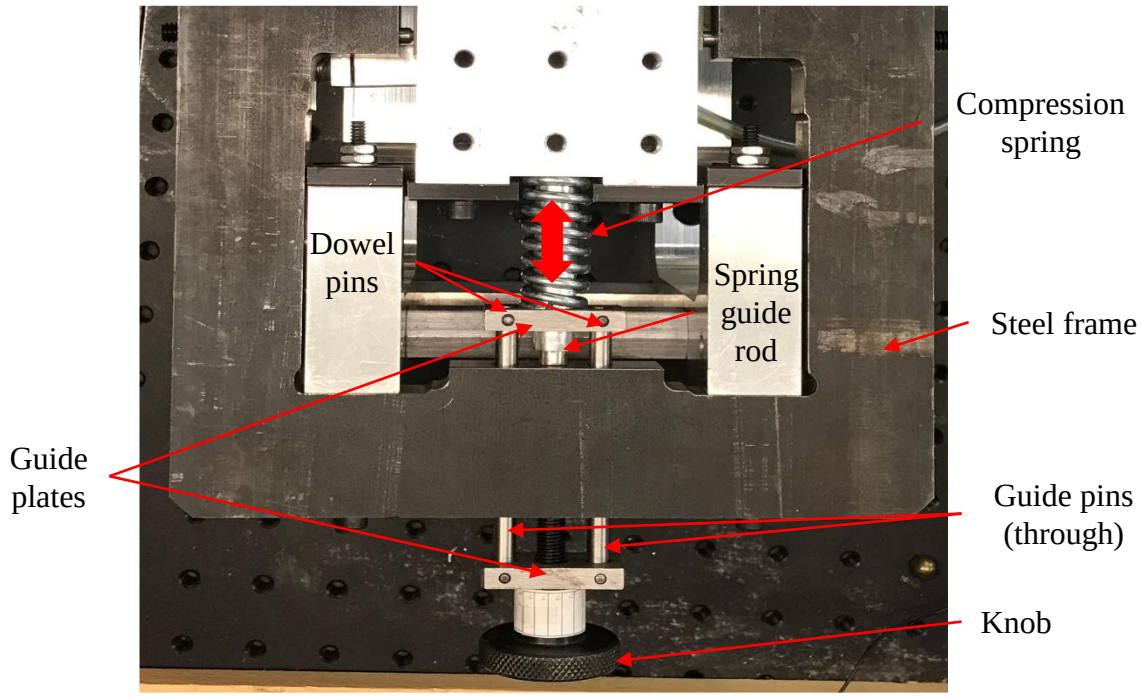


Figure 29. Preload structure assembled using knob, plates, guide pines, compression spring, and guide rod.

To guide the spring along the desired direction of the applied force and flexure motion, a spring guide was manufactured. Figure 30 shows the spring guide rode was machined on a manual

lathe from 0.5” OD Aluminum rod stock. On the mounting end of the guide 5/6-24 threads were made to fix it to the frame.

Figure 30. Spring guide rod.

### 2.5.4 KNIFE HOLDER AND OPTICAL SENSOR

The knife holder shown in Figure 31 (left picture) was used for holding the knife in the knife-edge sensor system in Figure 32. The knife holder structure was machined from stock aluminum material. Holes were drilled using a 0.25” standard drill bit and a #7 standard drill bit. Threads were added as the clamping mechanism using 1/4-20 tap. The knife slot was cut using a fine-tooth band saw. The RPI0352E sensor and two resistors are soldering on a PCB board, as showing in Figure 31 (right picture).

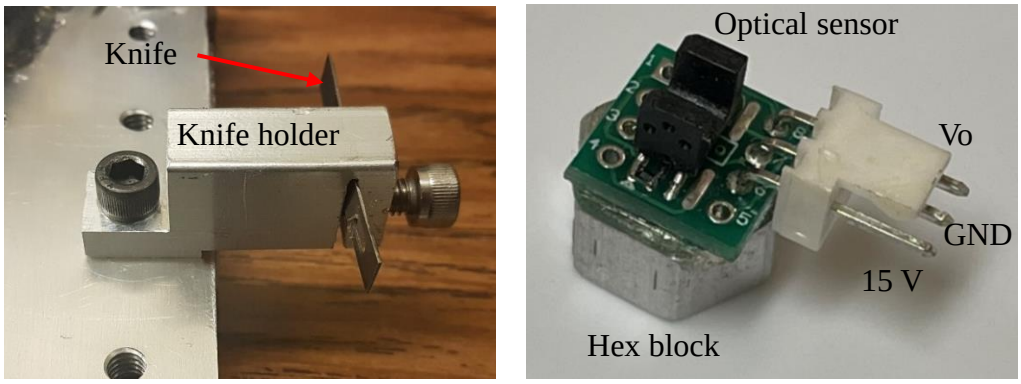


Figure 31. Left picture is showing the manufactured Knife-edge blade hold and right picture is showing the fabricated optical knife-edge sensor.

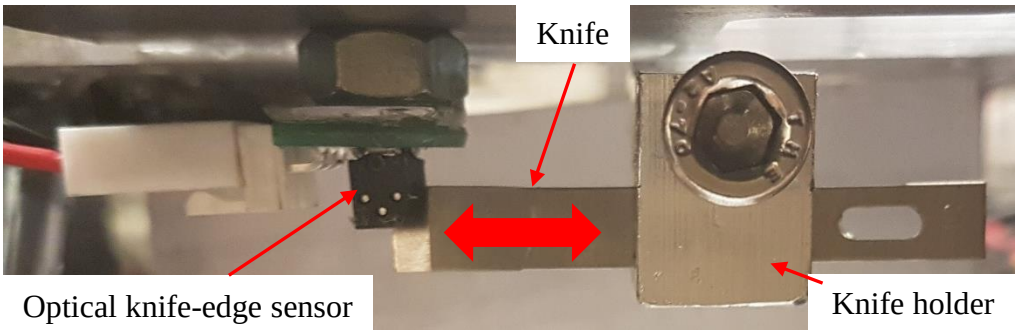


Figure 32. The assembled optical knife-edge displacement sensor.

## 2.6 PROTOTYPE OF THE FINAL DESIGN

Since Ni-Cr wire radiation heating has a large percentage of energy waste to the surrounding environment, the new design switched to the more efficient induction heating. The efficiency of an induction heating system depends on several factors: the design of the inductor, the amount of temperature change required for the application, and the geometry, thermal and electrical properties of the actuator tube. The new heating system consists of induction coil made of hollowed copper tube that surround the aluminum tube. Cooling water is continuously pumped through the hollow tube to minimize temperature variation at the surface of this element. The heat generated by the eddy current inside the tube is distributed in the tube according to the aluminum's thermal properties.

The total length of the actuator tube is 150 mm and the wall thickness is 0.889 mm in the final design. The heat transfer is affected by the thermal conductivity and diffusivity of the material. Energy losses occur through heat conduction from the actuator tube to the connections at each end as well as thermal radiation to the air when heating. When cooling, the induction coils are turned off and the flow of air and water mist through the tube provides significant heat transfer. In practice, to determine the profile of current density in the actuator tube it is necessary to use the model of section 2.2. This current in the induction coil produces a rapid alternating magnetic field that

penetrates into the aluminum tube and generates eddy currents to provide the heat inside the tube actuator. This heat will drive the mechanical system to move. In this new design, the thermal actuator is in the middle of the frame and the stage. The two sides of the actuator structure are connected to the frame and the stage through multi layered sandwiched glasses insulator with epoxy in between the layers for better contact and sealing of the air and mist cooling. Figure 33 shows the new induction heaters system that includes water cooled induction coils made of hollow copper coils surrounding the aluminum actuator tube.

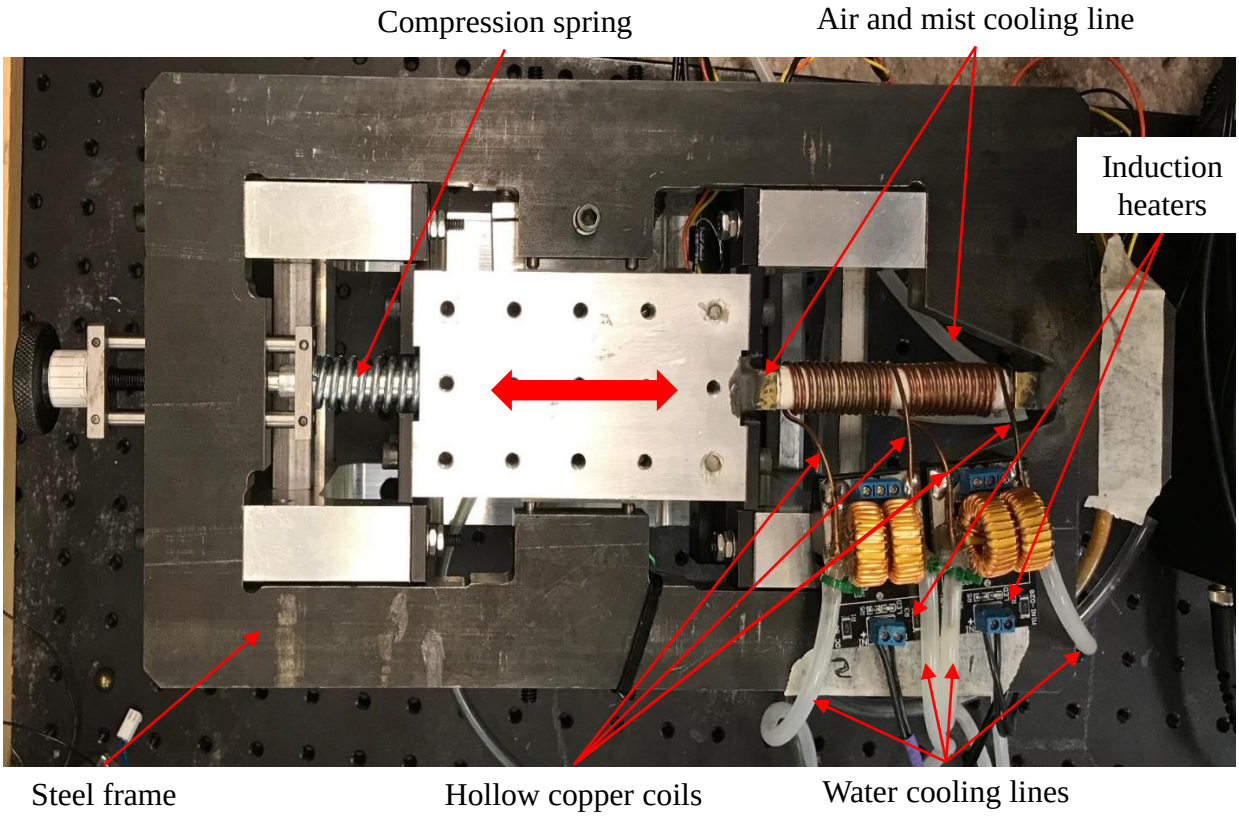


Figure 33. New prototype shows that the induction heaters system includes water cooled induction coils made of hollow copper coils surrounding the aluminum actuator tube.

### 2.6.1 NEW HEATING SYSTEM

The new heating system consists of an induction coil made from hollow copper tube surrounding the aluminum actuator tube. The induction coil driver uses a zero voltage switching circuit comprising an LC oscillator and power MOSFETs (Figure 34) [27]. Each of the two induction coil drivers (Cytron DC motor driver, model MDD 10 A) are supplied by a 120 W (12V / 10 A) power source (TDK-lambda DPP-120-12-1).

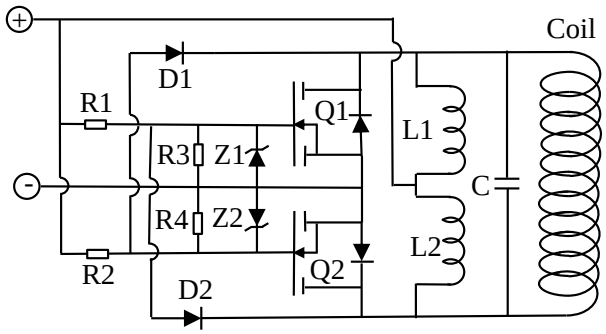


Figure 34. Schematic of zero voltage switching oscillator circuit.

A LCR meter was used to measure the inductance of the coil as shown in Figure 35. The effect of adding an actuator tube is equivalent to adding a resistance in parallel with the inductance of the coil.


Figure 35. The impedance of the induction coil in this research was measured by using BK PRECISION 891 LCR meter.

The excitation frequency for the induction coil will be a function of the induction circuit (such as zero-voltage-switching circuit, number of coils, duty cycle, and materials of the induction coils and actuator tube). In this study, the induction coils are excited with a 220 kHz alternating current (AC) of 43.4 A peak when the duty cycle is 100 percent (measured by Tektronix MDO 3024 and TCP 0150). Figure 36 shows how to measure the alternating current by using oscilloscope and current probe.

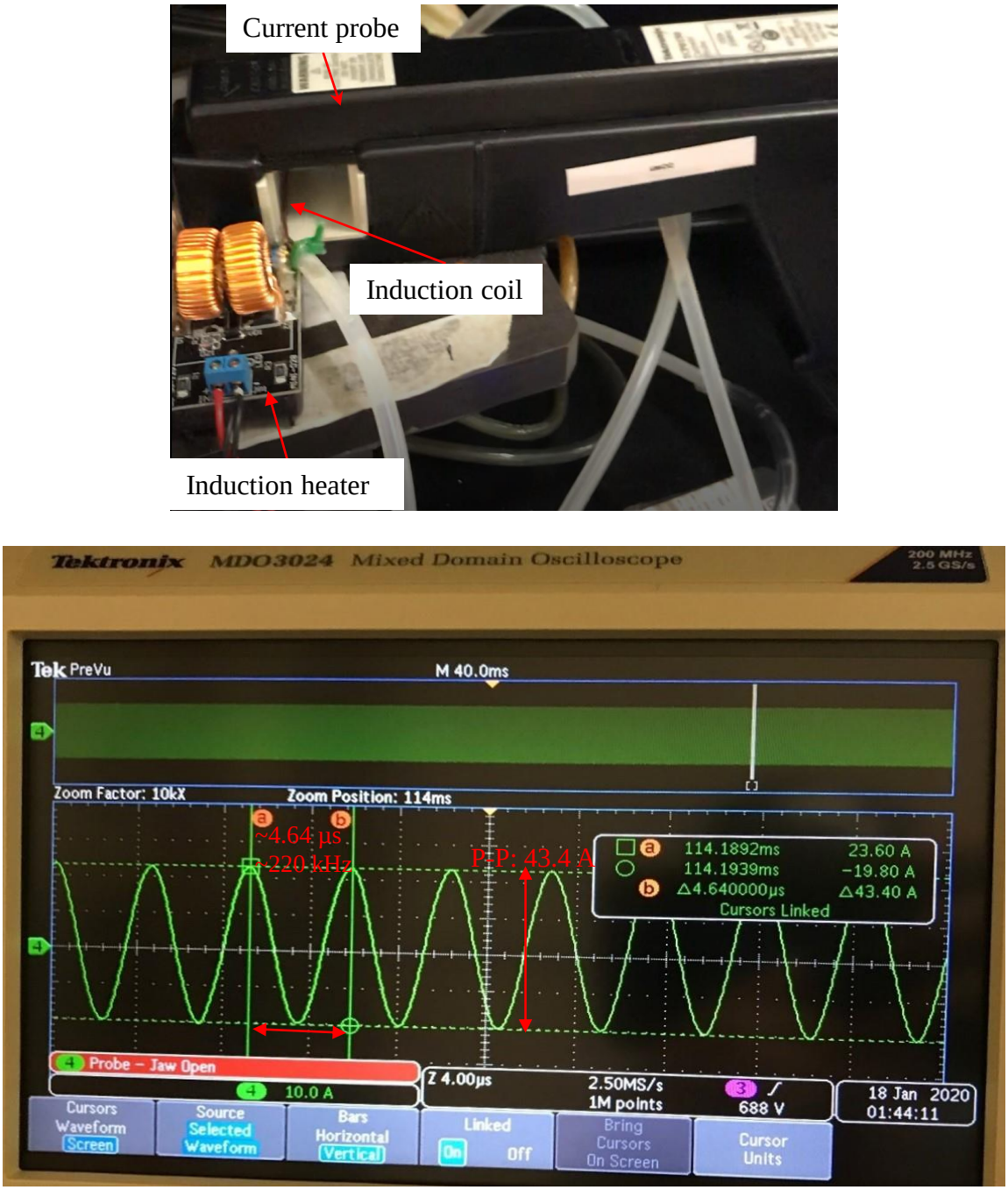


Figure 36. Experimental alternating current measurements of zero voltage switching oscillator circuit using Tektronix current probe (top) and screenshot of the oscilloscope (bottom).

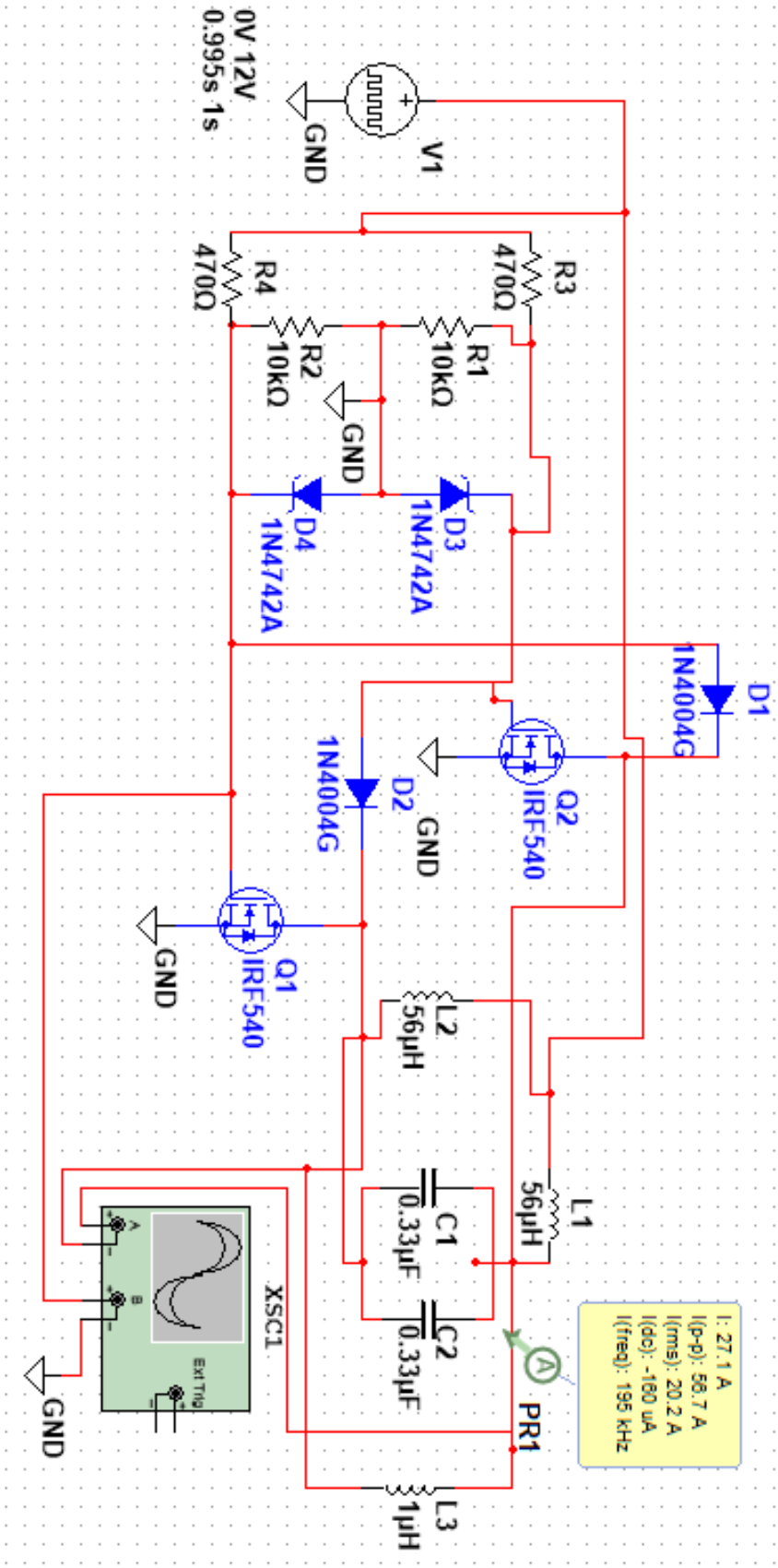


Figure 37. Simulation of zero voltage switching oscillator circuit.

The simulation of the induction heater shows that the varying current of the induction coil is around 56.7 A at 195 kHz when a 99.5 percent duty cycle power source was used, and it is showing in Figure 37.

### 2.6.2 NEW COOLING SYSTEM

While water cooling did provide rapid contraction of the actuator, the residual water that remained on the inner wall of the actuator tube slowed down the heating response and rate of this slowing down appeared to vary unpredictably. Air cooling and air-water mist cooling switching methods are used for the new cooling system. Figure 38 shows that the cooling air or mist line flows through the inner of the tube actuator lines to drain away the heat.

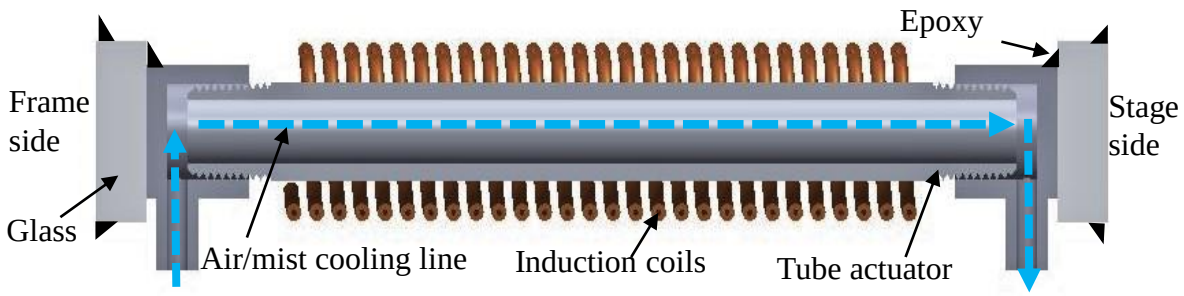


Figure 38. Cooling air or mist line flows through the inside of the tube actuator and is exhausted from the outlet to the ambient environment.

A three-position, solenoid actuated, pneumatic valve is used to switch between the air and mist cooling (see Figure 39). The return ports on the inlet side (ports S and R) are plugged to prevent unwanted airflow in the opposite direction during a specific cooling type selection.

The left spool position of the valve corresponds to compressed air only as the flowing media, that is desirable when heating the actuator tube. Two flow restrictors provide flow control of the compressed air or mist entering the actuator. The flow from the left side of the directional

controlled valve is prevented from exiting the valve by a before-mentioned plugged port S. This plug forces the cooling media to exit through the actuator (modeled here as a heat exchanger) and into a cooling sink.

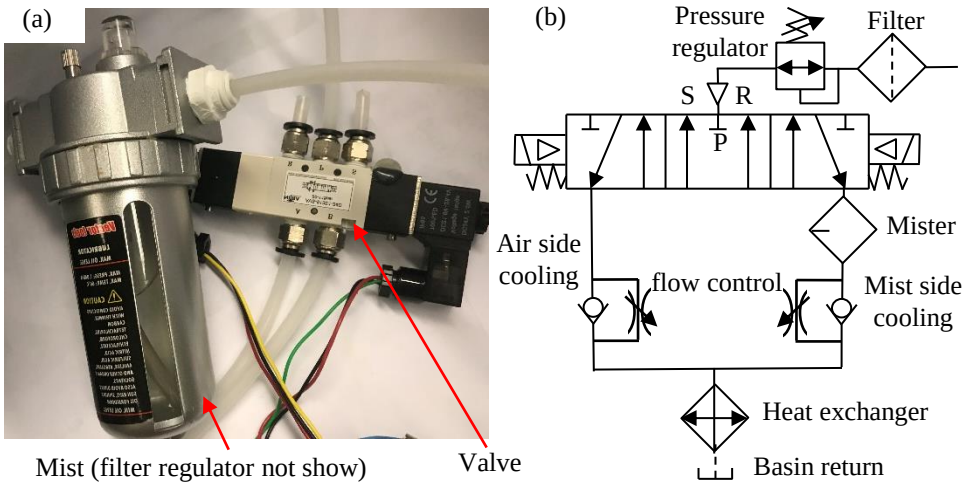


Figure 39. Air mist cooling system (a) photograph of lubricator and solenoid actuated, three-position, five-port valve (b) circuit diagram of the pneumatic system.

The right spool position corresponds to the mist - a mixture of compressed air and room temperature water - as the cooling media. A commercially available mister is used to add a small portion of room temperature water to the air stream. Similar to the compressed air only side, there is a flow restrictor to limit the flow rate of the cooling media inside the actuator and prevent any reverse flow.

### 2.6.3 NEW CONTROL SYSTEM

The heating coil wound around the actuator was connected to constant 12V/10A power supply (TDK Lambda DPP120-12-1). A PID controller is used for the induction heater, and digital on-off signals are used to control the air or water-mist cooling line. During heating and steady-

state, the air-line will be turned on, but during the cooling phase the mist line is turned on. A block diagram of the major components of the controller and PWM driver is shown in Figure 40.

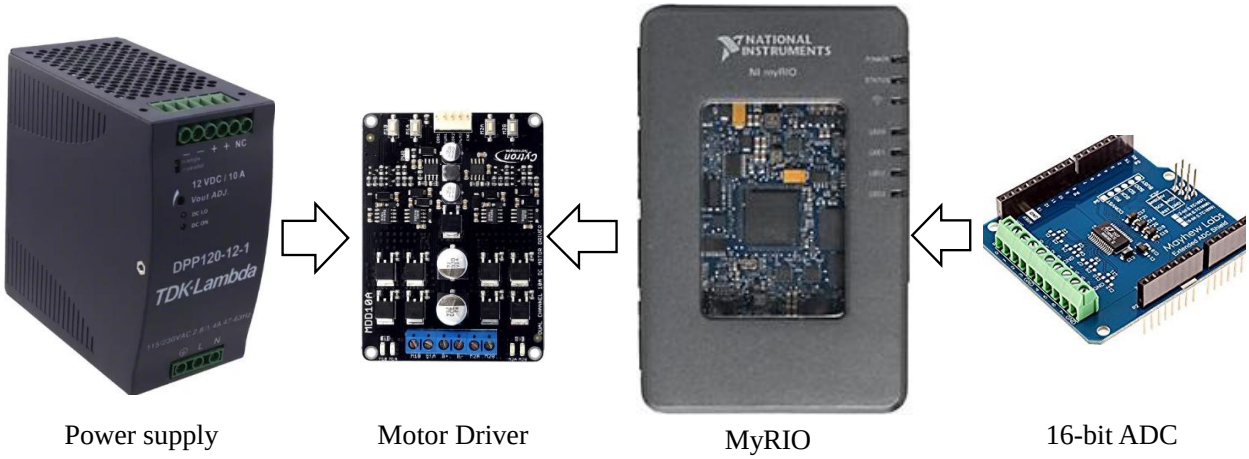


Figure 40. A block diagram of the major components of the controller include power supply, motor driver, myRIO, and external 16-bit ADC.

The control block diagram (Figure 41) shows that the controller attempts to minimize the error over time by adjustment of the control variable. The displacement of the flexure stage is measured by an optical knife-edge sensor. The output voltage of the optical sensor is measured with a 16-bit ADC, and this is then converted to displacement from the calibration curve. Depending upon this feedback and the desired position input, by changing the duty cycle of the PWM output, the energy into the induction coil can be controlled.

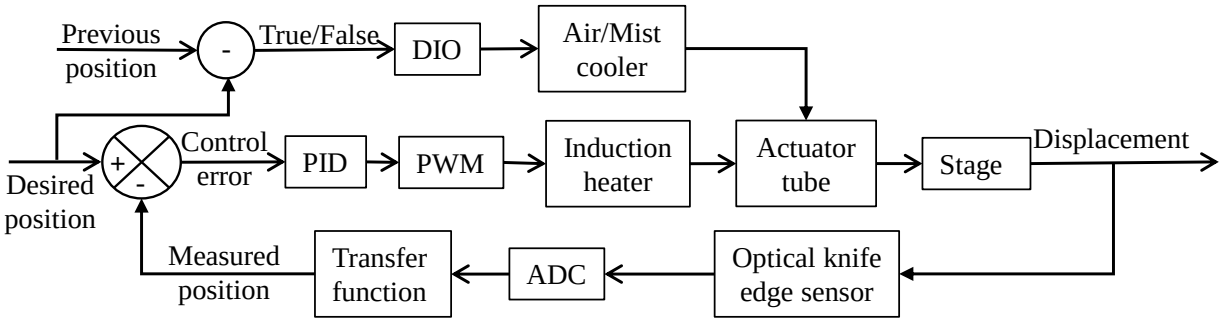


Figure 41. Control block diagram of the thermal actuator system.

Cooling in the form of air or mist flowing through the actuator tube is controlled by comparing the previous position and the current measured position: when the previous position is larger than the current measured position, the mist line will be turned on and the air-line will be off; in contrast, when the previous position is equal or smaller than the measured position, the mist line will be turned off and the air-line will be turned on to flush the mist and enable maintaining or heating of the actuator.

The induction coil driver was a zero-voltage-switching circuit comprising an LC oscillator and power MOSFETs in section 2.6.1. This circuit is resonating AC current at frequency around 220 kHz. By changing the duty cycle of the pulse width modulation (PWM) output through the motor driver, the energy input from the induction heater can be controlled. Figure 42 shows how a controlled current generated inside the induction coil for the driven power of the actuator.

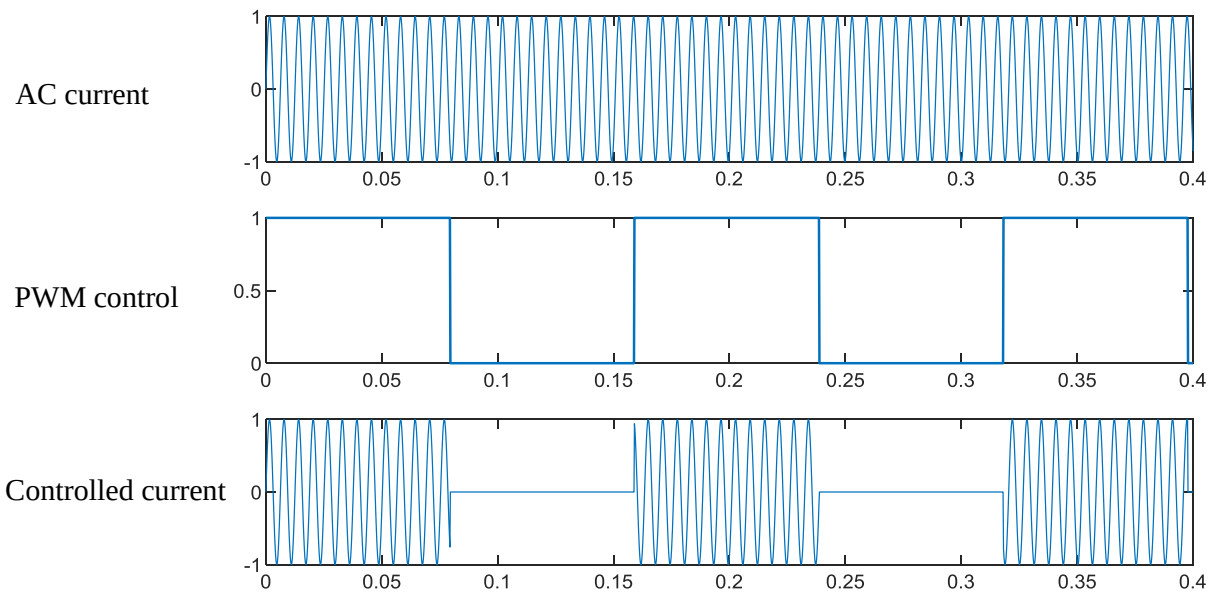


Figure 42. PWM controlled current generated inside the induction coil for the driven power of the actuator.

### 2.6.4 OPTICAL KNIFE-EDGE SENSOR EVALUATION

The next step involved the calibration of the RPI 0352E optical knife edge sensor using a micrometer. This sensor has a response of change in voltage with respect to the change in intensity of infrared light that was controlled by the penetration of knife-edge due to translation of moving block into the sensor area giving voltage change and hence proportional displacement. The maximum range of the optical sensor mounted on a micrometer gauge is around 350 µm as the working range for 150 µm. The voltage response of the sensor with change in displacement and the noise measurement and stability tests are shown in Figure 43a,b,c. A 0.25 µm position deviation range from a nominal displacement of 66.8 µm of three drift tests is shown in Figure 43d.

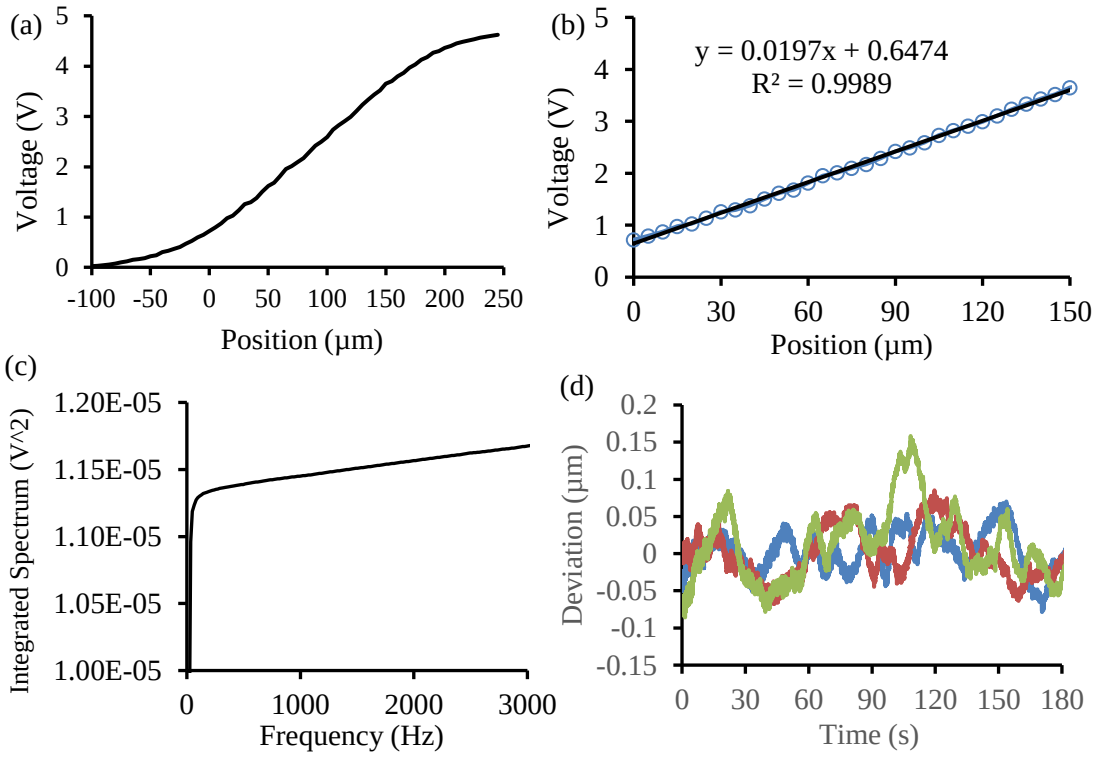


Figure 43. (a) Full range of voltage position response (b) Working range of voltage position response (c) Noise measurement of the optical sensor (d) Stability tests of the optical sensor.

### 2.6.5 THERMAL MODEL EVALUATION

The thermodynamics of this system were evaluated. The aluminum tube used in this study requires a change in temperature of 56.5 °C to produce a 100 µm displacement, and 113 °C to produce a 200 µm displacement. For heating the actuator, two methods were explored, direct heating coil and induction heating. Larger-heat loads could be readily generated using direct heating coils, but there were significant problems with heat radiation into the surrounding structures and the increased coil resistance with increase in temperature. Choosing induction heating enabled the use of cooled heating coils that substantially eliminated these issues. For cooling the actuator, two methods were explored: water cooling and air-water mist cooling.

This section outlines theoretical models for predicting both thermal and dynamic performance of this type of positioning system. Fundamentally, the thermal power balance for a control volume is given by

$$\dot{Q}_{gain} = \dot{Q}_{storage} + \dot{Q}_{loss} + \dot{W} \approx \dot{Q}_{storage} + \dot{Q}_{loss}. \tag{2.16}$$

Where $\dot{Q}_{gain}$ is the heat flowrate provided by the induction heater, $\dot{Q}_{storage}$ is the rate of internal-energy stored in the actuator, $\dot{Q}_{loss}$ is the rate of heat loss due to thermal convection, and $\dot{W}$ is the rate of work being done by the thermal system. Detailed calculations indicate that the rate of work is small (typically a small fraction of a Watt estimated from work divided by the system time constant) in comparison to the internal-energy gained over the time constant of the system and, in particular, the rate of heat loss. Analytical models to evaluate these terms are presented in sub-sections 2.6.6 through 2.6.9. The major topics of discussion are:

1. Induced eddy currents that provide the energy source in the actuator tube,

2. Conduction of heat to effectively create a uniform heat source in the volume of the actuator tube,
3. Thermal storage energy due to the heat capacity of the aluminum tube,
4. Loss of heat predominantly via convective heat transfer from the inner and outer cylindrical surfaces of the tube.

For the actuator tube alone, the first law of thermodynamics indicates that the total energy sum includes heat input, internal energy storage and work done by the actuator.

### 2.6.6 INDUCTION HEATING POWER

The plotting of eddy current density induced by a single coil at different frequency was showing in Figure 3. This 29 coil wrap prototype has a measured 220 kHz 43.4 A resonant AC current as described in section 2.6.1. To get an eddy current density plot for this 29 coils design, a superposition method was used. Figure 44 shows the plotting of eddy current density induced by 29 coils using 43.4 A current at around 220 kHz.

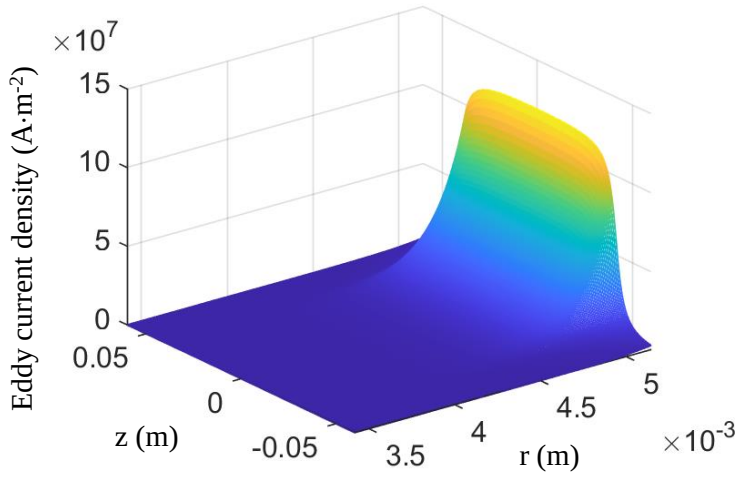


Figure 44. The eddy current density generated by 29 coils with AC current of 43.4 A and a frequency of 220 kHz with the axis of the radial direction spanning the inside to the outside of the actuator tube.

Equations (2.11) and (2.14) plotted in Figure 45 show that as the excitation frequency of the induction coil increases, the induced eddy current increases, while induced eddy current amplitude increases relatively slowly after 30 kHz. And the higher frequency will cause more efficient power. The power generated by 29 coils with AC current of 43.4 A and a frequency of 220 kHz is calculated around 18.4 W in this research and it is showing in Figure 45.

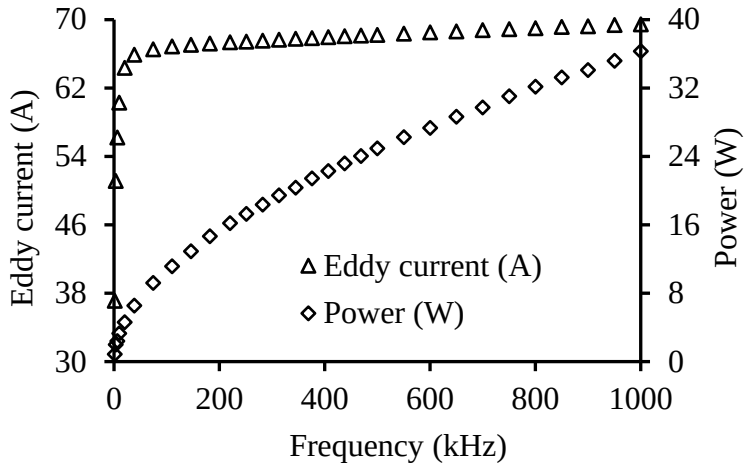


Figure 45. The induced eddy current and heating power as a function of excitation frequency.

### 2.6.7 THERMAL CONDUCTION

The time it takes for the heat to conduct through the aluminum tube of thin wall thickness and small volume is negligible in comparison to the rate of heat transfer in air (thermal conductivity of aluminum is 205 $W \cdot m^{-1} \cdot K^{-1}$, thermal conductivity of air is 0.026 $W \cdot m^{-1} \cdot K^{-1}$). An early design used water cooling but was abandoned due to the additional thermal mass of the liquid adding to the thermal mass of the system. Instead, an air-water mist was incorporated as the cooling medium due to its lower thermal mass. A consequence of this is that for finite element analysis (FEA) modeling purposes, it is reasonable to assume a uniform heat source within the material volume of the tube.

### 2.6.8 THERMAL STORAGE

The heat flow rate into the actuator can be calculated from:

$$Q_{storage} = mc_{p,Al}\left(T_{steady} - T_{initial}\right), \tag{2.17}$$

where, $m$ (0.042 kg) is the mass of the actuator tube and the hose fitting, $c_{p,Al}$ (902 $J \cdot K^{-1} \cdot kg^{-1}$) is the heat capacity of the aluminum actuator tube at constant pressure, $T_{steady}$ (84 °C) is the highest steady-state temperature, and $T_{initial}$ (20 °C) is the initial temperature. Based on Eq. (2.17), the stored heat is around 2430 J. The measured time is around 200 s for the full 180 μm range (reference to 84 °C), at 100% duty cycle as previously reported [28]. Then the average power required to generate the stored thermal energy is around 12.1 W compared to the higher value of the inductive power 18.4 W calculated in section 2.6.6.

### 2.6.9 THERMAL LOSS

To simulate convective heat transfer, it is necessary to know the heat transfer coefficients for the inside surface of the tube with and without airflow. For the range of operating temperatures of the actuator and relatively large convective and conductive heat flows, radiation effects can be neglected. The thermal model of the actuator in Figure 46 shows that paper is wrapped around the outside of the tube, and air is flowing through the inside of the tube. The purpose of the paper is to electrically insulate the induction coil and the aluminum tube. For the actuator stack, each end of the actuator has a glass insulator and behind each glass insulator is cooling water. The temperature of the actuator would be relatively uniform, hence, there will likely be a temperature gradient through the glass endplates. Therefore, the energy loss is mainly from convection (outside

through paper and glass, inside through air), and this convective heat transfer is increased due to the flow of the air. Heat transfer to the air flowing through the actuator tube can be calculated from

$$\begin{aligned}\dot{Q}_{loss} &= \frac{k_{paper}A_{paper}\left(\overline{T}_{tube}-\overline{T}_{ambient}\right)}{t_{paper}} + 2\frac{k_{glass}A_{glass}\left(\overline{T}_{tube}-\overline{T}_{ambient}\right)}{t_{glass}} + \rho_{air}w_{air}c_{p,air}\left(T_{outlet}-T_{inlet}\right) \\ &= \frac{k_{paper}A_{paper}\left(\overline{T}_{tube}-\overline{T}_{ambient}\right)}{t_{paper}} + 2\frac{k_{glass}A_{glass}\left(\overline{T}_{tube}-\overline{T}_{ambient}\right)}{t_{glass}} + \overline{h}\overline{A}\overline{\Delta T}.\end{aligned} \tag{2.18}$$

Where $k_{paper}$ (0.05 W·m$^{-1}$·K$^{-1}$) is the thermal conductivity of the insulating paper, $A_{paper}$ (0.004 m$^2$) is the outside circumferential surface area of the insulating paper, $\overline{T}_{tube}$ (84 °C during steady-state) and $\overline{T}_{ambient}$ (20 °C) are the mean temperature of the tube and ambient environment respectively, $t_{paper}$ (0.003 m) is the thickness of paper. Then, the energy loss from the paper conduction is around 4.8 W. Where $k_{glass}$ (0.8 W·m$^{-1}$·K$^{-1}$) is the thermal conductivity of glass, $A_{glass}$ (0.00014 m$^2$) is the surface area of the interface between the glass and the actuator, $t_{glass}$ (0.006 m) is the thickness of glass. Then, the energy loss from these two glasses is around 2.4 W. $\rho_{air}$ (1.1 kg·m-3) is the density of air at the average temperature between inlet and outlet, $w_{air}$ (1.7·10$^{-4}$ m$^3$·s$^{-1}$) is the average volumetric flow rate of air, $c_{air}$ (1000 J·K$^{-1}$·kg$^{-1}$) is the specific heat capacity of the air, $T_{inlet}$ (20 °C) and $T_{outlet}$ (80 °C) are the temperature of the air at the inlet and outlet of the tube respectively, see Figure 46. Then, the energy loss from the laminar flow is around 11.2 W. $\overline{h}$ is the average heat transfer coefficient of the air inside the tube, $\overline{A}$ is the surface area of the inner diameter, $\overline{\Delta T}$ is the temperature difference between the tube and the air. In practice, the convective heat transfer coefficient is difficult to predict.

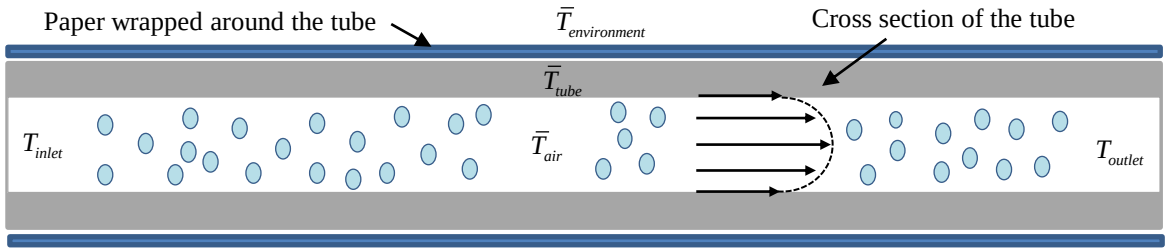


Figure 46. Schematic diagram indicating parameters for heat transfer modeling (hose fitting was calculated, not showing).

To provide estimates of the heat transfer coefficient, finite element analysis (FEA) thermal simulations (Abaqus, COMSOL, and SOLIDWORKS) were performed. COMSOL was used to calculate the eddy current and compare with the theoretical model. The Solidworks analysis used the inductive heat power from the theoretical model to calculate the heat flow into the actuator. From the heat balance equation, it was then possible to determine the heat convection coefficient. ABAQUS was used to cross-check the Solidworks results. Given that the input power to the actuator and the steady-state temperatures are known from experiments, a reasonable estimate of the heat transfer coefficient can be obtained. Based on the simulation results shown in Figure 47, for a temperature of 210 °C with an input heat power of 18.4 W, the average convective heat transfer coefficient, $\bar{h}$ , corresponds to 5 $W \cdot m^{-2} \cdot K^{-1}$ at steady-state with no air flowing in the actuator. When there is air flowing inside of the tube, the steady-state temperature of the actuator drops to 84 °C, for which $\bar{h}$ corresponds to 75 $W \cdot m^{-2} \cdot K^{-1}$.

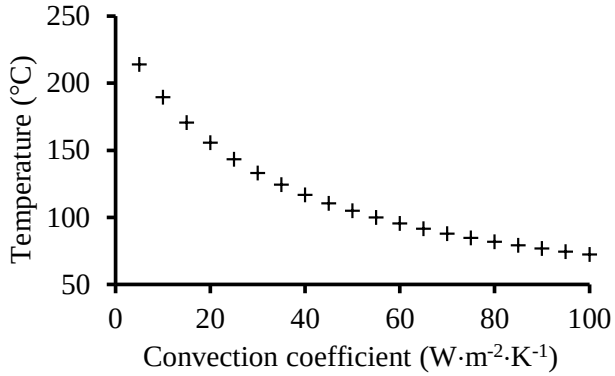


Figure 47. Simulation results to determine the steady-state temperature at different convection coefficient with an input heat power of 18.4 W.

## 2.7 RESULTS AND DISCUSSION

The prototype of the thermal actuator (Figure 48) was fabricated and tested to verify whether the system meets the requirement. The same procedure was repeated with preloads of 0 N, 500 N and then 1000 N. The forward and backward steps are 20 µm displacements.

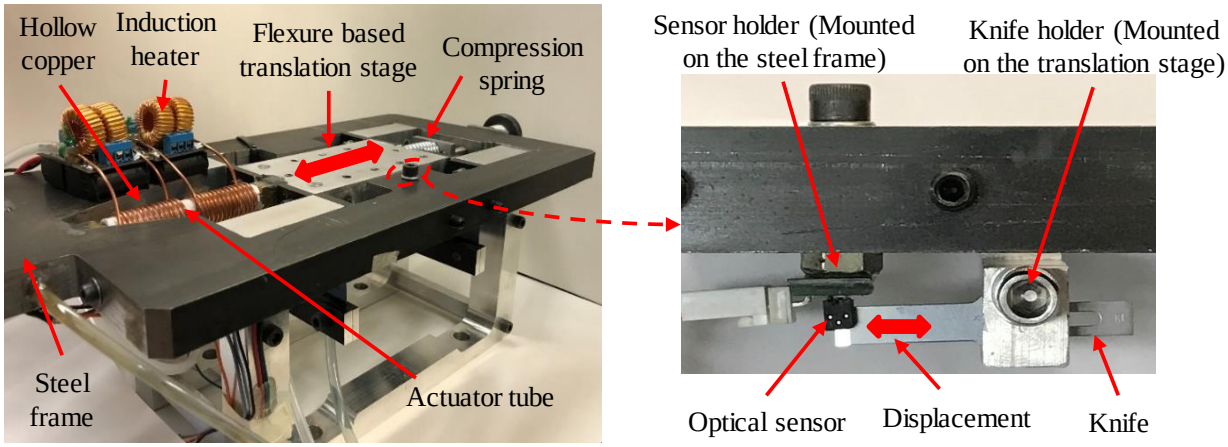


Figure 48. Prototype of the thermally actuator and Incremental displacement test.

To evaluate performance over the displacement range of the actuator, a ramp comprising 20 µm steps both increasing and decreasing to form a triangular response is used. Two power sources have been used in these experiments, the first comprising two 12 V and 10 A power supplies (240 W), the other comprising two 24 V and 10 A power supplies (480 W). The major

difference is that the 240W source provides a total range of 100 µm, and the 480 W source a range of 200 µm. The same test procedure was used for both power supplies. To measure the thermal isolation of the system, two temperature sensors were mounted on the frame and moving platform of the flexure-based translation stage.

### 2.7.1 DYNAMIC PERFORMANCE

In this subsection, for optimizing dynamic performance, it is necessary to determine the open-loop time constant for controller tuning and to balance the heating and cooling response under closed-loop control. The performance is evaluated by studying step and frequency responses. The thermal time constants during heating cycle for this system are tested by using 0.25, 0.5, 0.75 and 1.00 duty cycle. From the step response data shown in Figure 49, the time constant is around 60 seconds for open loop control.

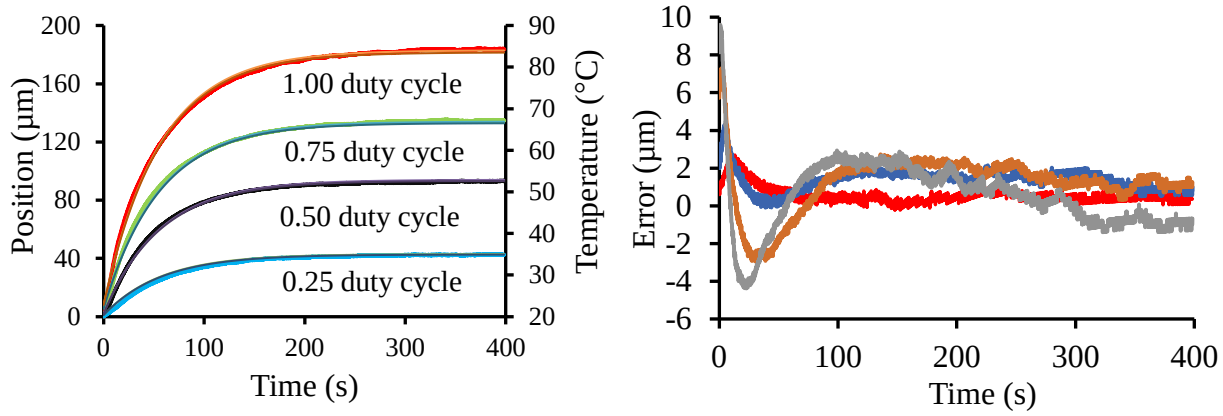


Figure 49. a) Time-position and time-temperature tests for 0.25, 0.50, 0.75 and 1.00 duty cycle show that the time constant for this open loop is around 60 seconds. b) Residue errors after exponential curve best fitting.

To determine the open loop heating time constant, the induction coil was energized with 40% duty cycle, and the subsequent response to this step input was measured. From a series of thirty measurements, time constants for heating were around 51.54 ± 3.63, 51.14 ± 0.76, and 49.94

± 0.65 seconds under 0, 0.5, and 1 kN preloads, respectively. The open loop cooling time constant was determined by first giving an initial displacement to the actuator. The heating was switched to 0% duty cycle, and the mist cooling line was turned on. The subsequent displacement versus time chart provides the cooling time constants as 10.82 ± 1.31, 11.11 ± 0.75, and 10.66 ± 0.69 seconds under 0, 0.5, and 1 kN preloads. While in both the heating and cooling cases, the standard deviation decreases with increasing load, the time constant does not change significantly.

To balance the heating and cooling closed-loop response for 100 µm full range, air and mist cooling were tested and time-position curves were measured, as shown in Figure 50. The 240 W heating system needs 30 seconds to translate the 100 µm range and the cooling system need 180 seconds to return to the original position when cooled by air (left side of plot). The cooling mist reduces the reaction time to 60 seconds (right side of plot).

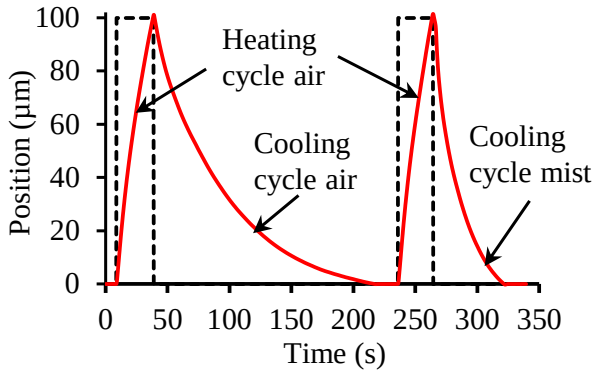


Figure 50. Closed-loop position response for heating and cooling system.

The closed-loop frequency response for the gain and phase lag is shown in Figure 51. Because of the asymmetry in heating and cooling, measured phase shifts are different during the heating and cooling processes in each cycle. The response under all three pre-loads were the same within the repeatability of the measurement.

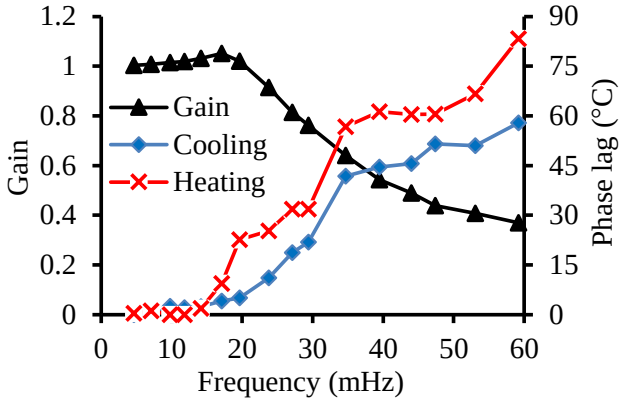


Figure 51. Steady state frequency response for amplitude demands of 100 µm; gain (triangular marker), phase lag during heating component cycle (cross marker), phase lag during cooling component cycle (diamond marker).

### 2.7.2 DISPLACEMENT RESULTS WITH 240 W POWER SUPPLY

Initially, the test was carried out under 0 N preload. Figure 52a shows a graph of the desired position and the measured position of the stage. The RMS controller error between the desired position and the measured position reached by the actuator is within 15 nm, calculated from each individual step segment in Figure 52d. At the same time, Figure 52a shows that the variation in the temperature of the moving stage and frame (i.e. the structural elements of the stage) are within 1 ℃. Similar temperature variations and steady-state errors are obtained for all experiments with higher preloads.

As the total displacement increases, this will require a higher temperature in the actuator, and it was apparent that the induction coil temperature was increasing as well. Because of this, a larger flow rate of cooling water through the induction coil is necessary to reduce the temperature increase. Additionally, as the temperature increases, there will be more heat loss from the actuator since the temperature differences are getting larger. As a result, step response times are longer towards the fully extended end of the range.

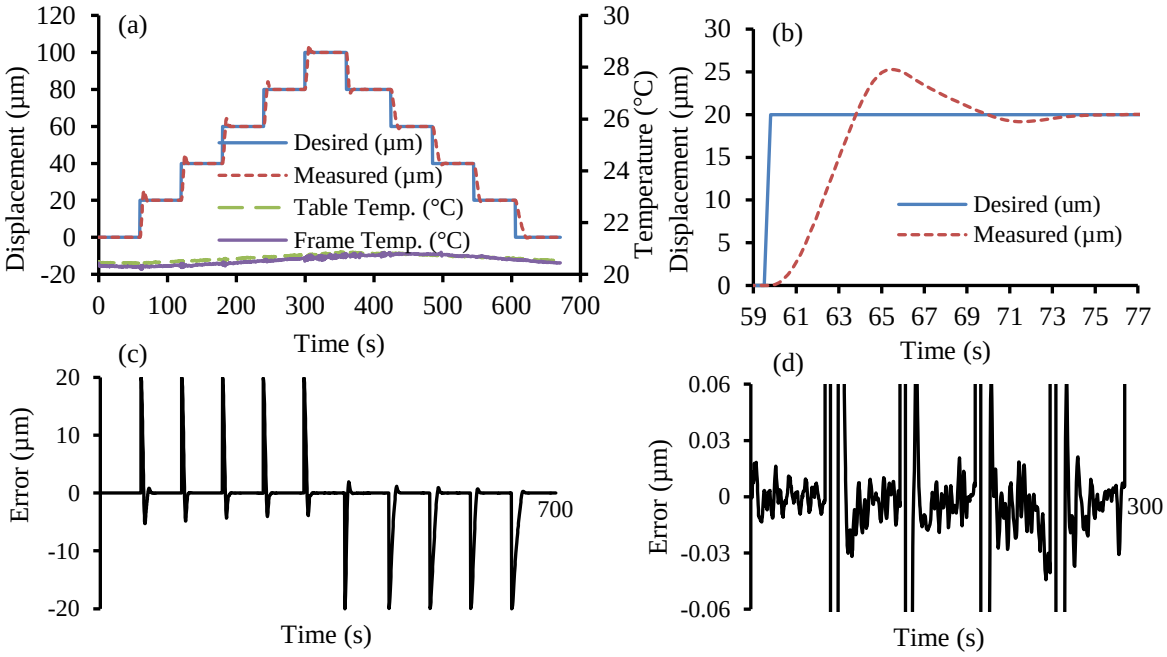


Figure 52. Representative step response measurement: (a) Displacement control test under 0 N load with 20 µm increments up to 100 µm, and 20 µm decrements to initial position, second vertical axis is the temperature measurement of the stage and the frame, (b) zoomed in view of the first step increment, (c) error in the displacement, (d) zoomed in view of error in the displacement.

The same procedures were repeated with preloads of 500 N and 1000 N from the compression spring. The step response to different preloads was used to determine steady-state RMS controller error, slew rate, overshoot, and settling times. A summary of these measurements containing average values of these parameters is listed in Table 3 with more detailed values for individual steps listed in tables in APPENDIX A. For increasing step displacements (increasing actuator temperature, heating process), Figure 52b illustrates how these measures have been calculated. The immediate response to the step demand is a nearly linear change of the error to the first zero crossing. A straight line fit to this initial portion of the error yields a gradient that is called the slew rate, around 6 µm·s$^{-1}$ in Figure 52b. After this first zero crossing there is an overshoot of magnitude around 6 µm and the error settles to within a 60 nm band within around 14 seconds

from the time of the initial step demand. The values in Table 3 have been calculated for each experiment and averaged over the five steps for each direction (heating and cooling).

For increasing steps, the slew rate, overshoot and settling time remains relatively constant independent of the load. On the other hand, for decreasing steps (decreasing actuator temperature, cooling process), there is considerable variability in these parameters (more details refer to table in APPENDIX A). While the RMS controller error is relatively constant as might be expected, the settling time increased for decreasing steps, visible in Figure 52a and Figure 52c. Typically, the slew rate at 100 μm displacement was around 4 $\mu m \cdot s^{-1}$, and increased to around 7 $\mu m \cdot s^{-1}$ near to the original environmental displacement value. More interestingly, the slew rate decreased by approximately 43% as the displacement was varied from 0 μm up to the final displacement of 100 μm. The same decrease in slew rate was observed with all three preloads. One possible explanation for this is the 240 W power supply has insufficient power at the higher displacement values and is therefore operating near to capacity at the high end of the displacement range (see observation in the 480 W case). Thermodynamically, the volume expansibility and compressibility are not expected to vary significantly for the moderate change in pressure experienced by the actuator tube [31].

A variability of the settling time for decreasing steps was observed and is thought to be, in part, due to variation in the temperature of the coil's cooling water, and the concentration and temperature of the misting produced by the air lubricator, both of which are not easily controlled.

Table 3. Average closed loop step response values for varying preloads using 240 W power supply, see APPENDIX A.

| Process | Preload (N) | Slew rate ($\mu m \cdot s^{-1}$) | Magnitude overshoot ($\mu m$) | Settling time (s) |
|---|---|---|---|---|
| Increasing | 0 | 5.8 | 5.6 | 13.5 |
| Increasing | 500 | 5.6 | 5.6 | 13.9 |
| Increasing | 1000 | 5.5 | 5.4 | 12.8 |
| Decreasing | 0 | 3.5 | 3.3 | 15.1 |
| Decreasing | 500 | 4.2 | 4.4 | 15.7 |
| Decreasing | 1000 | 4.2 | 4.4 | 15.2 |

### 2.7.3 DISPLACEMENT RESULTS WITH 480 W POWER SUPPLY

The work presented in this paper used two induction heaters with current limited by the MOSFET's (30N06) and two power sources limited to 120 W (240 W total). After using two 24 V / 10 A power supplies capable of delivering 480 W and a new circuit with high current MOSFET's (IRFP260N), it is possible to increase the actuator's temperature. The frequency of this induction circuit is 200 kHz, again significantly higher than the minimum of 30 kHz determined in section 2.6.6. Results of tests for step response and time-constants are shown in Figure 53a. For this higher wattage power supply, it was possible to increase the translation range to 200 μm (corresponding to an actuator temperature of approximately 100 °C) and maintain steady-state RMS controller errors within 35 nm, calculated from each individual step segment in Figure 53d. At 100% duty cycle, this implies a steady-state temperature at two-thirds of the melting temperature of aluminum. To achieve this steady-state temperature, it is implied that the temperature localized within the eddy current skin-depth will be much higher. With the higher actuator temperature, the surrounding frame and translation stage temperatures (Figure 53a varied by around 2.5 °C and 1 °C respectively.

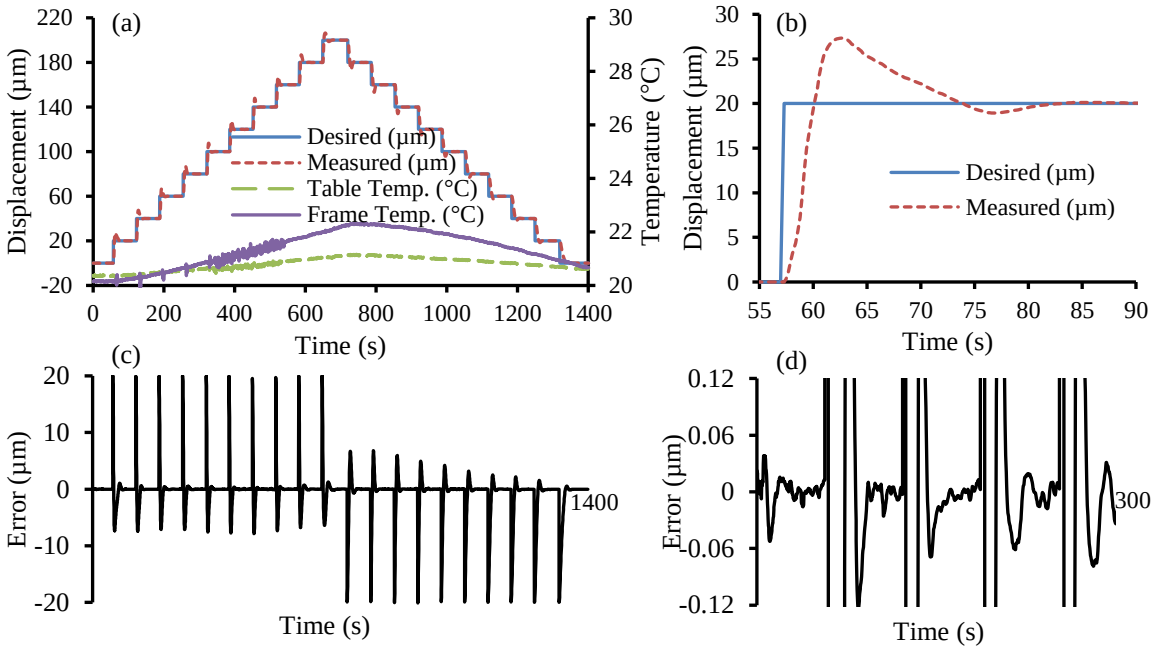


Figure 53. Representative step response measurement: (a) Displacement control test under 0 N load with 20 µm increments up to 200 µm, and 20 µm decrements to initial position, second vertical axis is the temperature measurement of the stage and the frame, (b) zoomed in view of the first step increment, (c) error in the displacement, (d) zoomed in view of error in the displacement.

Table 4 shows the closed loop controller response to the step inputs using the 480 W power supply. With twice the power supply voltage, the slew rate of the heating process changed by a factor 1.3 in comparison with the previous supply. On average, the slew rate of the cooling process was not significantly different between the 240 W power supply measurements and the 480 W power supply measurements. However, with this more aggressive heating system, there is significant overshoot (approximately two times) and more than a doubling of the RMS controller error for a steady demand signal (Figure 53d, Figure 52d).

The observation of the decrease in slew rate when heating with the 240 W power supply (43% change) was not observed with the 480 W power supply. With the 480 W power supply, the average slew-rate change when the actuator was increasing its displacement was 6%. This

indicates the 480 W power supply has the additional capacity to supply the needed current to the actuator at the higher displacement (or temperature) values than the 240 W power supply.

Table 4. Average closed loop step response values for varying preloads using 480 W power supply, see APPENDIX A.

| Process | Preload (N) | Slew rate ($\mu m \cdot s^{-1}$) | Magnitude overshoot (μm) | Settling time (s) |
|---|---|---|---|---|
| Increasing | 0 | 7.7 | 7.3 | 19.3 |
| Increasing | 500 | 7.2 | 7.1 | 20.4 |
| Increasing | 1000 | 7.5 | 7.4 | 22.7 |
| Decreasing | 0 | 4.1 | 4.6 | 17.6 |
| Decreasing | 500 | 4.9 | 5.8 | 20.5 |
| Decreasing | 1000 | 4.8 | 5.2 | 19.6 |

Using the 480 W supply the percentage change in slew rate during cooling reduced by 60% on average when changing the displacement from 200 μm to the origin position. Correspondingly, there was a 30% reduction in slew rate for the 240 W supply when changing the displacement from 100 μm to the origin position. This might be expected with the higher temperature at higher power given the constant air and mist cooling flows in all experiments. Some possible changes to the cooling system to help mitigate this issue are discussed in Section 2.8. Again, dynamic parameters for all measured steps are tabulated in APPENDIX A.

## 2.8 CONCLUSION

This section of the dissertation has described the design, modeling, and performance of a thermally actuated translation stage that is simple, rigid, and relatively inexpensive. Additionally, the high work density of this actuation method enables the positioning of high loads using a relatively compact actuator. This thermal actuator is simple, rigid and relatively inexpensive. Induced eddy currents generate the heating from inside the actuator itself using electromagnetic fields. Using the cooling mist can improve the cooling efficiency compare with air. Additionally,

the high work density of this actuation method enables the positioning of high loads using a relatively compact actuator. The flexure stage can cover its full displacement range in approximately within 30 seconds independent of the pre-load applied and can even cover double its intended range (200μm) in additional 40 seconds. The testing system measured the displacement accuracy under 0N, 500 N and 1000 N preload. The downside, however, is the high-power consumption of the actuator to produce appreciable displacements and the risk of thermal failure from the repeated heating and cooling cycles.

The testing system demonstrated displacement control under 0 N, 500 N, and 1000 N preload. The RMS controller error during steady state is 15 nm. The flexure-based translation stage can cover its 100 μm full displacement range in approximately 30 seconds not relying on the pre-load applied and can even cover to 180 μm extended range in an additional 40 seconds. The settling time was primarily influenced by the cooling system, see comments below. The downside, however, is the high-power consumption of the actuator to produce appreciable displacements and the risk of thermal failure from the repeated heating and cooling cycles under preload.

Experiments using a 480 W source resulted in higher temperatures, a larger displacement range (currently limited to 200 μm), and an increase of the slew rate response by a factor of 1.3. In the process of controller tuning, temperature spikes would reach the decomposition temperature of the epoxy adhesive at each end of the actuator tube and, occasionally, the combustion point of the paper insulator between the actuator tube and induction coils. Additionally, the induction coils were noticeably warmer to the touch indicating that the resistance, and therefore losses, were also higher. While it was apparent that higher power heating systems can increase dynamic response, it was also apparent that increased cooling rates for the induction coil, translation stage, and frame

are necessary with this design. Future designs will replace the paper insulator with 3M electrical tape 27 that is capable of withstanding temperatures of up to 150 °C.

For the actuator stack, each end of the actuator contacts a glass insulator and behind each glass insulator is cooling water. The temperature of the actuator was relatively uniform. Hence, there will likely be a temperature gradient through the glass endplates. Because of the low thermal conductivity of glass, a thermal expansion mismatch will also occur at the actuator-glass contact interfaces, both of these effects will result in stress cycling. No effort has been made to evaluate this effect. However, this actuator has been used for more than three years without noticeable damage of either the epoxy or any frame components. It should be noted that the epoxy surrounds the actuator glass interfaces and it is not within the loaded contact faces.

The limits of operation have not been explored in this paper. Future work on thermal actuators includes an investigation of the feasibility of manufacturing and implementation of a compact system that can be integrated into systems scaled between MEMS devices and devices smaller than 25 mm. With a decrease in the overall dimensions of the actuator, it is expected that the dynamic properties will improve while continuing to support loading in excess of 1000 N for displacement control.

Two aspects of cooling should be addressed. The increase in cooling slew rate with preload has yet to be fully understood and will be further explored. The higher power supply made possible higher actuator temperature (larger displacement range) at the expense of higher controller RMS error and overshoot. These disadvantages may be mitigated by the addition of the ability to control mist concentration, and air flow. In addition to adding cooling flow control, the variation of slew

rate with temperature might be reduced by utilizing cooling water to the induction coils at a lower temperature than the operating environment.

Finally, future actuators will be tested for precision operation in environments where temperatures range from ambient laboratory temperature to 200 °C or greater.

Portions of this chapter are reproduced from the paper of Fan et al. 2021 with permission from Elsevier publishing.

# CHAPTER 3: INSTRUMENTATION DESIGN OF THE ROTARY MEASUREMENT DURING NANOINDENTATION

The goal of this study is to measure any twisting force transmitted to the indenter that might be produced during nano-indentation experiment. The traditional nano-indentation tests only provide depth of indentation (displacement) as a function of normal force applied, called the load-displacement curve and do not have the capabilities to measure twisting force [32-38]. A new instrument has been designed and fabricated to obtain the rotation, load, and displacement data simultaneously. The outputs are the raw-data which are calibrated for the penetration depth (calculated from the calibrated displacements of the actuator stage and the load-cell stage), time, load applied to the sample (calculated from the calibrated stiffness and displacement of the load-cell), and rotational angle. A brief outline of rotation measurements is presented in section 3.1 and 3.2 to define parameter symbols and relevant equations. Experimental procedures are also detailed as well as post-measurement analysis methods.

There are great challenges to determine rotation effects during a nano-indentation test. First of these, theories related to rotation effects during an indentation process have not been developed. Second, nobody has looked into measuring twisting forces as the indenter penetrates into the material. Third, quantitative results are experimentally difficult in the nanonewton and nanometer level. A major challenge to the design of an instrument to measure tip twisting force is to align the indenter tip to the axis of an extremely precise and stiff freely rotating bearing.

To achieve the alignment of the indenter tip with the rotary axis of the bearing, a coarse and fine adjustment mechanism is used to locate the indenter tips to be coincident with the rotation axis of the air bearing. A microscope is used to do rough alignment of the indenter to the rotation axis of the bearing. Fine adjustment is facilitated using a highly sensitive centering apparatus that

can detect off-axis errors with nanometer precision. UNC Charlotte has state of the art measurement tools to calibrate the stiffness and the relative displacements of components of the apparatus as well. Indenter forces are determined by a spring-based load-cell and loads are calculated by the multiplication of calibrated stiffness and the displacement of the spring. A precision air bearing (Precision Instruments air bearing 30-62792-073A) is used to provide the required performance. Such a bearing also requires precise angular measurements and the tip, attached to the spindle of the bearing, must be aligned to be within nanometers of its axis of rotation.

## 3.1 INTRODUCTION AND LITERATURE REVIEWS

This work represents the first time that there has been an effort to detect any rotational force during nano-indentation.

Nanoindentation is used in research communities and industries for evaluating surface and near sub-surface performance characteristics: surface hardness of materials, tribological properties, coating quality, thin film deposited layers, dislocation stresses, strain hardening effects, fracture toughness, polymer viscoelastic and material creep behavior [32-34]. Engineers are interested in the surface hardness because this is a major factor that influences wear (i.e. machines typically fail since wear over time) and indicates issues with materials processing. Hardness is defined as a measure of material resistance to plastic deformation. Measuring the hardness of the material is very important since it is the most important factor for defining the wear life of most devices. There are a lot of methods for hardness testing and it has been studied for more than one hundred years. For instance, indentation using a spherical tip was used since 1900s, and it is called Brinell hardness measurement. After the year 1914, because it uses a smaller cone tip as the indenter, the Rockwell hardness test was developed since it is less destructive compared with the Brinell test.

Vickers hardness test was built after 1924. Vickers indenter uses a four-faceted pyramid-shaped tip and has smaller dimension, and with its development an optics magnification system was added resulting in measurement that were at the time more accurate than the Rockwell hardness test. In the 1990s, Berkovich designed a three-sided pyramidal indenter (indenter used in these studies) to provide the same projected area as the Vickers indenter. With a different angle between faces, the modified Berkovich is designed to provide the same indent surface area as the Vickers indenter. This shape allows the tip to be theoretically manufactured with an atomically sharp point enabling indentations having penetration depths measured in nanometers. The nanoindentation experiments include different measurement modes. This research uses the method to continuously measure the depth-dependent properties of a material.

In-situ nanoindentation tests with further sensing of the indent region have enabled the study of mechanical, biological, thermal, and electrical properties by continuously measuring the reaction force and penetration depth. Nano-indentation test has the capability to measure force, in sub-micro-newton resolution, and displacement, with sub-nanometer to nanometer resolution. It is also useful when a large data set is needed for the statistical analysis of material properties. And properties measurement for various materials ranging from hard super-alloys to soft biomaterials is available as well. For instance, thin-film properties can be measured by utilizing advanced analytical solutions to remove the substrate effect in the data. The scratch resistance and adhesive force measurements enable users to evaluate various function related properties in many research, industrial and educational settings.

Additionally, the changes in electrical properties (insulator to conductor transition under high pressure) and phase transformation (i.e. cubic diamond structure to beta silicon for a single

crystal silicon sample during nano-indentation) [35-36] are also detected during nano-indentation test. As an example of possible anisotropic behavior, the single crystal silicon has an alpha diamond cubic structure, however once the applied pressure is above 12.5 GPa, the structure will be compressed to a beta-silicon structure. This transition was shown in research conducted at Colorado State University by Ian L. Spain [39] using diamond anvil cells. This change in crystallographic state is named a phase transformation. The transformation from Cubic (alpha) to Tetragonal (beta) is thought to occur by the rotation of the atomic bonds throughout the crystalline structure. During nano-indentation test [35-36], experimental studies using Berkovich indenters show that phase transformation takes place with indenter loads between 15 and 30 mN with a corresponding indentation depth of 350 to 450 nm. It is the purpose of this experiment to determine whether or not rotational forces during phase transformation may be mechanically measured. However, it is also typical to consider that during indentation, the material is compressed to a metal-like flow for which rotational effects would not be expected.

A nano-indentation system that includes a high voltage (HV) amplifier, an actuation stage, a load-cell stage, a rotation stage, a lock-in amplifier and LabVIEW with National instrument data acquisition system (NI DAQ), is developed, A block diagram indicating major components of the nano-indentation system is showing in Figure 54. The technique involves an actuation process to apply a load, and load-cell to transfer the load to the indenter. The piezoelectric actuated flexure and load-cell flexure stages will displacement during an indent and are measured to determine penetration of the indenter into the sample (like silicon). The displacement of each stage will be measured by capacitance gages. The signals of these capacitance gauges are transmitted to a lock-in amplifier and transformed into signals that can be calibrated to determine displacement. The

rotary air-bearing supporting the indenter can freely rotate and the rotation measured to determine the presence of rotational (torsional) moments. The whole system is housed in a metrology laboratory environment under the constant temperature (20 ± 0.1°C).

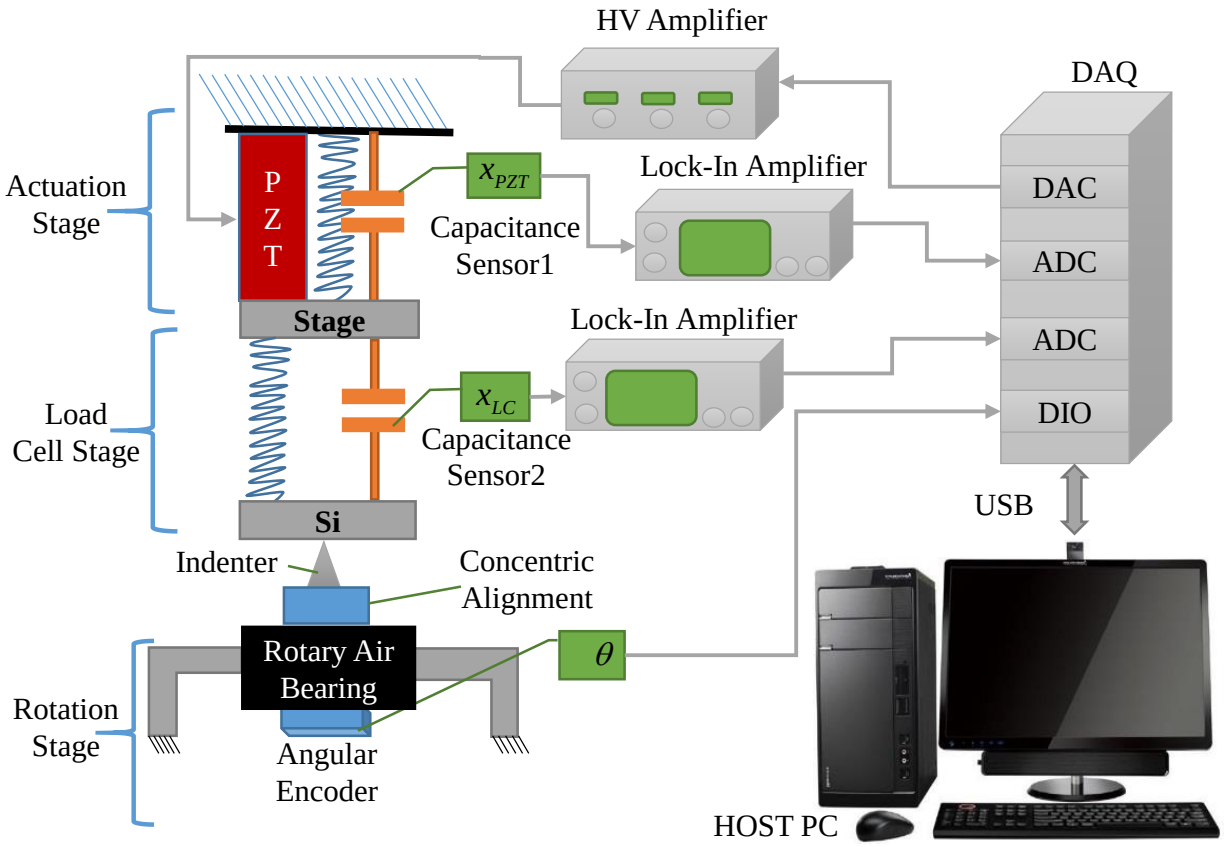


Figure 54. Basic structure of nano-indentation system.

## 3.2 DESIGN AND PROTOTYPE

The experimental apparatus shown in Figure 55 indicates major features of the new instrument. These features include:

(1) A precision micrometer stage to adjust the position of the nano-indentation system relative to the indenter and air bearing assembly;

(2) A piezoelectric actuated stage to push the indenter into the sample with 0.1 nm resolution;

(3) A load-cell stage to measure the displacement with 0.1 nm resolution;

(4) A concentric alignment apparatus to maintain the diamond indenter tip and the rotary stage axis of the air bearing in the same line;

(5) A coarse and fine adjustment tip alignment mechanism on the rotary air bearing and a precision rotary encoder to measure the change in angle with 0.2 arc second resolution.

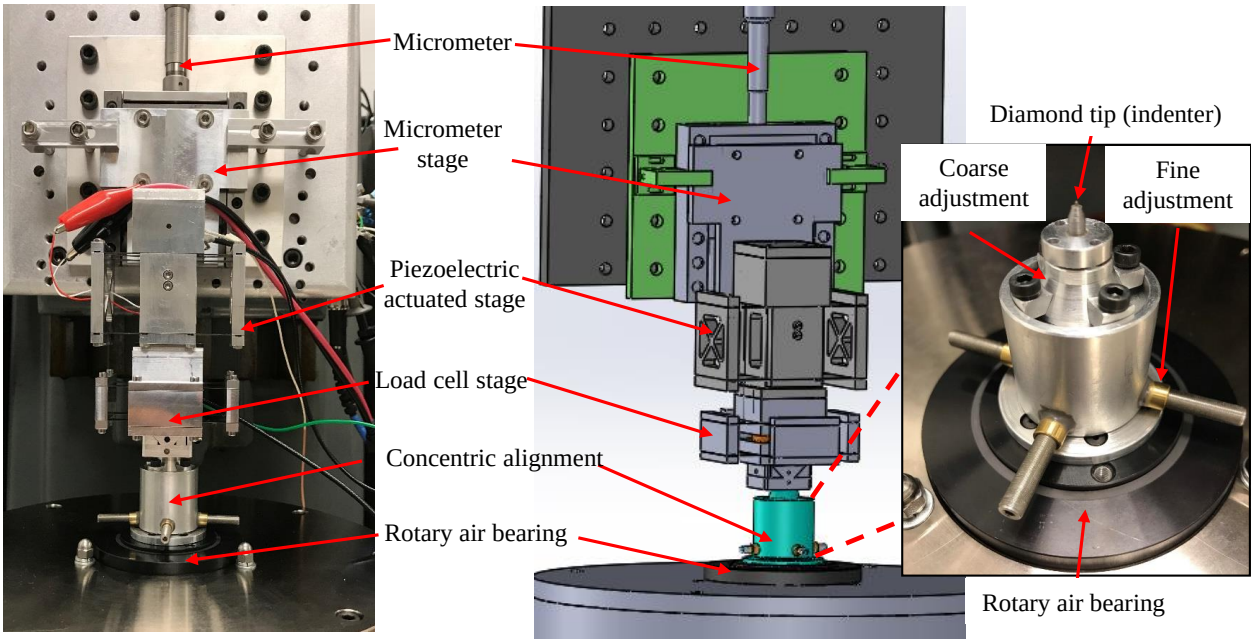


Figure 55. Experimental facility showing relations between alignment, actuation, and sensing mechanisms.

The concentric alignment system is used for minimizing diamond tip rotational error along the rotation axis of the air bearing. The angular rotation of the air bearing is measured using a rotary encoder header (MicroE Mercury 3500) and a glass radial scale ring. The scale of the encoder is mounted on the rotation pad at the bottom of the rotary air bearing and the encoder

header is mounted on the station pad at the bottom of the rotary air bearing. A screw is used to fasten the scale of the encoder between a flat washer and an O-ring, as shown in Figure 56. This rotary encoder system provides 0.2 arc second resolution and the encoder header is mounted to the bottom end of the air bearing spindle using an encoder header mounting plate.

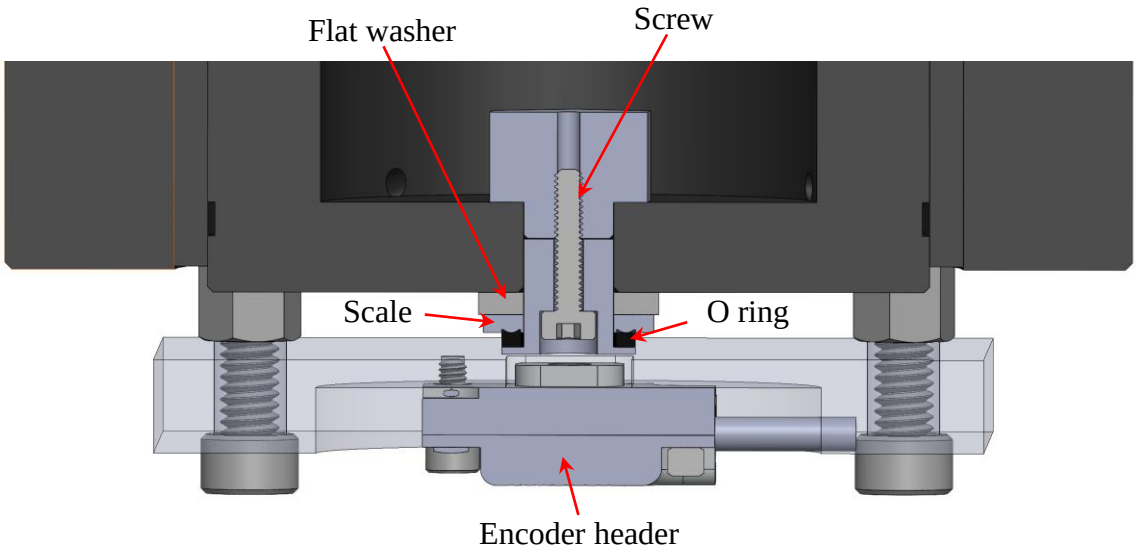


Figure 56. Rotary encoder header and scale are mounted in the stationary and rotary stage of the air bearing separately.

With reference to Figure 54 and Figure 55, the motion of the actuation stage and load-cell stage are measured using two capacitance gauges within a dual-flexure system. The first actuation stage flexure is driven by a Lead Zirconate Titanate (PZT) piezoelectric actuator, in section 3.4. The second load-cell stage is a leaf spring flexure structure attached a dovetail sample mounting structure, see section 3.5. Test specimen will be glued at the bottom of the dovetail structure. A single crystal diamond (Berkovich) tip was mounted on the center of the top plate, and can be removed and switched out using M2 screws, as shown in Figure 57. The specimen to be tested is attached to the moving platform of the load-cell flexure that bends in response to the indentation

and the deflection of the load-cell is measured and recorded using capacitance gage via a 16-bit DAQ system.

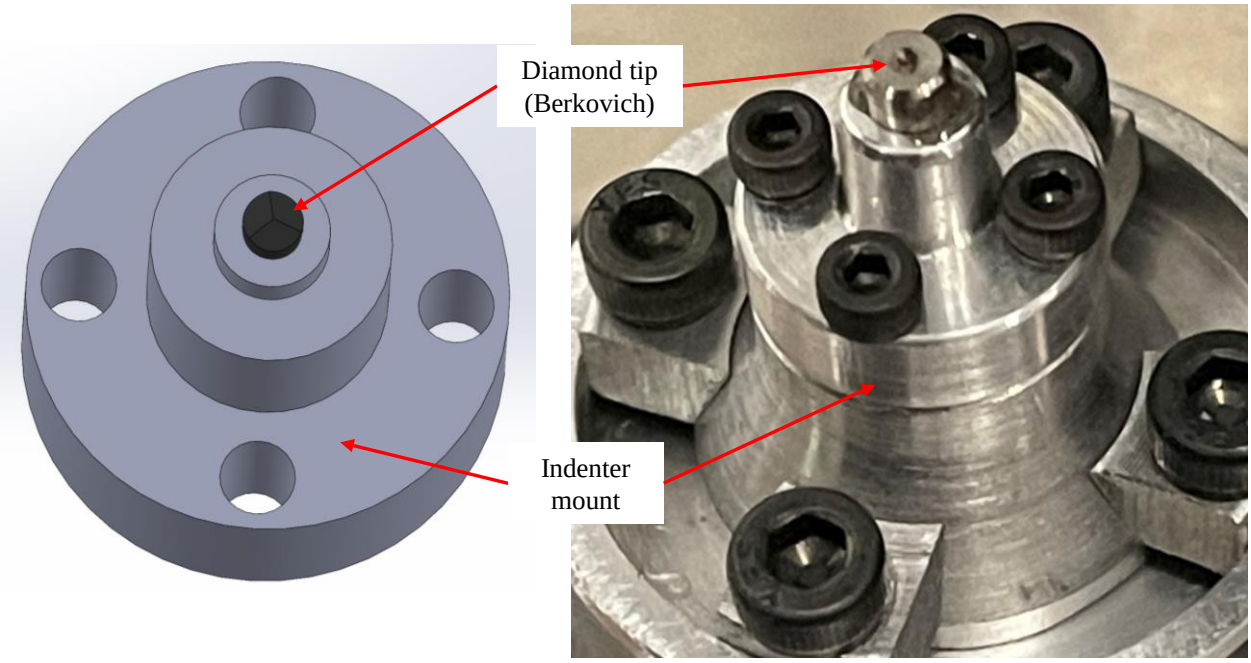


Figure 57. Single crystal diamond Berkovich tip was mounted on the center of the indenter mount by screws.

## 3.3 ROTARY STAGE AND ALIGNMENT

The entire rotary system was mounted on the XY table of a Moore measuring machine for testing. Figure 58 show that the rotary stage includes a rotary air bearing, a concentric apparatus (centering adjustment) and a rotary encoder (encoder header and ring scale). The concentric apparatus for coaxial alignment between indenter tip and rotary axis of air bearing is assembled on the rotary pad of the air bearing. The air bearing has radial and axial stiffness of 2.3 N-m/mrad and 17 N/μm respectively. The air bearing error motions of ±25 nm at 280 kPa with flight height of 3.7 μm (quote from Professional Instrument). The system stability test is shown in section 5.6.

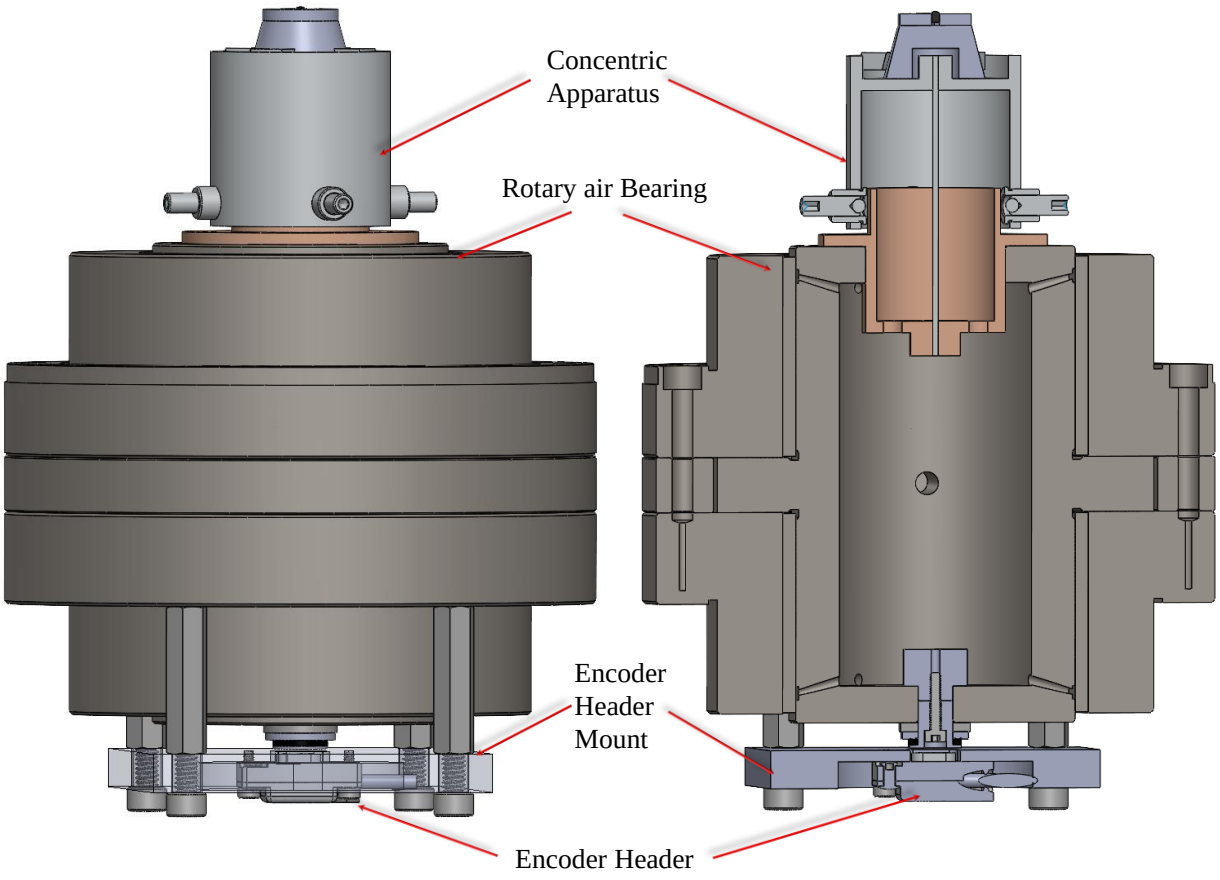


Figure 58. Rotary stage with concentric alignment apparatus, rotary air bearing, and encoder.

The concentric centering system is to minimize the coaxial error between the diamond tip and the rotation axis of the air bearing by using a single-plane flexure rod design. Figure 59 shows how the flexure rod is assembled on the concentric (centering) apparatus. The flexure rod is connecting with the upper and lower cylindrical supporting structure by epoxy glue. The lateral force to the flex rod is applied at the midpoint between each end to eliminate x or y rotation of the indenter tip. Four precision fine screw (thread insert) adjusters were used for the coaxial alignment between the indenter tip and rotary axis of the air bearing. These fine thread inserts were chosen as they provide a very small (~ 0.3 mm) adjustment per full 360-degree rotation and can be tightened against one another in order to provide more precise adjustment. The rough adjustment

system consists of a shifting, trapezoidal cone which is set on top of the precision adjustment cylinder. Four adjustment screws and blocks set between the "parapet" of the adjustment cylinder and the trapezoidal cone pin the cone in place.

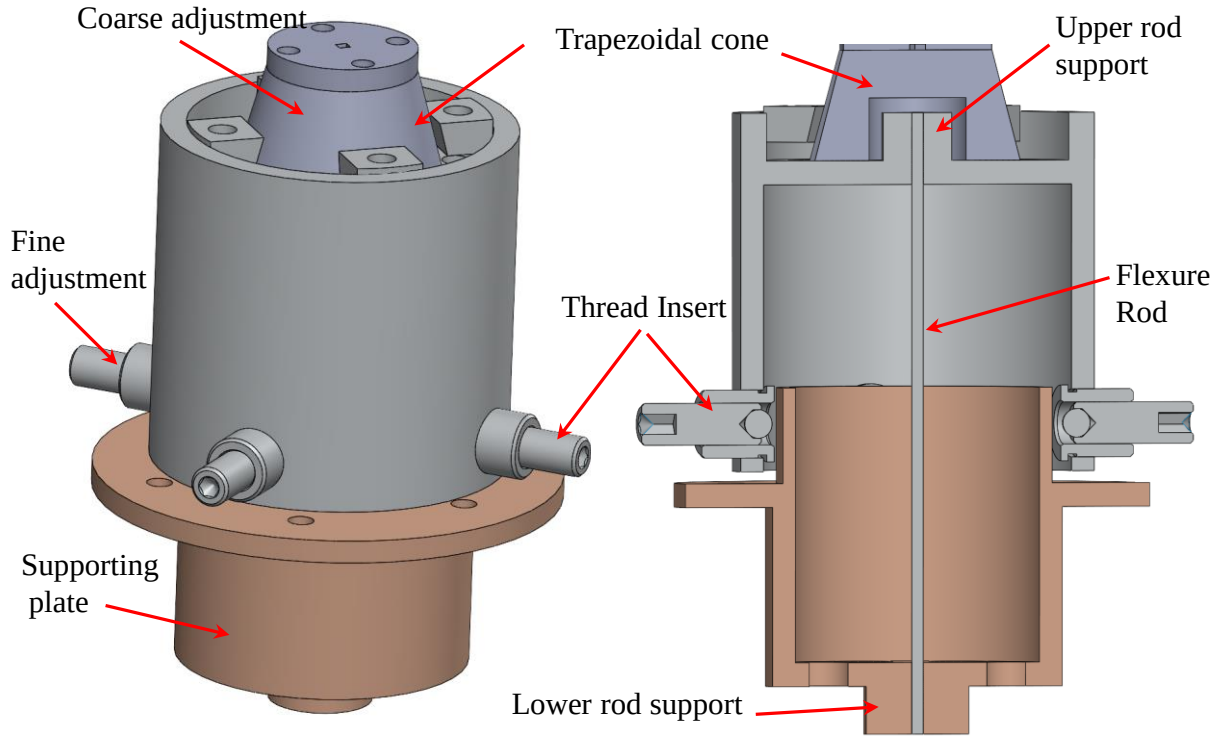


Figure 59. Flexure rod design of the centering apparatus.

For fixed-fixed end flexure rod, the deformation angle will be zero if the load is aligned along the middle plane of the rod [25]. When loads applied at the middle plane are changing by adjusting the fine screws, the axial line of the upper cylindrical supporting structure will be adjusted in a motion for which the upper cylinder remain parallel to the lower cylindrical supporting structure (i.e., a planar motion normal to the axis of the rod). The relevant equation to predict the lateral stiffness of the rod is

$$k = 12EI/L^3 \tag{3.1}$$

First, mounting the concentric centering apparatus on the top portion of the air bearing spindle. Second, the coarse adjustment structures will position the indenter tip relative to the rotation center of the centering apparatus. Then, a digital microscope camera (Jiusion 40 to 1000x Magnification Endoscope) is setting up as the top view or the side view of the diamond tip, Figure 60a and Figure 60b. When the diamond tip is rotating with the rotary centering system, the diamond tip is drawing a circle and the diameter of the circle will be recognized on the screen of the camera vision system. Figure 60c is a screenshot of the diamond tip and its mirror image from a polished sample. The fine adjustment screws will be tuned so that the rotational circle of the diamond tip will be minimized. Figure 60 shows the assembly rotary stage.

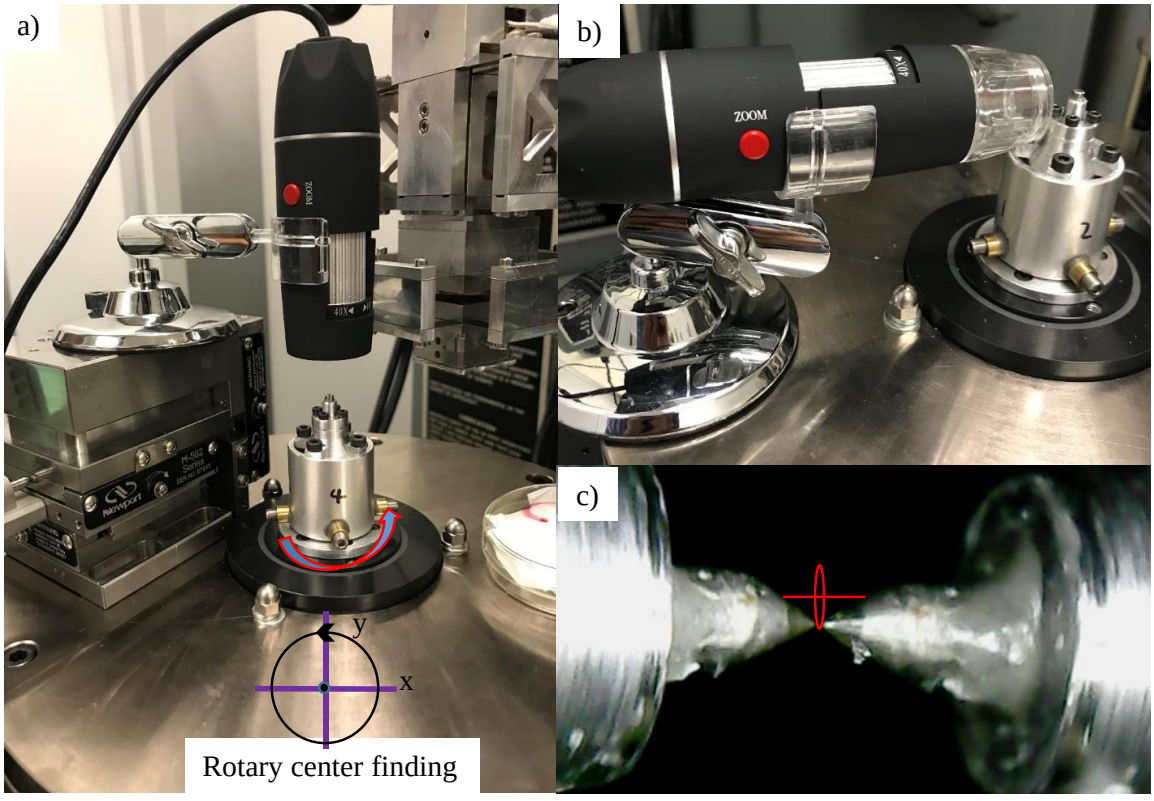


Figure 60. The assembled rotary stage and its rotary center finding. (a) A digital microscope camera is setting up as the top view of the diamond tip to minimize the coaxial error between the tip and the rotational axis of the air bearing spindle (b) A camera side view of the diamond tip (c) Picture of a cone diamond tip and its mirroring image from a polished sample.

## 3.4 ACTUATION STAGE RECTILINEARITY

For the nano-indentation process, it is important to have precise linearity of the actuation stage for the indentation process to minimize the measurement uncertainty. The abbe principle [40] states that: "In order to improve measurement accuracy, the measurement target and the scale of the measuring instrument must be placed in a collinear fashion in the measurement direction." In this design, the PZT actuator is collinear with movement direction of the flexure-based stage as well as the capacitance gage sensor (Figure 61). The forward and backward movement of the actuation stage is recorded by the capacitance displacement sensor and explained in the section 5.4.

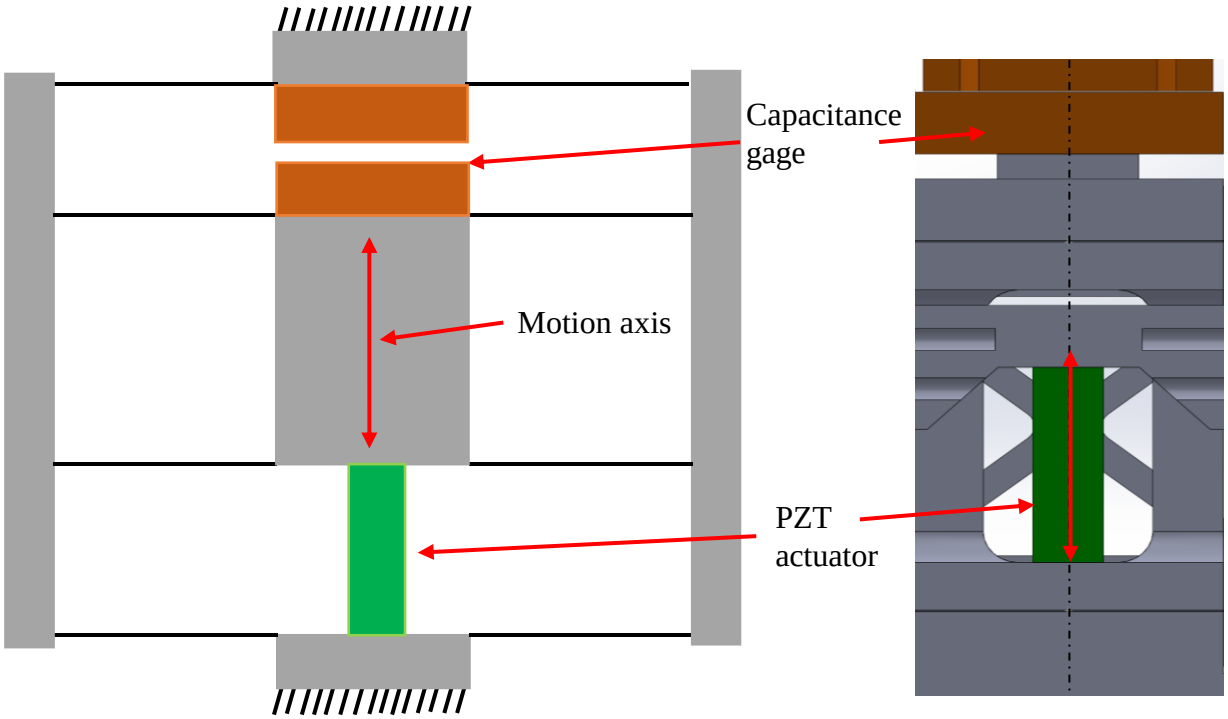


Figure 61. PZT actuator, capacitance gage sensor, and flexure motion axes are all collinear thereby conforming with Abbe's principle.

Symmetric flexure design (double-compound flexure) in parallel is frequently used for motion studies and the angular motion error is evaluated using an autocollimator. This project uses

a typical flexure mechanism, and the 3D drawings and cross-section views (SECTION A-A) of the actuation stage are illustrated in Figure 62.

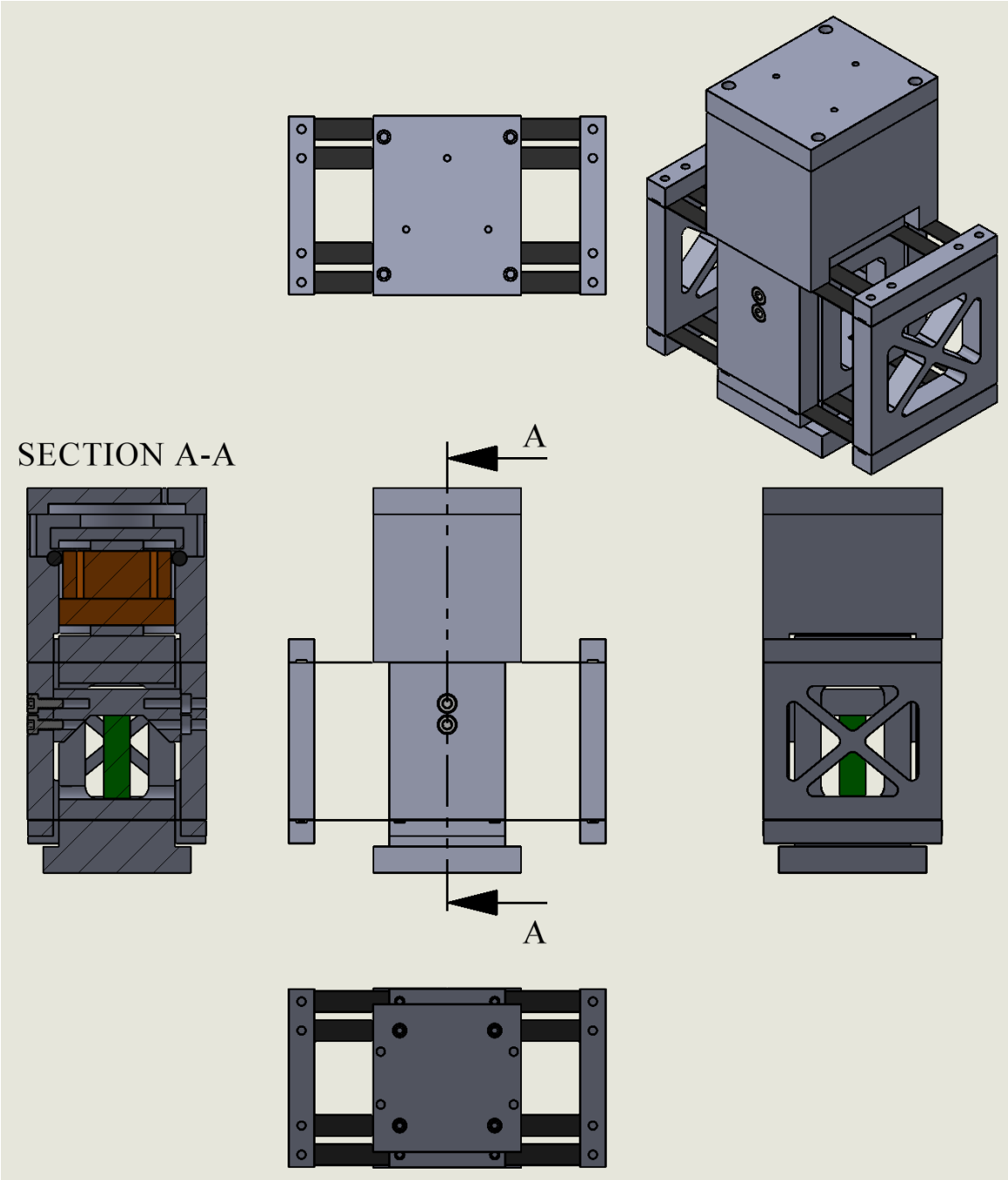


Figure 62. 3D drawings and cross-section views of the actuation stage.

The motion axis of the 3D structure, PZT actuator, and the capacitance gage are coaxial. The motion stage was constraint by leaf springs and was able to move along the PZT actuator. It can be regarded as combination of two double parallelogram linear springs in parallel, see also section 2.3.5. The overall stiffness of the 3D flexure-based actuation stage can be increased since more parallel springs are added.

Experimental tilt test is used to evaluate the linearity of the actuation stage. An autocollimator (resolution of 5 arc seconds) with CCD camera is setting to measure the tilt angle, at the same time, the displacement of the stage is recording from a LVDT displacement sensor. When the actuation stage moves 16 μm displacement, the maximum tilt angle is less than 0.05 arc sec as showing in Figure 63.

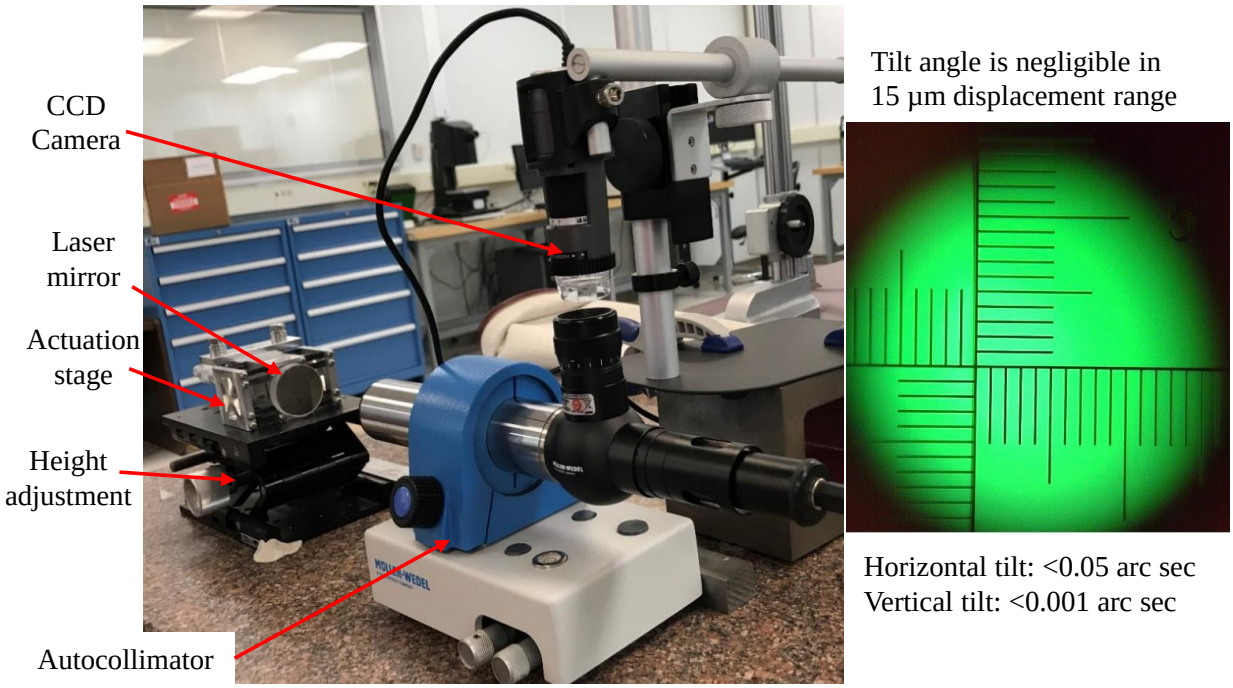


Figure 63. Autocollimator tilt measurements get negligible tilt angle.

## 3.5 LOAD-CELL STAGE BUILD AND SAMPLE MOUNT

The load-cell stage includes two flexures in serial design and the capacitance gage is mounted on top and bottom of the structures. Figure 64 shows the assembled load-cell stage and its flexures, capacitance gages, and structures.

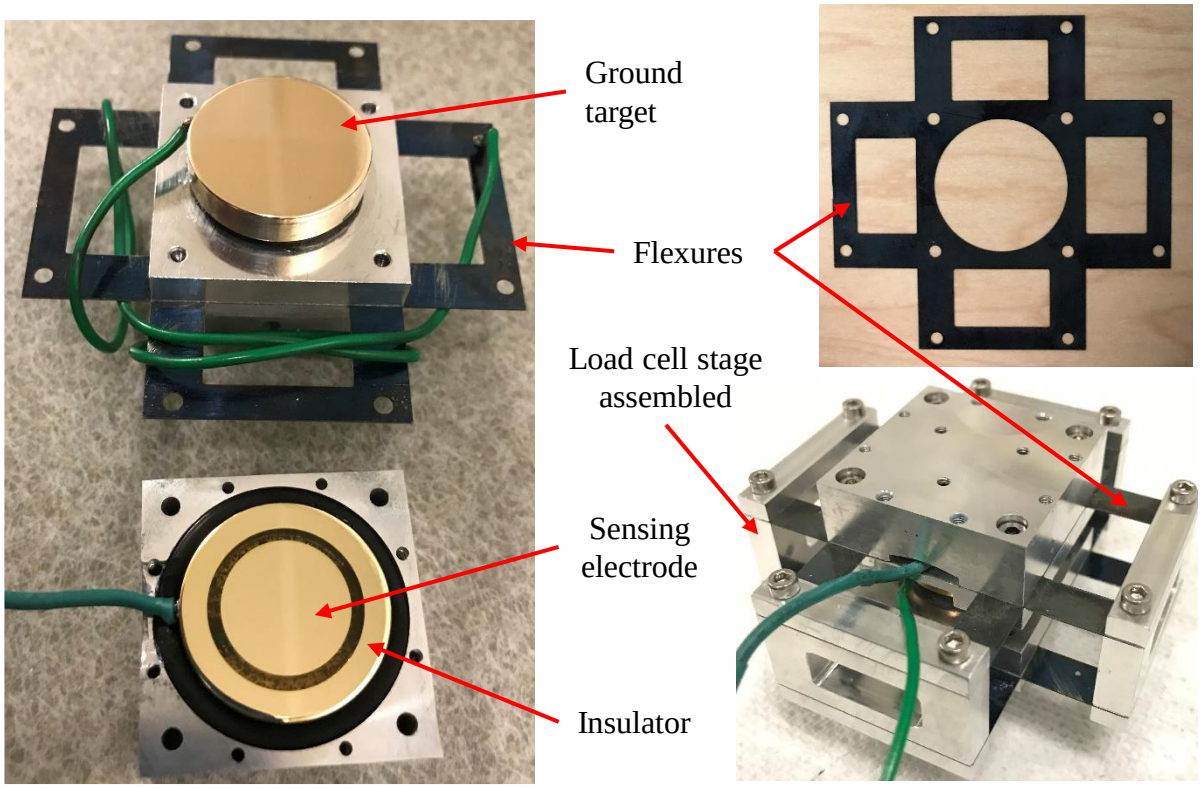


Figure 64. Load-cell capacitance gage, flexures, and structures parts and assembled.

This part explains how a polished metal specimen is glued at the bottom of the dovetail structure using epoxy. The ideal dimensions of the specimen will be like a 10 mm square shape and the thickness of the specimen could be around 0.5 mm to a few mm. Before testing, the sample is glued on a flat surface on a specimen mount that slid in and out of the test region on the dovetail structure. A photograph of how samples are mounted using a locking dovetail structure is shown in Figure 65.

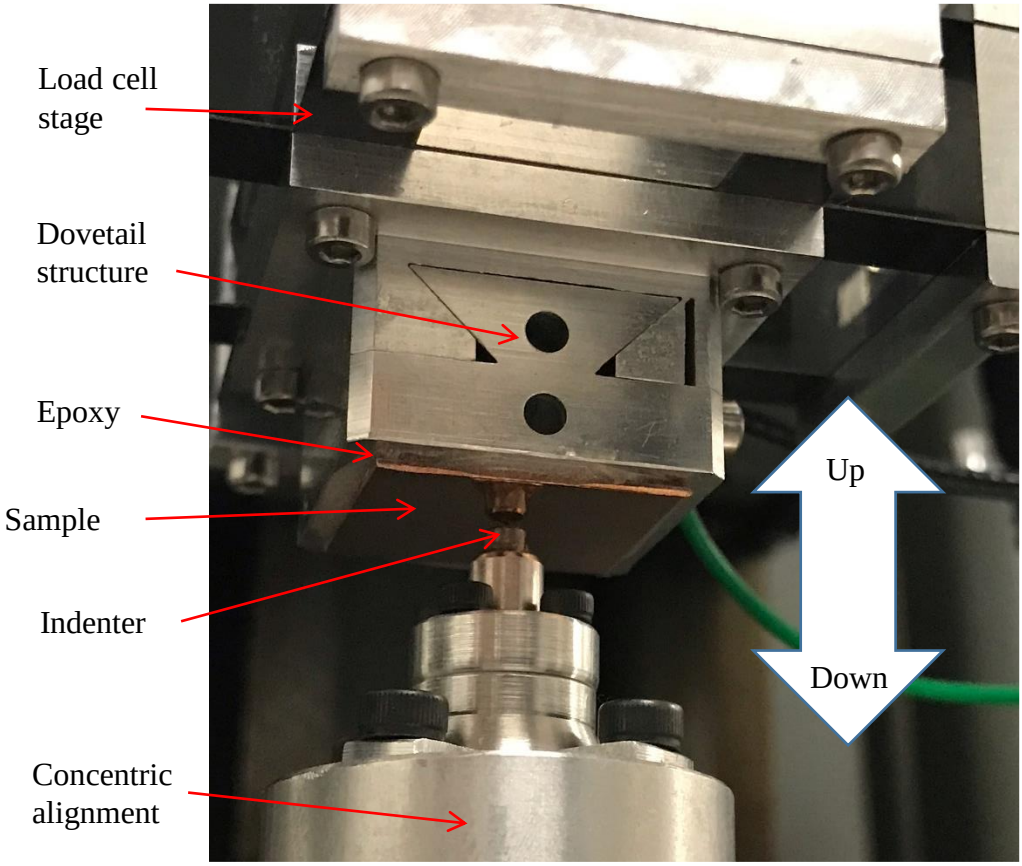


Figure 65. A polished sample mounted on the load-cell of Nano-indentation for material testing.

## 3.6 BALANCED LINE DRIVER FOR CAPACITANCE GAGE CIRCUITS

For each capacitance gage circuit, one audio-balanced line driver (DRV135), and one instrumentation amplifier (AD630) were used, and the schematic of the capacitance gage circuit is showing in Figure 66. The DRV135 can generate two signals: one is same as Vin signal, and another signal is 180 degrees phase-shifted with the Vin. For instance, a 20 kHz 2 V amplitude sinusoidal input signal $Vin = 2\sin(2\pi * 20{,}000 * t)$ will get two symmetric output signals: $V_{12} = 2\sin(2\pi * 20{,}000 * t)$ and $V_{78} = 2\sin(2\pi * 20{,}000 * t + \pi)$ . Those two signals will pass through a low dielectric-losses polystyrene reference capacitor ($C_{ref.}$), a load-cell capacitor or actuator stage capacitor ($C_{var.}$). Those two capacitators will act as a voltage divider, therefore the

imbalance signal will pass to the Pin 3 of the AD630 amplifier. The amplifier used to transfer the signal Vo through a long cable to the Lock-in amplifier.

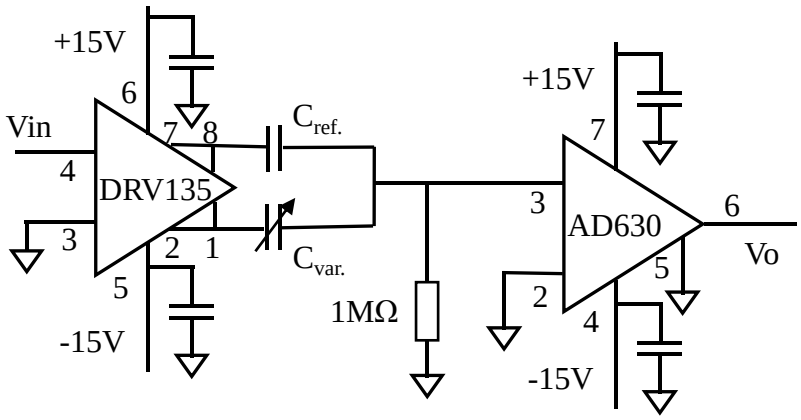


Figure 66. Schematic of capacitance gage circuits used for this nanoindentation research.

## 3.7 16-BIT ADCS AND DACS

A high-resolution analogy-to-digital (ADC) and digital-to-analog (DAC) Data Acquisition (DAQ) were designed and manufactured for this nano-indentation system. Resolution refers to the number of binary levels an ADC can use to represent a signal. A N-bit DAQ means one part in $2^N$ resolution, and this gives the DAQ the capability to send out or acquire more precise signals. To illustrate this point, imagine how a sine wave would be represented if it were passed through an ADC with different resolutions are presenting in Figure 67 (6-bit and 16-bit ADC). A 6-bit can represent 64 ($2^6$) discrete voltage levels and a 16-bit ADC can represent 65536 ($2^{16}$) discrete voltage levels. The representation of the sine wave with a 6-bit resolution looks more like a step function than a sine wave where the 16-bit ADC provides a clean-looking sine wave as shown in Figure 67.

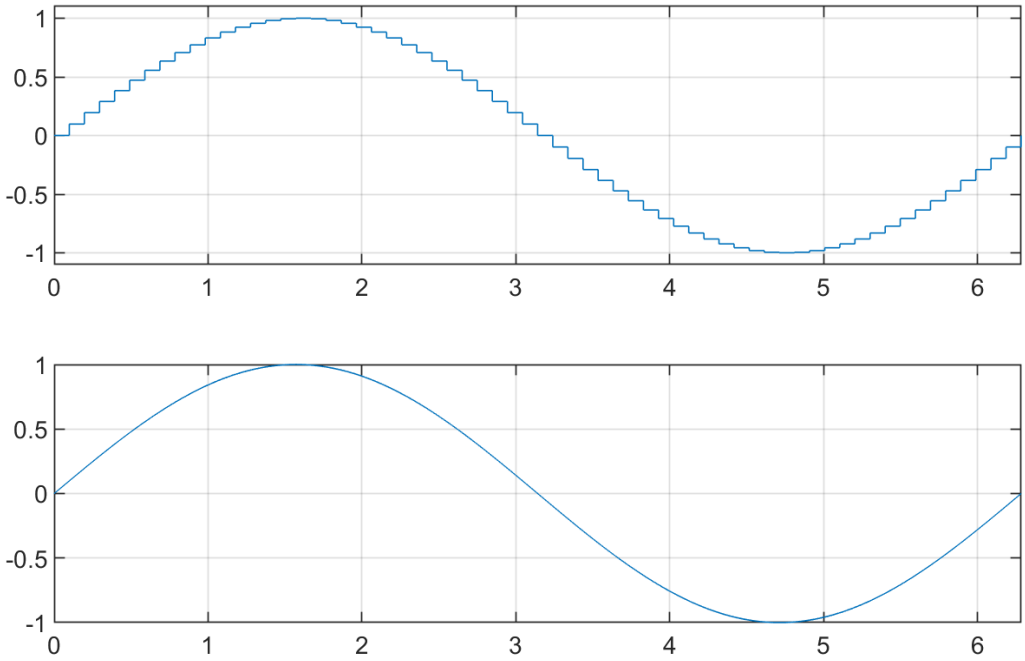


Figure 67. A 6-bit ADC and a 16-bit ADC signal.

The LTC1859CG ADC has multiple inputs to accept programmable input ranges of 0 - 5 V, 0 - 10 V, ±5 V, and ±10 V. Figure 68 shows the schematic of 16-bits ADCs. Selecting the channels to be read and input voltage range for each channel is achieved using the supplied myRIO and LabVIEW software.

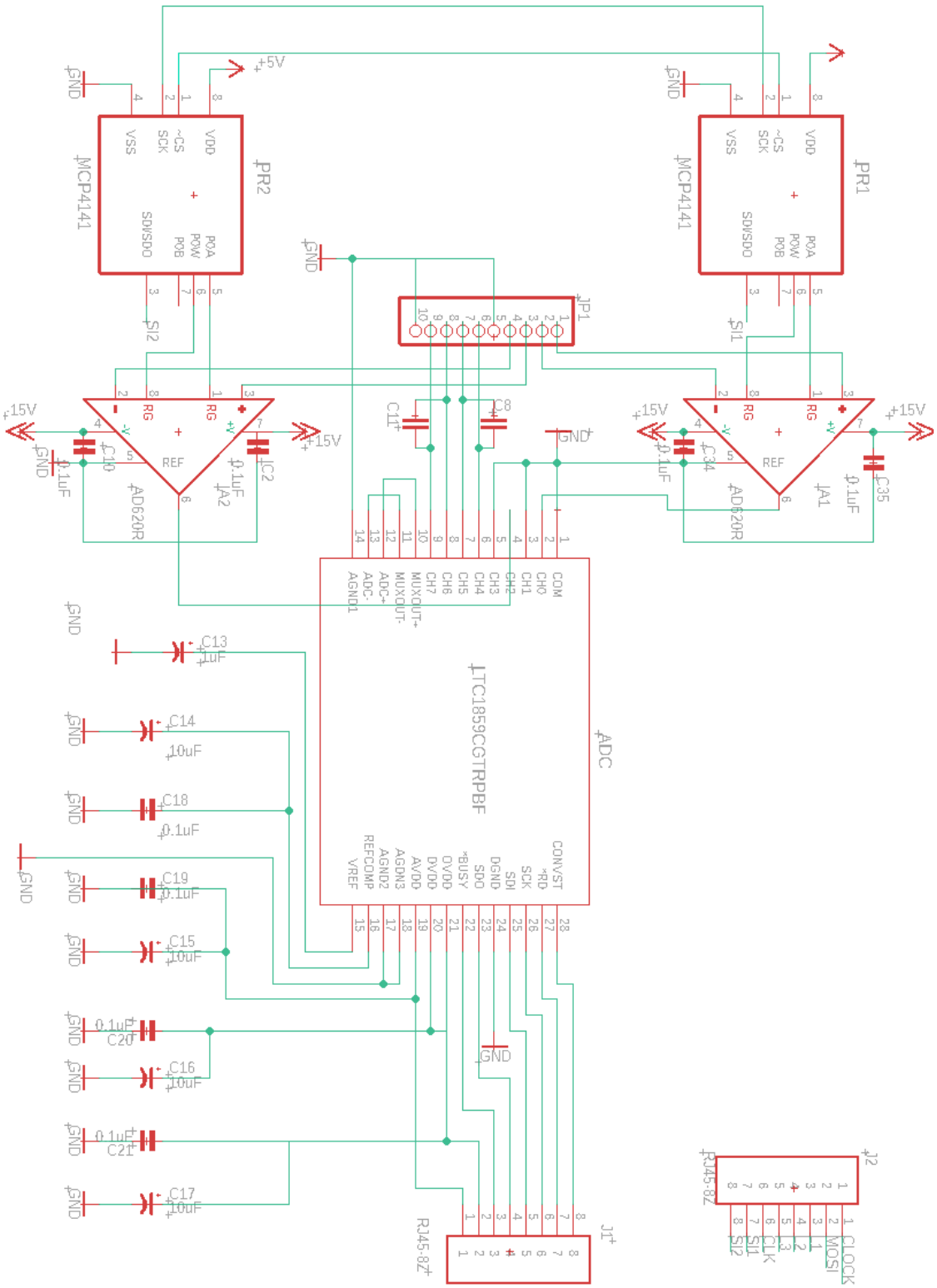


Figure 68. Schematic of LTC1859CG ADCs for 16-bit signals.

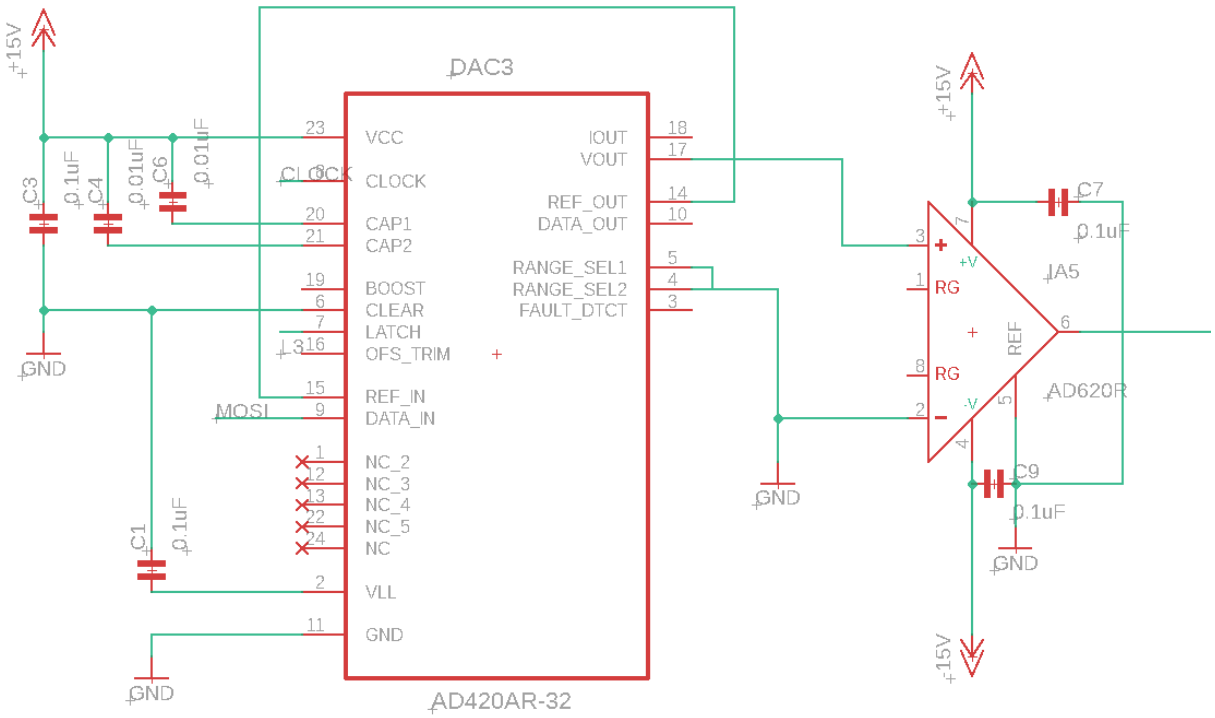


Figure 69. Schematic of AD420AR DACs for 16-bit out signals.

The 16-bit DACs (Figure 69) are designed to provide 0 to 10 V to the inputs of the high voltage amplifiers to drive PZT actuator stage. The output from each DAC is filtered using a 2$^{nd}$ order Salen-Key low pass filter with a cut-off at 10 kHz for which the theoretical frequency response is shown in Figure 70. Standard BNC connectors on the front and back panel of the amplifier box are used to connect voltage signals to the ADCs and DACs.

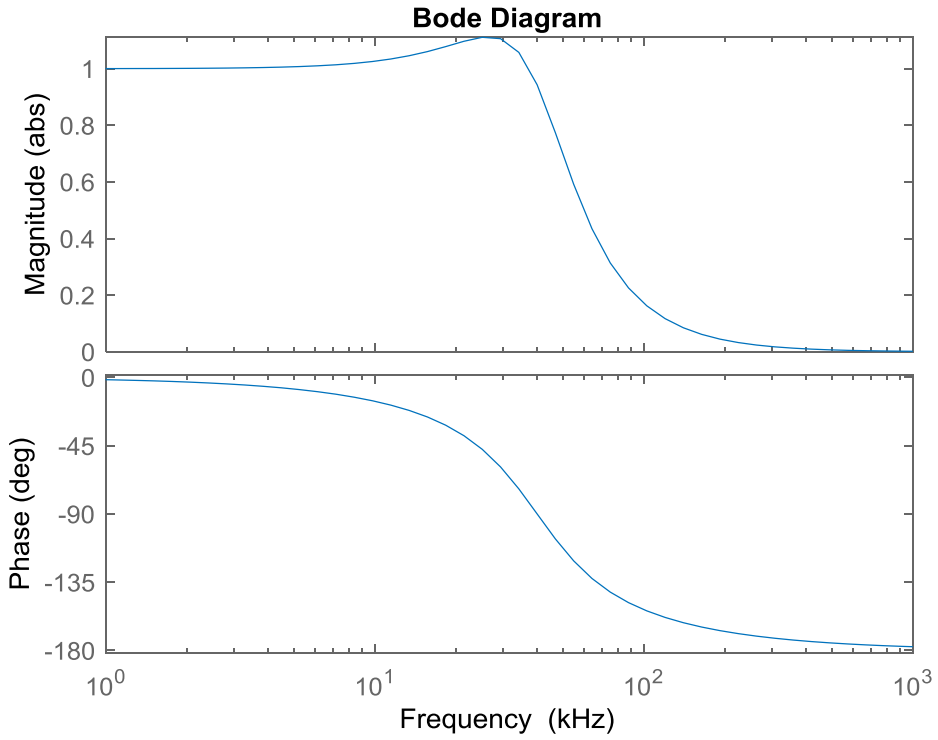


Figure 70. A 2nd order Salen-Key low pass filter with a cut-off at 10 kHz.

Figure 71 (top) is the bode plot diagram of this fabricated circuit of the Salen-Key low pass filter and shows that a 10 kHz low pass filter match the design requirement using HP 35665A dynamic signal analyzer (HP DSA). Figure 71 (bottom) is the bode plot diagram from the poles and zeros from the HP DSA measurement.

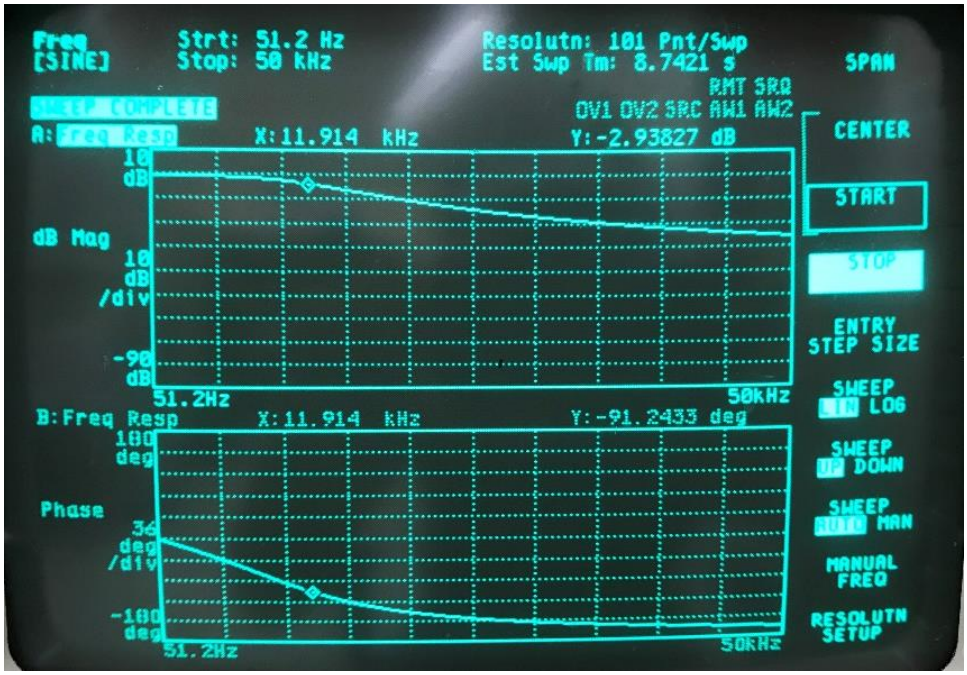


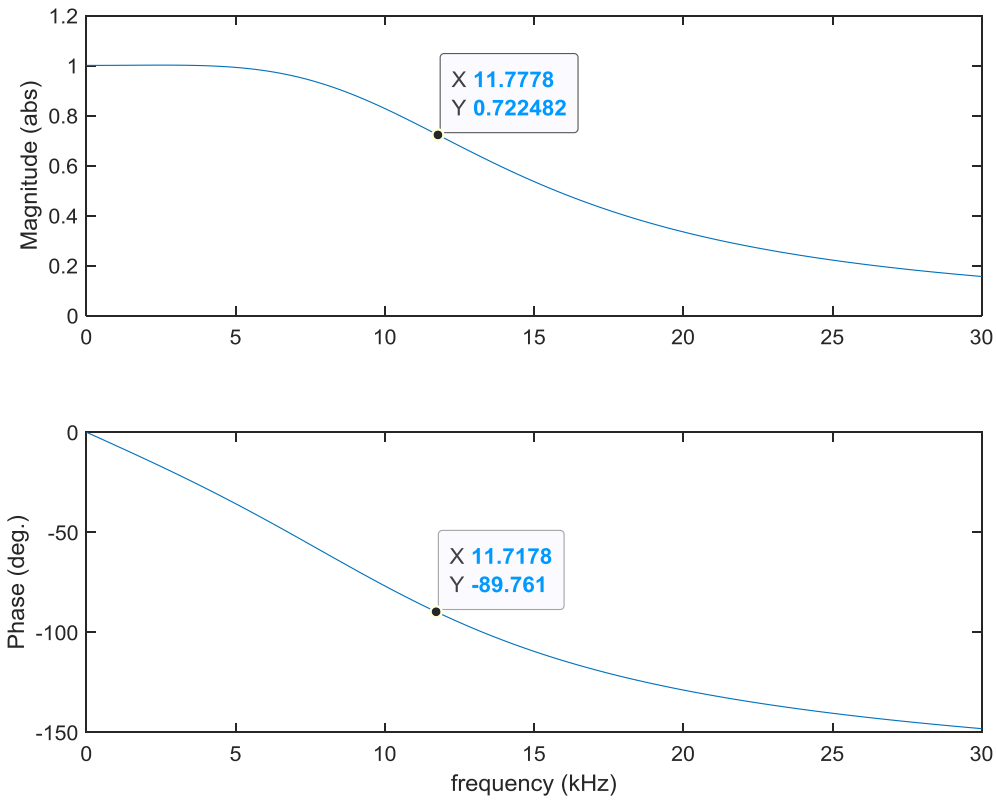


Figure 71. Top: Bode plot diagram from the HP DSA that the 10 kHz low pass filter match the design requirement. Bottom: Bode plot diagram from the poles and zeros from HP DSA shows that a 10 kHz low pass filter match the design requirement.

A circuit board layout is shown in Figure 72. After fabrication and assembly, the PCB prototype of 16-bit ADCs and DACs is showing in the Figure 73.

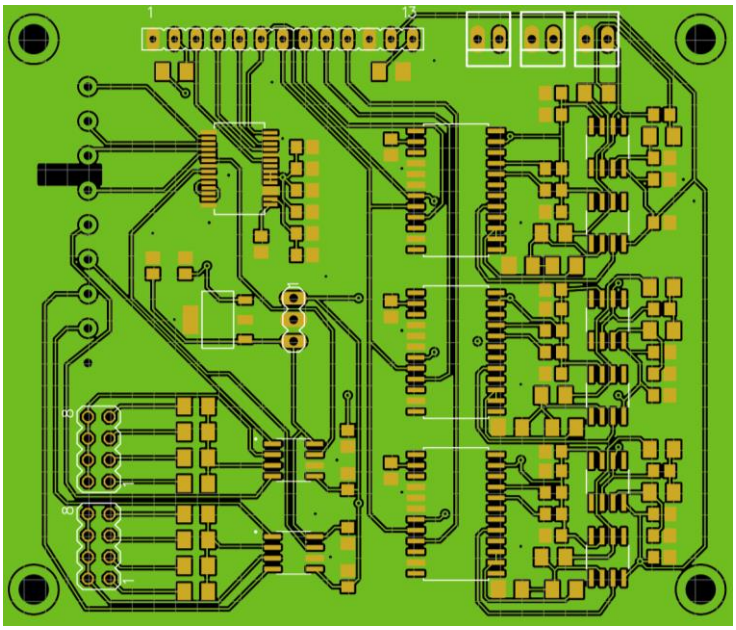

Figure 72. The circuit board layout of the prototyped 16-bit ADCs and DACs.

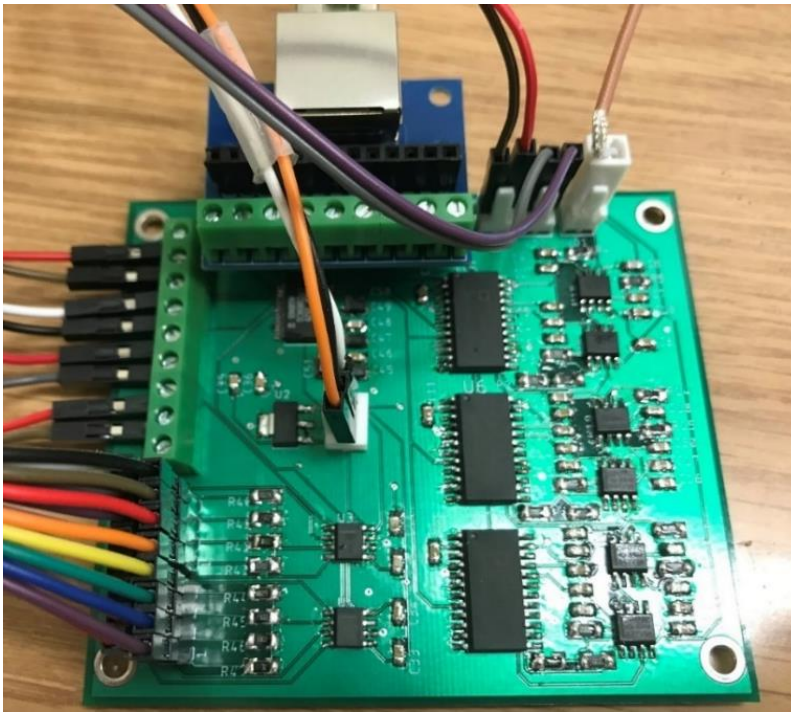

Figure 73. The PCB board of the prototyped 16-bit ADCs and DACs.

Figure 74 is one of the calibration curves for the prototyped 16-bit ADCs comparing with Keithley digital multimeter (DMM), and the residual is shown in the second vertical axis (orange). The 16-bit DAC outputs have a linear fitting curve that reference to the Keithley DMM with a gain of 0.99790951 has R-square value of 0.99999999. Figure 75 is one of the calibration curves for the prototyped 16-bit ADCs comparing with Keithley digital multimeter (DMM), and the residual is shown in the second vertical axis (orange). The ADC inputs have a linear fitting curve that reference to the DMM with a gain of 0.9866782 has R-square value of 0.9999991.

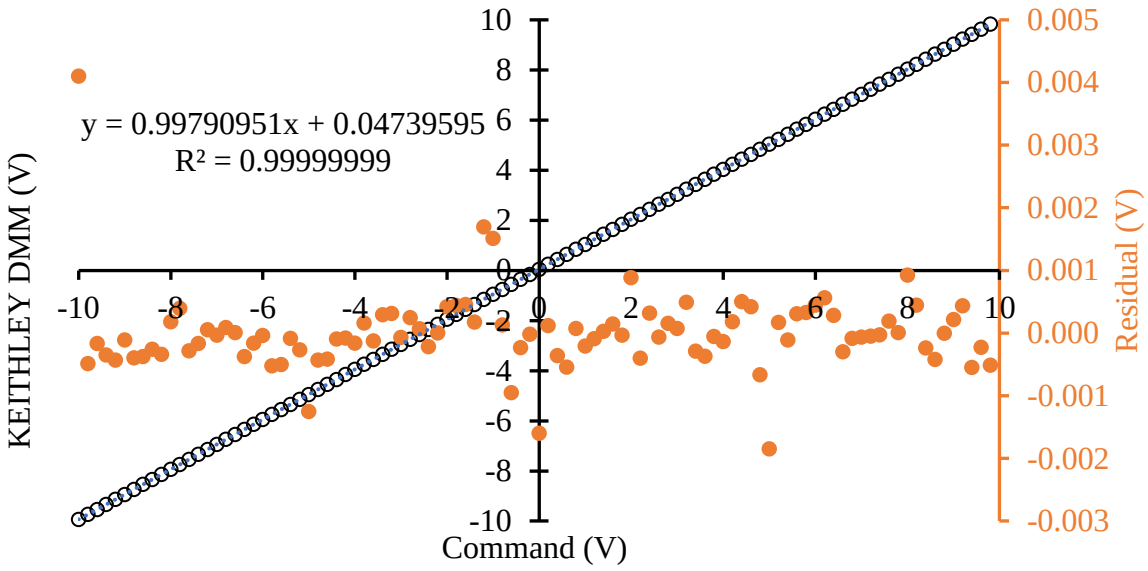


Figure 74. One of the comparison curves for the command output from the prototyped 16-bit DACs and the measured data from the Keithley digital multimeter (DMM).

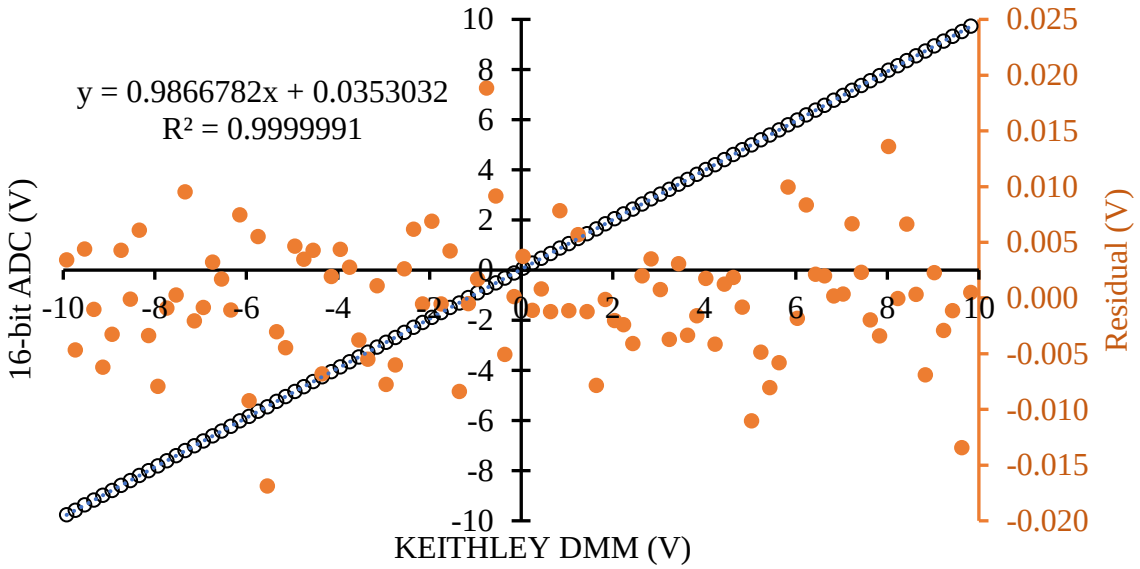


Figure 75. One of the comparison curves for the measured data via the prototyped 16-bit ADCs and the measured data from the Keithley digital multimeter (DMM).

# CHAPTER 4: CAPACITIVE SENSOR DESIGN AND PERFORMANCE CHARACTERIZATION

The capacitive sensor has been used for precision engineering for more than 100 years (Maxwell 1873). Being non-contact and capable of relatively high precision measurement, capacitive sensors are one of the most popular sensors for high resolution displacement and, indirectly, pressure, velocity and acceleration. Capacitive sensor works by measuring the amount of voltages between the probe sensing surface and a target. When an alternating voltage is applied across the probe and the target electrodes, current flows through the capacitor that is a result of the electrodes area and, inversely, the electrode separation. The closer the probe to the target, the greater the capacitance and the greater the current flow. For sensing current to flow, it must find a path to ground. Any resistance to the current flow to ground can interfere in the measurement. Therefore, the effect of using an ungrounded target depends on the alternate path. The sensing current takes to ground and the amount of resistance it encounters along that path often ungrounded targets such as spindle rotors have a significant amount of their surface area very near a grounded surface. Errors caused by ungrounded targets may include offset errors which are related to the measurement of absolute distance to the target and sensitivity errors which relate to measurement of changes in the target position. Offset errors usually not consequently because capacitive measurements are typically taken relative to some point rather than absolute gap measurements. Since capacitance uses alternating current (AC) measurement, the offset can be removed with a high-pass filter as well. Sensitivity errors can be more problematic because of its direct relationship to measured displacement. Electrical noise may also increase with ungrounded target. The following sections 4.1 and 4.2 present the design, manufacturing, and assembly of the capacitive gage.

## 4.1 DESIGN OF CAPACITIVE GAUGE

The design of a capacitance gage will include the mechanical and electrical parts. The mechanical parts include both a probe and target electrode. The electrical parts include reference capacitance with high stability and a balance line drive is used for sending out two 180 phase different sinusoidal signals having a frequency of 20 kHz. A Lock-in amplifier is used to detect the amplitude changing of the signal, and then convert this change into DC voltage. 16-bit ADCs were used to measure all voltages after which the displacement can be recorded from prior calibration. Additionally, the displacements of the actuation stage and the load-cell stage are also recorded during the nano-indentation process.

The electrode (probe) diameter of the capacitance gage is 16 mm, the nominal displacement of the capacitance gage is chosen around 22 µm, and the capacitance value will be 80 pf. The total range of the capacitance gage is designed to be 16 µm (± 8µm).

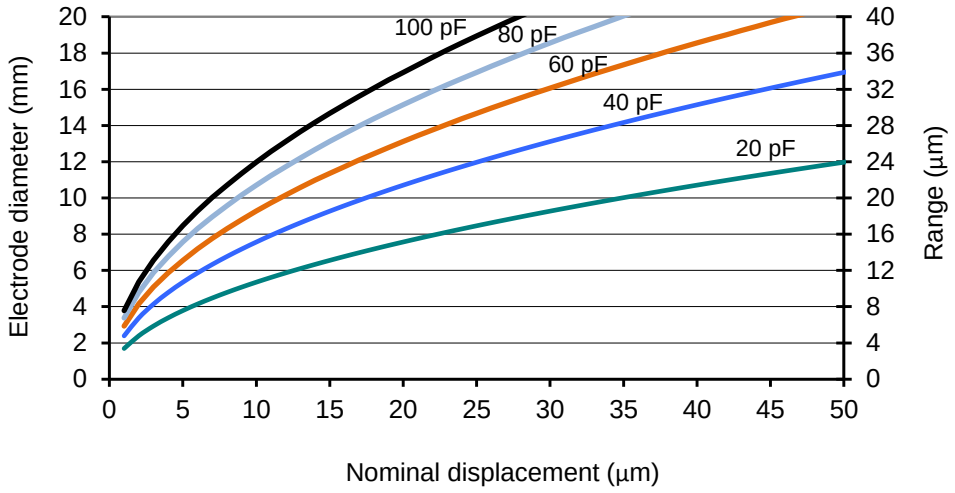


Figure 76. Electrode diameter and capacitance gage range as a function of nominal electrode separation.

The parallel-plate capacitors are used and the capacitance is determined by the equation $C = (\varepsilon_0 \varepsilon_r A) / d$ . Ideally, the fixed values are the area of the parallel conductive plates $A$, and the dielectric coefficient of air $\varepsilon_r$ in the lab by keeping atmospheric conditions at 20 °C, and $\varepsilon_0$ is the permittivity of free space or the dielectric constant of the vacuum. The capacitances will change when changing the gap between the parallel conductive plates. In this research, the vacuum permittivity $\varepsilon_0$ (also called permittivity of free space or the electric constant) is 8.8541878 pF·m$^{-1}$, the dielectric coefficient of air $\varepsilon_r$ is 1.0006 at 20 °C, and the area $A$ of the capacitance probe is calculated as 0.000201062 m$^2$. $C$ will be calculated by changing the $d$ term and for this electrode area. Figure 77 shows the relationship between the electrode separation and capacitance values.

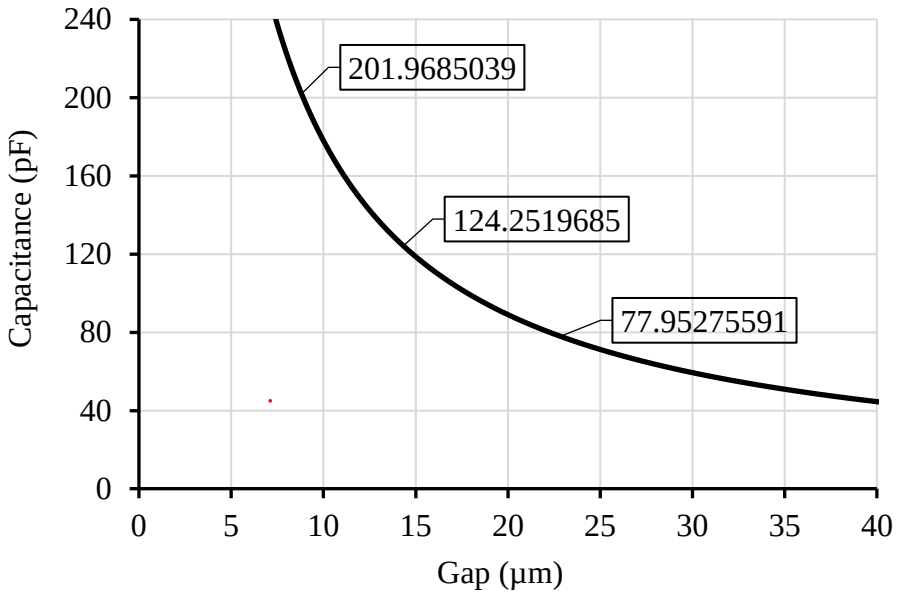


Figure 77. The electrode separation and capacitance curve.

For two parallel electrodes (lower and upper) surfaces capacitance gage design, the misalignment is analyzed, and its mathematic model is discussed in this section. The lower electrode is considered to be horizontal with the upper electrode separated a distance $d_o$ at one edge and inclined at an angle theta. If the gap has a homogeneous permittivity, there is a uniform potential over each plate, and fringing fields can be ignored. The capacitance, $C$, can be obtained by summing individual strips along the electrode inclined at theta degrees [44], i.e.

$$C = \int_0^{D\cos\theta} \frac{\varepsilon L(x)dx}{d_0 + x\sin\theta} \tag{4.1}$$

This is a relatively straightforward integral of a round shape capacitance gage, the solution of which is given by

$$C = \frac{\varepsilon L}{\sin\theta}\ln\left(\frac{d_0 + D\cos\theta\sin\theta}{d_0}\right) = \frac{\varepsilon L}{\sin\theta}\ln\left(\frac{d_0 + \frac{D}{2}\sin 2\theta}{d_0}\right) \tag{4.2}$$

A useful check is the limit as the angle between plates becomes zero (i.e. parallel plate capacitors). This can be derived using L'Hopital's Rule

$$\lim_{\theta\to 0}\frac{f(\theta)}{g(\theta)} = \lim_{\theta\to 0}\frac{f'(\theta)}{g'(\theta)} = \lim_{\theta\to 0}\frac{D\cos 2\theta\varepsilon L}{\cos\theta\left(d_0 + \frac{D}{2}\sin 2\theta\right)} \Rightarrow \frac{\varepsilon LD}{d_0} \tag{4.3}$$

Thus, it has been shown that in the limit this is consistent with parallel plate capacitor theory. For a circular electrode it is necessary to choose a tilt axis that is colinear with its center.

Selecting a vertical strip of width $dx$ and length $L$ can be shown that the total area of the strip is given by

$$A = 2\left[1-\left(\frac{x}{\cos\theta}\right)^2\right]^{\frac{1}{2}} dx \tag{4.4}$$

Figure 78 indicates an orthogonal view from which the height of the strip, $D$, from the base electrode is given by

$$D = d_0 + x\sin\theta \tag{4.5}$$

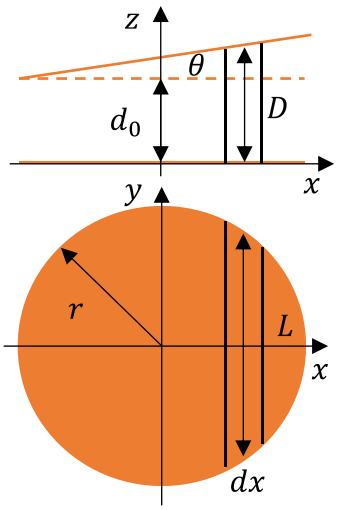


Figure 78. An orthogonal view of the non-parallel plate capacitance design with a θ tilt error.

Equations 4.4 and 4.5 can be combined to yield the total capacitance between the two plates given by the integral equation

$$C = 2\varepsilon \int_{-r\cos\theta}^{r\cos\theta} \frac{\left[r^2-\left(\frac{x}{\cos\theta}\right)^2\right]^{\frac{1}{2}}}{d_0 + x\sin\theta} dx = \frac{2\varepsilon r}{d_0} \int_{-r\cos\theta}^{r\cos\theta} \frac{\left[1-\left(\frac{x}{r\cos\theta}\right)^2\right]^{\frac{1}{2}}}{1+\frac{x\sin\theta}{d_0}} dx \tag{4.6}$$

Using two successive substitutions, $\sin\phi = \dfrac{x}{r\cos\theta}$ and $t = \tan(\dfrac{1}{2}\phi)$

Equation 4.6 can be rearranged to give the integral equation

$$C = \frac{4\varepsilon r^2 \cos\theta}{d_0} \int_{-1}^{1} \frac{\left(1-t^2\right)^2}{\left(1+t^2+2kt\right)\left(1+t^2\right)^2} dt \tag{4.7}$$

Where $k = \dfrac{r\cos\theta\sin\theta}{d_0} = \dfrac{r\sin 2\theta}{2d_0}$

It can be easily verified that the constant can range between zero (parallel plates) and unity. Upon reaching a value of unity, the two electrodes are in contact and the original model is no longer valid. The equation in the integral can be expanded into partial fractions to give

$$\frac{Cd_0}{4\varepsilon r^2 \cos\theta} = \int_{-1}^{1} \left[ \frac{\left(k^2-1\right)^2}{k^2\left(t^2+2kt+1\right)} + \frac{\left(t^2+1-2kt\right)}{k^2\left(1+t^2\right)^2} \right] dt = I_1 + I_2 \tag{4.8}$$

The integrals $I_1$ and $I_2$ can be solved individually to give

$$I_1 = \frac{\left[-\left(1-k^2\right)\right]^{\frac{1}{2}}}{k^2} \left[ \tan^{-1}\left( \frac{k+1}{\sqrt{1-k^2}} \right) - \tan^{-1}\left( \frac{k-1}{\sqrt{1-k^2}} \right) \right]_{-1}^{1} = \frac{\left[-\pi\left(1-k^2\right)\right]^{\frac{1}{2}}}{2k^2} \tag{4.9}$$

$$I_2 = \frac{1}{k^2} \left[ \tan^{-1}(t) + \frac{1}{k\left(1+t^2\right)} \right]_{-1}^{1} + \frac{\pi}{2k^2} \tag{4.10}$$

Equations 4.9 and 4.10 can be substituted into equation 4.8 which can be rearranged to give an explicit expression for the capacitance $C$ given by

$$C = \frac{2\pi\varepsilon r^2 \cos\theta}{d_0} \frac{\left[1-\left(1-k^2\right)^{\frac{1}{2}}\right]}{k^2} \tag{4.11}$$

Although the expression in parenthesis in equation 4.11 converges to a value of a half as $k$ tends to zero, it is convenient to expand this expression using binomial series for computational purposes. Ignoring terms of the order $k^8$ equation 4.11 becomes

$$C = \frac{\pi\varepsilon r^2 \cos\theta}{d_0}\left[1+\frac{k^2}{4}+\frac{k^4}{8}+\frac{5k^6}{32}..\right] \tag{4.12}$$

From this equation it can be seen that slight tilts of the capacitor electrode will result in an additive error containing only even harmonics. Equation 4.12 can be normalized to the capacitance value for parallel plates to give

$$\frac{C}{C_0} = \cos\theta\left[1+\frac{k^2}{4}+\frac{k^4}{8}+\frac{5k^6}{32}\right] \tag{4.13}$$

This has been plotted in Figure 79 for varying ratios of the average separation to radius of the electrodes over a range of values typical to many high sensitivity gauges. Error terms up to the twelfth order are included in this computation.

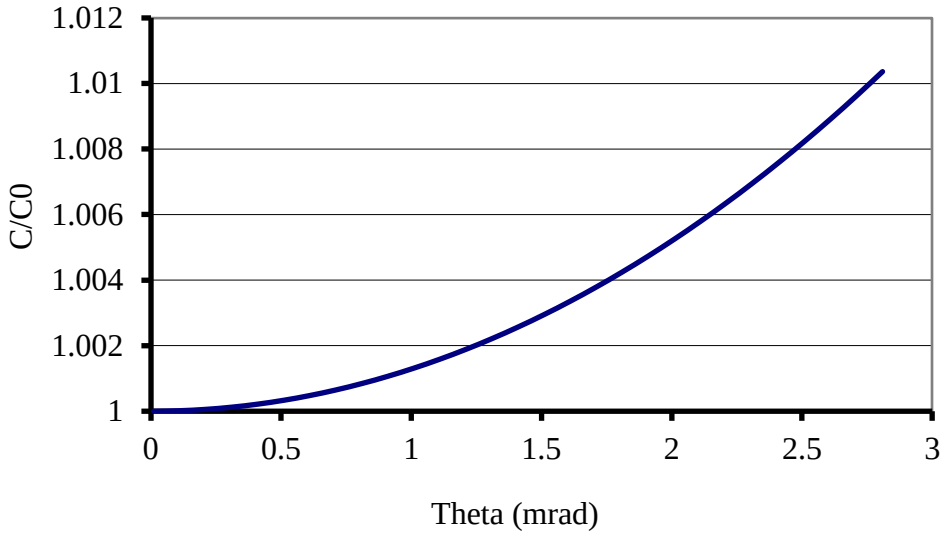


Figure 79. Effect of tilt on capacitance of circular electrodes.

## 4.2 CAPACITANCE GAUGE MANUFACTURE AND ASSEMBLY

The gap $d$ and the area $A$ will be not exact as it desires since of the diameter manufacturing error and the area manufacturing error of the flat surface. The design of the capacitance gage can be chosen as 16 µm range for actuation stage, and 10 µm for the load-cell stage. Figure 80 illustrates the steps of a precision surface manufacturing of the probe and target electrode include: lapping, grinding, and polishing. Testing data shows that the minimum gap for the probe and target can be adjusted to provide a capacitance of up to 300 pF after the lapping and polishing process.


Figure 80. Capacitance gage probe and target manufacturing: lapping, grinding, and polishing.

To optimize the system, measuring the surface topography of the capacitance probe and target electrodes sensor is necessary. Interferometer is used for the surface metrology of the probe and target electrode. After lapping and polishing, all measured root-mean-square (RMS) values are less than 1.4 um. The gap of the capacitance gages is around 25 μm, then the tolerance will be 1.4/25, which is around 6%. Figure 81 shows the prototype of capacitance gages and a surface RMS value. Figure 82 shows a surface profile of a probe measured using zygo white light interferometer (Nexview).

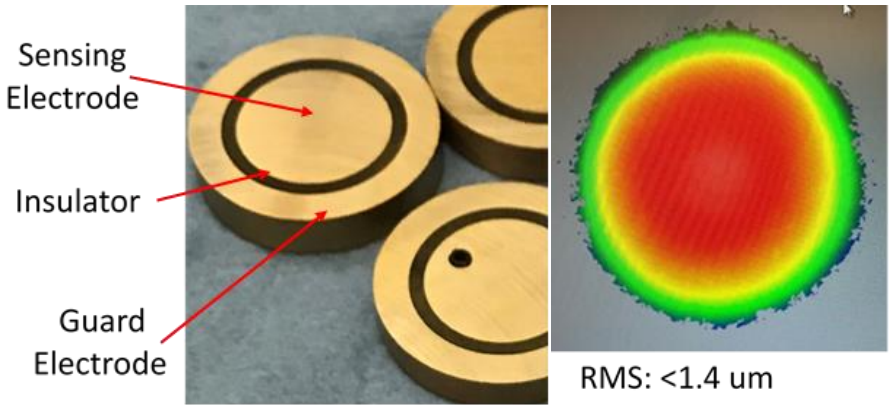


Figure 81. Prototype of cap gauges and the largest RMS values of the capacitance probe and the ground.

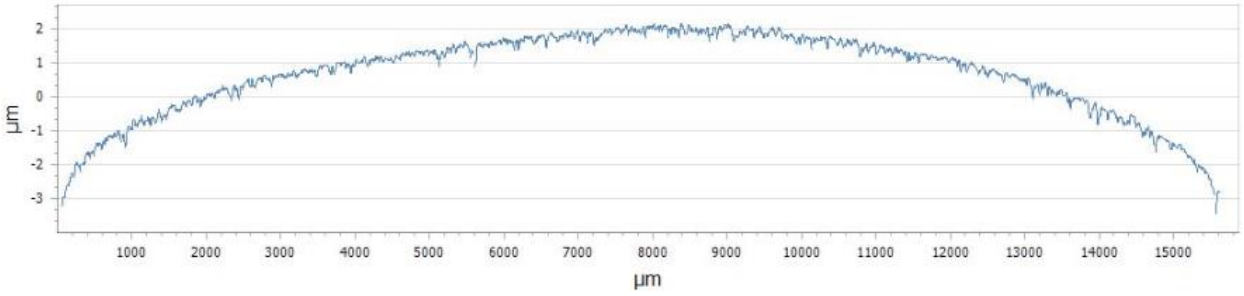


Figure 82. One surface profile of a 16 mm diameter probe across its major axis.

Surface asperities of the target or probe are generated from manufacturing defects. When the two surfaces of the capacitance gage come into contact, initially they only touch at a few of these asperity points. And this will cause dielectric loss for the capacitance gage. The term

dielectric loss refers to the energy that is lost to heating if a variable voltage is applied. A precision surface grinding, lapping, and polishing are necessary for getting ideal flat and polished surfaces. After precision surface generation, the dielectric loss number measured by HP 4284A precision LCR meter changed from 0.002 to 0.0002. Figure 83 shows how those self-made capacitive sensors are assembled inside the actuation stage and load-cell stage.

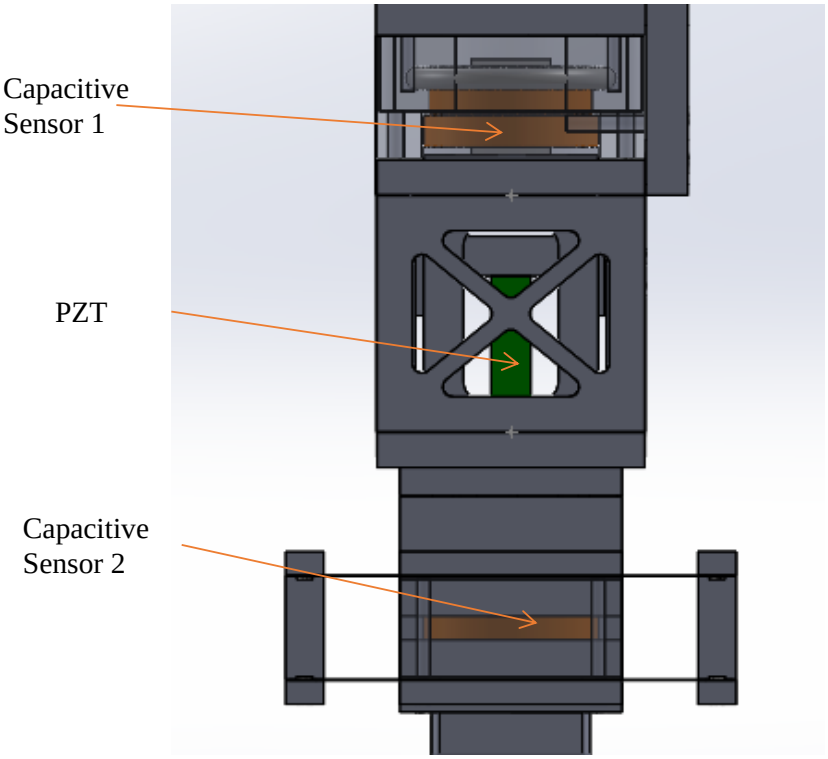


Figure 83. Capacitance gages are assembled inside the actuation stage and load-cell stage.

## 4.3 BLOCK DIAGRAM OF SIGNAL PROCESS

After the capacitance gages are assembled to the actuation stage and load-cell stage, the signal processing sequence for the capacitance gage is shown in the Figure 84. A 20 kHz sinusoidal signal generated from the lock-in amplifier was sent to the balance line driver (DRV135), then two 180 phase shift signals are sending to a fixed capacitor and the self-made varying capacitor. A superposition of previous capacitance sensor is sending through a buffer (AD630) and sending

back to the lock-in amplifier. The lock-in amplifier will use this signal and the internal referenced sine wave to measure the changing amplitude of this signal. A 16-bit ADC will record this changing amplitude signal and transfer this voltage signal to displacement or force values. And this displacement and force values will be post-processed using the data processing stage explained in section 5.

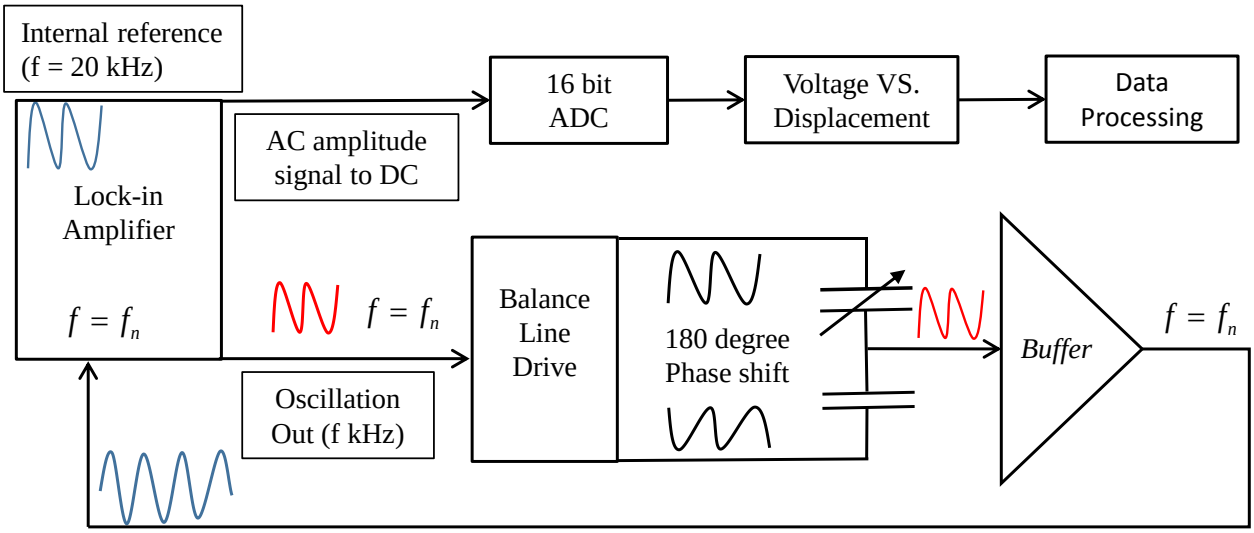


Figure 84. Block diagram of signal process for nano-indentation.

# CHAPTER 5: SYSTEM CHARACTERIZATION

This chapter presents performance testing of the system. Performance characteristics to be measured include: the noise analysis (noise source), indentation algorithm, load-cell stage stiffness calibration, stability test and uncertainty budgets of the system. The system characterization will experimentally quantify the performance of the sub-system components of the indentation facility. To determine the limiting resolution of the sensor sub-systems, the noise sources and noise levels are identified and measured, as shown in section 5.1. For minimizing the eccentric error between the diamond tip and the rotary air-bearing, a floating platform is demonstrated in section 5.2. The block diagram to explain the indentation control algorithm is shown in section 5.3. Load-cell stiffness is calibrated in section 5.4. The displacement calibrations of the actuation stage and load-cell stage are demonstrated in section 5.5. The stability of the system is described (in section 5.6) so that the performance of this instrument can be plotted out in short measurement time and long drift test. The force loop stiffness of the nano-indentation instrument is measured and calculated in section 5.7. The uncertainty budgets can be estimated based on the system characterization, and this is presented in section 5.8 as well.

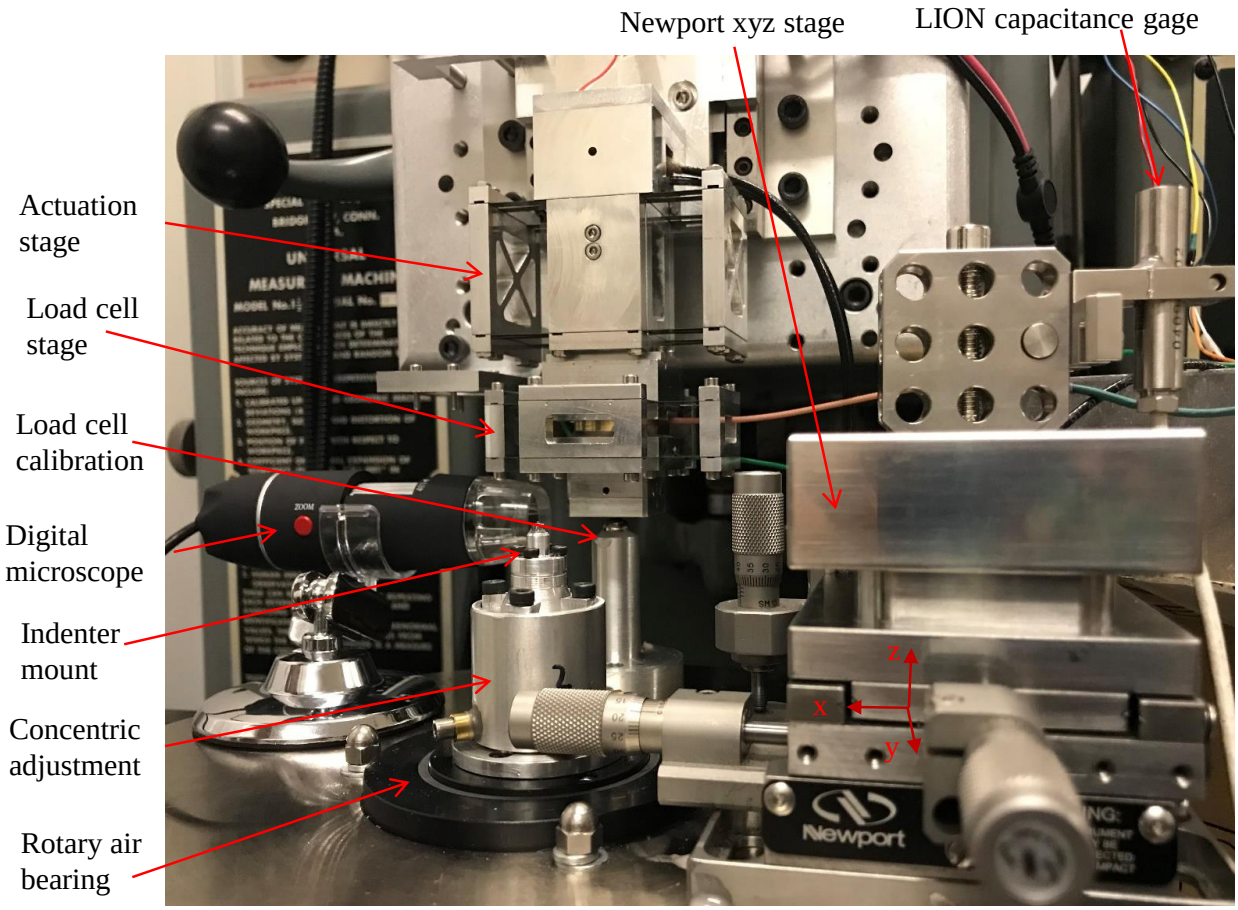


Figure 85. Nanoindentation instrument build and assembled.

Figure 85 and Figure 86 show the main optical, electrical, and mechanical components used for this system. Optical components include digital microscope and MicroE optical encoder. Electrical components include audio-balanced line driver circuits, 16-bit ADCs and DACs, High voltage amplifier, Lock-in amplifiers, myRIO, Lion capacitance gage, and oscilloscope. Mechanical components include MOORE machine, linear micrometer, actuation stage, load-cell stage, capacitance gage, dovetail sample mounting structure, Berkovich diamond indenter, indenter mounting structure, concentric adjustment apparatus, rotary air-bearing (Professional instrument company) and its supporting structure, rotary encoder mounting structure, Newport xyz stage and air-bearing gas-line dryer filter regulator (D4-A).

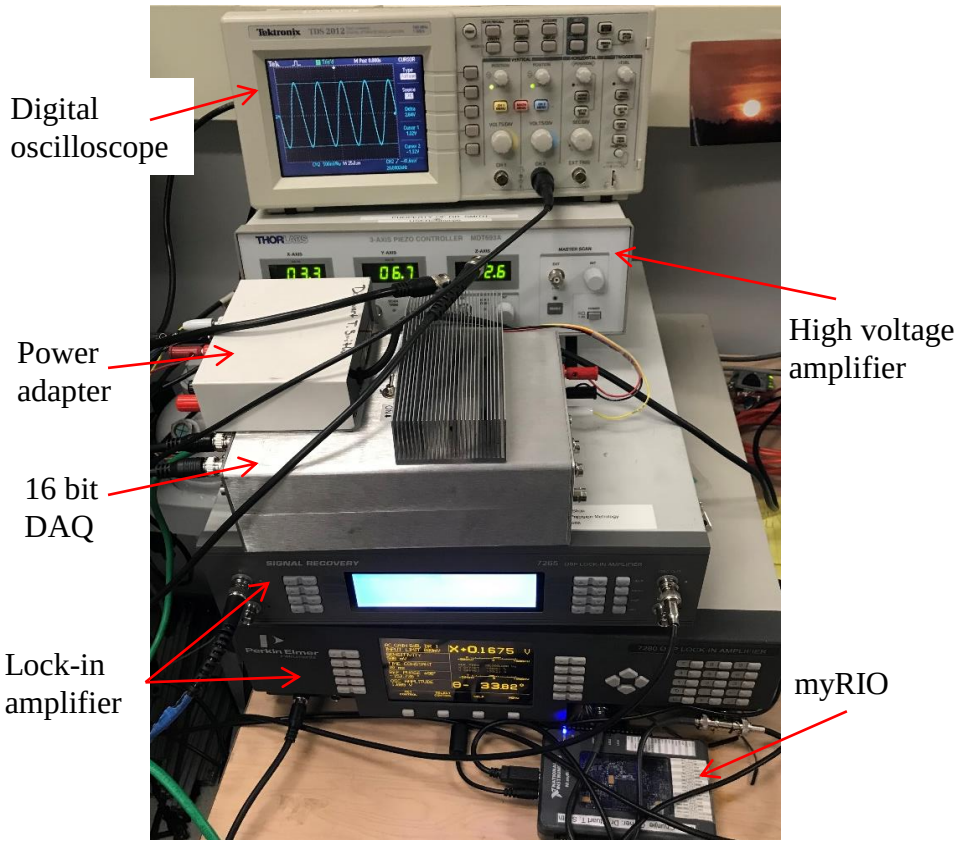


Figure 86. Instruments used for the signal process.

## 5.1 NOISE PERFORMANCE

The positioning accuracy of the load-cell stage is generally limited by the capacitance sensor, quantization noise, mechanical (ground borne acoustic) noise, vibration, thermal drift, hysteresis, straightness and rotation error from parasitic motions, Abbe error, and Cosine error. Analysis of the noise sources was proved by using the equations in section 5.1.1. An experimental signal collecting test in section 5.1.2 shows the changing of displacement with respect to the time. To determine the resolution and the bandwidth of the system, the noise spectrum with a frequency responded signal were measured. Power spectrum and sum of spectrum (integral of the spectrum) were plotted out in section 5.1.3 as well.

### 5.1.1 NOISE SOURCES

This section is a function of the oscillators chosen and will manifest as combinations of amplitude and phase components. Typically, it is the amplitude that is most difficult to control. However, this situation is changing with digital oscillators. This will be considered an inextricable noise present in the carrier signal and having both $1/f$ and white components.

For noise analysis, the amplifier is to operate with the input being a single harmonic carrier frequency the amplitude of which is dependent upon the imbalance of a capacitance bridge. Stray capacitance effects will not be included in this analysis. The output noise per root frequency, $e_s$, from the amplifier of voltage gain $G_V$ with zero impedance from the source is given by

$$e_s = e_n G_V \tag{5.1}$$

where $e_n$ is the input noise typically of the order 1 nV $Hz^{-1/2}$ for a precision instrumentation amplifier at frequencies above 1 kHz. Because we will be using carrier frequencies of 1 kHz or greater the $i/f$ noise component is considered negligible.

Adding a source impedance $Z_s$ the amplifier output noise is given by

$$e_s^2 = \left[ e_n^2 + 4kTZ_s + (i_n Z_s)^2 + e_o^2 \right] BG_V^2 \tag{5.2}$$

Where $i_n$ is the input noise (often less than 1 pA $Hz^{-1/2}$ at frequencies higher than 1 kHz), $B$ is the bandwidth, $k$ is Boltzmann's constant (1.3806503 x $10^{-23}$ $J \cdot k^{-1}$), $T$ is the absolute temperature and $e_o$ is the oscillator noise per root Hertz (assumed to be zero for the present

purposes). The above values have been incorporated into the spread sheet used to derive Figure 87.

For a source of the form of a transformer ratio source on one arm and matched capacitances making up the other. This looks like a half bridge input to one terminal and a zero-source impedance on the other. Calculated as the Thevenin equivalent circuit, the source impedance is

$$Z_s = \frac{Z_1 Z_2}{Z_1 + Z_2} = \frac{1/\omega_c^2 C_o C}{1/j\omega_c C + 1/j\omega_c C_o} \approx \frac{1}{2C_o\omega_c} \tag{5.3a}$$

Typically, a range incorporating capacitance in the ratio 1:2:3 was used for capacitance gage design. This gives rise to the important relationship that the range of the capacitance gage is 4/3 times the nominal value defined at the center value of capacitance.

In general, the capacitance ratio from a nominal value can be expressed by

$$k_1 C_o : C_o : k_2 C_o \tag{5.3b}$$

The range is given by the difference between the maximum and minimum displacement given by

$$\frac{x_o}{k_1} - \frac{x_o}{k_2} = x_o\left(\frac{1}{k_1} - \frac{1}{k_2}\right) \tag{5.3c}$$

It can be readily verified that the 1:2:3 ($k$ values of 1/2 and 3/2 respectively) rule provides a capacitance range of 4/3 of the nominal electrode separation.

Consequently, at the maximum electrode separation the capacitance will be reduced to a value of 1/2 of the reference. This will increase the source resistance by 17% (1/6). Substituting (5.3) into (5.2) for the maximum source resistance yields

$$e_s^2 = \left[ e_n^2 + 4kT / 3C_o\omega_c + (2i_n / 3C_o\omega_c)^2 + e_o^2 \right] BG_V^2 \tag{5.4}$$

In practice this appears to be dominated by the amplifier current noise followed by thermal noise.

The output voltage from the transformer ratio bridge for small changes in capacitance is given by

$$V_{out} = \left( \frac{V_{bs} G_V}{4x_o} \right) x = S_d x \tag{5.5}$$

Additionally, the nominal separation is related to the nominal capacitance by

$$x_o = \frac{\varepsilon A}{C_o} \tag{5.6}$$

Where $x$ is the displacement of the capacitance electrode and $V_{bs}$ is the bridge supply voltage and $S_d$ is the sensitivity of the bridge circuit in units of volts per meter. This can be expressed in alternative forms

$$S_d = \left( \frac{V_{bs} G_V}{4x_o} \right) = \left( \frac{V_{bs} G_V C_o}{4\varepsilon A} \right) \tag{5.7}$$

From equations (5.4), (5.5) and (5.6), the displacement noise is given by

$$\frac{e_x^2}{B} = \left[e_n^2 + 4kT/3C_o\omega_c + (2i_n/3C_o\omega_c)^2 + e_o^2\right] G_V^2 \left(\frac{1}{S_d}\right)^2$$

$$= \left[e_n^2 + 4kT/3C_o\omega_c + (2i_n/3C_o\omega_c)^2 + e_o^2\right] \left(\frac{4\varepsilon A}{V_{bs}C_o}\right)^2 \qquad [\mathrm{m^2\ Hz^{-1}}] \tag{5.8}$$

$$= \frac{16x_o^2}{V_{bs}^2}\left[e_n^2 + 4kT/3C_o\omega_c + (2i_n/3C_o\omega_c)^2 + e_o^2\right]$$

In general, the carrier frequency is given by the synchronous demodulator design. Using the niner lock-in amplifiers this is around 20 kHz. Taking the square root of equation (5.8) gives the displacement noise of the circuit

$$\frac{e_x}{\sqrt{B}} = \frac{4x_o}{V_{bs}}\sqrt{e_n^2 + 4kT/3C_o\omega_c + (2i_n/3C_o\omega_c)^2 + e_o^2} \tag{5.9}$$

In the design of a capacitance gage, there are three considerations: range, electrode dimension and noise floor. Basically, it is required that the noise floor of the capacitance gage is less than a design goal. Typically, this would be the desired resolution of the measurement system at an acceptable bandwidth. In practice, this could always be achieved with a sufficiently large electrode area. However, this is impractical for reason of electrode alignment requirements (acceptable parallelism) and volume occupied. A comparison of these trade-offs can be seen from the design charts of Figure 87.

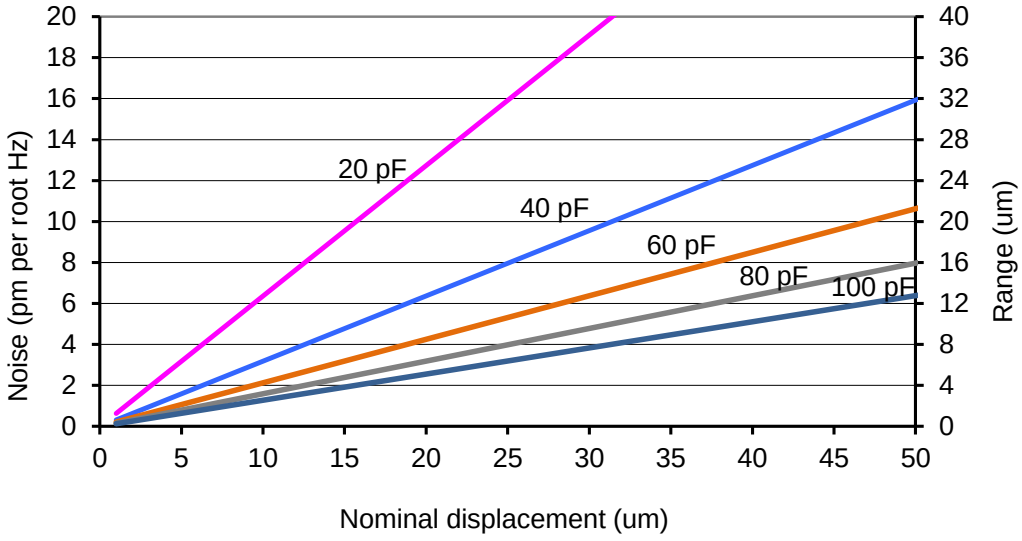


Figure 87. Capacitance gage noise as a function of nominal separation between electrodes, with nominal values of 20, 40, 60, 80 & 100 pF.

### 5.1.2 EXPERIMENTAL SIGNAL COLLECTING

Figure 88 shows an unfiltered drift measurement plot of the load-cell stage using capacitance gage. This experimental raw data was recoded for 2.5 seconds with a variance of 3.2 nm. The filtered plot will be presented and is discussed in section 5.5.

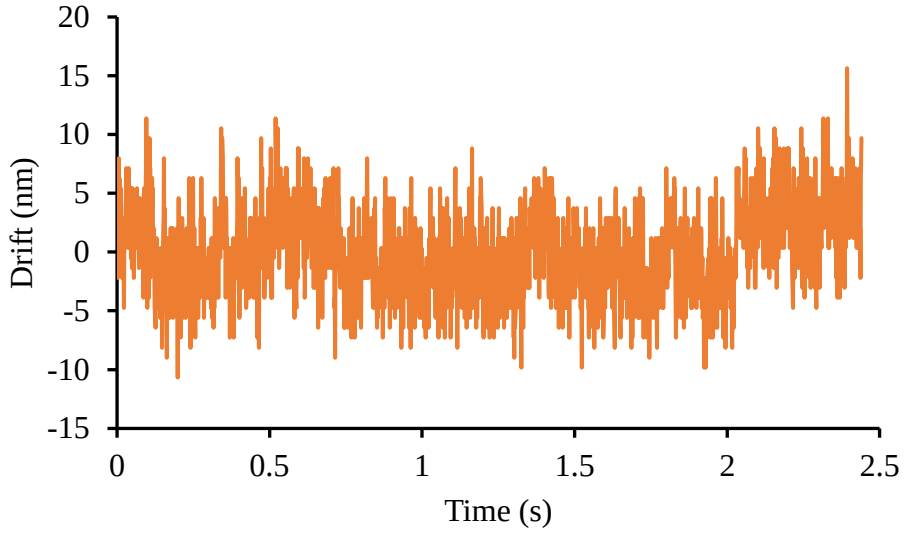


Figure 88. An experimental drift measurement without filtering for 2.5 seconds.

### 5.1.3 SPECTRUM ANALYZING FOR THE EXPERIMENTAL TESTS

Experimental tests to determine the noise of the system and the bandwidth of the system were recorded using Hewlett-Packard 35665A dynamic signal analyzer (HP 35665A DSA). The noise power spectrums for the actuator stage capacitance gage, load-cell stage capacitance gage, and LION reference capacitance gage were measured in Figure 89. The integrated power spectrums were computed and plotted in Figure 90.

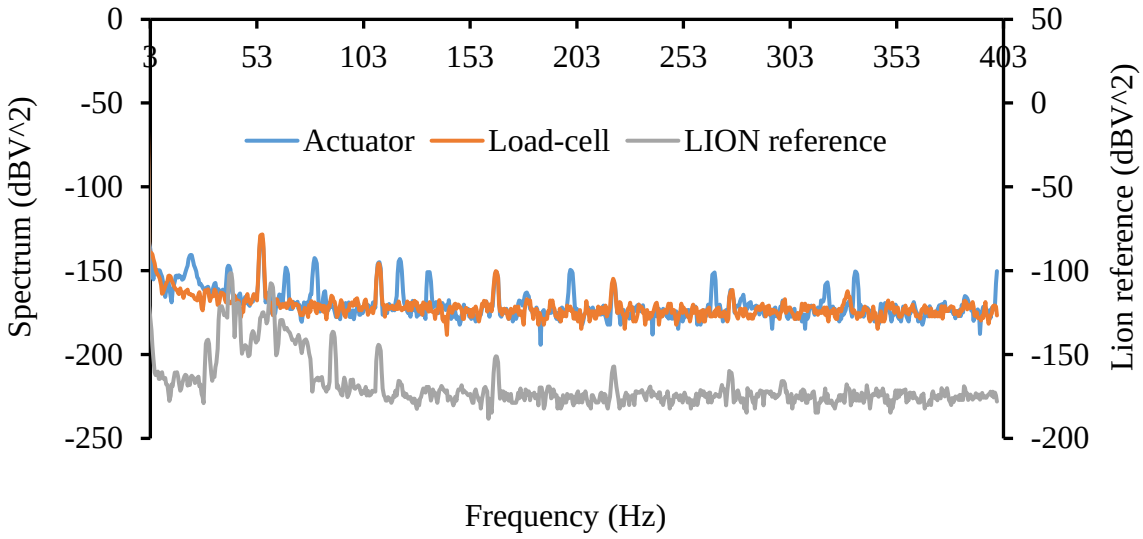


Figure 89. Power spectrum of noise plot for actuator capacitance gage, load-cell capacitance gage, and LION reference capacitance gage.

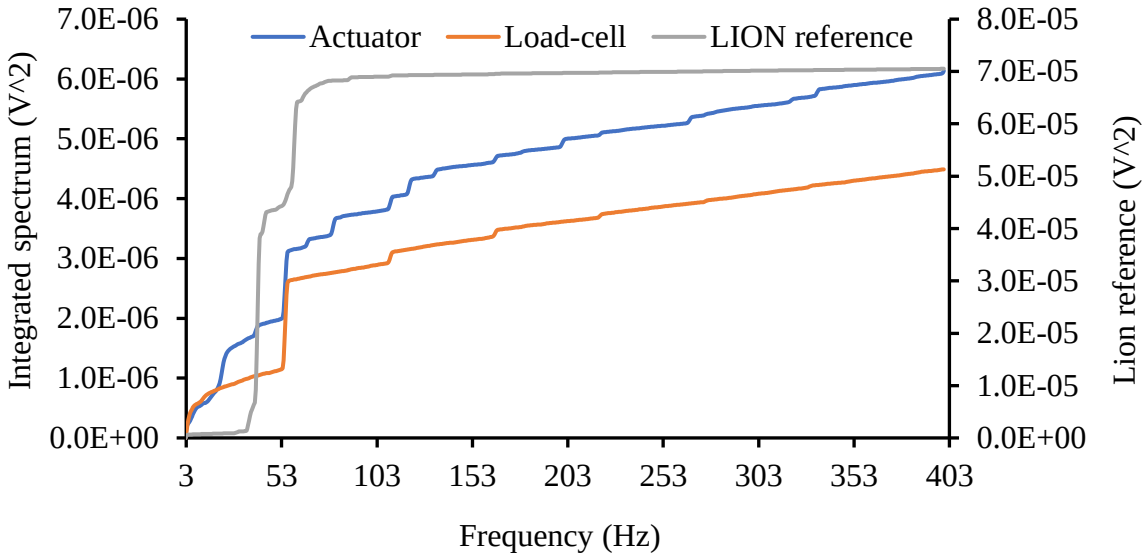


Figure 90. Integrated power spectrum of noise plot for actuator capacitance gage, load-cell capacitance gage, and LION reference capacitance gage.

## 5.2 FLOATING PLATFORM FOR MINIMIZING ECCENTRIC ERROR

A high precision floating apparatus (includes linear and tilt adjustment stages, fibers hanging ropes, "floating" plate, capacitance gages) and indenter mounting on the rotary stage were designed to measure eccentric error for the nano-indenter. The linear stage was used to adjust in the z direction and the tilt stage (Rx & Ry) was used to adjust the rotations along the x and y axis. By adjusting on this linear and tilt stages, the floating plate will move, and the contact between the bottom of the floating plate and the indenter will be adjusted as well. Two capacitance gage probes were used to record the movement of the plate in the x and y direction. Figure 91 shows the design of the high precision floating apparatus and the indenter mounting on the rotary stage (Rz).

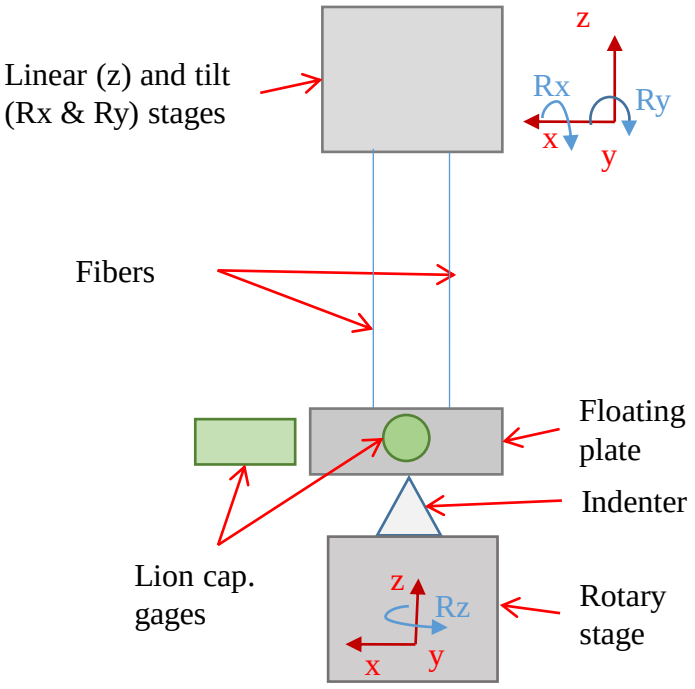


Figure 91. The "floating" apparatus and the indenter mounting on the rotary stage to align the indenter tip with the rotary stage.

Figure 92 shows the prototype of a high precision floating apparatus to measure eccentric error for the nano-indenter. The floating platform includes a vertical micrometer driven linear stage, kinematic tilt adjustment stage, optical fibers hanging structure supporting four corners of a square aluminum plate on which is mounted a level indicator. The linear stage will be used to adjust the gap between the indenter and the floating aluminum plate. A level indicator is used to observe the parallelism of the plate to the gravity. The tilt adjustment stage is used to minimize the tilt angle of the bottom aluminum "floating" plate. By contacting the indenter with the aluminum plate and manually rotating the air-bearing, misalignments between the bearing axis an indenter tip will produce frictional forces causing the plate to move. Two Lion$^{TM}$ capacitance probes was used to measure the displacements of this plate and capacitance gages were mounted on the kinematic movement stage in Figure 92.

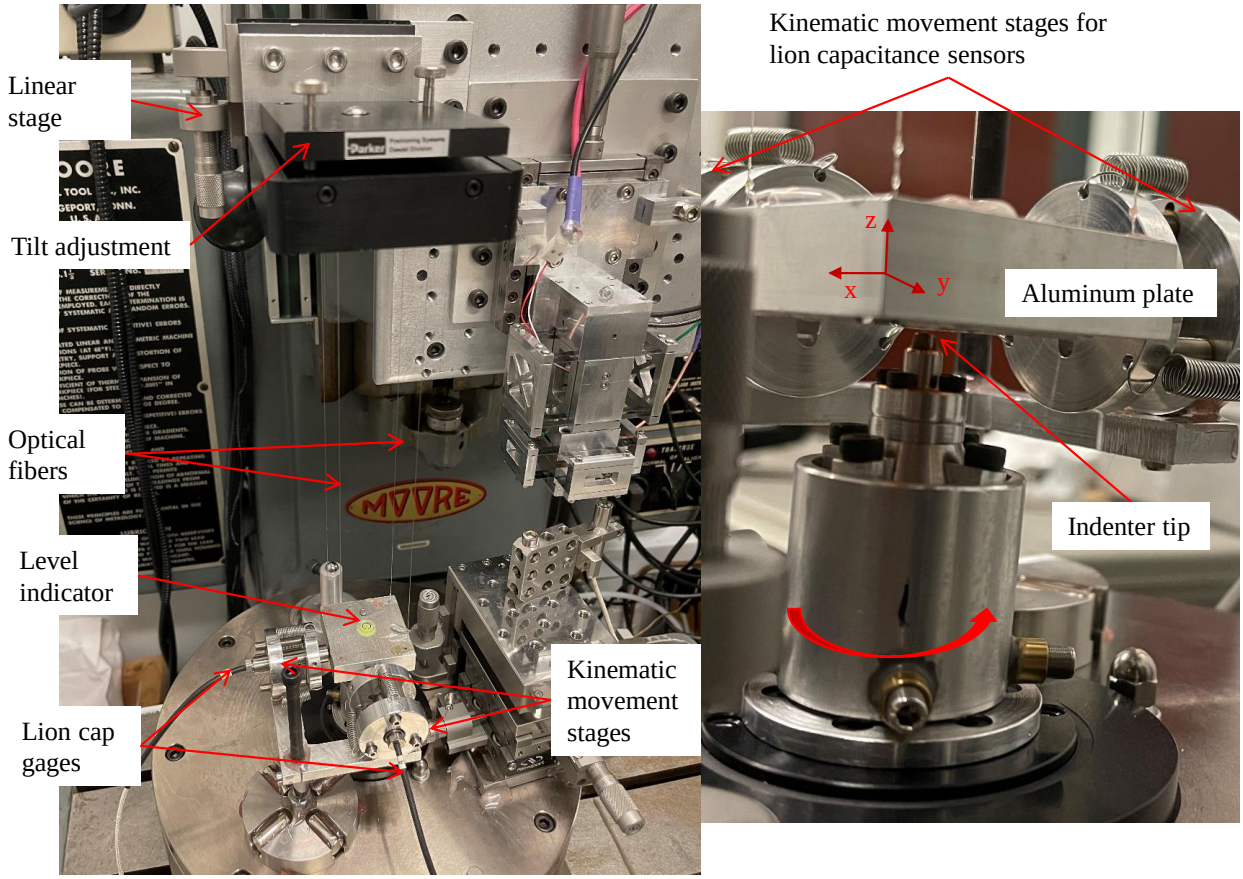


Figure 92. A high precision floating apparatus to measure eccentric error for the nano-indenter.

Four similar length fibers were used between two plates so that each fiber will share the similar load from the bottom plate during calibration. Figure *93* shows how the optical fibers were glued between the two aluminum plates for the floating structure. Three standard 1-2-3 blocks were placed between those aluminum plates so that the length between the two surfaces were nominally the same as well as being parallel. Two stationery clips were used to clamp two ends of each optical fiber so that they give tensional preloads for each fiber. Epoxy is used to hold a tensile force and fix the location end of each end of each fiber relative to the Aluminum plates.

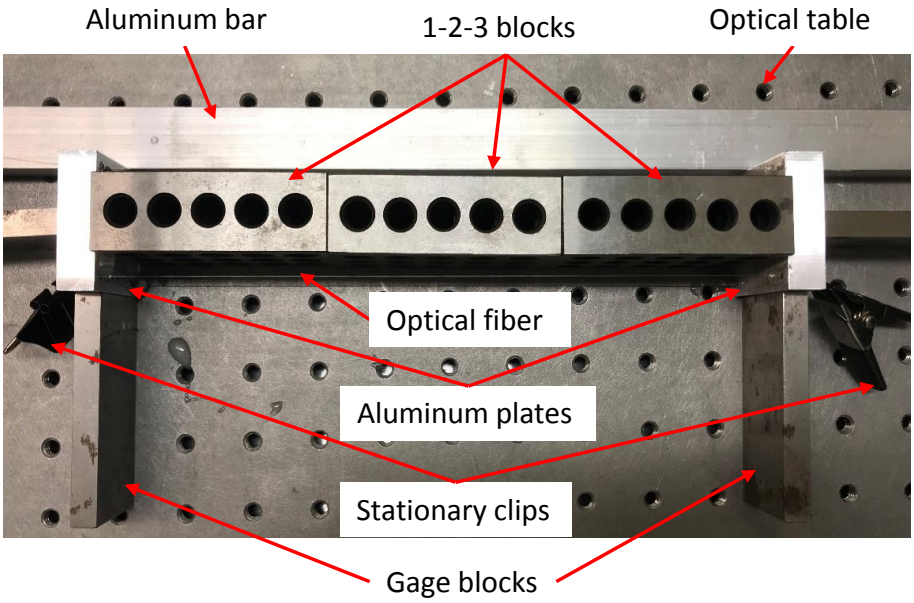


Figure 93. Optical fibers were glued together with two aluminum plates for the floating structure.

Kinematic assembly is recognized as one of the best designs because of exact six-degree freedom constraint, and from Maxwell criteria, this design has the highest repeatability capability [42]. The primary objective of kinematic assembly was to develop a simple, accurate, and low-cost mechanism. Those six points of contact exactly constraint system was able to crosscheck the performance of the nano-indentation instrument by comparing the drift values of them. More details of the kinematic movement stage used for the tilt and distance adjustment are shown in Figure 94. A cylinder bar plate was made by using a round pad with six bars that were used to build V bocks for the kinematic design. After using epoxy glued those six bars on the pad, three spheres with load blocks were used to fix the position of the bars in case of dislocation in case of the shrinkage of the epoxy. Tension springs and fine screws were used as well so that the lion displacement sensor can be adjust for at least three degrees of freedom.

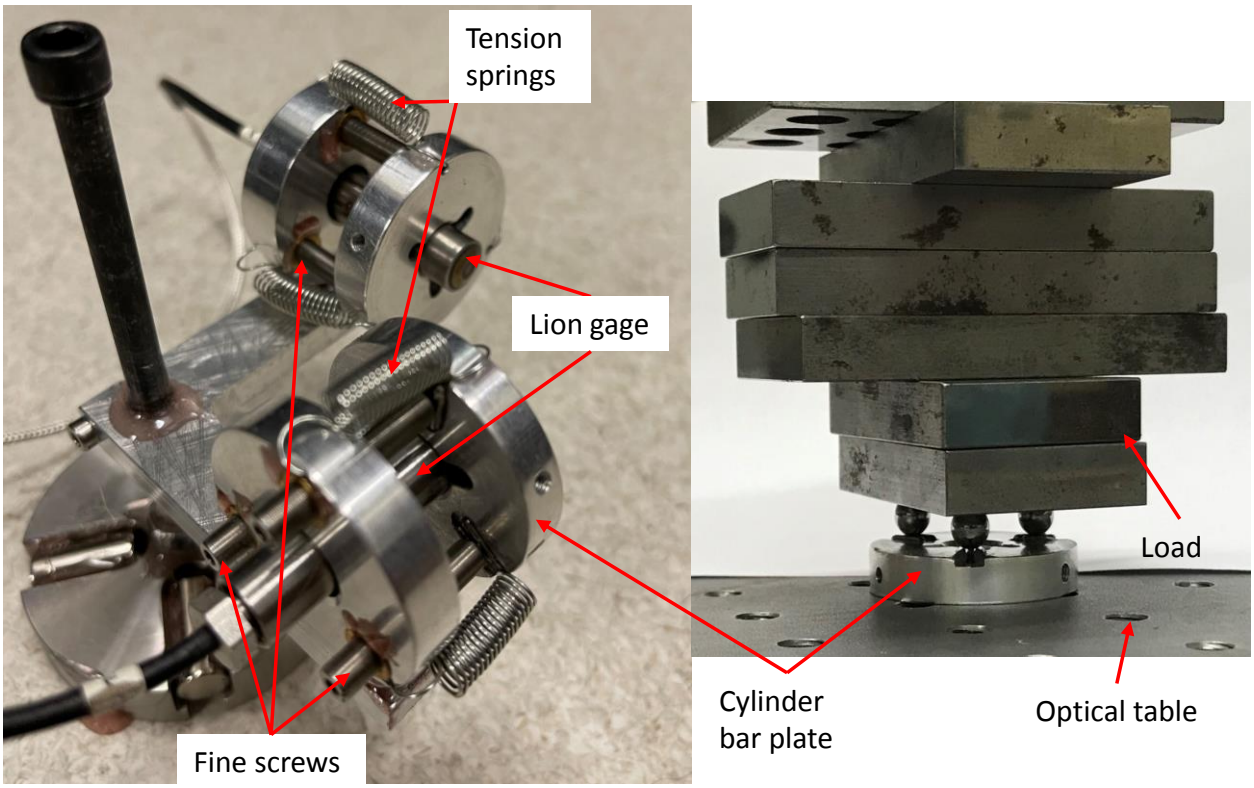


Figure 94. Kinematic stages used for the tilt and distance adjustment to align the two capacitance gages.

The Lion™ capacitance gage was able to measure the changing displacement of the floating plate. However, there are several challenges during coaxial alignment (minimizing eccentric error between the indenter tip and the rotary air-bearing). When manually rotating the air bearing, the rotation can only run for several seconds. The continuity made this too difficult for coaxial alignment between indenter and rotational axis of the bearing.

## 5.3 INDENTATION ALGORITHM

An open loop triangle ramp signal is applied to the actuator stage to move the specimen surface towards and away from the indenter. The block diagram shown in Figure 95 indicates all of the components involved in the control and measurements during an indent cycle.

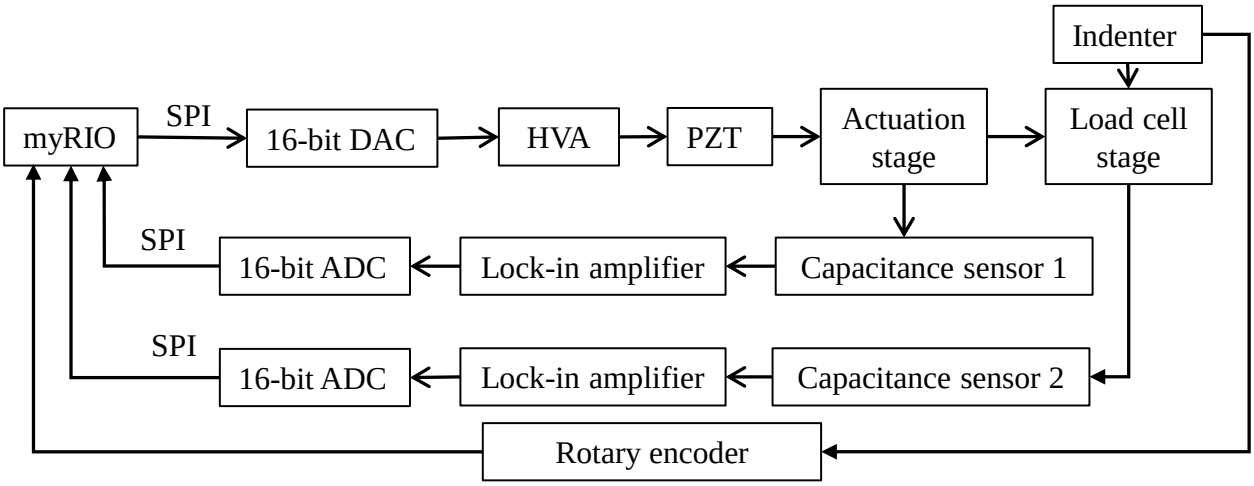


Figure 95. Bock diagram for the PZT driven actuator stage.

The LabVIEW GUI (APPENDIX F) and myRIO controller are used to determine the amplitude and velocity of the ramp signal that is transferred to an external 16-bit DAC. Information and controls of both ADC and DAC are communicated using four SPI buses. The control voltage of this 16-bit DAC for the PZT driver is from 0 to 10 V range. This control voltage is sending to the high voltage amplifier driver with a gain of 15, and then this amplified voltage will be transmitted to the PZT that will change its length. This change length of PZT will drives the actuation stage forward or backward. Since the load-cell stage is stacking together with the actuation stage, it is moving with the actuation stage moving platform. When the load-cell stage moves to the indenter, the indenter will provide a reaction force back to the load-cell stage, that in turn induces a displacement of the load-cell stage. Two capacitance sensors will record the displacement of both the actuation stage and the load-cell stage and the resulting changes in signals from each sensor will be analyzed using Lock-in amplifiers (Perkin Elmer instruments 7265 DSP and 7280 DSP LOCK-IN AMPLIFIER). Simultaneously with these measurements, the rotary encoder will be recorded to measure the any rotational movement from the indenter. The 16-bit ADCs will record the analyzed capacitance gage signals transfer these values to be converted into

displacements of the actuator and load-cell. Figure 96 shows a 0.5 V offset with 5 V maximum triangle voltages signal for which by changing the maximum voltage different penetration depths can be obtained.

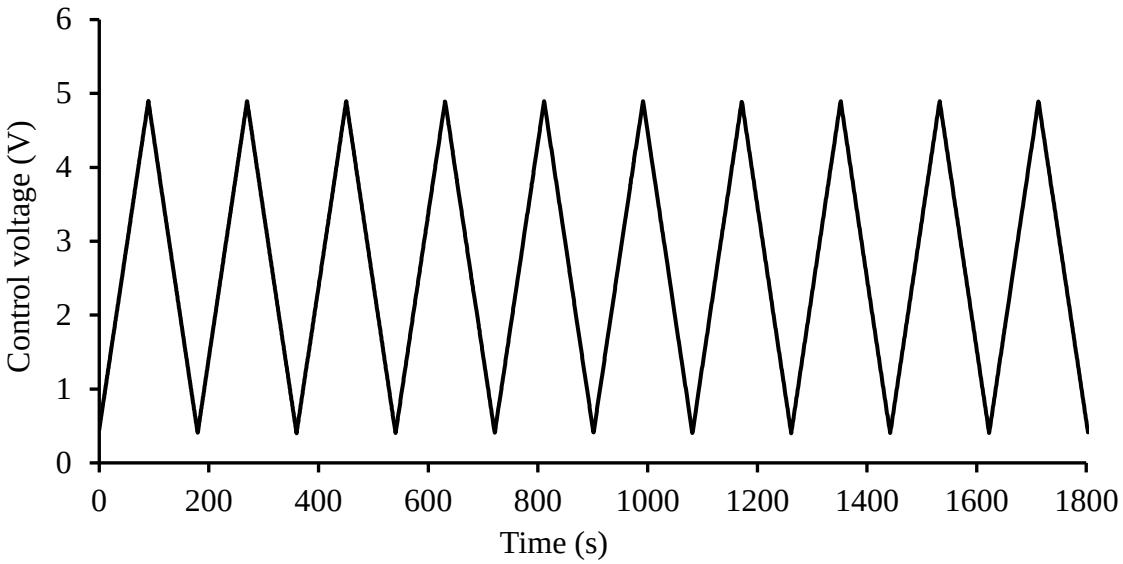


Figure 96. Controlled triangle ramp voltage output increases for the PZT driven actuator stage.

## 5.4 LOAD-CELL STAGE STIFFNESS CALIBRATION

The force to penetrate the sample surface is calculated from the load-cell displacement, Xlc (negative displacement), and the stiffness of the load-cell structure. The penetration depth is calculated from the equation Xact+Xlc, where Xact is the displacement of the actuation stage. The stiffness calibration is achieved using precision calibrated spheres as reference weights and hanging these from the actuation and load-cell. The suspension thread is sliding at the middle of the dovetail slot of the load-cell stage and the hanging rope is used to connect the load sphere basket with the suspension thread. The set-up for calibration is shown in Figure 97.

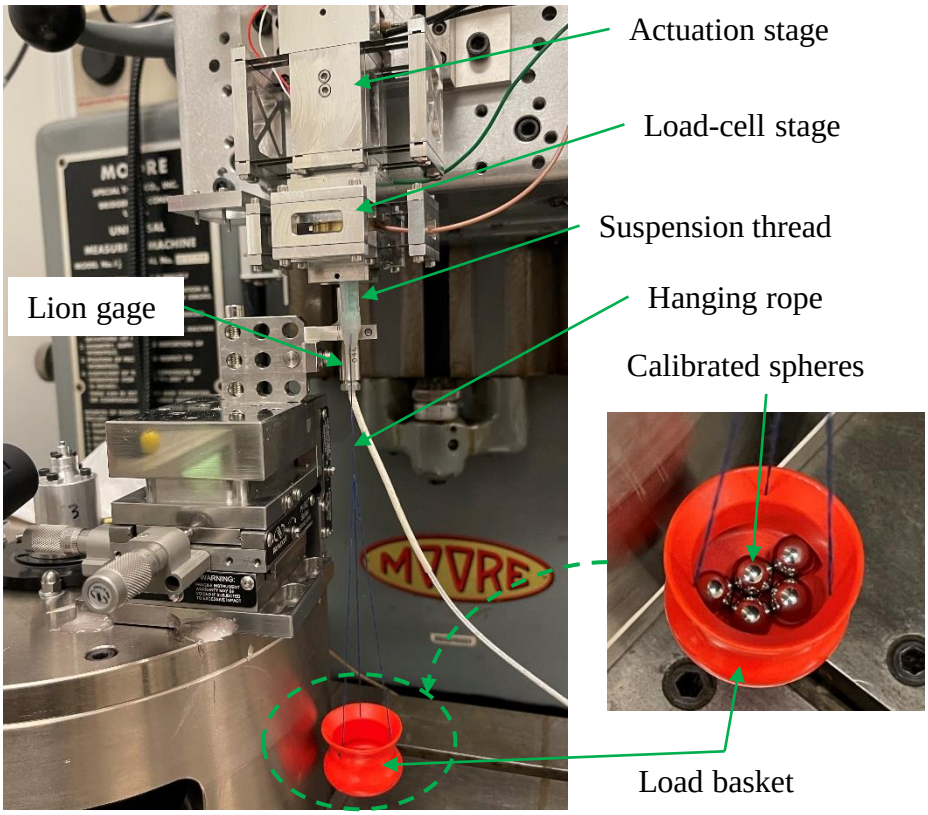


Figure 97. The calibration measurement for load-cell stiffness.

The mass of the sphere is measured using a precision weight stage. The calibration process includes the recording of the displacements for the actuation stage and load-cell stage as each weight is added on the load-cell stage. The displacement of the actuation stage is negligible, and the displacement of the load-cell stage is measured using the lion gage. Ten spheres (with known weight) were added to the basket one by one, and the displacement of the load-cell stage for each added load were recorded simultaneously. The load-cell stiffness calibrations of a thin flexure and a thick flexure were achieved separately. Figure 98 and Figure 99 show the plots of the load with respect to the displacement. The stiffness of the thin flexure was calculated as 29.573 $kN \cdot m^{-1}$, and the stiffness of the thick flexure was calculated as 99.393 $kN \cdot m^{-1}$.

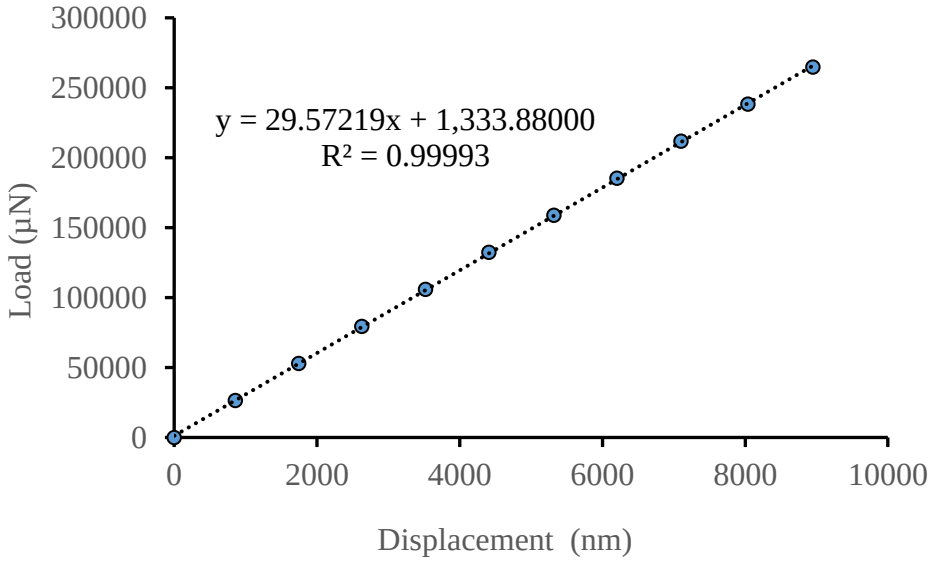


Figure 98. The stiffness of the thin flexure was calculated as 29.573 kN·m$^{-1}$.

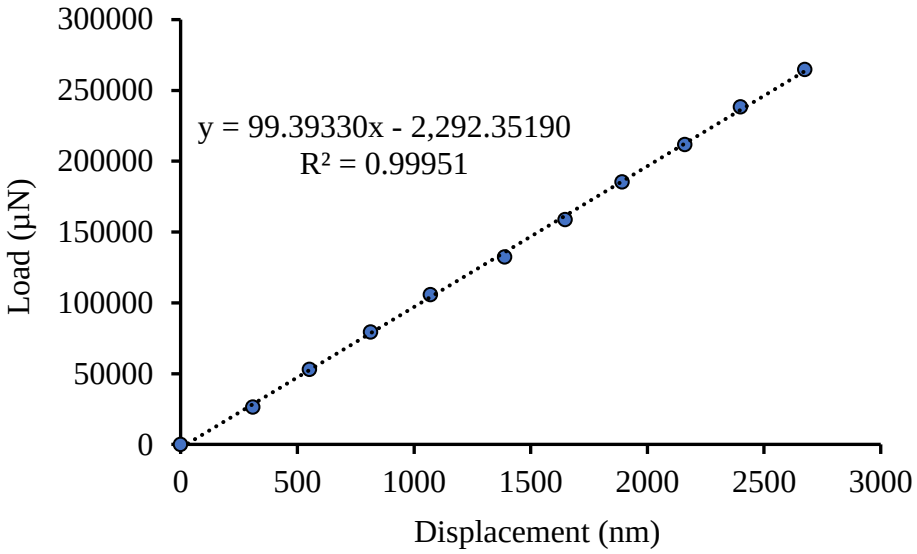


Figure 99. The stiffness of the thick flexure was calculated as 99.393 kN·m$^{-1}$.

## 5.5 DISPLACEMENT CALIBRATION OF ACTUATOR AND LOAD-CELL STAGES

Experimental investigations of piezoelectric material hysteresis are carried out by applying a periodic, constant-amplitude signal to the actuator and measuring the subsequent displacement response. For this research, a 16 bits 0 to 10 V triangle signal is amplified to 0 to 150 V using THORLAB high-voltage piezo amplifier (MDT693A). The hysteresis curves (non-repeatable

forward and backward movement) of this piezoelectric material were recorded in terms of the actuator voltage and Lion™ displacement gage.

### 5.5.1 ACTUATION STAGE CALIBRATION

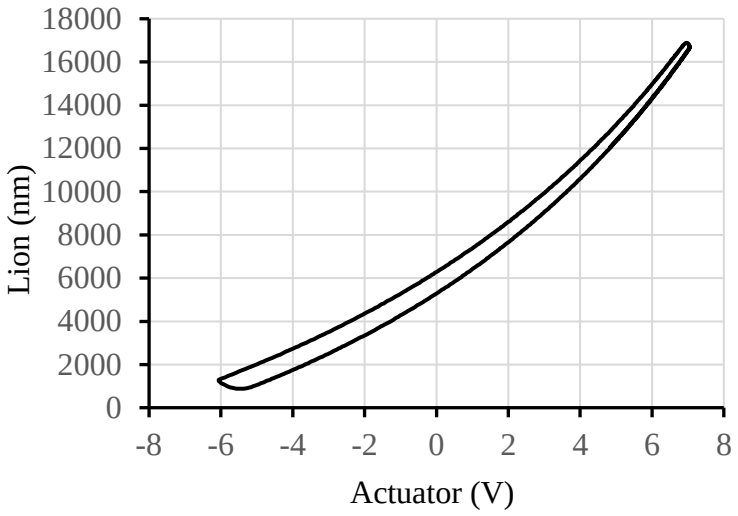


Figure 100. Forward backward irreversible calibration.

Figure 100 shows the forward and backward movement are not merged since hysteresis of the thermal drift and creep behavior inside the PZT actuator. This will cause non-repeatable measurement data for nano-indentation test. After the systems was “warmed up” for 4-6 hours, the forward and backward cycle curve attains equilibrium as is shown in the Figure 101.

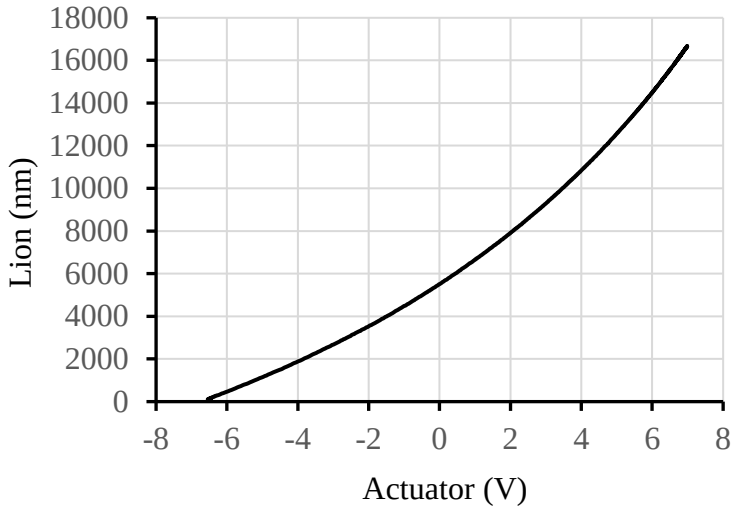


Figure 101. Forward backward reversible calibration.

Figure 102 is a time-based plot of the LION capacitance gage displacement and the measured actuation stage displacement (top), and the residuals between the lion gage and the actuation stage displacement is within 70 nm for 600 seconds (bottom) over a ~16 µm cyclic displacement.

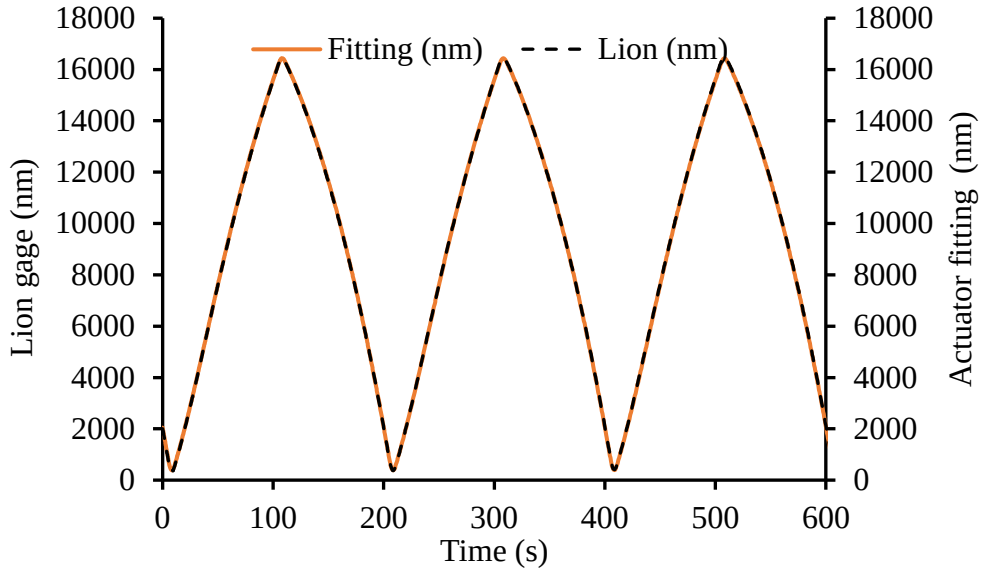

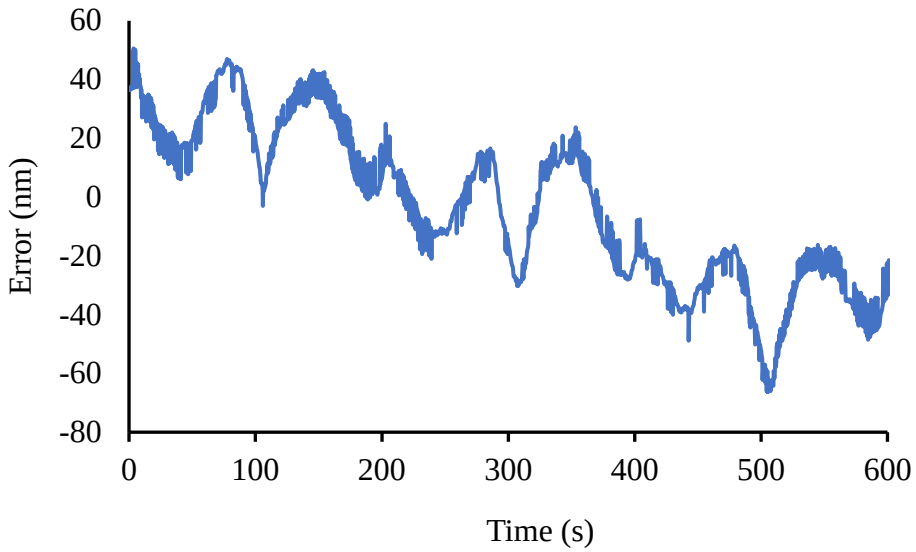


Figure 102. Top plot shows the lion gage displacement vs the actuation stage displacement. Bottom plot shows the residuals between the lion gage and the actuation stage displacement after curves fitting.

### 5.5.2 LOAD-CELL STAGE CALIBRATION

After the actuation stage is calibrated, the load-cell will be calibrated by using the actuator stage. When the actuation stage translated from around 300 nm to 15800 nm, the changing voltage of the load-cell stage was simultaneously recorded. Figure 103 shows a 62 cycles plot of the load-cell voltage and actuator displacement data. Since the contact area between the load-cell and the load-cell calibration structure will be growing and shrinking (surface come-in and come-out are in contacting), there will be a deformation in the load-cell stage calibration curves.

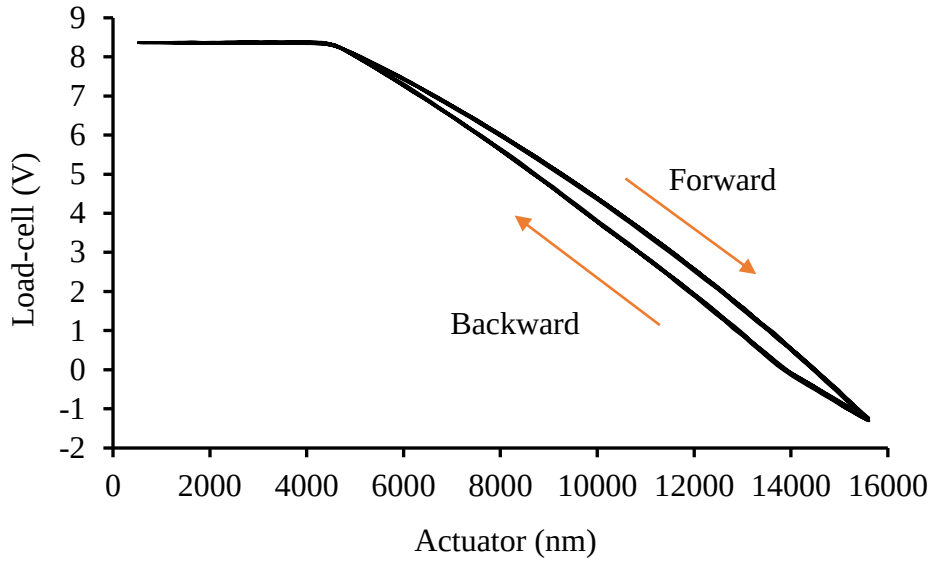


Figure 103. 62 cycles repeatable forward backward load-cell stage calibration plotted against actuator stage displacement.

For the maximum load of around 1.2 N counted here, Hertz contact theory estimates that the contact deformation is around 240 nm for a flat Nickel sample and a steel sphere (4.3 mm radius). The forward actuator displacement and load-cell voltage curve was used for the load-cell capacitance gage calibration. Figure 104 is one of the plots of actuator stage displacement with respect to load-cell voltage shown in blue, and exponential plus first order fitting curve shown is in orange. Figure 105 is one of the plots of actuator stage displacement with respect to load-cell voltage shown in blue, and third order polynomial fitting curve is shown in orange.

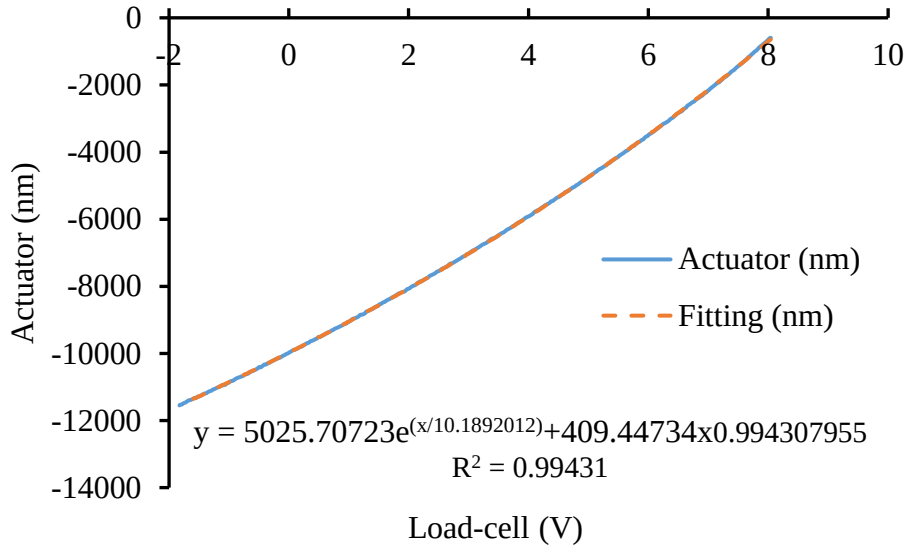


Figure 104. Plot of actuator stage displacement with respect to load-cell voltage shown in blue, exponential plus first order fitting curve shown in orange.

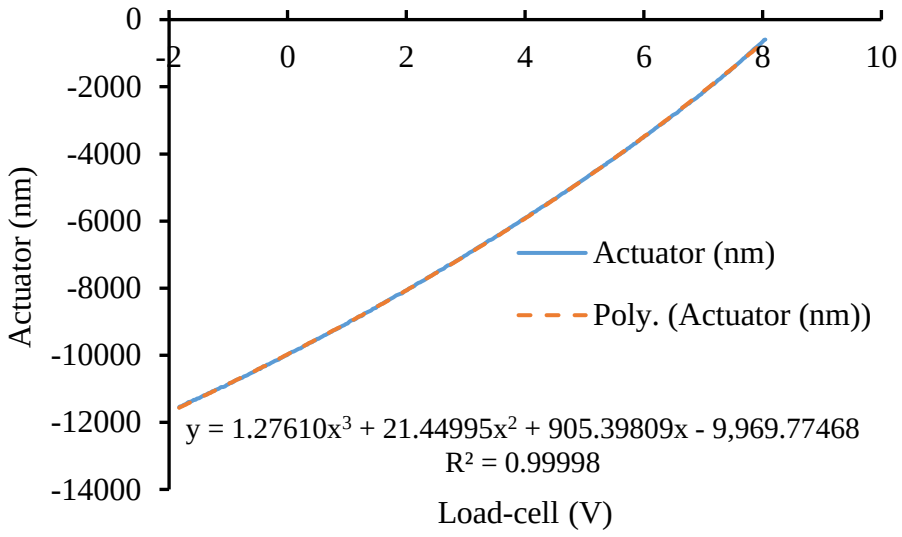


Figure 105. Plot of actuator stage displacement with respect to load-cell voltage shown in blue, third order polynomial fitting curve shown in orange.

Curve fitting is used to find the relationship between actuator displacement and load-cell voltage. With goal of defining a "best fit" model of the relationship, exponential and polynomial curves fitting are used for validation and goodness-of-fit tests. The residual plots between the

fitting curves and the experimental data are shown in Figure 106. From this residual plot, the larger the voltage of the load-cell stage, the larger the residual error.

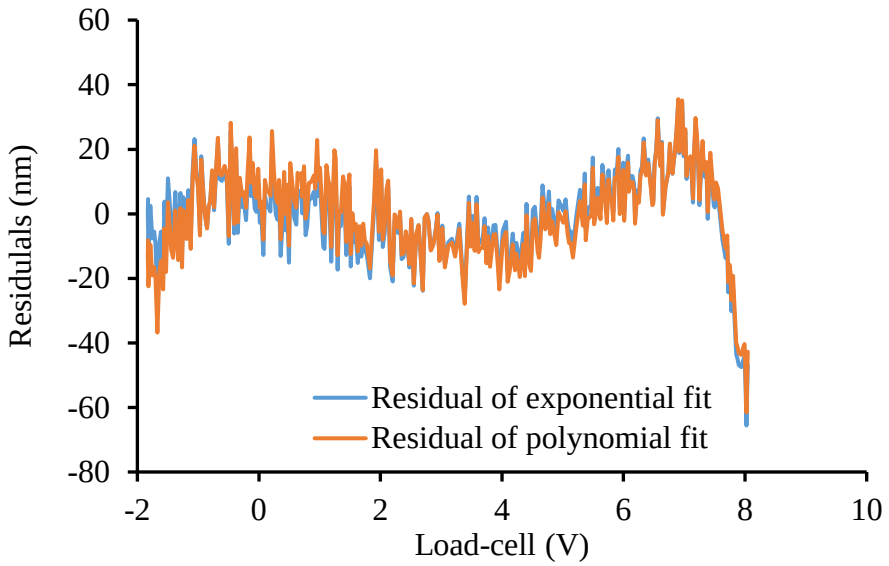


Figure 106. Residual plots between the fitting curves and the experimental data, blue line is the exponential fit, orange line is the third order polynomial fit.

## 5.6 STABILITY TESTING

The goal of the stability test is to check the performance of the equipment over the duration of a full nano-indentation measurement process. Figure 107 shows the metrology loop for the actuator stage using capacitance gage and the metrology loop for the MOORE machine frame using a Lion™ capacitance sensor. Since the materials, structures, and dimensions for each metrology loop are different, the time constant will be different between the actuator metrology loop and the frame metrology loop. The target value of stability test is to maintain measurement drift to within 10 nm over 10 minutes. Figure 108 plots measured displacement of the actuator stage and the Lion sensor over 48 hours indicating drifts of around 200 nm and 450 nm respectively. The drift measurement for the actuator and the MOORE machine frame metrology loop becomes correlated after 20 hours.

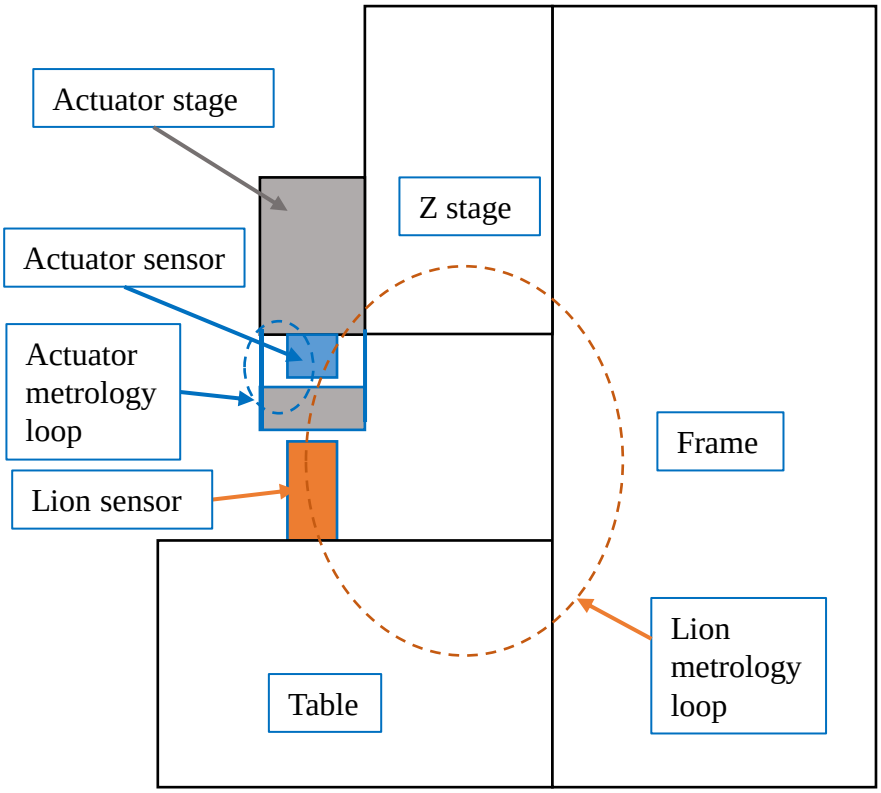


Figure 107. Actuator metrology loop and frame metrology loop.

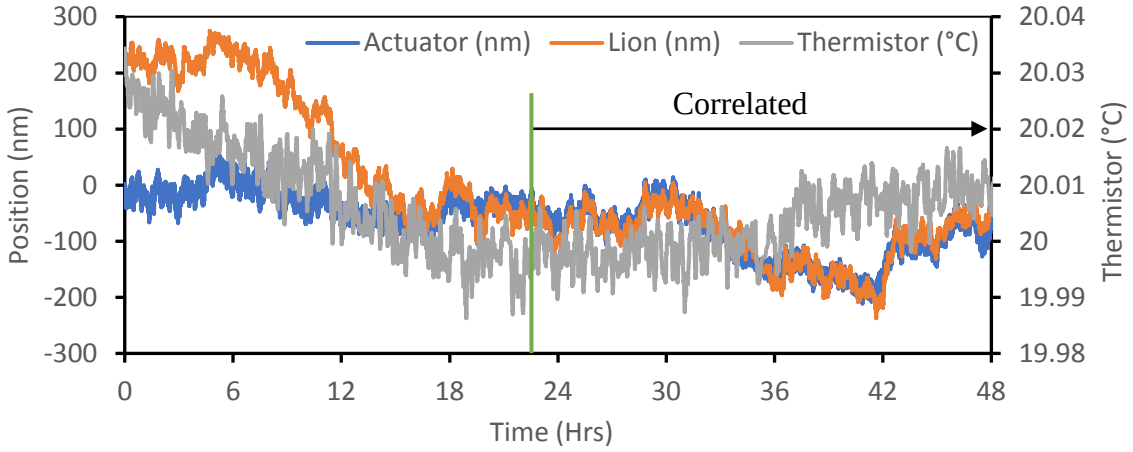


Figure 108. Stability test of the actuator stage and Lion™ sensor.

To test the stability of the load-cell, data was collected from its capacitance sensor over a period of 4.5 seconds at a sample interval of 1 ms. For these measurements, the load-cell outputs

were measured with the platform free and in contact with the indenter, see Figure 109 to Figure 112.

Results for the plots shown in Figure 109 and Figure 110 have been filtered from the actuator and the load-cell displacement signals. To determine the influence of filtering, a filtered signal is comparing with the raw data in Figure 109 and Figure 110. The average filter works by moving through the signals, replacing each value with the average value of neighboring signals, including itself. In this research, a continuous penetration process was recorded (blue) and the averaging filter works for this study is 100 box-car filter (orange). Following Figure 109 and Figure 110 demonstrate the noise measurement of the capacitive gage before average and after one hundred points average filter.

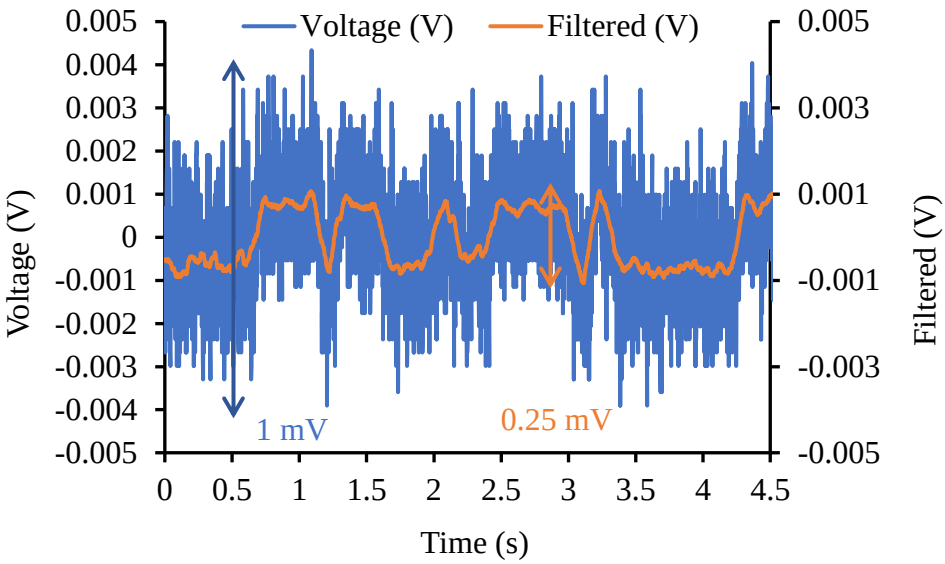


Figure 109. Noise measurement of the capacitive gage, Blue: before average, the noise level of the load-cell stage is 1 mV. Orange: after applying one hundred points averages, the noise level of the load-cell stage is 0.25 mV. This means the filter increases the data accuracy 4 times. Total sample time is 4.5 second.

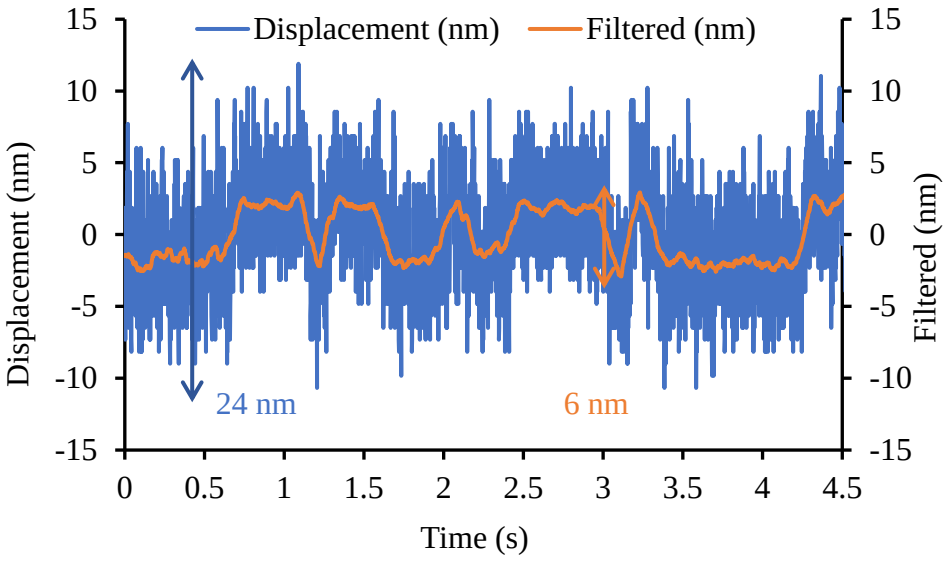


Figure 110. Noise measurement of the capacitive gage, Blue: before average, the noise level of the load-cell stage is around 24 nm. Orange: after applying one hundred points averages, the noise level of the load-cell stage is around 6 nm (0.6 µN). This means the filter increases the data accuracy 4 times. Total sample time is 4.5 second.

The noise level of the load-cell stage is around 1 mV or 24 nm before filtering. After applying one hundred points averages, the noise level of the load-cell stage is around 0.25mV or 6 nm (0.6 µN). This means the filter increases the data accuracy ~4 times.

### 5.6.1 OPEN LOOP NON-CONTACT

In this stability test, the flexure spring structure of the load-cell stage is hanging freely. The voltage to displacement signal is calibrated using Lion™ ultra-precision capacitance gage. The Lion™ gage is mounted on the XY stages of the Moore machine, Figure 85. Two sensors are used to record the room temperature. By comparing the voltage signal from the Lion™ gage and the actuator stage and load-cell stage, the stability test data were recorded and are plotted in Figure 111.

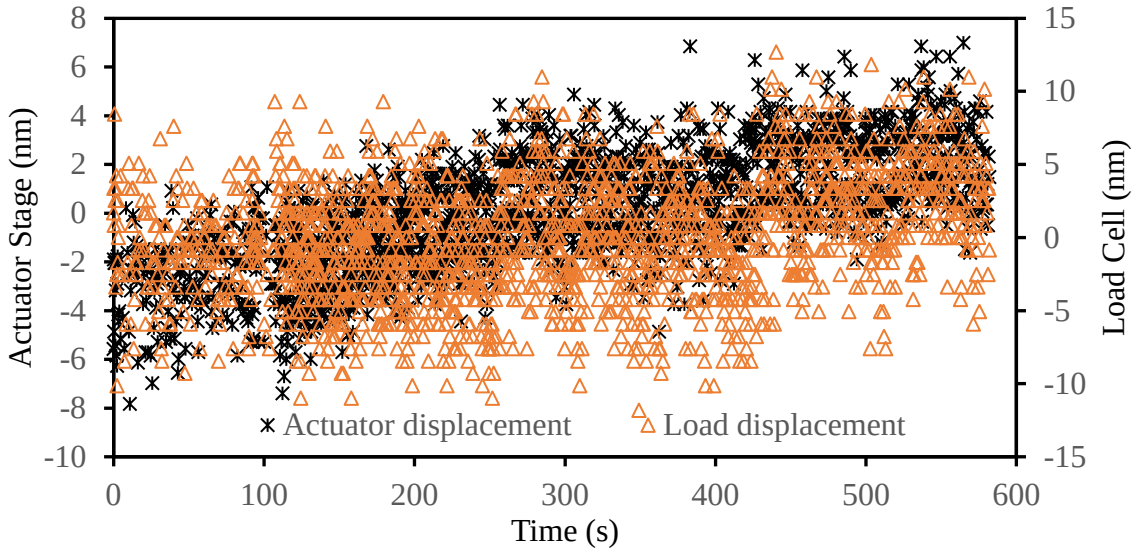


Figure 111. Stability test for actuator stage and load-cell stage during non-contact mode.

Over a 10-minute period, the actuator stage has a drift less than 16 nm, and the load-cell stage has a drift of less than 25 nm. For load-cell stage stiffness of ~100 kN/m, this corresponds to a drift less than 2.5 μN over 10 minutes. The metrology laboratory temperature is maintained at 20 ± 0.1 °C. No clear correlation was found between the temperature and the drift displacement in this test.

### 5.6.2 OPEN LOOP CONTACT

In this stability test, the flexure spring structure of the load-cell stage is contacted with the indenter of the rotary stage. The stability of the rotary stage will be recorded by using rotary encoder. By comparing the voltage signal from the Lion™ gage with the actuator stage and load-cell stage, the stability test data for contact model were recorded over a duration of 10 minutes and are plotted in Figure 112.

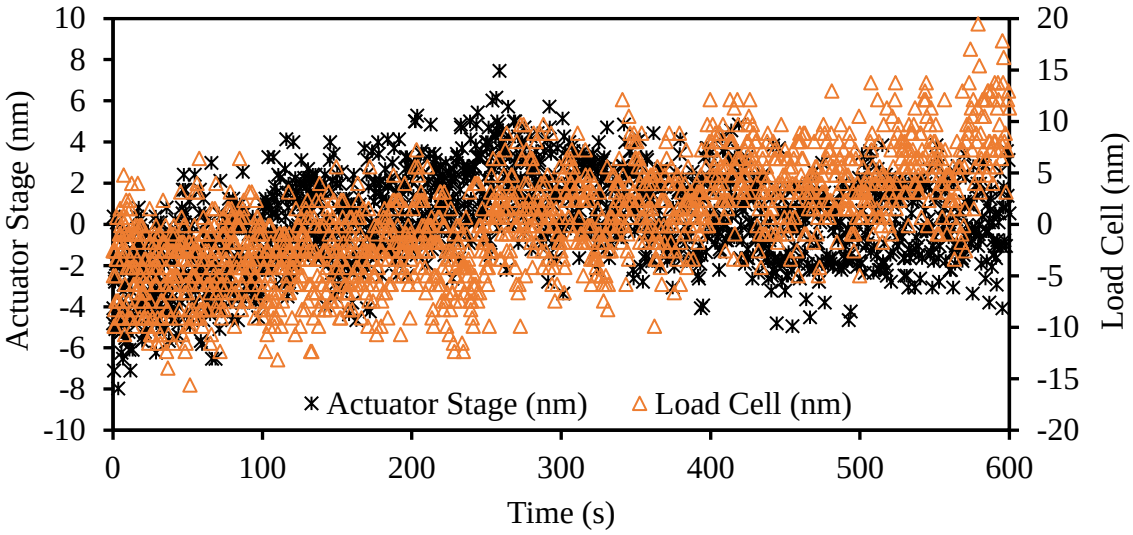


Figure 112. Stability test for actuator stage and load-cell stage during contact mode.

After 10 minutes periods, the actuator stage has a drift of less than 16 nm, and the load-cell stage has a drift of less than 35 nm. For load-cell stage stiffness of ~100 kN/m, this corresponds to a drift less than 3.5 μN over 10 minutes. From the rotary stage encoder measurement, the rotation angle was found to vary less than 20 microradian. As for the experiments of previous section, the room temperature is maintained at 20 ± 0.1 °C. No clear correlation was found for the temperature and the drift displacement in this test.

## 5.7 SYSTEM FORCE LOOP STIFFNESS

The system was built by some components, include MOORE machine frame, table, z gage, actuator stage, load-cell stage, flexure rod, and air-bearing, as seen in Figure 113. The frame stiffness is estimated around 5000 kN/m, and this estimation is based on the actuation stage displacement with respect to the load-cell stage displacement with the indenter replaced by a 4.7 mm radius steel sphere. Plotting this shows a 2 percent error for the linear curve fitting between the actuation stage and the load-cell stage. In principle, the ratio for the actuation stage and the

load-cell stage should be -1 for an infinite stiff metrology frame. The 2 percent different from an idea ratio value could be from errors of the actuation and load-cell stage displacement, that were calibrated more than two months before this experiment. Nevertheless, using this 2 percent different to indicate a stiffness of the metrology frame loop has a stiffness around 5000 kN/m. This metrology loop stiffness is greater than the 4120 kN/m flexure rod theoretically predicted stiffness, however, there is additional stiffness in parallel due to the fine adjustment clamping mechanism. The metrology loop stiffness is less than the air-bearing stiffness that is also one of the serial components in the metrology loop.

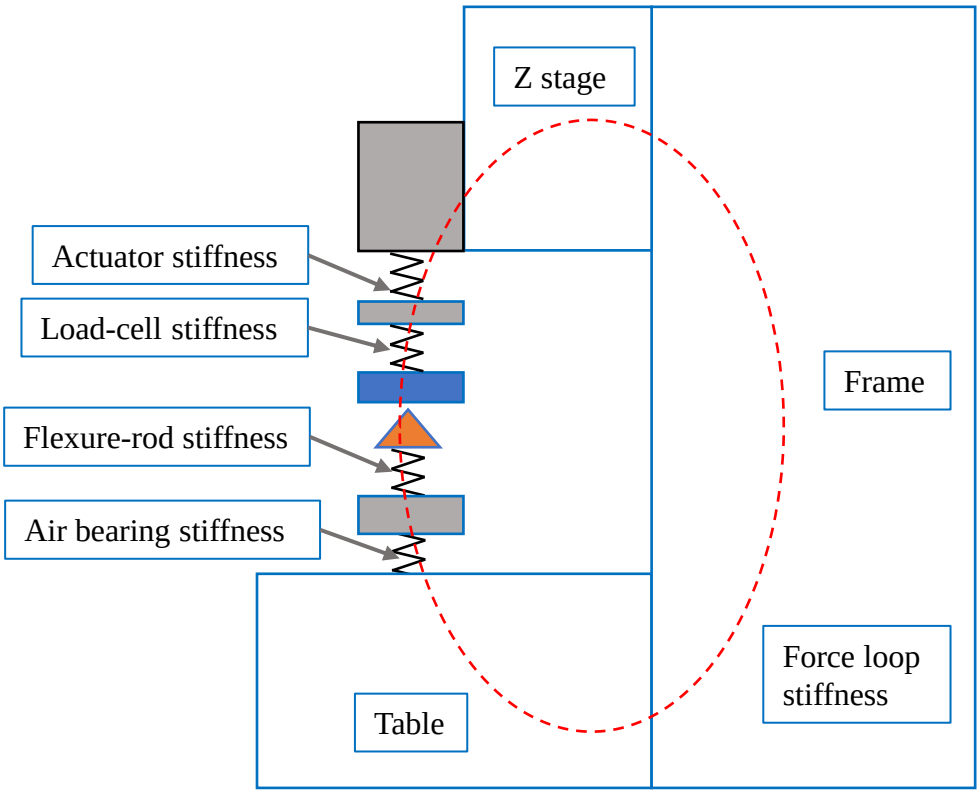


Figure 113. Force loop stiffness was calculated from the measured load and deformation.

## 5.8 UNCERTAINTY BUDGETS

During the manufacturing and assembly process of the instrument, the effect of geometric error, and the assembly position error of the parts has to be considered in Figure 114. Some other factors, like whether the structure design follows Abbe's principle or not, are there any friction influences for the system, and what is the force and deformation behavior for the subsystem component. After the system is assembled, thermal and temporal drift, residual stress, and vibrations should be considered as the error source.

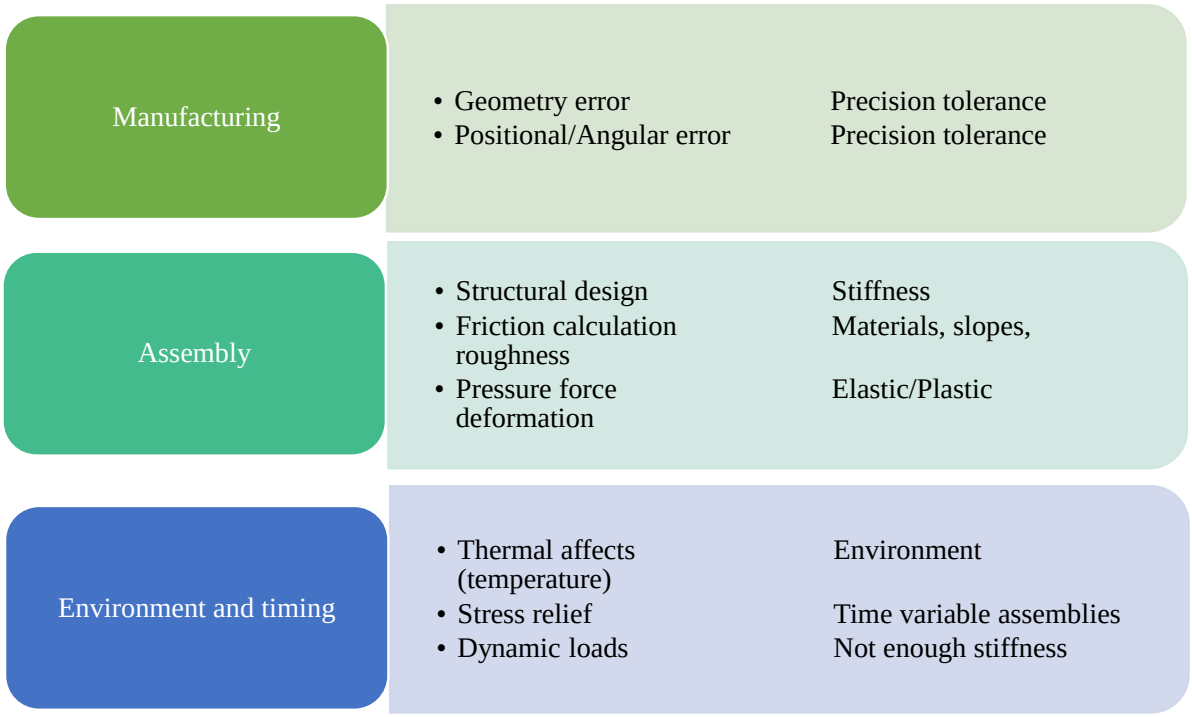


Figure 114. Typical error budgets for the nano-indentation instrument.

Additionally, the electrical noise of the system from encoder, temperature sensor, electrical system, vibration, plus air bearing pressure, are recorded during the measurements, type A evaluation of GUM is used to define the uncertainty budgets. Since correlation measurement between environmental factors and measurement results (rotational angle and penetration depth) are not detected from the measurement results. The uncertainty budgets is used to estimating of

the standard deviation from rotation angle and penetration depth. Factors influencing these estimates are presented by the Ishigawa diagram [40] shown in Figure 115.

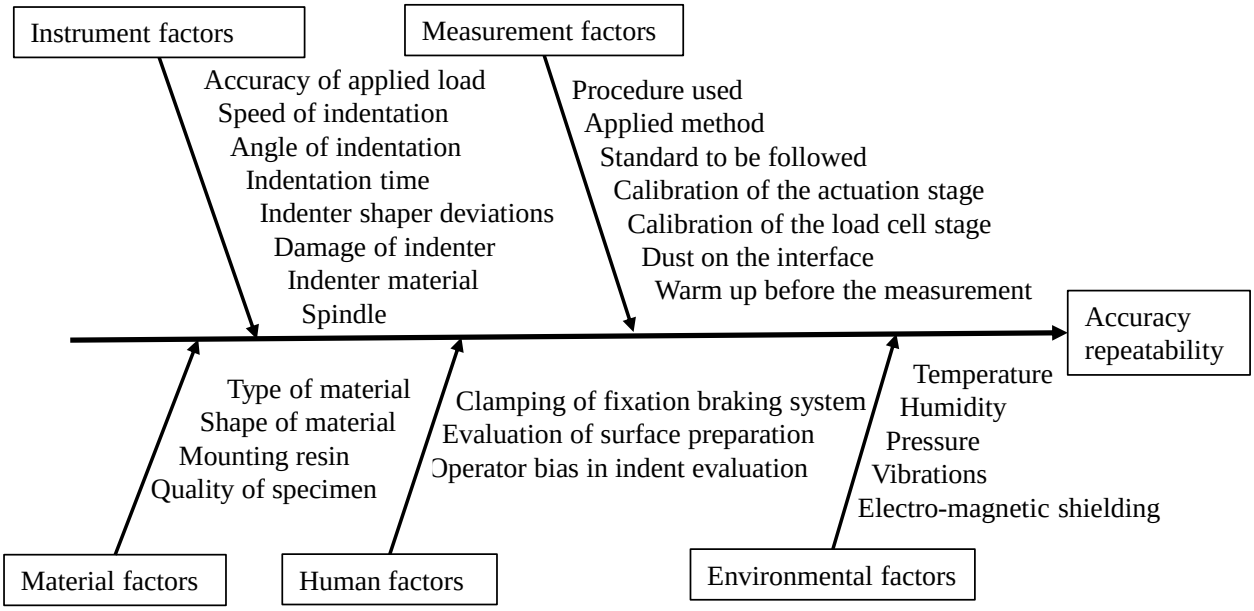


Figure 115. Uncertainty factors for the indentation (Reproduced from reference [40]).

Some important factors that should be considered for rotation measurement during nano-indentation process are listed in the following:

- External factors such as dirt, vibrations, temperature, and humidity should be controlled.
- The tester and stage should be secured on a solid horizontal table, and the sample should be clamped or held in a holder or solid mounted on the sample holder using epoxy.
- The tested surface of the samples should be perpendicular to the indentation axis.
- The tip the indenter should be coaxial to the rotational axis of the rotary air-bearing.
- The air pressure for the air-bearing should be maintained.
- The system should be recalibrated/verified every time you change the indenter or samples.

Since correlation between temperature and drift was not found, the stability test is used to calculate the total uncertainty. Table 5 shows the uncertainty values from the stability test for 10 minutes.

Table 5. The total uncertainty from stability test for 10 minutes.

| Uncertainty | Load-cell stage stability u | Actuator stage stability u |
|---|---|---|
| Noise ($f_{nyq}$ = 5 Hz) non-contact | 5 nm (standard deviation) | 3 nm (standard deviation) |
| Noise ($f_{nyq}$ = 5 Hz) in contact | 7 nm (standard deviation) | 3 nm (standard deviation) |

# CHAPTER 6: MEASUREMENT RESULTS

This chapter presents results from indents on materials, ranging from insulators to metals and polymers. The sample preparation is described in section 6.1. The experimental procedures are listing in the section 6.2. Materials measured are single crystal silicon, polysilicon, aluminum, copper, pure copper, brass, lead zirconate titanate (PZT ceramic), Germanium, Teflon (PTFE), amorphous Ni-P, carbon fiber reinforced polymer, fused silica, and steel (grain size ~100μm). Each material measurement is presented in the subsection of section 6.3. During the nanoindentation process, the instrument can measure the displacement of the actuation stage, load-cell stage, and the rotation of the rotary stage. The displacement of the load-cell stage will be used to calculate the load during indentation. The penetration is calculated from the displacement of the actuation stage and the load-cell stage. To validate the instrument as a hardness tester, an indent on pure copper is analyzed in section 6.4.

## 6.1 SAMPLE PREPARATION

Al, Cu, Brass, Fe, Si, Teflon, Ge, Ni-P, CFRP, $SiO_2$ samples were prepared for this research. Grain sized Fe and Cu samples are prepared by annealing and polishing. More detailed explanations of the process and surface measurements are shown in this section. Annealing is a heat treatment that alters the physical and sometimes chemical properties of a material to increase its ductility, or to reduce its hardness, or change the grain structure (for this research). The annealing process involves heating a material above its recrystallization temperature, maintaining this temperature for several hours based on desired grain size and then slowly cooling it to the room temperature. All samples were cut into a suitable size for further polishing steps. Initial surface preparation begins with coarse polishing process using coarse sandpaper followed by finer sandpaper until a surface is produced smooth enough for polishing. The polishing motion is the

same but using finer sandpaper, then a 90 degrees rotation movement is changed for next finer polishing. For instance, hand polishing goes from coarse to finer sandpaper till the polish marks appears straight and uniform. Once hand polishing is complete, polishing of a soft sample begins with a fine grit wheel with micrometer to sub-micrometer particles ($Al_2O_3$). After sample has gone through the final polishing step, it is washed and dried. It is then dipped into an etching agent for a prescribed period of time then dipped into water to halt the reaction. After it is dried by air, it is ready for observation using an optical microscopy (Olympus BX51) to detect the grain size. Figure 116 shows the surface images of an annealed steel sample with grain size around 100 µm and, Figure 117 shows the surface of an annealed Cu with a grain size around 100 µm.

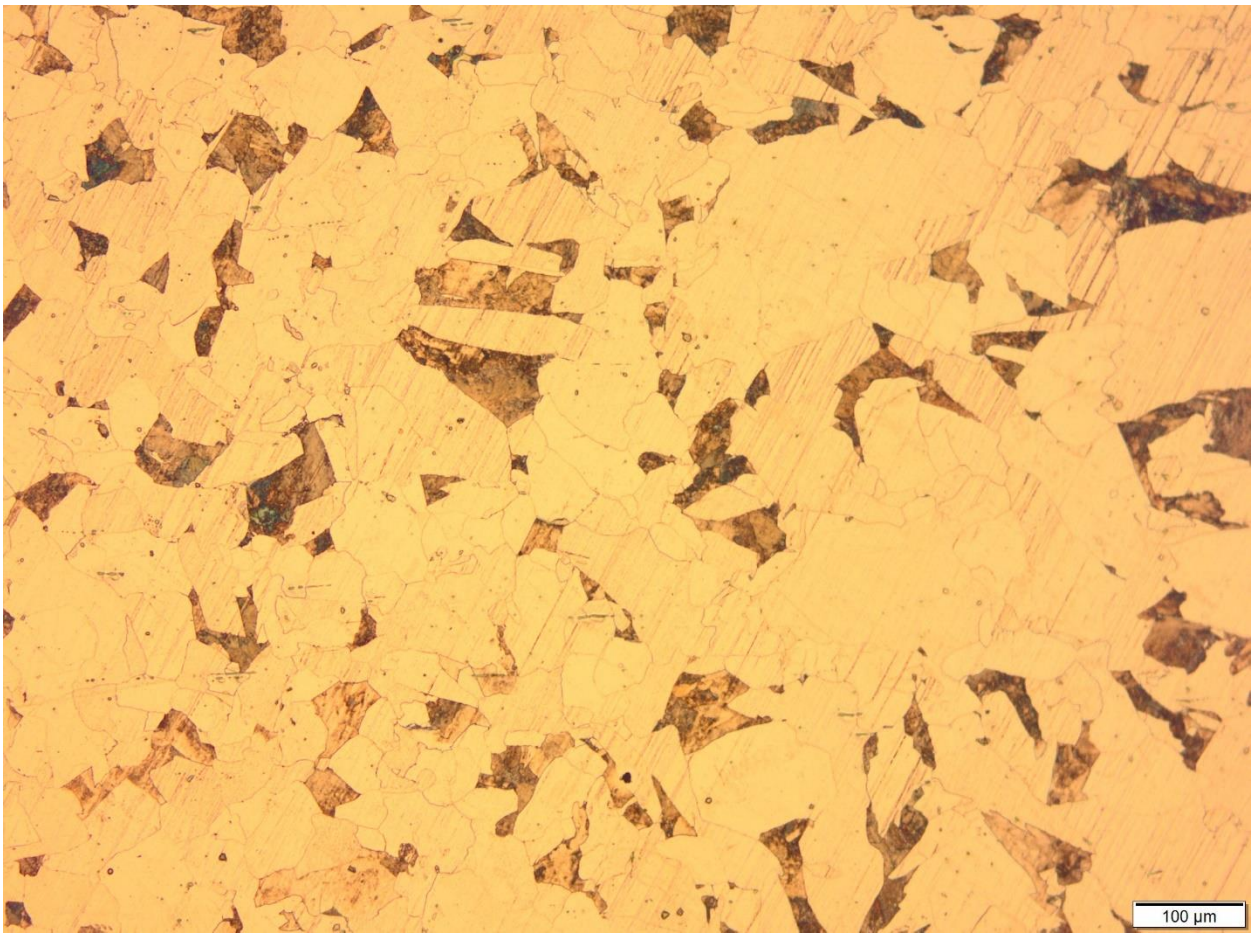

Figure 116. Optical micrograph of an annealed steel sample with grain size of around 100 µm.

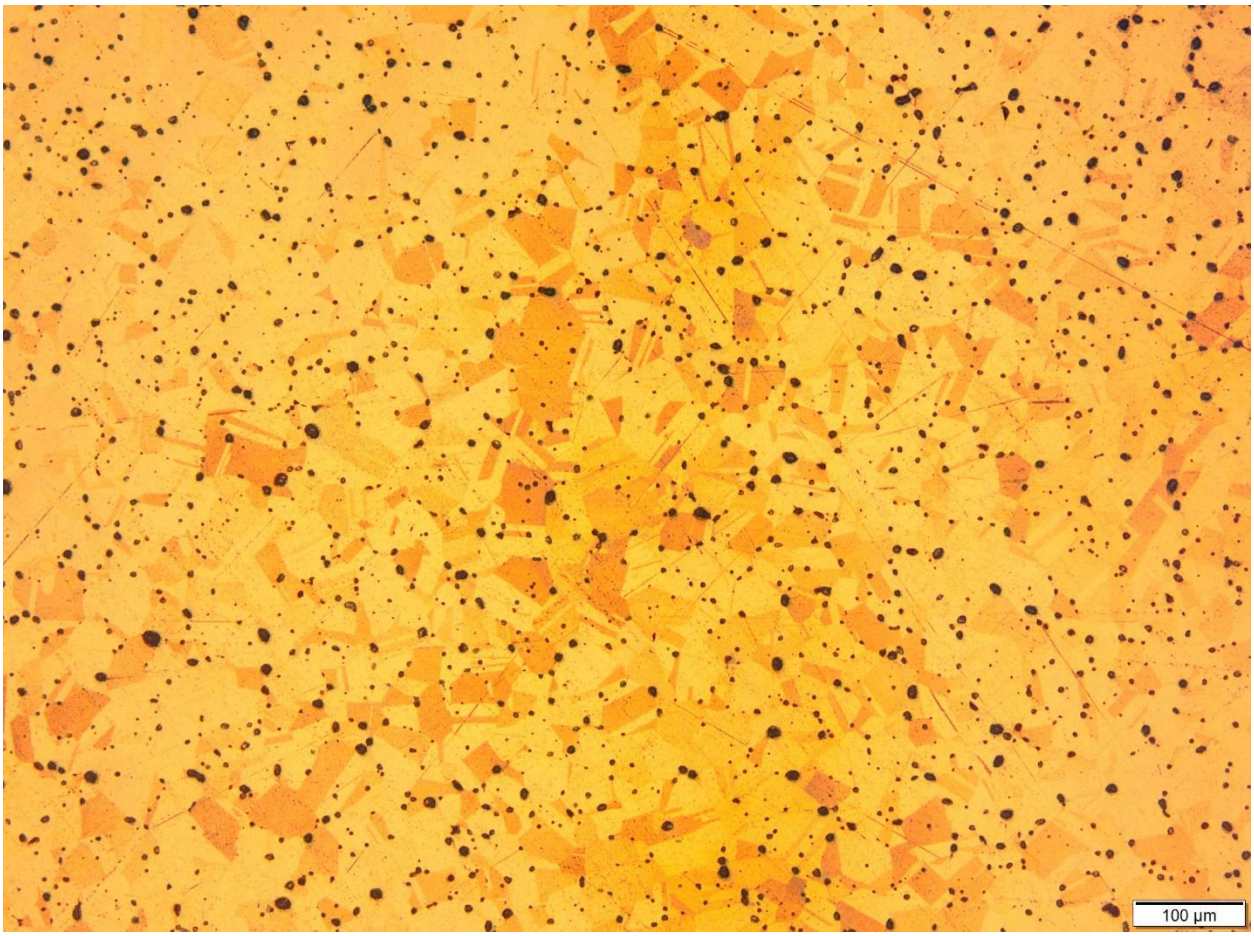


Figure 117. A surface images of an annealed Cu sample with grain size of around 100 µm.

## 6.2 EXPERIMENTAL PROCEDURES

All tests in this chapter used Berkovich diamond tip to penetrate the polished samples. Crystalized epoxy interface is used between the sample and the dovetail mounting structure that can be fastened to the load-cell. The system for aligning the indenter tip to the rotary bearing axis uses a rough and fine adjustment centering system. The sample surfaces were optical quality polished before testing. The experimental procedures are shown in the following steps.

- Thoroughly clean the mounting surface and sample surfaces using alcohol.
- Using adhesive (AB epoxy) to solidly bound the sample on the dovetail mounting structure.

- Move the Z stage of the Moore machine so that the sample close to the indenter (0.05 to 0.5 inches gaps), lock the Z stage use the brake system.
- Adjust the XY stage of the Moore machine so that the indenter is located to the center arear of the load-cell structure.
- Run the LabVIEW program so that the ADCs can record the signals from rotary encoder, capacitance gages, and temperature sensors.
- Rotate the micrometer knob to minimize the gap between the sample and the indenter until the load-cell stages are showing the attraction force from the electrostatic, Vander Wall, and capillary action force.
- Lock the micrometer stage using the braking system.
- Send a ramping voltage (around 4 Vpp) signal to the actuation stage.
- Gradually increase the ramping voltage (Increase 2 Vpp) of the actuator stage so that the penetration depth will be increased for each cycle.
- Repeat last step two more times so that the total Vpp of the stage is 10 Vpp.
- Record all the measurement results to excel.

## 6.3 RESULTS

The tests results reported in this section include a time-based recording of environmental temperature, piezoelectrical actuator stage ramping voltage, actuation stage displacement, load-cell stage displacement, and rotation angle measurements. Several samples, like aluminum, copper, single crystal silicon, single crystal Germanium, and amorphous nickel phosphorous, were used for the rotational measurement during nano-indentation.

### 6.3.1 SILICON

The expansion of the actuator, Xact, and the contraction of the load-cell stage, Xlc, are measured using two capacitance gages, as shown in Figure 118. The penetration depth in the horizontal axis is achieved using the equation Xact+Xlc, the first vertical axis is the loads applied between the sample and the indenter, and the rotation angle during nanoindentation is plotting out at the second vertical axis, in the Figure 119.

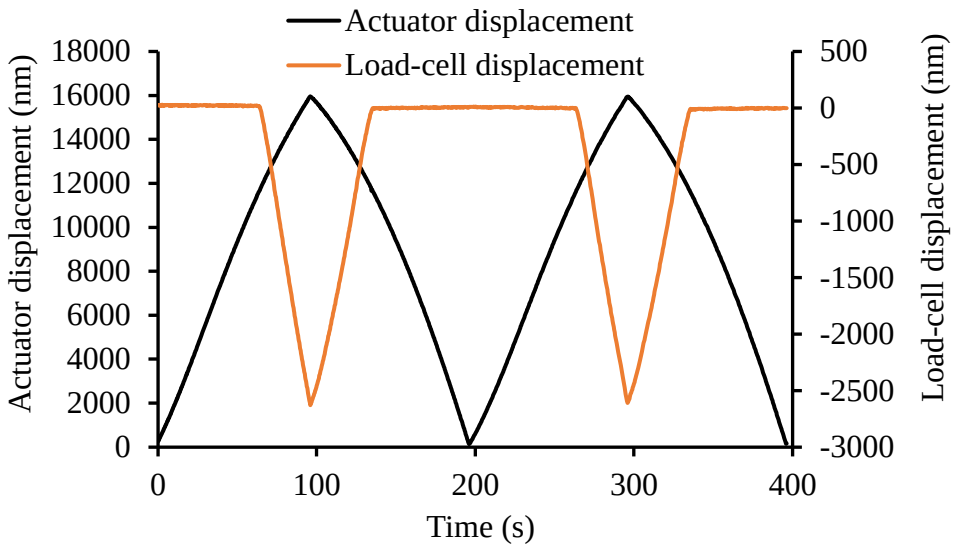


Figure 118. The expansion of the actuator and the contract of the load-cell stage are recorded simultaneously.

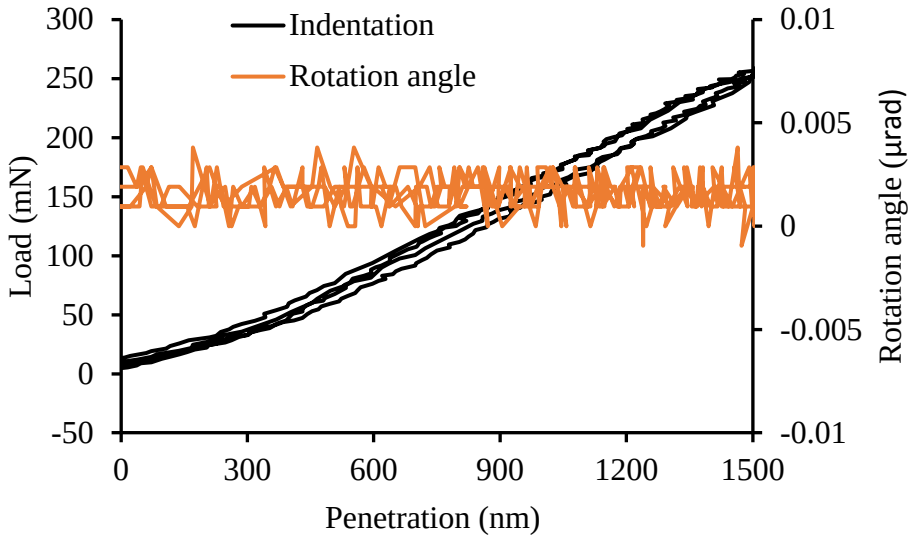


Figure 119: Single crystal silicon penetration depth is calculated from the expansion of the actuator and the contract of the load-cell stage and the load between the indenter and sample is calculated. Rotation angle during nanoindentation is plotting out at the second vertical axis.

Pop-in was observed for the silicon sample during nano-indentation. The penetration depth is achieved using the equation Xact+Xlc in the Figure 120 and the loads applied between the sample and the indenter, and the rotation angle during nanoindentation is plotting out at the second vertical axis, in the Figure 121.

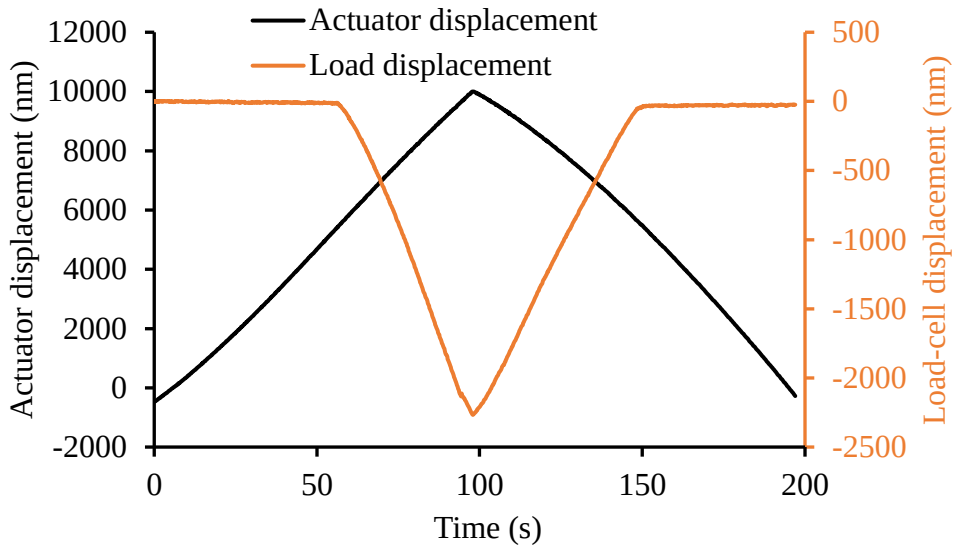


Figure 120. The expansion of the actuator and the contract of the load-cell stage are recorded simultaneously. Popping out was observed during unloading process at 134 seconds.

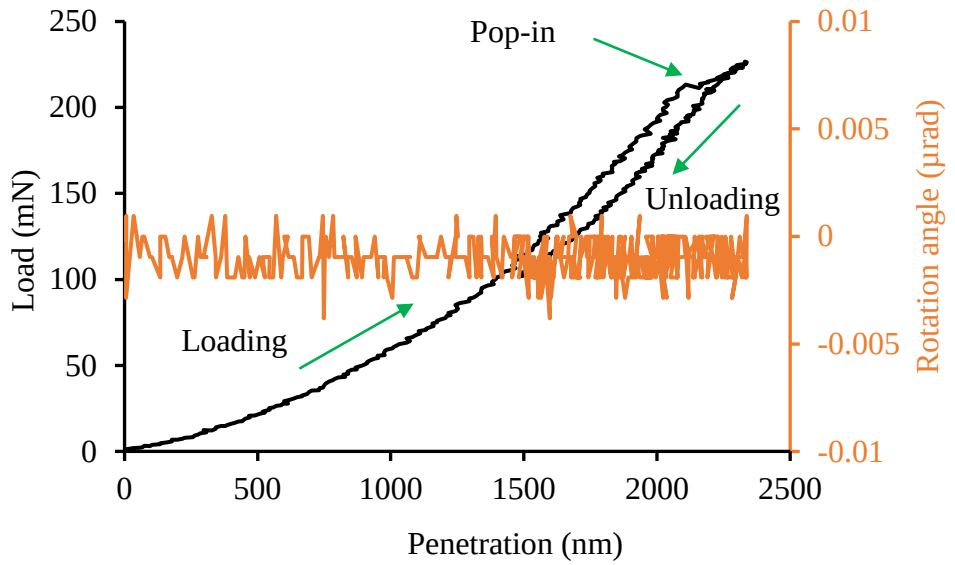


Figure 121. The single crystal silicon penetration depth is calculated from the expansion of the actuator and the contract of the load-cell stage and the load between the indenter and the sample is calculated as well. Popping out was observed during unloading process.

The expansion of the actuator, Xact, and the contraction of the load-cell stage, Xlc, are measured using two capacitance gages, as shown in Figure 122. Rotation angle was detected only

during macroscopic catastrophic fracturing for single crystal silicon and the SEM image of the macroscopy catastrophic fracturing is shown in the Figure 123. The penetration depth is achieved using the equation Xact+Xlc, and the loads applied between the sample and the indenter, and the rotation angle during nanoindentation is plotting out at the second vertical axis in the Figure 124.

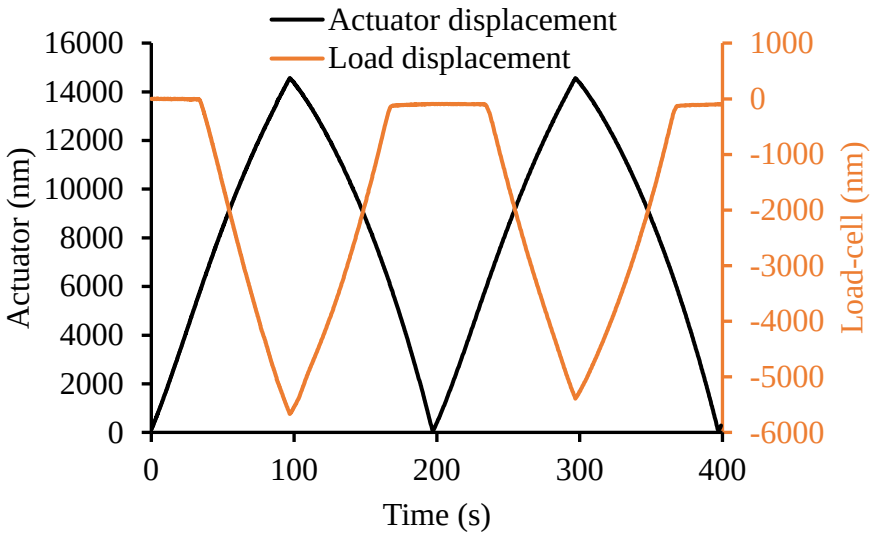


Figure 122: The expansion of the actuator and the contract of the load-cell stage are recorded.

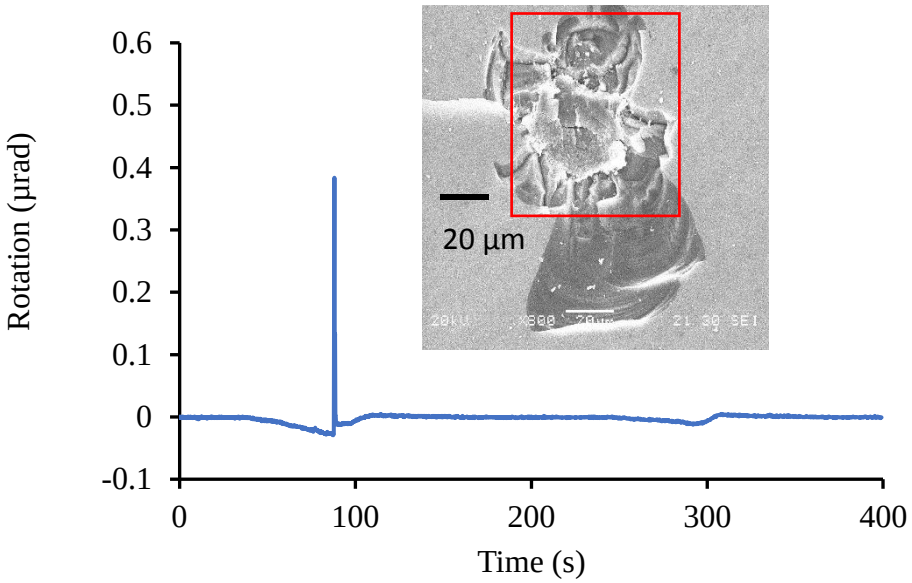


Figure 123: Rotation angle was detected during macroscopic catastrophic.

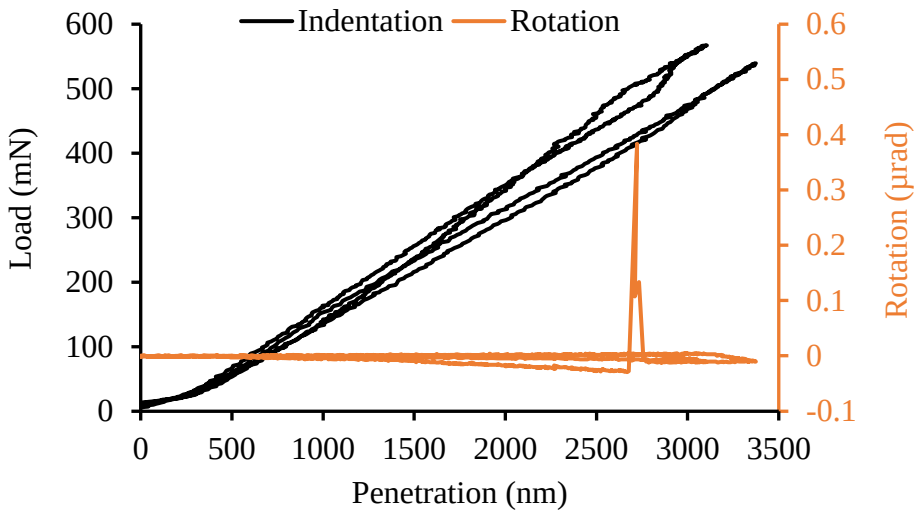


Figure 124: The single crystal silicon penetration depth is calculated from the expansion of the actuator and the contract of the load-cell stage and the load between the indenter and the sample is calculated as well. Popping out was observed during unloading process.

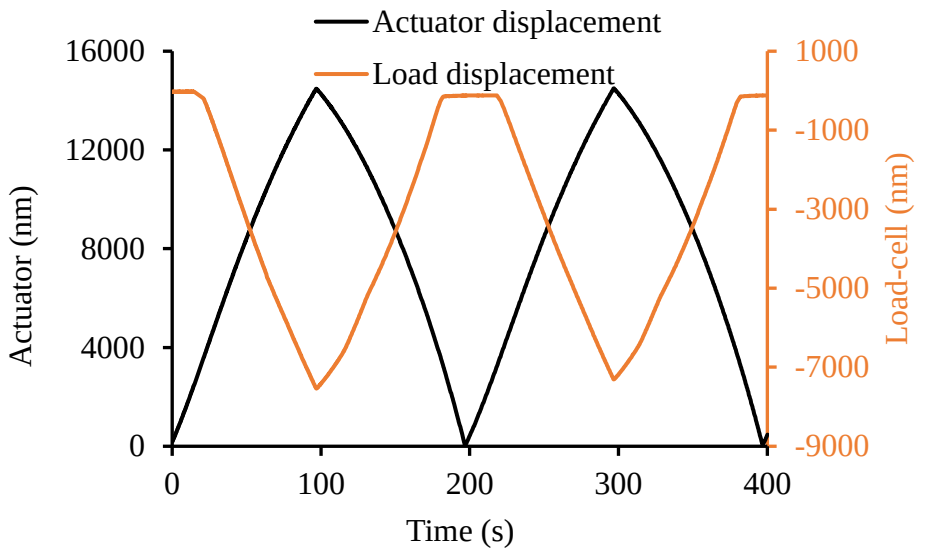


Figure 125: The expansion of the actuator and the contract of the load-cell stage are recorded.

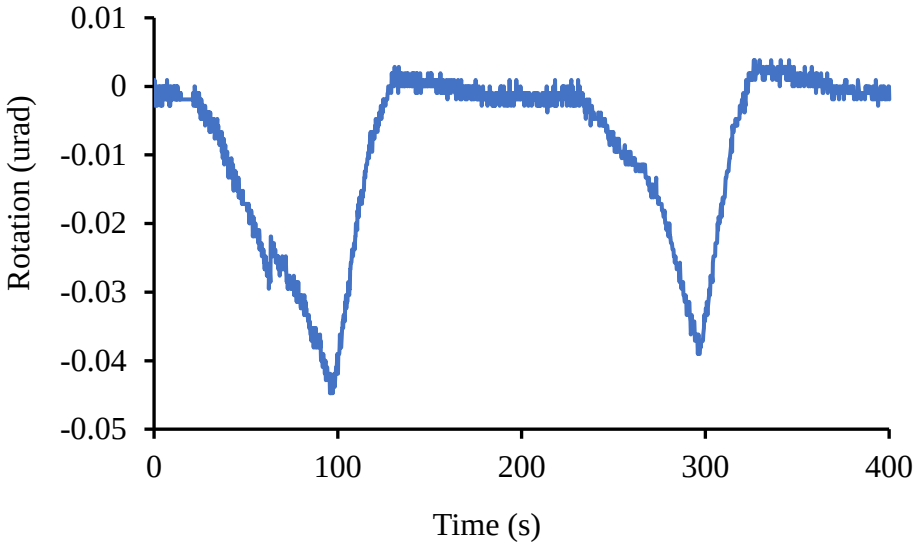


Figure 126: Rotation angle was detected during macroscopic catastrophic fracturing for single crystal silicon.

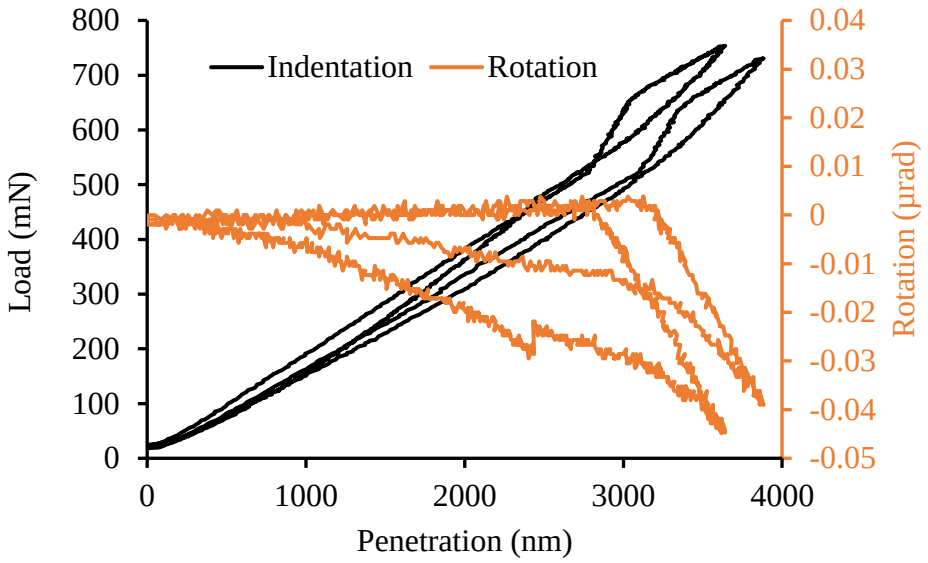


Figure 127: The single crystal silicon penetration depth is calculated from the expansion of the actuator and the contract of the load-cell stage and the load between the indenter and the sample is calculated as well. Popping out was observed during unloading process.

### 6.3.2 POLYSI

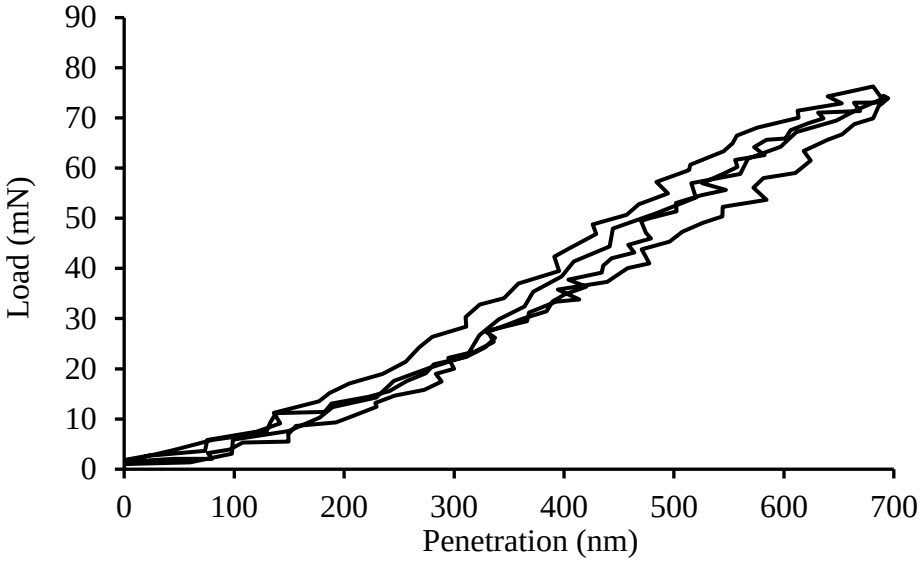


Figure 128. The poly-silicon penetration depth is calculated from the expansion of the actuator and the contract of the load-cell stage and the load between the indenter and the sample is calculated as well.

### 6.3.3 AL

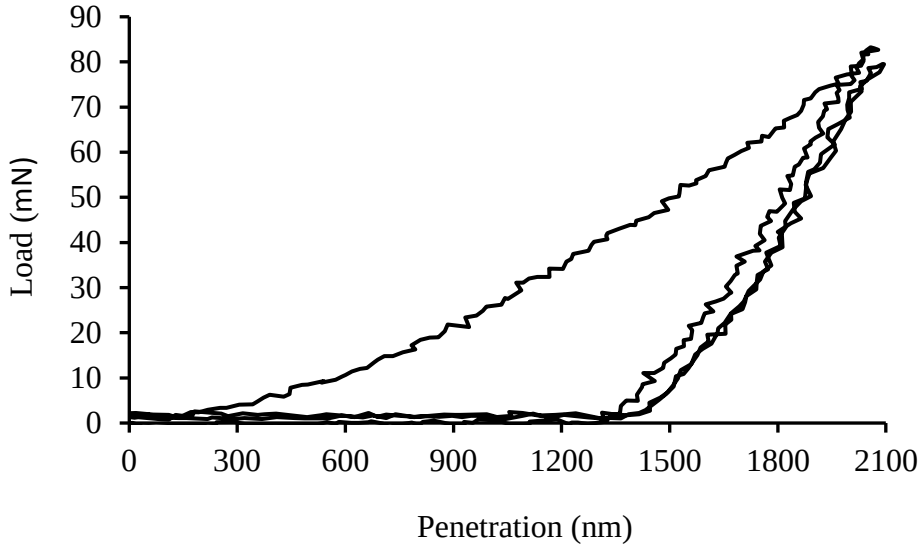


Figure 129. The Al penetration depth is calculated from the expansion of the actuator and the contract of the load-cell stage and the load between the indenter and the sample is calculated.

### 6.3.4 CU (GRAIN SIZE ~100 µM)

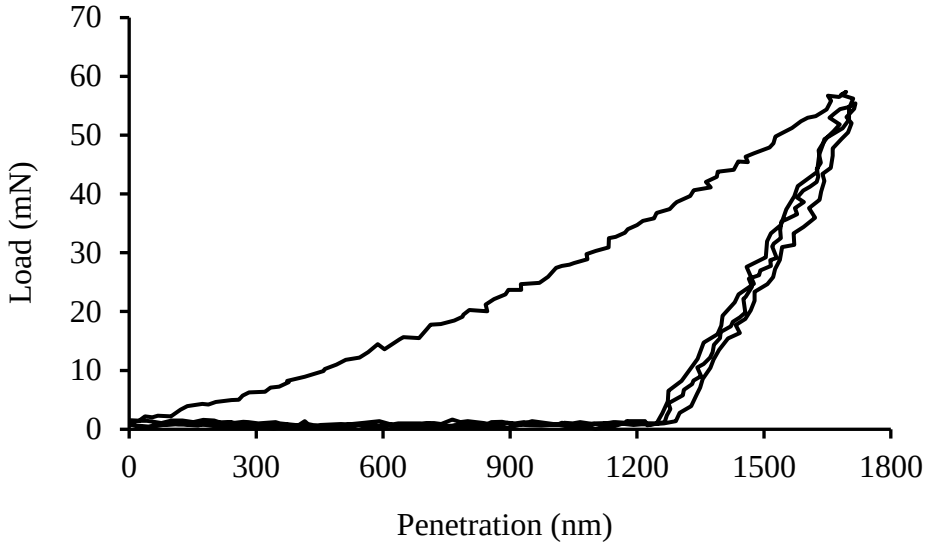


Figure 130. The Cu penetration depth is calculated from the expansion of the actuator and the contract of the load-cell stage and the load between the indenter and the sample is calculated.

### 6.3.5 PURE CU

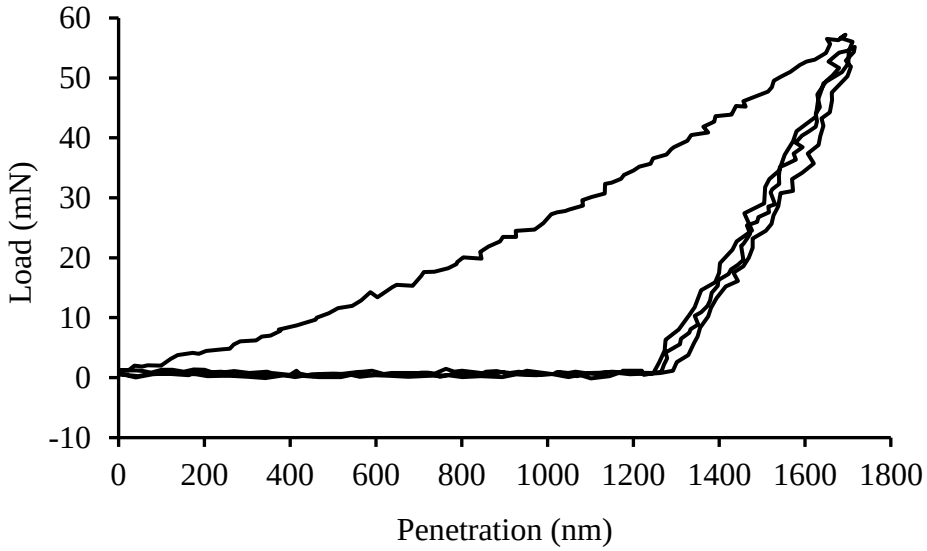


Figure 131. The pure Cu penetration depth is calculated from the expansion of the actuator and the contract of the load-cell stage and the load between the indenter and the sample is calculated.

### 6.3.6 BRASS

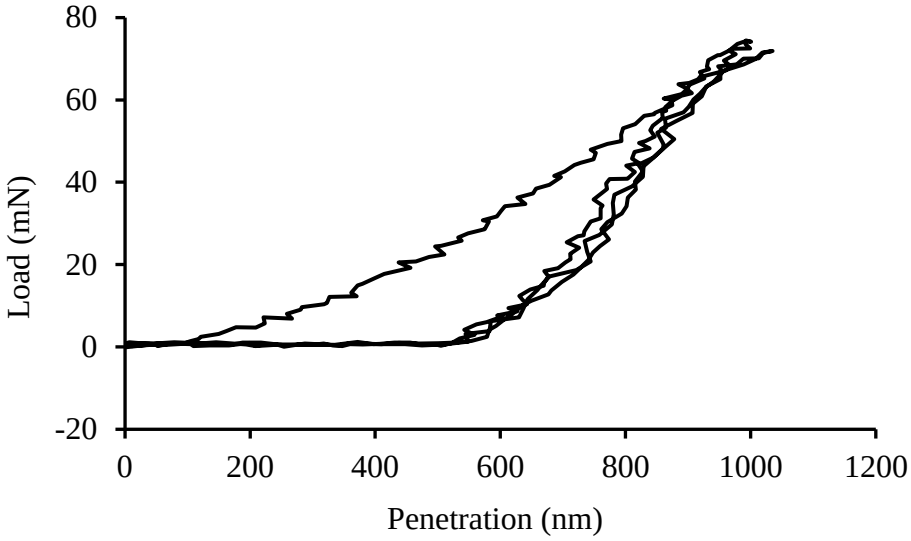


Figure 132. The brass penetration depth is calculated from the expansion of the actuator and the contract of the load-cell stage and the load between the indenter and the sample is calculated.

### 6.3.7 LEAD ZIRCONATE TITANATE (PZT MATERIAL)

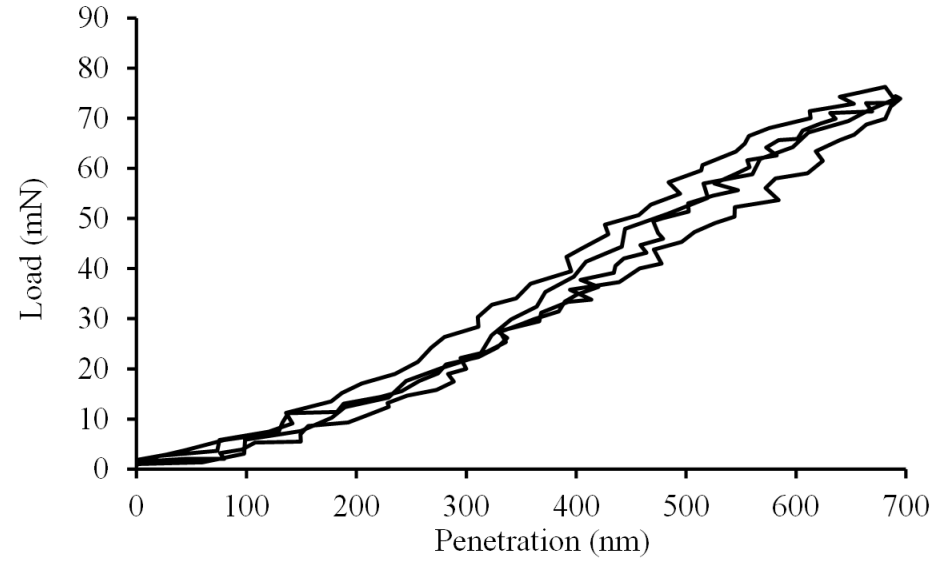


Figure 133. The PZT penetration depth is calculated from the expansion of the actuator and the contract of the load-cell stage and the load between the indenter and the sample is calculated.

6.3.8 GE

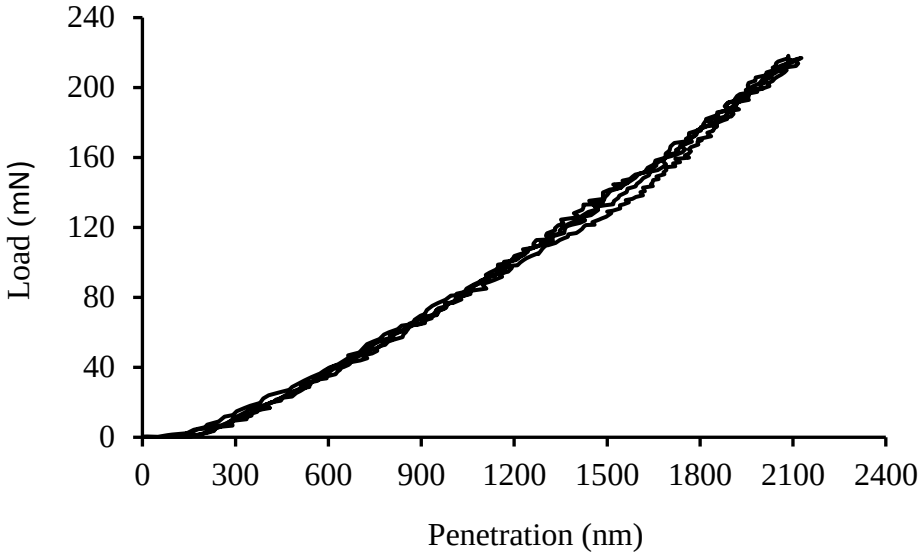


Figure 134. The single crystal germanium penetration depth is calculated from the expansion of the actuator and the contract of the load-cell stage and the load between the indenter and the sample is calculated as well.

6.3.9 TEFLON (PTFE)

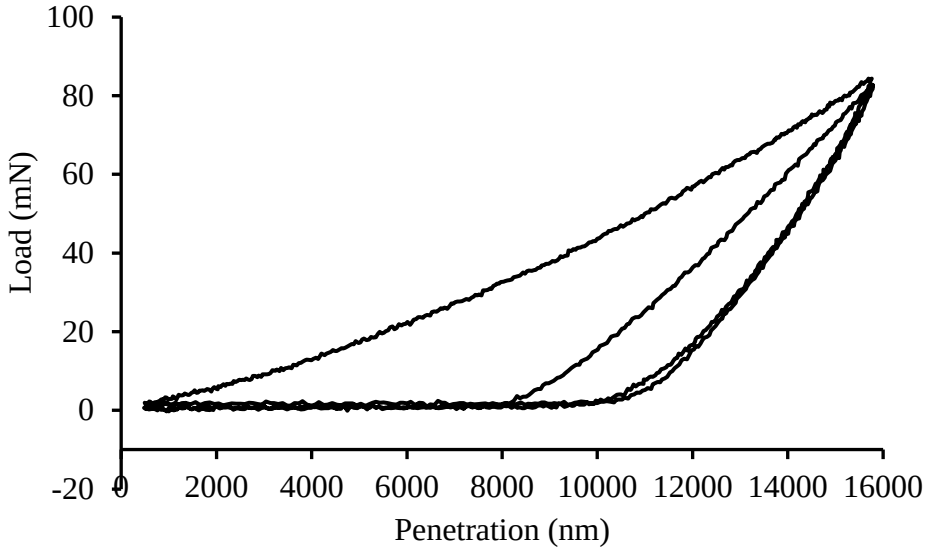


Figure 135. The PTFE penetration depth is calculated from the expansion of the actuator and the contract of the load-cell stage and the load between the indenter and the sample is calculated.

6.3.10 NIP

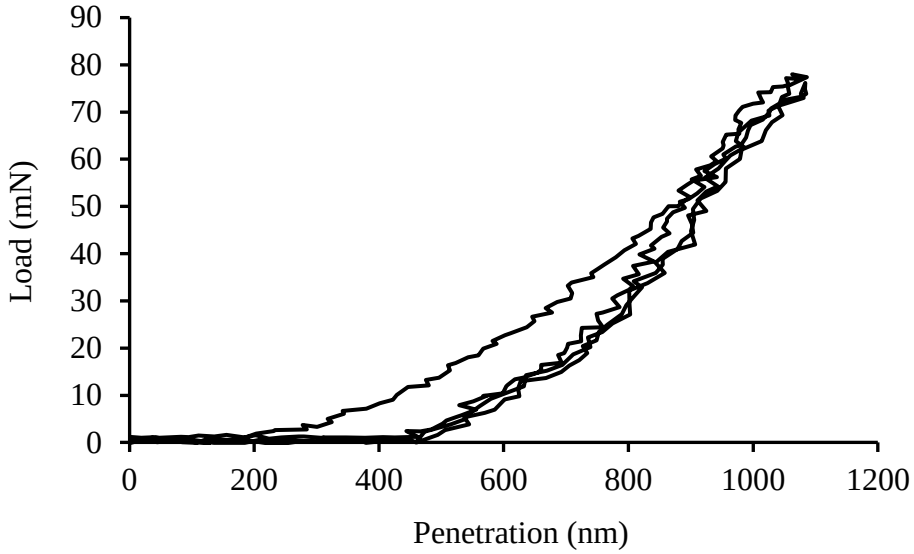


Figure 136. An amorphous nickel phosphorus penetration depth is calculated from the expansion of the actuator and the contract of the load-cell stage and the load between the indenter and the sample is calculated as well.

6.3.11 CARBON FIBER REINFORCED POLYMER

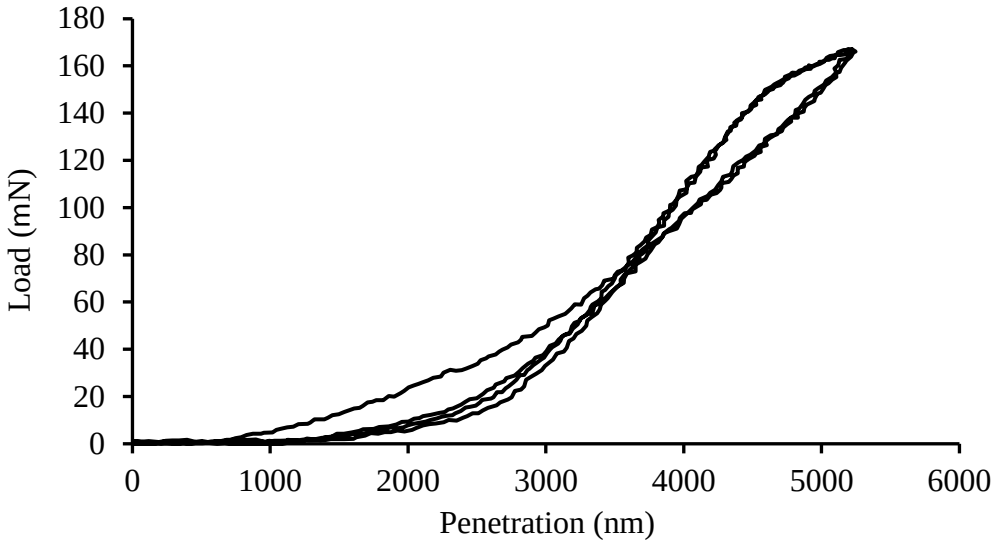


Figure 137. The CFRP penetration depth is calculated from the expansion of the actuator and the contract of the load-cell stage and the load between the indenter and the sample is calculated.

### 6.3.12 FUSED SILICA

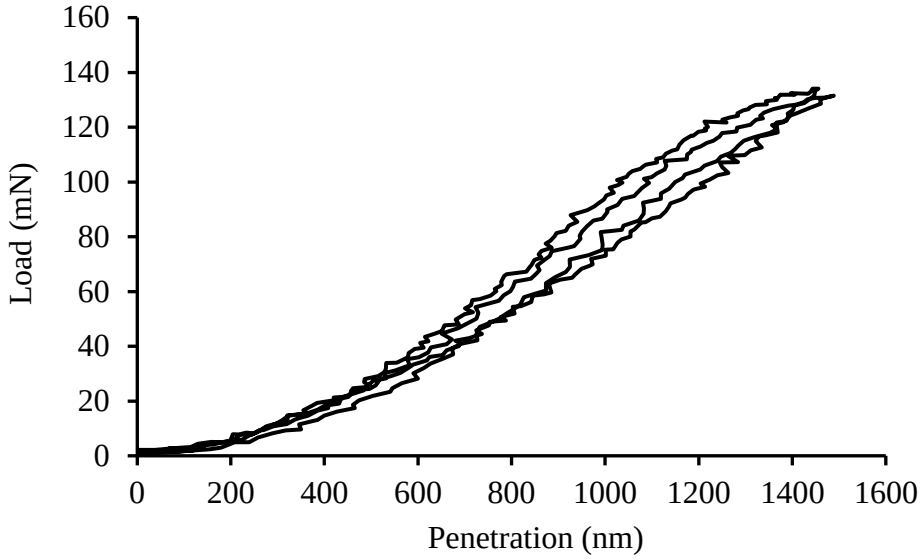


Figure 138: The fused silica penetration depth is calculated from the expansion of the actuator and the contract of the load-cell stage and the load between the indenter and the sample is calculated as well.

### 6.3.13 STEEL (GRAIN SIZE ~100 μM)

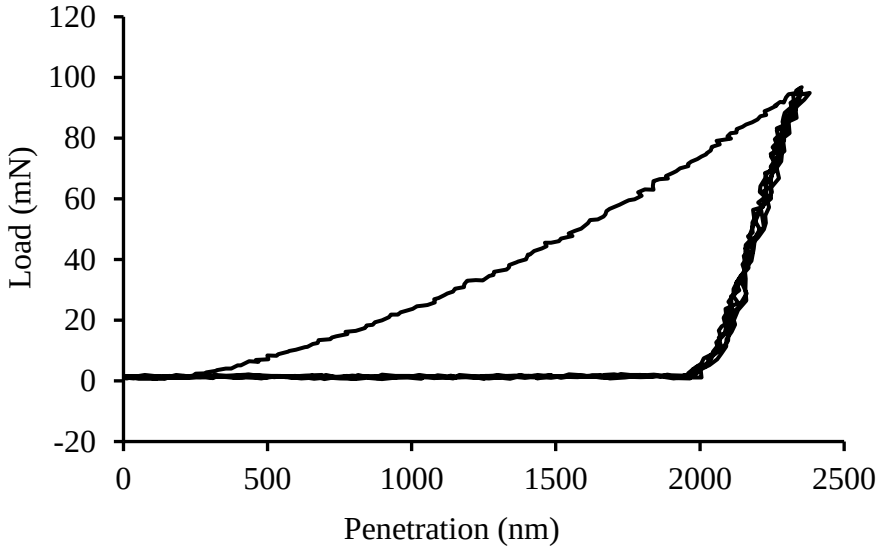


Figure 139: The steel penetration depth is calculated from the expansion of the actuator and the contract of the load-cell stage and the load between the indenter and the sample is calculated.

## 6.3.14 ZINC

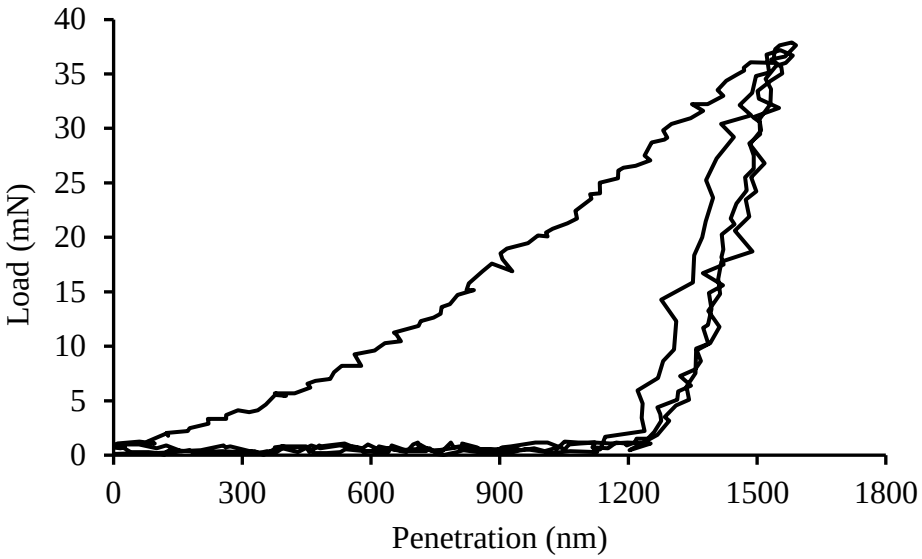


Figure 140: The zinc penetration depth is calculated from the expansion of the actuator and the contract of the load-cell stage and the load between the indenter and the sample is calculated.

## 6.3.15 OPTICAL IMAGES

The surface topography of the indent is measured by using Olympus digital microscope (shown in Figure 141) and also an atomic force microscope (Digital Instruments Nanoscope Dimension 3100 Metrology) image is shown in Figure 142. The results shows that the dent has a depth of ~220 nm, and a peak has a peak of ~230 nm and piling outs are observed in Figure 143. Atomic force microscope (AFM) imaging has similar topology surface as the scanning electron microscopy (SEM), shown in Figure 144.

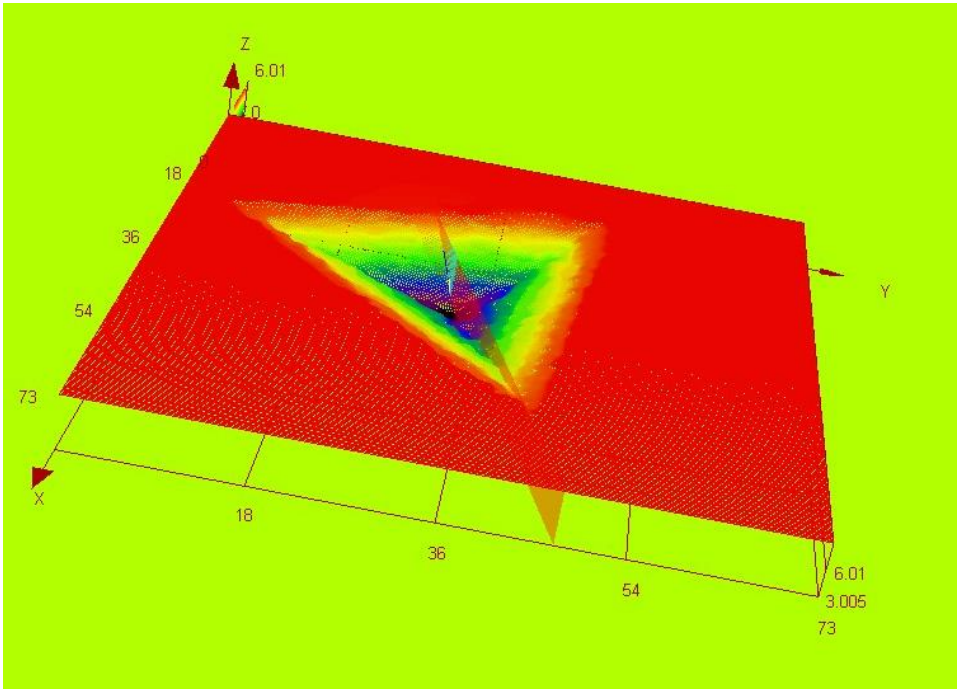


Figure 141: The surface map of an indent measured by the digital microscopy for amorphous NiP.

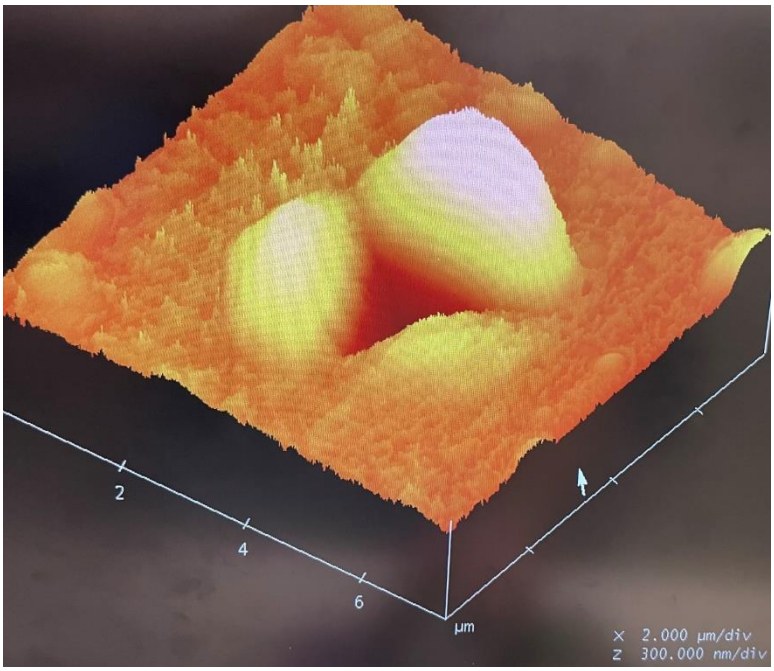


Figure 142: Atomic force microscope imaging of NiP amorphous sample after indentation test at a load of 100 mN.

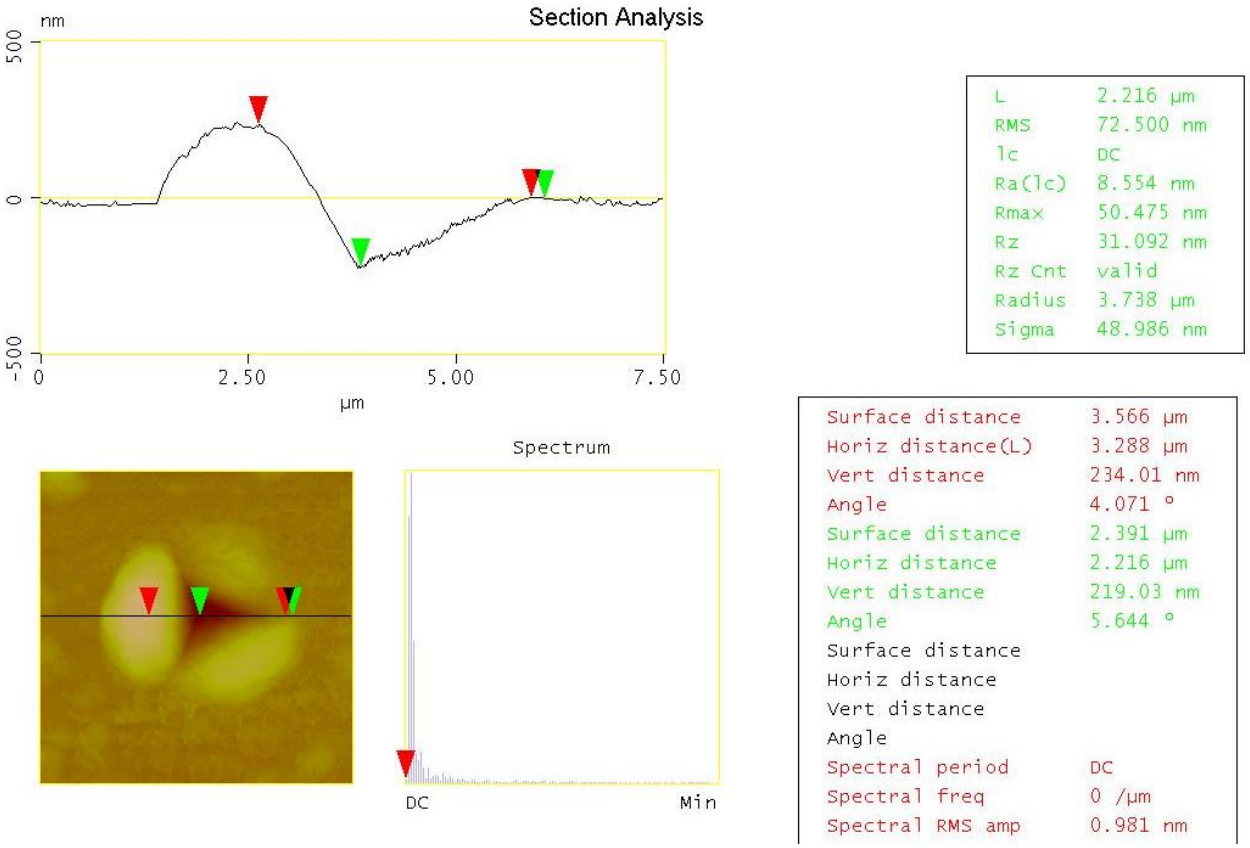


Figure 143: Atomic force microscope imaging of NiP amorphous sample after indentation test at a load of 50 mN.

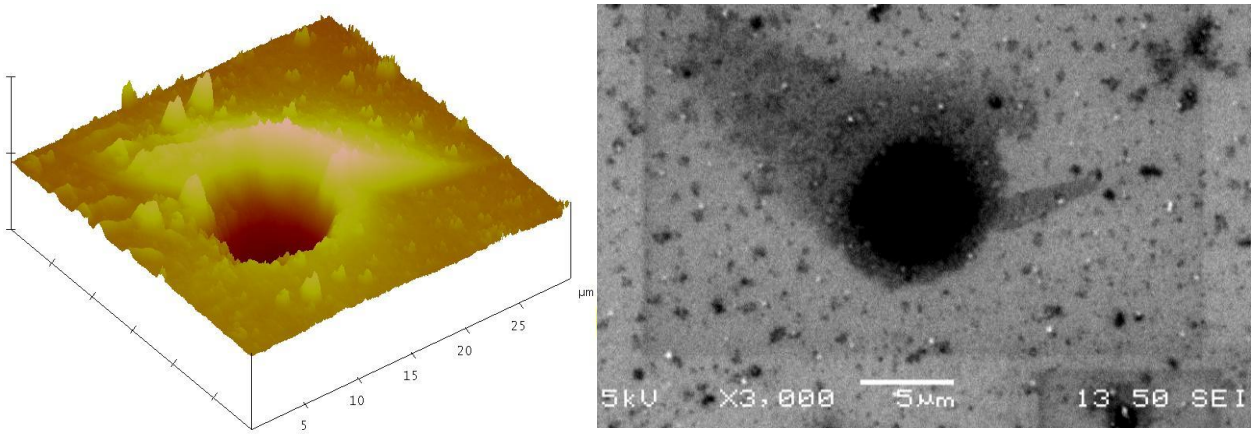


Figure 144: Atomic force microscope imaging has similar topology surface as the scanning electron microscopy for single crystal silicon.

## 6.4 HARDNESS INDENT CHARACTERISTIC

There are a wide variety of material studies that can derive information from micro/nano-scale indentation analysis, for materials ranging from metals and alloys (Steel, Al, Al alloy) to plastics (Polyethylene), and crystal materials (Si, Ge, Silica). A nanoindentation test comprises measurement of the indenter load and subsequent the penetration depth during loading and unloading cycles using a diamond indenter, shown in Figure 145. During nanoindentation process, the load-cell stage records the force between the indenter tip and the specimen. The maximum load force happens at the maximum penetration depth for the loading process. During unloading process, a constant slope range (~25% of the unloading curve), $S = dP/dh$, can be calculated from the load and penetration curve. For ideal tip geometry, the contact area of the nanoindentation is calculated from this equation $A_c = 24.56h_c^2$, where $A_c$ is the contact surface area, and $h_c$ can be observed from the load and penetration plot.

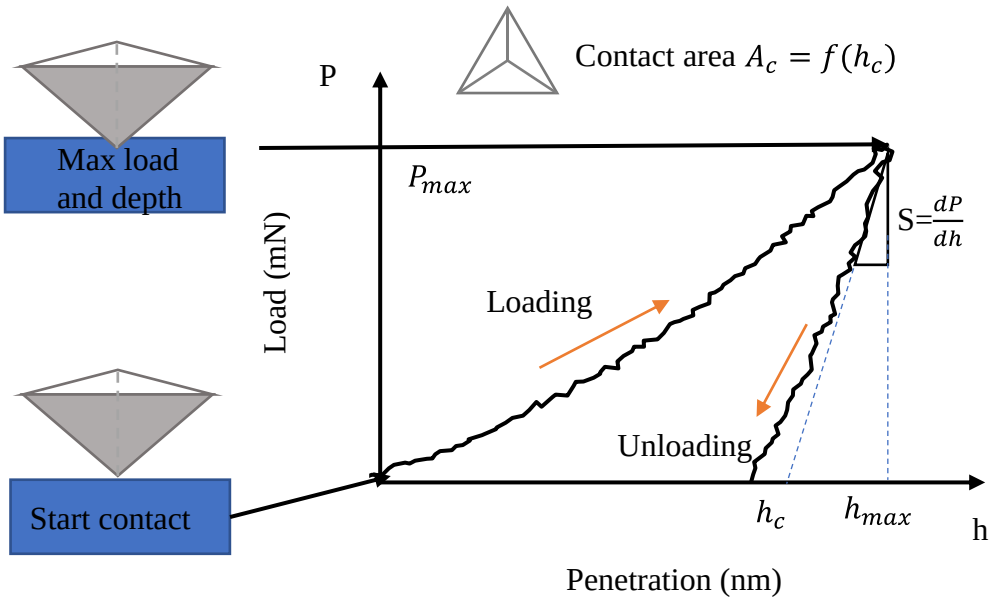


Figure 145. The penetration depth vs. the load applied between the indenter and the sample.

Broadly, hardness is inversely related to wear which is, in general, an industrial expense estimated at around 3% of global cost [41]. The maximum load, $P_{\max}$, can be observed from the plot and easily extracted from the measurement data. Hardness is calculated from the equation

$$H = P_{\max} / A_c .$$

Figure 146 is a nanoindentation measurement of pure copper, and the displacement and load during nanoindentation is plotting out. The slope of the curve during unloading process demonstrates the stiffness was the sample, shown in Figure 147. Figure 148 shows the hardness values is calculated between 370 MPa to 1640 MPa that is comparable with the annealed pure copper hardness values (390 MPa) [43].

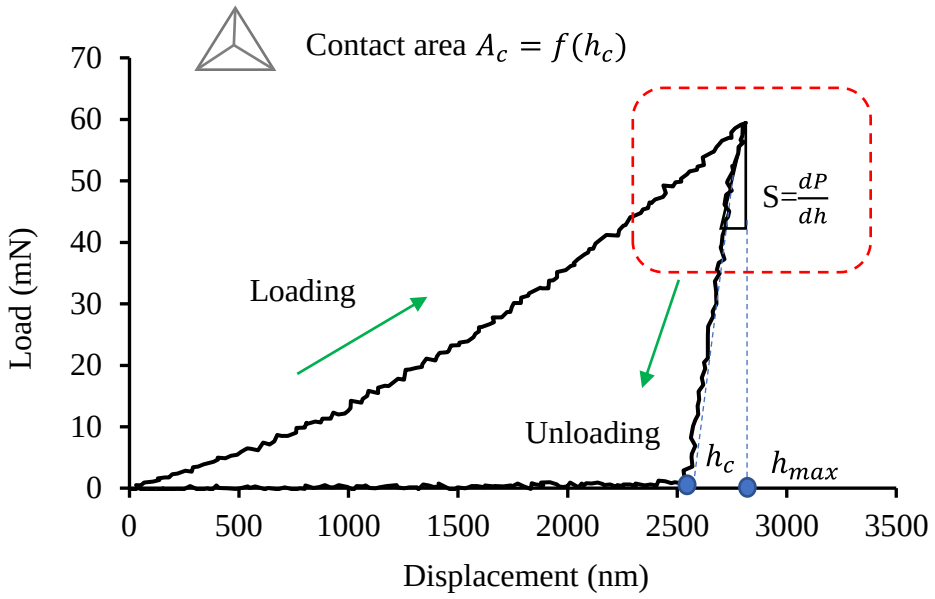


Figure 146: A nanoindentation measurement of pure copper to record the displacement and load curves.

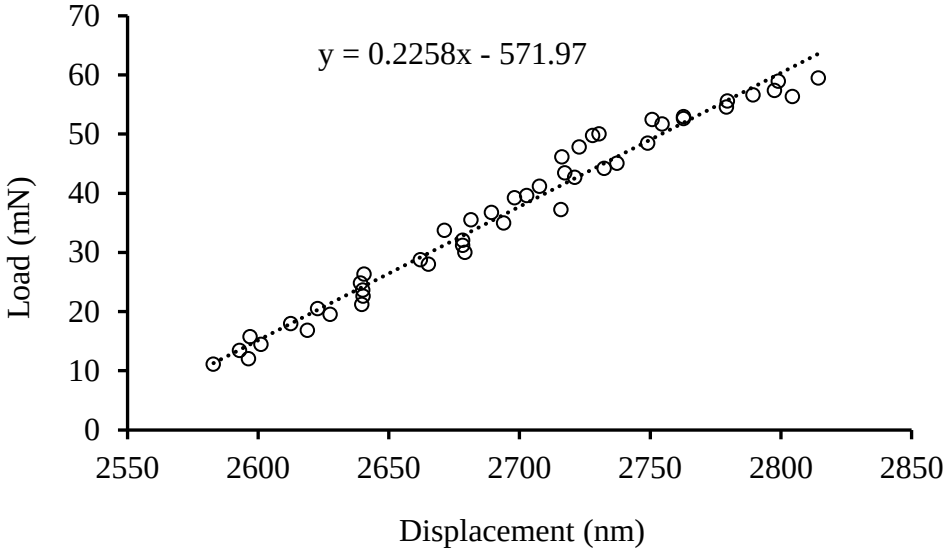


Figure 147: The slope of the unloading process shows the stiffness of pure copper sample.

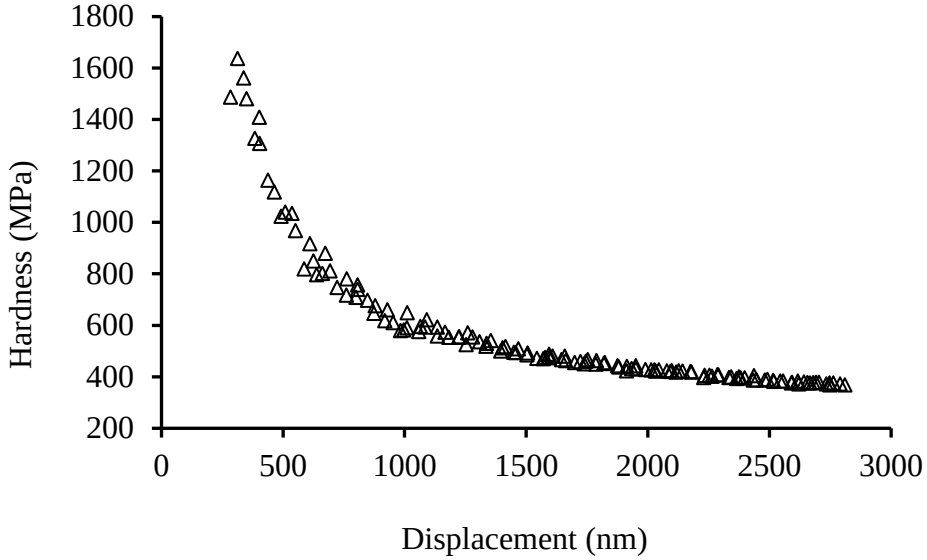


Figure 148: Hardness values of the pure copper sample is calculated and compensated with frame stiffness showing values between 370 MPa to 1640 MPa from 2.8 µm to 0.4 µm displacement range.

## 6.5 DISCUSSION OF RESULTS

The hard material, particularly the brittle materials, like Si and Ge, produce a substantially elastic response at low load values. PTFE, on the other hand, shows continued plastic deformation with duration of indent that is characteristic of viscoelastic materials. CFRP, during unloading process, maintains the force during the initial portion of the unload cycle, resulting in an "S" shape unloading curves. Reasons for this are not clear although it is noted that the specimens came in the form of plates that are difficult to bond to the dovetail specimen platform and may not be as flat as the other specimens. The effect of pushing the predominantly elastic fibers of CFRP into the polymer substrate may also contribute to this unusual plot.

From the measurement results, no rotational effects were observed in crystalline and amorphous metals, semi-conductors (Si, Ge), ceramic, PZT ceramic, CFRP, PTFE, and insulators.

# CHAPTER 7: OVERVIEW OF THE PROJECT

## 7.1 THERMAL ACTUATORS FOR PRECISION MOTION CONTROL

This research presents calculation of the eddy current density and induced eddy current power in a cylindrical aluminum tube. A zero-voltage-switching circuit is evaluated using PWM control signal for delivering the power to the thermal actuator. Experimental tests show the actuator provides a range of 200 μm and the steady state controller error is within ±70 nm. The steady state controller error and the dynamic response of the system is maintained for preloads up to 1 kN. Combining water and air-mist for cooling improved the symmetry of the control and the dynamic response.

Continuation of this research will aim to produce a compact actuator (25 mm) that can operate in a higher temperature environment. Because cooling of the wire is not easily implemented, Litz wire will be explored. Another consideration is the embedding of a feedback displacement sensor within the actuator body. In this case, it will be necessary to create a displacement sensor that can provide the necessary accuracy and precision in a harish environment.

## 7.2 NANO-INDENTATION AND MATERIAL SCIENCE STUDIES

A nanoindentation instrumentation has been designed and built, that can measure the penetration, load and rotation simultaneously.

In our studies, the affecting factors for this nanoindentation research include, thermal drift of the sample and the instrument, the initial penetration depth of the indentation process, instrument compliance, piling-up and sinking-in situation during indentation, surface roughness or residual stress of the sample, and indenter alignments.

This nano-indentation could be extended to scratching and ploughing behavior for the plastic deformation research. Three-dimensional force and torque measurements may provide additional insights into deformation processes. Additionally, increasingly desired to explain deformation processes at atomic scales. To do this, higher resolution instrumentation is needed, for example to operate inside a transmission electron microscope (TEM) so that more detailed rotation force or phase-transformation can be visualized at the atomic level.

# REFERENCES

[1] R. H. Baughman, C. Cui, A. A. Zakhidov, Z. Iqbal, J. N. Barisci, G. M. Spinks, G. G. Wallace, A. Mazzoldi, D. De Rossi, A. G. Rinzler, O. Jaschinski, S. Roth, and M. Kertesz, "Carbon nanotube actuators," *Science,* vol. 284, no. 5418, pp. 1340-1344, 1999.

[2] C.-K. Lee and F. C. Moon, "Modal sensors/actuators," *Journal of applied mechanics,* vol. 57, no. 2, pp. 434-441, 1990.

[3] L. N. Cattafesta III and M. Sheplak, "Actuators for active flow control," *Annual Review of Fluid Mechanics,* vol. 43, pp. 247-272, 2011.

[4] Y. Yamagata, T. Higuchi, N. Nakamura, and S. Hamamura, "A micro mobile mechanism using thermal expansion and its theoretical analysis. A comparison with impact drive mechanism using piezoelectric elements," in *Micro Electro Mechanical Systems, 1994, MEMS'94, Proceedings, IEEE Workshop on*, 1994: IEEE, pp. 142-147.

[5] J. Huber, N. Fleck, and M. Ashby, "The selection of mechanical actuators based on performance indices," *Proceedings of the Royal Society of London. Series A: Mathematical, physical and engineering sciences,* vol. 453, no. 1965, pp. 2185-2205, 1997.

[6] S. T. Smith and R. M. Seugling, "Sensor and actuator considerations for precision, small machines," *Precision engineering,* vol. 30, no. 3, pp. 245-264, 2006.

[7] Y. Zhu, A. Corigliano, and H. D. Espinosa, "A thermal actuator for nanoscale in situ microscopy testing: design and characterization," *Journal of micromechanics and microengineering,* vol. 16, no. 2, p. 242, 2006.

[8] Y. Zhu and T.-H. Chang, "A review of microelectromechanical systems for nanoscale mechanical characterization," *Journal of Micromechanics and Microengineering,* vol. 25, no. 9, p. 093001, 2015.

[9] H. D. Espinosa, Y. Zhu, and N. Moldovan, "Design and operation of a MEMS-based material testing system for nanomechanical characterization," *Journal of Microelectromechanical Systems,* vol. 16, no. 5, pp. 1219-1231, 2007.

[10] J. J. Snyder, "Accurate, inexpensive, thermal expansion microtranslator," *Review of scientific instruments,* vol. 64, no. 5, pp. 1351-1354, 1993.

[11] J. Lawall and E. Kessler, "Michelson interferometry with 10 pm accuracy," *Review of Scientific Instruments,* vol. 71, no. 7, pp. 2669-2676, 2000.

[12] R. Hickey, D. Sameoto, T. Hubbard, and M. Kujath, "Time and frequency response of two-arm micromachined thermal actuators," *Journal of Micromechanics and Microengineering,* vol. 13, no. 1, p. 40, 2002.

[13] L.-S. Zheng and M. S.-C. Lu, "A large-displacement CMOS-micromachined thermal actuator with capacitive position sensing," in 2005 IEEE Asian Solid-State Circuits Conference, 2005: IEEE, pp. 89-92.

[14] L.-S. Zheng and M. S.-C. Lu, "A large-displacement CMOS micromachined thermal actuator with comb electrodes for capacitive sensing," *Sensors and Actuators A: Physical,* vol. 136, no. 2, pp. 697-703, 2007.

[15] H. Sehr, I S Tomlin, B Huang, S P Beeby, A G R Evans, A Brunnschweiler, G J Ensell, C G J Schabmueller and T E G Niblock, "Time constant and lateral resonances of thermal vertical bimorph actuators," *Journal of Micromechanics and Microengineering,* vol. 12, no. 4, p. 410, 2002.

[16] L. Li and D. Uttamchandani, "Dynamic response modelling and characterization of a vertical electrothermal actuator," *Journal of Micromechanics and microengineering,* vol. 19, no. 7, p. 075014, 2009.

[17] L. Schönemann, O. Riemer, and E. Brinksmeier, "Control of a thermal actuator for UP-milling with multiple cutting edges," *Procedia CIRP,* vol. 46, pp. 424-427, 2016.

[18] S. Sherrit, "Smart material/actuator needs in extreme environments in space," in *Smart Structures and Materials 2005: Active Materials: Behavior and Mechanics*, 2005, vol. 5761: International Society for Optics and Photonics, pp. 335-346.

[19] G. A. Geithman and D. F. Olsen, "Induction heater and apparatus for use with stud mounted hot melt fasteners," ed: Google Patents, 1982.

[20] S. Kalpakjian and S. Schmid, *Manufacturing, Engineering and Technology SI 6th Edition-Serope Kalpakjian and Stephen Schmid: Manufacturing, Engineering and Technology*. Digital Designs, 2006.

[21] D. Miyagi, A. Saitou, N. Takahashi, N. Uchida, and K. Ozaki, "Improvement of zone control induction heating equipment for high-speed processing of semiconductor devices," *Magnetics,* vol. 42, no. 2, pp. 292-294, 2006.

[22] H. Fujita, N. Uchida, and K. Ozaki, "A new zone-control induction heating system using multiple inverter units applicable under mutual magnetic coupling conditions," *IEEE Transactions on Power Electronics,* vol. 26, no. 7, pp. 2009-2017, 2011.

[23] C. Fan, S. T. Smith, and J. Tarbutton, "A linear positionning stage using a thermal actuator," 32nd American Society for Precision Engineering Conference, vol. 67, pp. 451-455, 2017.

[24] F. Lin, S. T. Smith, and G. Hussain, "Optical fiber displacement sensor and its application to tuning fork response measurement," *Precision engineering,* vol. 36, no. 4, pp. 620-628, 2012.

[25] S. T. Smith, "*Flexures: elements of elastic mechanisms*," Crc Press, Chapter 5, 2000.

[26] R. Jones, "Parallel and rectilinear spring movements," *Journal of Scientific Instruments*, vol. 28, no. 2, p. 38, 1951.

[27] L. Grajales, J. Sabate, K. Wang, W. Tabisz, and F. Lee, "Design of a 10 kW, 500 kHz phase-shift controlled series-resonant inverter for induction heating," in *Conference Record of the 1993 IEEE Industry Applications Conference Twenty-Eighth IAS Annual Meeting*, 1993: IEEE, pp. 843-849.

[28] C. Fan, D. Hastings, and S. T. Smith, "Aspects of design and performance of a thermally actuated linear translation stage," 34th American Society for Precision Engineering Conference, vol. 71, pp. 371-374, 2019.

[29] C. Dodd and W. Deeds, "Analytical solutions to eddy- current probe- coil problems," *Journal of applied physics*, vol. 39, no. 6, pp. 2829-2838, 1968.

[30] C. Dodd, W. Deeds, and J. Luquire, "Integral solutions to some eddy current problems," *International Journal of Nondestructive Testing*, vol. 1, pp. 29-90, 1969.

[31] P. W. Bridgman, "*The physics of high pressure*," G. Bell and Sons, London, Chapter 6, 1949

[32] Fischer-Cripps, A.C., 2006. Critical review of analysis and interpretation of nanoindentation test data. Surface and coatings technology, 200(14-15), pp.4153-4165.

[33] Li, X. and Bhushan, B., 2002. A review of nanoindentation continuous stiffness measurement technique and its applications. Materials characterization, 48(1), pp.11-36.

[34] Tabor, D., 1970. The hardness of solids. Review of physics in technology, 1(3), p.145.

[35] Ruffell, S., Sears, K., Bradby, J.E. and Williams, J.S., 2011. Room temperature writing of electrically conductive and insulating zones in silicon by nanoindentation. Applied Physics Letters, 98(5), p.052105.

[36] Dong, Z. and Song, Y., 2011. Novel Pressure-Induced Structural Transformations of Inorganic Nanowires. In Nanowires-Fundamental Research. InTech.

[37] Asif, S.S., Wahl, K.J. and Colton, R.J., 1999. Nanoindentation and contact stiffness measurement using force modulation with a capacitive load-displacement transducer. Review of scientific instruments, 70(5), pp.2408-2413.

[38] B. K. Nowakowski, D. T. Smith, S. T. Smith, L. F. Correa, and R. F. Cook (2013) Development of a precision nanoindentation platform - Rev. Sci. Instrum. 84, 075110 (2013); doi: 10.1063/1.4811195

[39] Ian L. Spain et al. Semiconductors at high pressure: New physics with the diamond-anvil cell

[40] Ishigawa diagram from website: https://www.keyence.com/ss/products/measure-sys/measurement-selection/basic/abbe-principle.jsp

[41] Holmberg, K. and Erdemir, A., 2017. Influence of tribology on global energy consumption, costs and emissions. Friction, 5(3), pp.263-284.

[42] Richard Leach, Stuart Smith, "Basics of precision engineering" CRC Press, Chapter 6, 2018.

[43] D. Tabor, “The hardness of metals” OUP Press, Appendix VI, page 167.

[44] Harb S.M., Chetwynd D.G. and Smith S.T., 1995, Tilt errors in parallel plate capacitance micrometry, in International Progress in Precision Engineering, Proceedings IPES 8, ed. Bonis M., Alayli Y., Revel P., McKeown P.A. and Corbett J., Butterworth/Heinmann, Boston, 147-150.

# APPENDIX A: TABLE OF DYNAMIC PERFORMANCE METRICS

Tables 6-B and Table 7-B contain the data analysis results for the step response studies discussed in Chapter 2 Section 2.7. SPV = setpoint value, PL = preload, MO = magnitude overshoot, TC = time constant, ST = settling time, SR = slew rate, AVG = average.

Table 6-B. Dynamic performance measurements for closed loop control of a ramp cycle using a 240 W power supply.

| Increasing steps (240 W, 100 µm) | | | | | | Decreasing steps (240 W, 100 µm) | | | | | |
|---|---|---|---|---|---|---|---|---|---|---|---|
| SPV (µm) | PL (N) | MO (µm) | TC (s) | ST (s) | SR (µm·s$^{-1}$) | SPV (µm) | PL (N) | MO (µm) | TC (s) | ST (s) | SR (µm·s$^{-1}$) |
| 20 | 0 | 7.5 | 2.5 | 13.8 | 7.1 | 100 | 0 | 2.6 | 4.6 | 12.3 | 3.2 |
| 40 | 0 | 6.6 | 2.6 | 13.5 | 6.7 | 80 | 0 | 5.5 | 4.4 | 17.1 | 4.2 |
| 60 | 0 | 5.4 | 2.8 | 12.8 | 6.0 | 60 | 0 | 4.4 | 4.5 | 16.1 | 4.4 |
| 80 | 0 | 4.5 | 3.2 | 13.3 | 4.9 | 40 | 0 | 2.8 | 5.1 | 16.2 | 3.7 |
| 100 | 0 | 4.0 | 3.9 | 13.8 | 4.2 | 20 | 0 | 1.2 | 7.2 | 13.6 | 2.3 |
| 20 | 500 | 7.6 | 2.6 | 14.5 | 6.9 | 100 | 500 | 6.0 | 3.9 | 15.5 | 4.4 |
| 40 | 500 | 6.6 | 2.6 | 13.8 | 6.7 | 80 | 500 | 6.1 | 4.3 | 17.3 | 4.5 |
| 60 | 500 | 5.5 | 2.8 | 13.6 | 5.8 | 60 | 500 | 5.0 | 3.9 | 16.9 | 4.8 |
| 80 | 500 | 4.5 | 3.4 | 13.9 | 4.6 | 40 | 500 | 3.6 | 4.6 | 16.4 | 4.3 |
| 100 | 500 | 3.7 | 3.8 | 13.8 | 3.9 | 20 | 500 | 1.4 | 6.5 | 12.2 | 2.8 |
| 20 | 1000 | 7.3 | 2.5 | 14.6 | 7.0 | 100 | 1000 | 5.9 | 3.9 | 15.8 | 4.0 |
| 40 | 1000 | 6.3 | 2.7 | 12.6 | 6.4 | 80 | 1000 | 6.4 | 3.8 | 13.2 | 5.1 |
| 60 | 1000 | 5.3 | 2.9 | 13.4 | 5.6 | 60 | 1000 | 5.2 | 3.9 | 16.4 | 4.9 |
| 80 | 1000 | 4.3 | 3.4 | 11.4 | 4.6 | 40 | 1000 | 3.3 | 4.7 | 16.4 | 4.1 |
| 100 | 1000 | 3.6 | 4.0 | 12.1 | 3.8 | 20 | 1000 | 1.5 | 6.9 | 14.2 | 2.7 |
| AVG | 0 | 5.6 | 3.0 | 13.5 | 5.8 | AVG | 0 | 3.3 | 5.2 | 15.1 | 3.5 |
| AVG | 500 | 5.6 | 3.0 | 13.9 | 5.6 | AVG | 500 | 4.4 | 4.6 | 15.7 | 4.2 |
| AVG | 1000 | 5.4 | 3.1 | 12.8 | 5.5 | AVG | 1000 | 4.4 | 4.6 | 15.2 | 4.2 |

Table 7-B. Dynamic performance measurements for closed loop control of a ramp cycle using a 480 W power supply.

| Increasing steps (480 W, 200 µm) | | | | | | Decreasing steps (480 W, 200 µm) | | | | | |
|---|---|---|---|---|---|---|---|---|---|---|---|
| SPV (µm) | PL (N) | MO (µm) | TC (s) | ST (s) | SR (µm·s$^{-1}$) | SPV (µm) | PL (N) | MO (µm) | TC (s) | ST (s) | SR (µm·s$^{-1}$) |

| | | | | | | | | | | | |
|---|---|---|---|---|---|---|---|---|---|---|---|
| 20 | 0 | 6.9 | 2.5 | 21.6 | 6.9 | 200 | 0 | 7.3 | 3.3 | 22.3 | 4.0 |
| 40 | 0 | 6.8 | 2.4 | 20.4 | 7.1 | 180 | 0 | 6.9 | 3.4 | 17.7 | 4.1 |
| 60 | 0 | 6.8 | 2.1 | 19.1 | 7.3 | 160 | 0 | 6.1 | 2.9 | 12.9 | 3.8 |
| 80 | 0 | 6.6 | 2.4 | 18.7 | 7.2 | 140 | 0 | 5.2 | 3.4 | 12.9 | 3.5 |
| 100 | 0 | 7.7 | 2.1 | 17.8 | 7.6 | 120 | 0 | 7.1 | 1.8 | 19.3 | 7.6 |
| 120 | 0 | 7.8 | 2.2 | 15.4 | 8.0 | 100 | 0 | 5.2 | 2.0 | 21.0 | 7.5 |
| 140 | 0 | 8.2 | 2.0 | 14.1 | 8.5 | 80 | 0 | 2.8 | 4.7 | 15.5 | 2.4 |
| 160 | 0 | 8.1 | 2.3 | 14.3 | 8.6 | 60 | 0 | 3.1 | 4.0 | 22.0 | 4.3 |
| 180 | 0 | 7.3 | 2.0 | 18.2 | 8.1 | 40 | 0 | 1.5 | 4.5 | 14.9 | 2.6 |
| 200 | 0 | 6.9 | 2.0 | 32.9 | 7.8 | 20 | 0 | 0.4 | 7.4 | 16.9 | 1.4 |
| 20 | 500 | 6.9 | 2.8 | 24.6 | 6.0 | 200 | 500 | 9.2 | 3.2 | 22.4 | 4.7 |
| 40 | 500 | 6.7 | 2.6 | 23.3 | 6.5 | 180 | 500 | 8.6 | 3.0 | 20.5 | 5.4 |
| 60 | 500 | 6.6 | 2.4 | 22.2 | 6.6 | 160 | 500 | 7.7 | 2.6 | 19.4 | 4.4 |
| 80 | 500 | 6.3 | 2.4 | 21.2 | 6.6 | 140 | 500 | 6.4 | 3.0 | 20.8 | 4.4 |
| 100 | 500 | 6.6 | 2.6 | 19.3 | 6.9 | 120 | 500 | 6.2 | 2.8 | 23.1 | 4.7 |
| 120 | 500 | 8.2 | 2.2 | 12.2 | 7.7 | 100 | 500 | 7.0 | 2.1 | 21.7 | 8.1 |
| 140 | 500 | 8.1 | 2.3 | 15.3 | 8.3 | 80 | 500 | 5.0 | 2.9 | 22.4 | 7.2 |
| 160 | 500 | 8.1 | 1.8 | 16.8 | 8.7 | 60 | 500 | 4.2 | 4.1 | 21.1 | 4.1 |
| 180 | 500 | 7.2 | 2.4 | 20.3 | 7.7 | 40 | 500 | 2.3 | 2.5 | 13.5 | 3.9 |
| 200 | 500 | 6.7 | 2.4 | 28.6 | 6.9 | 20 | 500 | 1.3 | 9.3 | 19.5 | 1.8 |
| 20 | 1000 | 7.1 | 2.7 | 23.8 | 6.5 | 200 | 1000 | 8.2 | 3.8 | 21.2 | 4.3 |
| 40 | 1000 | 7.0 | 2.2 | 21.4 | 7.0 | 180 | 1000 | 7.7 | 4.3 | 19.9 | 3.9 |
| 60 | 1000 | 6.8 | 2.5 | 19.9 | 7.3 | 160 | 1000 | 7.7 | 2.4 | 18.8 | 5.1 |
| 80 | 1000 | 6.9 | 2.4 | 21.3 | 7.3 | 140 | 1000 | 5.9 | 2.7 | 19.8 | 4.2 |
| 100 | 1000 | 7.3 | 2.3 | 19.9 | 7.5 | 120 | 1000 | 5.1 | 3.4 | 20.9 | 3.4 |
| 120 | 1000 | 7.9 | 2.2 | 11.8 | 8.2 | 100 | 1000 | 6.4 | 1.7 | 13.9 | 11.1 |
| 140 | 1000 | 8.5 | 2.1 | 16.9 | 8.5 | 80 | 1000 | 4.6 | 2.4 | 21.6 | 6.0 |
| 160 | 1000 | 8.0 | 2.0 | 16.0 | 8.7 | 60 | 1000 | 3.4 | 3.9 | 22.7 | 4.6 |
| 180 | 1000 | 7.3 | 2.1 | 45.9 | 8.1 | 40 | 1000 | 2.1 | 3.0 | 22.4 | 3.2 |
| 200 | 1000 | 7.0 | 2.4 | 29.7 | 6.0 | 20 | 1000 | 1.5 | 5.4 | 14.7 | 2.0 |
| AVG | 0 | 7.3 | 2.2 | 19.3 | 7.7 | AVG | 0 | 4.6 | 3.7 | 17.6 | 4.1 |
| AVG | 500 | 7.1 | 2.4 | 20.4 | 7.2 | AVG | 500 | 5.8 | 3.5 | 20.5 | 4.9 |
| AVG | 1000 | 7.4 | 2.3 | 22.7 | 7.5 | AVG | 1000 | 5.2 | 3.3 | 19.6 | 4.8 |

Table 8. Dimensional analysis of thermal actuator flexure elements.

| Flexure width b (m) | Flexure thickness t (m) | Flexure length L (m) | Young's modulus E (N·m-2) | Second moment of area I (m4) | Total stiffness K (N·m-1) |
|---|---|---|---|---|---|
| 0.0254 | 0.0008 | 0.0384 | $2.1 \cdot 10^{11}$ | $1.07 \cdot 10^{-12}$ | 96500 |

$$k = \frac{24EI}{L^3}$$

Table 9. Deformation analysis of thermal actuator tube with 1000 N preload.

| Tube outer diameter b (m) | Tube inner diameter a (m) | Tube arear A ($m^2$) | Tube length L (m) | Young's modulus E ($N \cdot m^{-2}$) | Force (N) | Deformation (μm) |
|---|---|---|---|---|---|---|
| 0.0051594 | 0.0034163 | $4.6447 \cdot 10^{-5}$ | 0.012 | $7 \cdot 10^{10}$ | 1000 | 3.6909 |

$$A = \pi(b^2 - a^2) \quad K = \frac{EA}{L} \quad \delta = \frac{FL}{EA}$$

Table 10. Critical buckling load of the actuator tube.

| Tube outer diameter b (m) | Tube inner diameter a (m) | Tube length L (m) | Young's modulus E ($N \cdot m^{-2}$) | Second moment of area I ($m^4$) | Critical buckling load (N) |
|---|---|---|---|---|---|
| 0.0051594 | 0.0034163 | 0.012 | 7·1010 | $4.5 \cdot 10^{-10}$ | 21568 |

$$I = \frac{\pi(D^4 - d^4)}{64} \quad P_{cr} = \frac{\pi^2 EI}{L^2} = 21.5kN$$

Table 11. Dimensional analysis of flexure elements in actuation stage.

| Flexure width b (m) | Flexure thickness t (m) | Flexure length L (m) | Young's modulus E ($N \cdot m^{-2}$) | Second moment of area I ($m^4$) | Total stiffness K ($N \cdot m^{-1}$) |
|---|---|---|---|---|---|
| 0.0254 | 0.0008 | 0.0384 | $2.1 \cdot 10^{11}$ | $1.07 \cdot 10^{-12}$ | 96500 |

$$k = \frac{48EI}{L^3}$$

Table 12. Dimensional analysis of flexure elements in load-cell stage.

| Flexure width b (m) | Flexure thickness t (m) | Flexure length L (m) | Young's modulus E ($N \cdot m^{-2}$) | Second moment of area I ($m^4$) | Total stiffness K ($N \cdot m^{-1}$) |
|---|---|---|---|---|---|
| 0.0254 | 0.0008 | 0.0384 | $2.1 \cdot 10^{11}$ | $1.07 \cdot 10^{-12}$ | 96500 |

$$k = \frac{48EI}{L^3}$$

Table 13. Dimensional analysis of flexure rod.

| Flexure rod diameter r (m) | Flexure rod length L (m) | Young's modulus E ($N \cdot m^{-2}$) | Second moment of area I ($m^4$) | Total stiffness K ($N \cdot m^{-1}$) |
|---|---|---|---|---|
| 0.0005 | 0.04 | $2.1 \cdot 10^{11}$ | $4.91 \cdot 10^{-14}$ | 3865.6 |

$$I_x = I_y = \frac{\pi r^4}{4} \quad k = \frac{12EI}{L^3}$$

Table 14. Axial stiffness analysis of flexure rod.

| Flexure rod diameter r (m) | Flexure rod length L (m) | Young's modulus E ($N \cdot m^{-2}$) | Total stiffness K ($N \cdot m^{-1}$) | Force (N) | Deformation (μm) |
|---|---|---|---|---|---|
| 0.0005 | 0.04 | $2.1 \cdot 10^{11}$ | | | |

$$A = \pi r^2 \quad K = \frac{EA}{L} \quad \delta = \frac{FL}{EA}$$

Table 15. Torsional stress analysis of flexure rod.

| Young's modulus E | Radius of the rod r (mm) | Length of the rod L (m) | Second moment of area I ($m^4$) | K | delta | Force (N) | Moment | Stress |
|---|---|---|---|---|---|---|---|---|
| $2.1 \cdot 10^{11}$ | 0.0005 | 0.04 | $4.91 \cdot 10^{-14}$ | 3865.63 | 0.0005 | 1.9328 | 0.0387 | |

$$J = \frac{\pi r^4}{2} \qquad \theta = \frac{TL}{JG}$$

# APPENDIX B: BILL OF MATERIALS FOR THERMAL ACTUATOR

Most of the standard components were procured online from McMaster Carr Website. The rest of the components were either manufactured as explained above or were readily available through stock in Dr. Smith's Lab (Duke 120).

| | Item | Part Number | Description | Material | Price ea. $ | Qty | Total Cost |
|---|---|---|---|---|---|---|---|
| Frame | Steel Plate | 9143K734 | 0.75'' thick, 8''x24'', 2 ft length | 1018 steel plate | 133.01 | 1 | 133.01 |
| | Screw | 91251A934 | Fastening actuator side for frame, 10-24 thread,5"1/2" lg. | Black-Oxide Alloy Steel | 3.19 | 2 | 6.38 |
| | Screw | 91251A260 | Fastening spring side of frame, 10-24 thread, 4 3/4" length | Black-Oxide Alloy Steel | 2.96 | 2 | 5.92 |
| | Washer | 90107A011 | Flat type washer with ID 0.203", OD 0.438", Thickness 0.024"-0.038" | 316 Stainless Steel | 4.24 | 1 | 4.24 |
| | Hex Standoff | 91780A245 | 5/8" OD, 1/4"-20 , 3 1/2" length, Female thread | 2011 Aluminum | 3.36 | 1 | 3.36 |
| | Nut | 91841A011 | 10-24, 1/8" thick, pack of 100 | 18-8 Stainless Steel | 3.50 | 1 | 3.50 |
| Actuator | Steel drive tube | 4830K116 | NPT Male Threaded on Both Ends, 1/8 Pipe Size, 4" Long | 304/304L Stainless Steel | 3.18 | 1 | 3.18 |
| Actuator | Aluminum drive tube | 44665K117 | NPT Male Threaded on Both Ends, 1/8 Pipe Size, 4" Long | Aluminum | 2.08 | 1 | 2.08 |
| | Brass hose barb | WP7362568 | 1/8 FNPT, 1/4" tube size, barbed, 90deg elbow | Brass | 4.34 | 4 | 17.36 |

| | | | | | | | |
|---|---|---|---|---|---|---|---|
| | Guide rods (flexure stage) | 8890K183 | 0.1990" OD 3 ft. 6 ft. | Tool Steel | 6.50 | 1 | 6.50 |
| | Set screws | 92765A311 | Oval tip, 1/4"-20 thread size, 1" length, Hex Coarse thread set screws | Alloy Steel | 10.17 | 1 | 10.17 |
| | Guide pins (compression screw) | 98381A554 | 1/4" OD, 3" length, dowel pin | Hardened Alloy Steel | 8.03 | 1 | 8.03 |
| | Knurled-Rim Knob | 6079K33 | 5/16"-24 x 1-3/4" Threaded Stud, 1-1/2" Diameter | Black-Oxide Steel | 5.59 | 1 | 5.59 |
| | Compression Spring | 9657K399 | Zinc-Plated, Music-Wire, Closed & Flat Ends, 2" Long, 3/4" OD, 294 lb/in | Zinc-Plated Music-Wire Steel | 1.71 | 10.3 | 17.61 |
| | Steal bar stock | 9517K433 | 1/4" thick, 3/4" wide, 2 ft length rectangular bar | Low-Carbon Steel | 20.34 | 1 | 20.34 |
| | Aluminum shaft stock | - | 15" OD (for spring guide) | 6061 Al | | 1 | |
| | Ni-Cr wire | 8880K11 | 0.064" Diameter, 1/4 lb. Spool, 21' Long | Nickel Chromium | 21.28 | 1 | 21.28 |
| Cooling and isolation | Round Seal | 12975K35 | O-Ring Cord Stock, 1/4" OD, 3' length. | Neoprene Rubber | 1.65 | 1 | 1.65 |
| | Plastic tubing | 51135K16 | Durometer 50A, 1/8" ID, 1/4" OD, 375F, 10ft | Silicone Rubber | 0.69 | 10 | 6.9 |
| | Plastic tubing | - | Cooling Pipes | PVC | - | - | - |
| | Glass | - | For low friction surface for guide rods against flexure | Glass | - | - | - |
| Controls | myRIO | - | Controller | - | - | 1 | - |
| | 16 bit ADC | - | Analog to Digital Converter | - | - | 1 | - |

| | | | | | | | |
|---|---|---|---|---|---|---|---|
| | 12V 10A power supply | - | TDK Lambda | - | - | 1 | - |
| Controls | Power amplifier | - | Amplifier | - | - | 1 | - |
| | ± 12 V Power supply | - | RIGOL Power Supply | - | - | 1 | - |
| | Temperature sensors | - | LM 35 | - | - | 2 | - |
| | Optical Sensor | - | RPI 0352E | - | - | 1 | - |
| | TOTAL | | | | | | 105 |

# APPENDIX C: DRAWINGS OF MANUFACTURED COMPONENTS

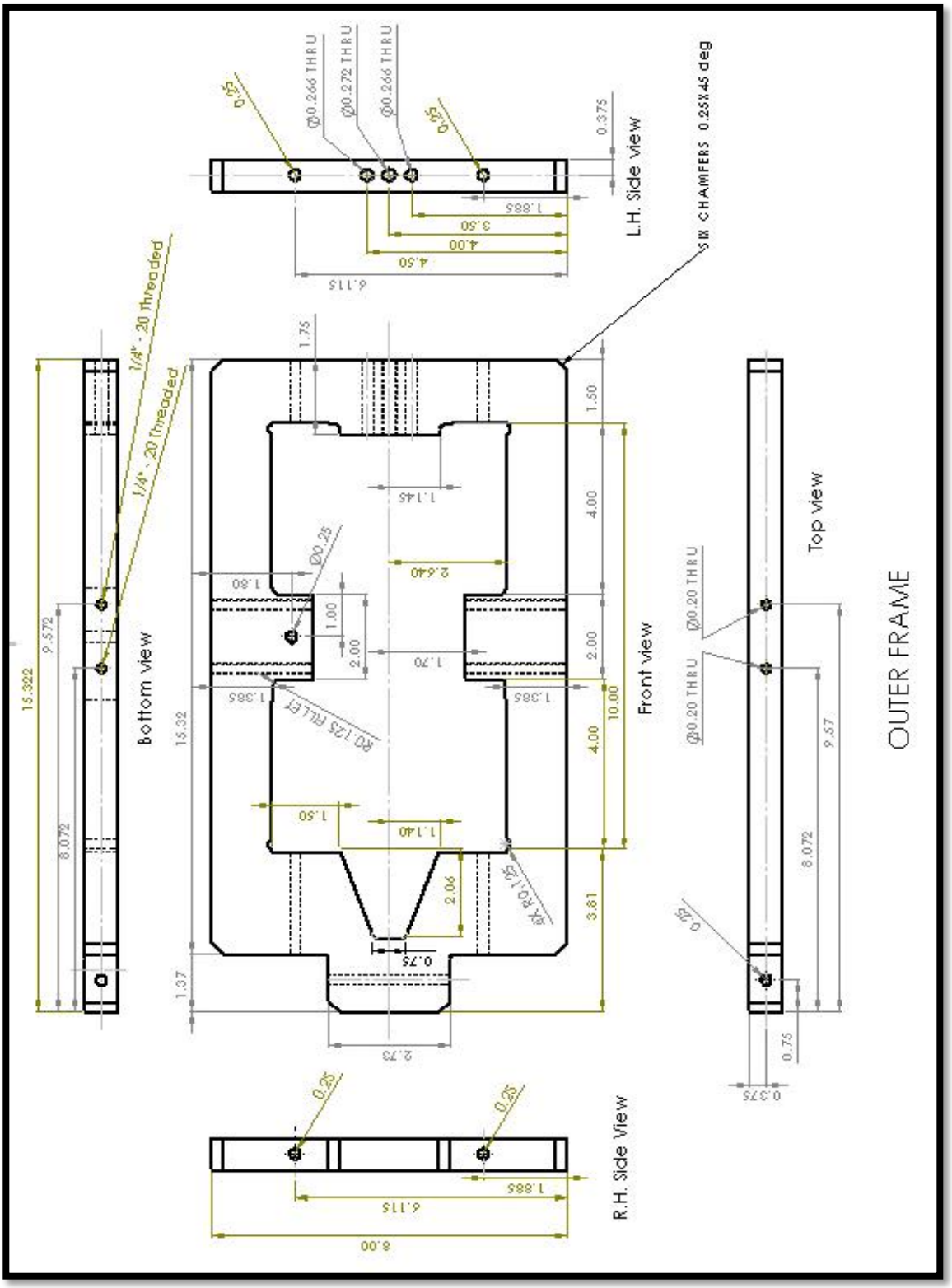

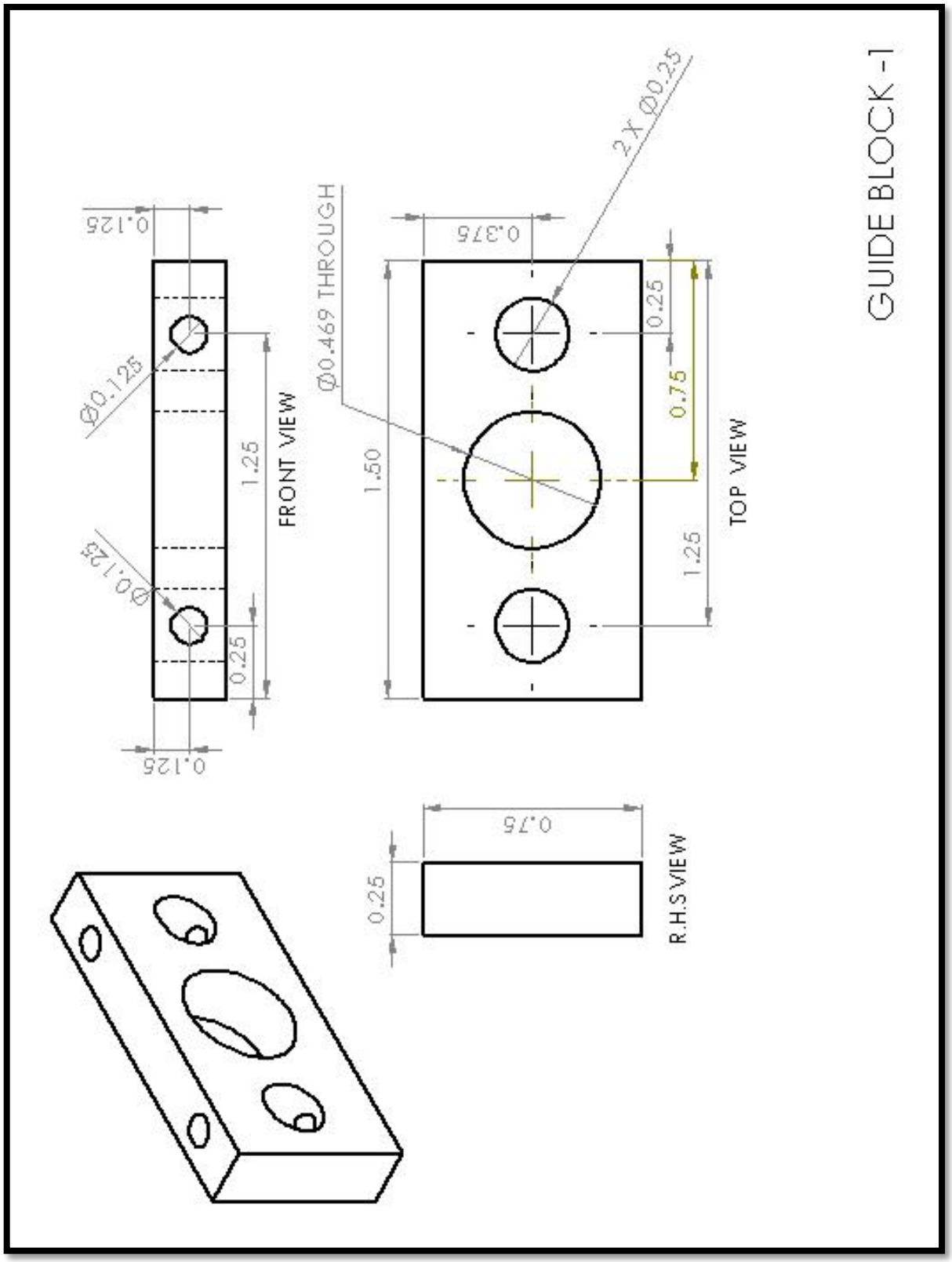
GUIDE BLOCK -1
FRONT VIEW
TOP VIEW
R.H.S VIEW
0.125
Ø0.125
1.25
0.25
0.125
0.125
Ø0.469 THROUGH
0.375
2 X Ø0.25
1.50
0.25
0.75
1.25
0.75
0.25

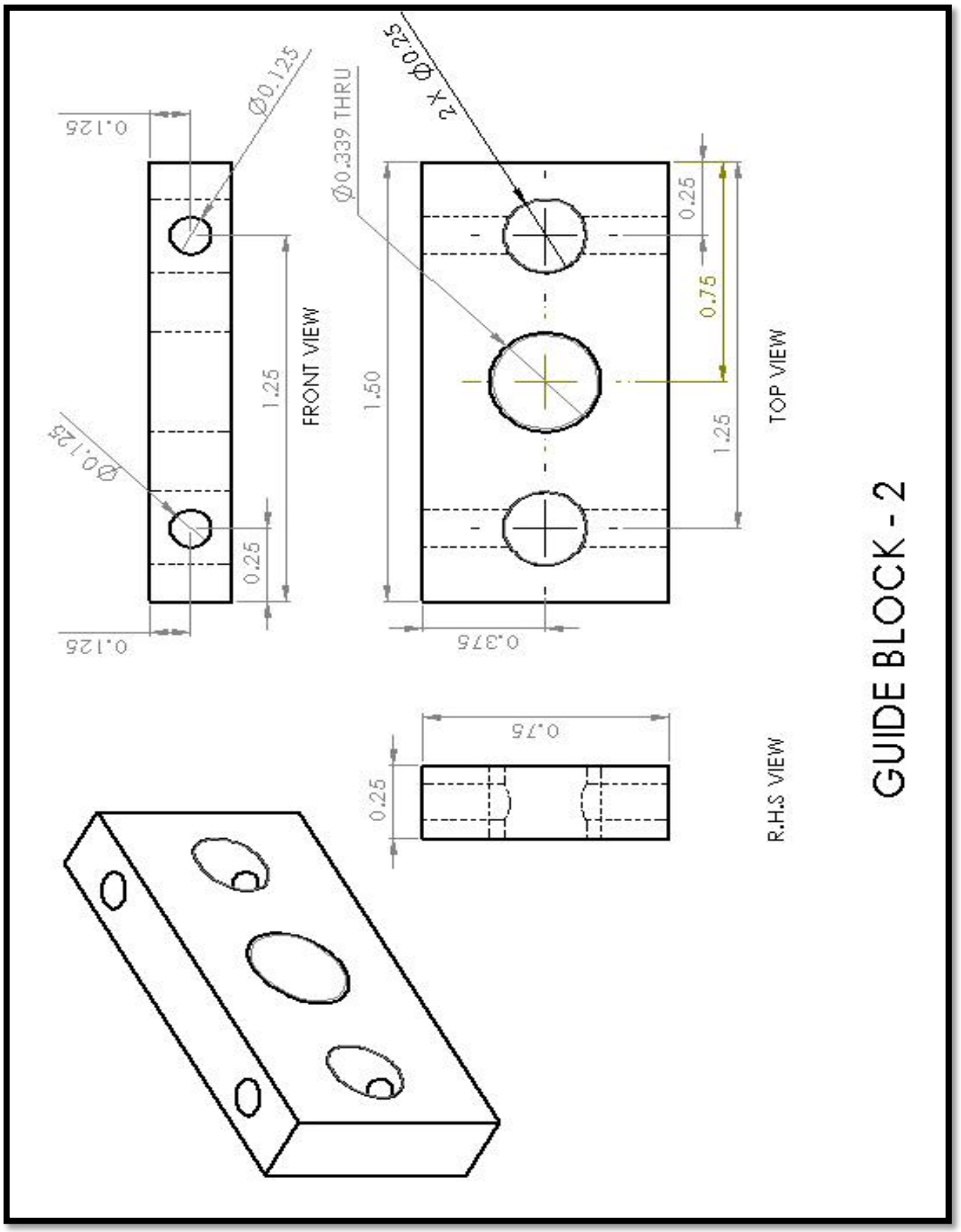
GUIDE BLOCK - 2
FRONT VIEW
TOP VIEW
R.H.S VIEW
Ø0.125
0.125
1.25
0.25
Ø0.125
0.125
Ø0.339 THRU
2x Ø0.25
1.50
0.25
0.75
1.25
0.375
0.75
0.25

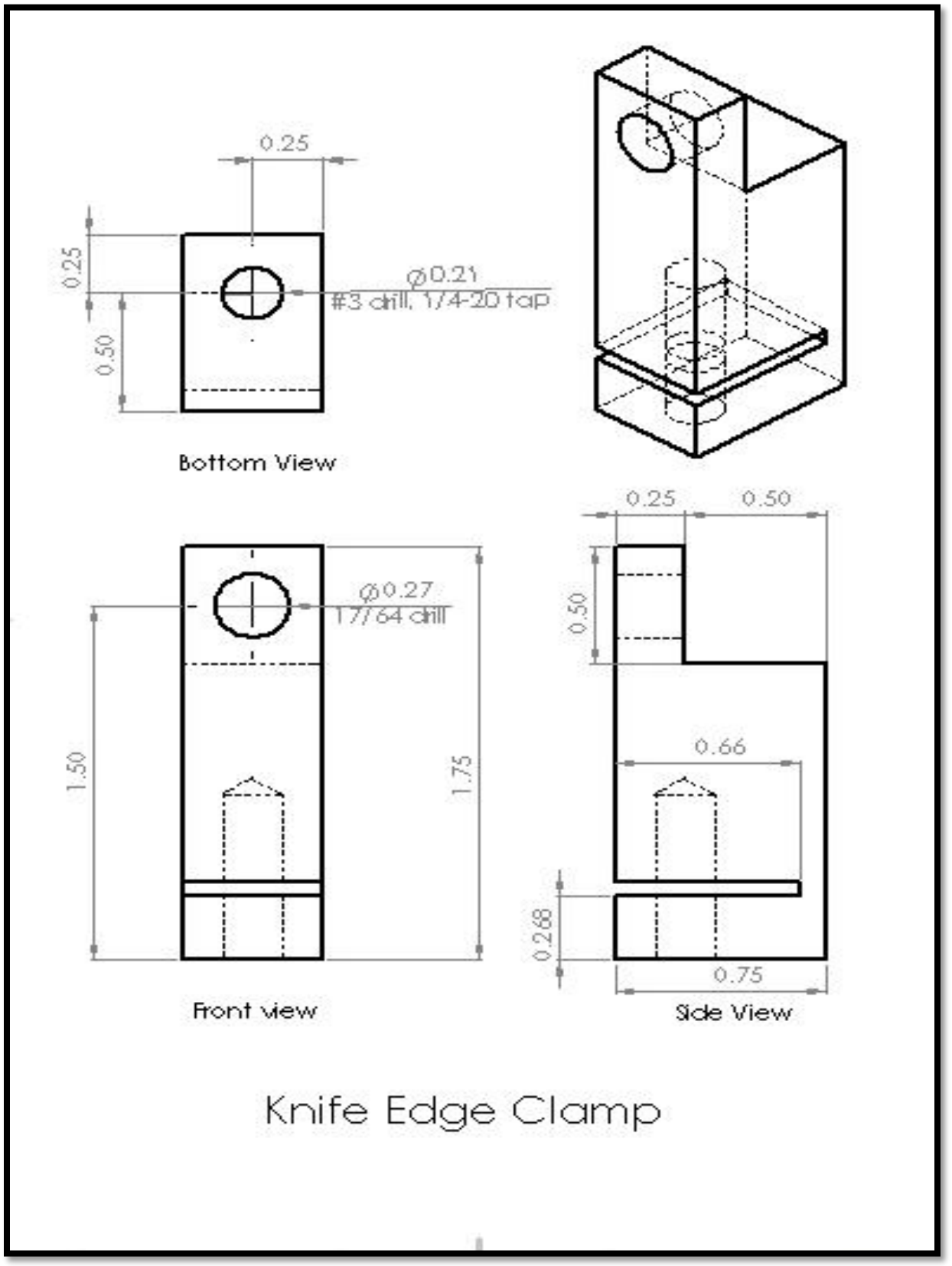
0.25
0.25
0.50
ø0.21
#3 drill, 1/4-20 tap
Bottom View
ø0.27
17/64 drill
1.50
1.75
Front view
0.25
0.50
0.50
0.66
0.268
0.75
Side View
Knife Edge Clamp

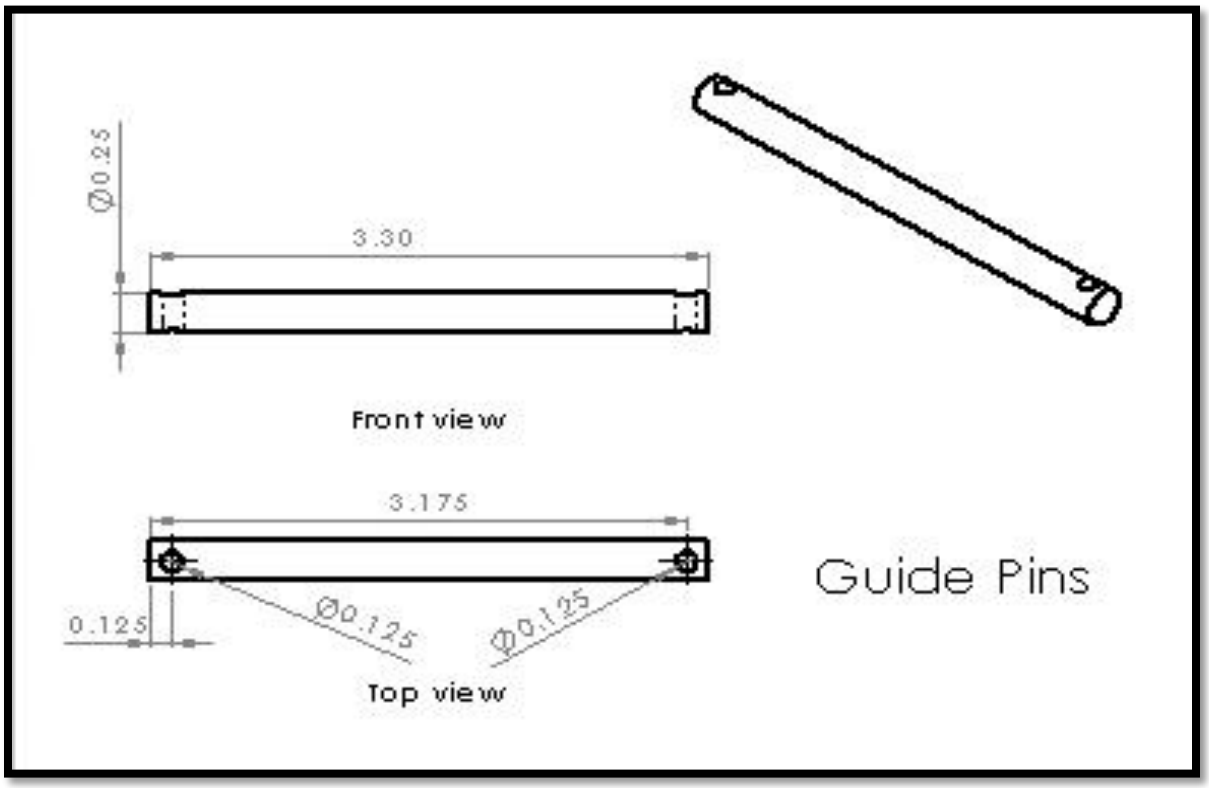
Ø0.25
3.30
Front view
3.175
0.125
Ø0.125
Ø0.125
Top view
Guide Pins

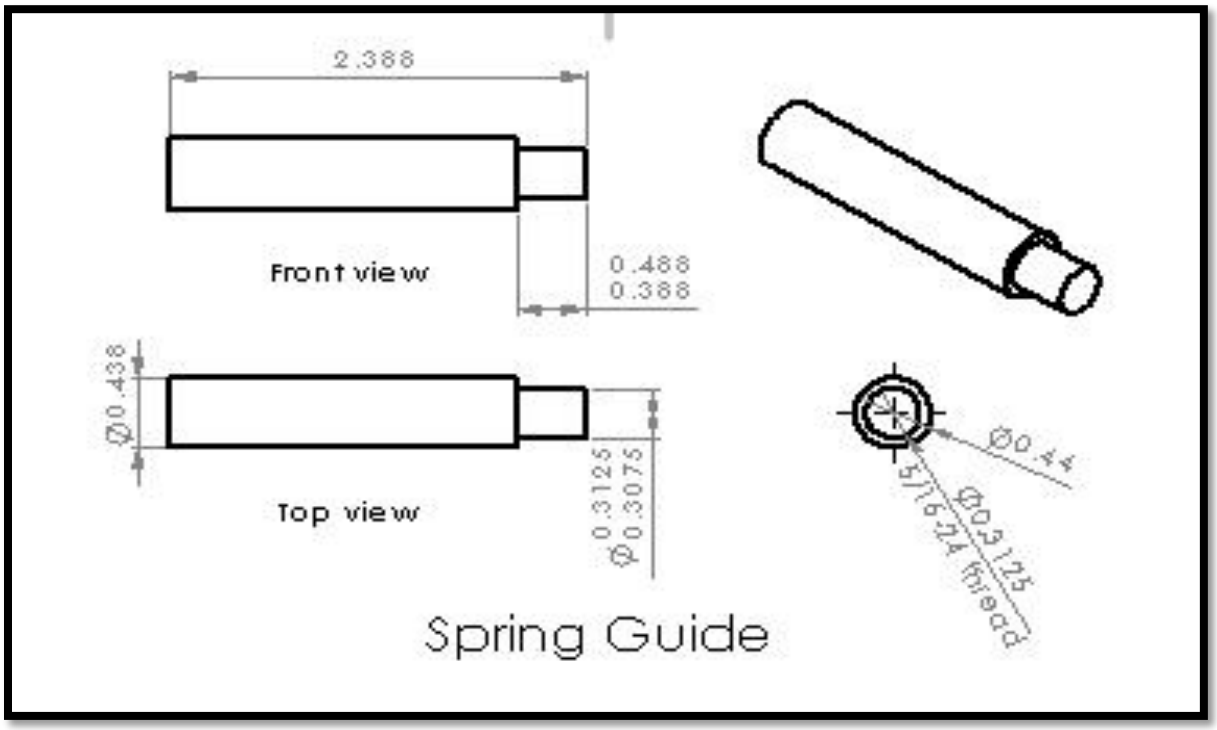
2.388
Front view
0.488
0.388
Ø0.438
Top view
0.3125
Ø0.3075
Ø0.44
5/16-24 thread
Ø0.3125
Spring Guide

The modifications have been dimensioned; the repeated hole pattern already exists.
A hole is created on the side of the block.
Two holes are created originating from the block's underside, and intersect the hole coming from the side.

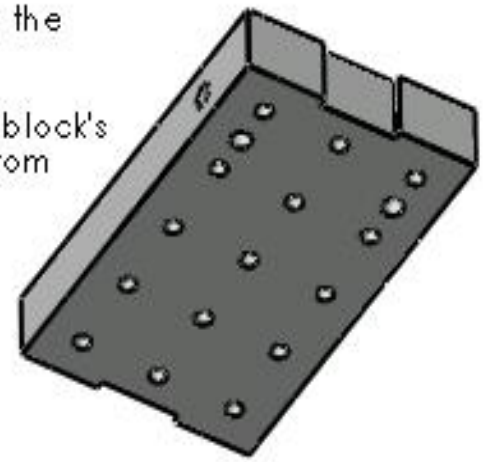

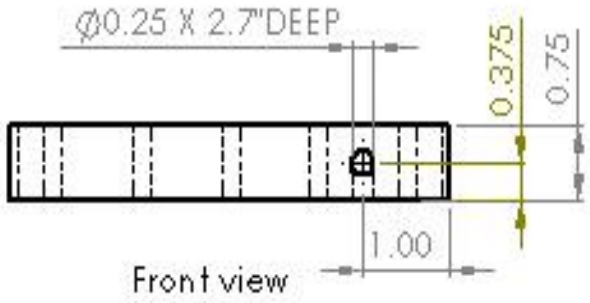


Front view

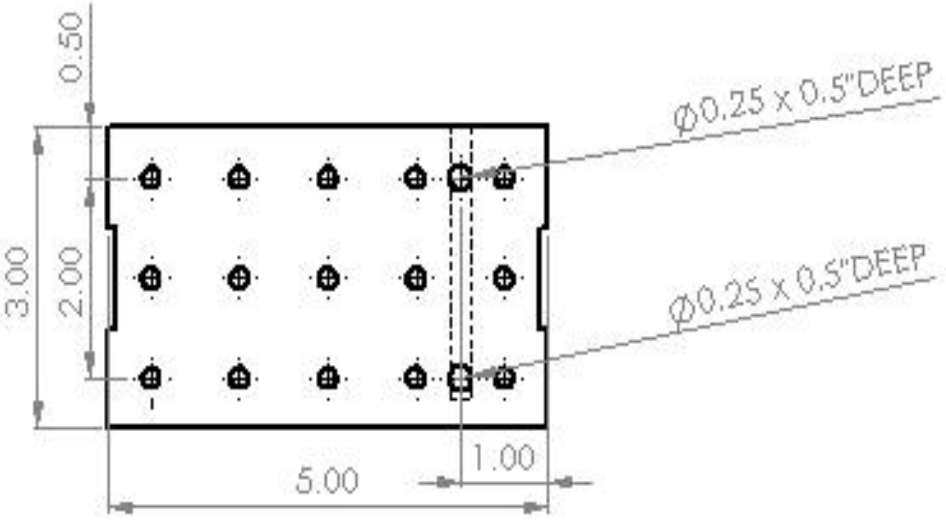


Top view

# Flexure stage modification

# APPENDIX D: BILL OF MATERIALS WITH ONLINE LINKS

| Item | Part Number | Website |
|---|---|---|
| Steel Plate | 9143K734 | https://www.mcmaster.com/#9143k734/=16twcmk |
| Screw | 91251A934 | https://www.mcmaster.com/#91251A934 |
| Screw | 91251A260 | https://www.mcmaster.com/#91251A260 |
| Washer | 90107A011 | https://www.mcmaster.com/#90107a011/=16t8lvh |
| Hex Standoff | 91780A245 | https://www.mcmaster.com/#91780a245/=16tr1ap |
| Nut | 91841A011 | https://www.mcmaster.com/#91841a011/=16r0qtd |
| Steel drive tube | 4830K116 | https://www.mcmaster.com/#4830k116/=16pnfxf |
| Aluminum drive tube | 44665K117 | https://www.mcmaster.com/#44665k117/=16sqd9c |
| Brass hose barb | WP7362568 | https://goo.gl/RISnV4 |
| Guide rods (flexure stage) | 8890K183 | https://www.mcmaster.com/#8890k183/=17ev8ns |
| Set screws | 92765A311 | https://www.mcmaster.com/#92765a311/=17eu0v9 |
| Guide pins (compression screw) | 98381A554 | https://www.mcmaster.com/#98381a554/=16trgpd |
| Knurled-Rim Knob | 6079K33 | https://www.mcmaster.com/#6079k33/=16sq0j8 |
| Compression Spring | 9657K399 | https://www.mcmaster.com/#9657k399/=16q6l6o |
| Steal bar stock | 9517K433 | https://www1.mcmaster.com/#9517k433/=17eu8b6 |
| Ni-Cr wire | 8880K11 | https://www.mcmaster.com/#8880k11/=17euypv |
| Round Seal | 12975K35 | https://www.mcmaster.com/#12975k35/=16twv9t |
| Plastic tubing | 51135K16 | https://www.mcmaster.com/#51135k16/=17eu5vw |

# APPENDIX E: ROTARY AIR-BEARING COMPLETE ASSEMBLY DRAWING

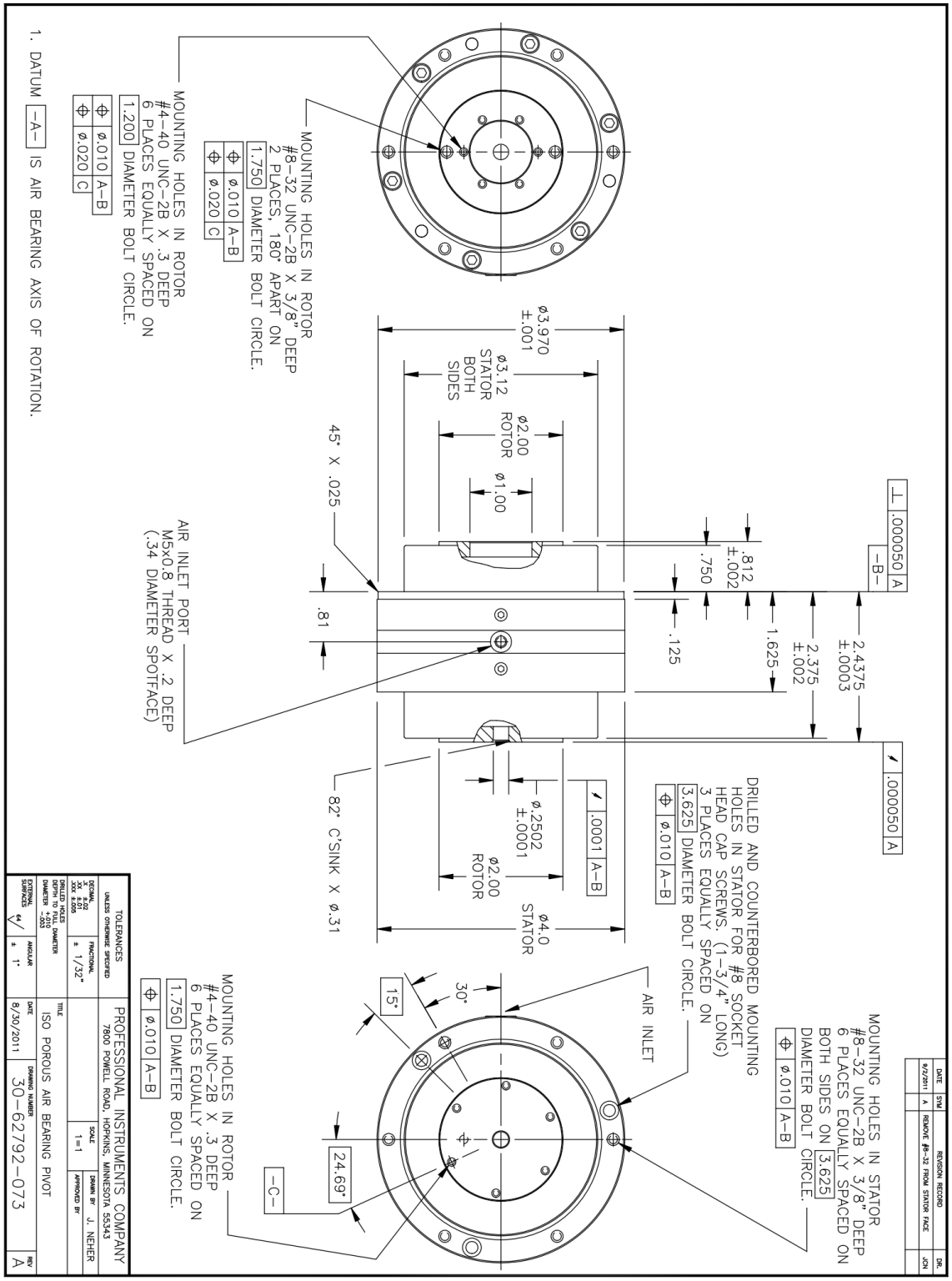

# APPENDIX F: LABVIEW GUI AND DIAGRAM PANEL

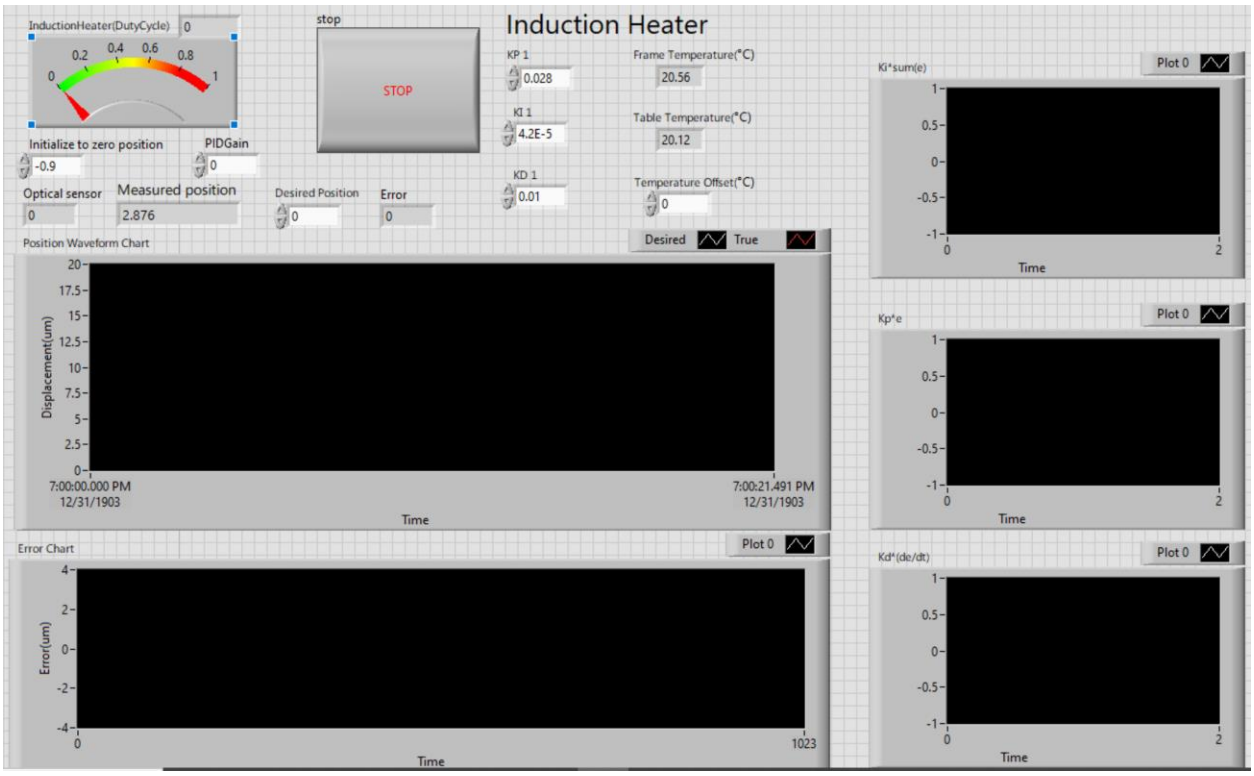


Rotation Measurement during Nano Indentation
Points
10000
offset
0.01
Ramp Vpp
1
Voltage
0.01
PZT
1
V_Actuator
-5.4351
Stop Button
STOP
Loop rate (Hz)
99.5525
ACS Offset
0
ACS
CH1A
CH2A
CH3A
CH4A
CH5A
LCS Offset
0
V_LoadCell
8.17492
LCS
712.78
18114.
Amplitude
Time
Lion
-24998.
Rotation
0.00

# APPENDIX G: STABILITY TEST FOR KINEMATIC ASSEMBLY

The stability test was set up at Duke 140 in Figure 149 and the measurement results were shown in Figure 150.

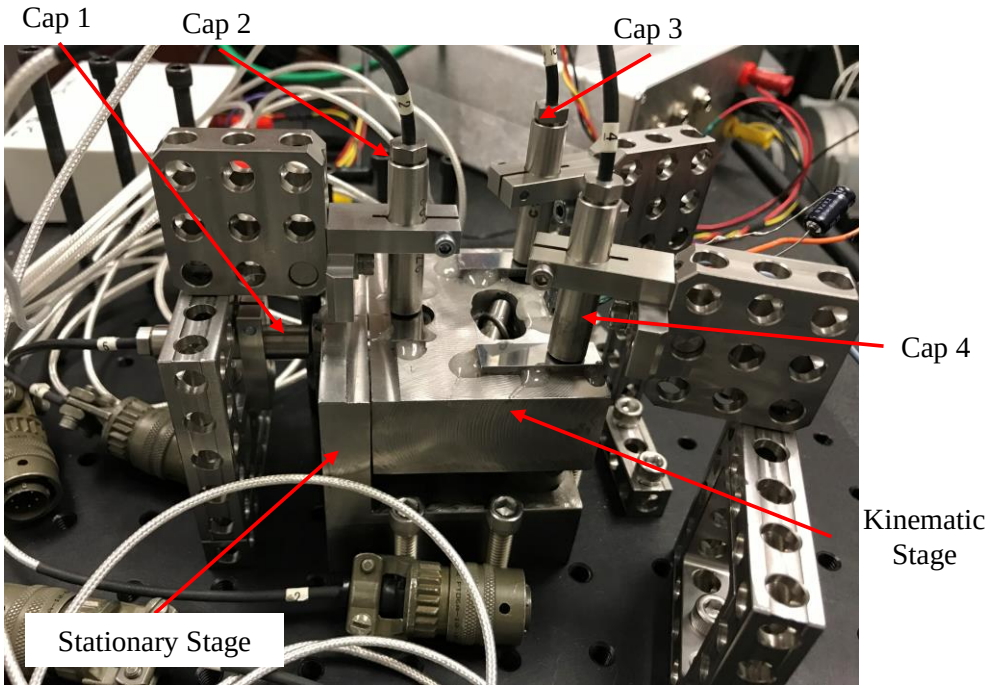


Figure 149: The stability test was set up for the kinematic assembly.

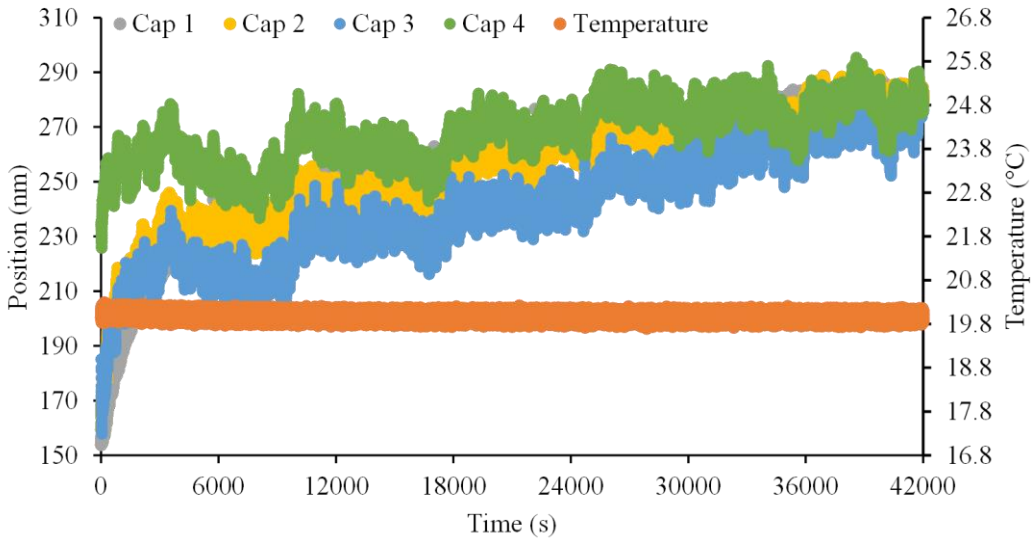


Figure 150: Stability measurements in the temperature-controlled lab.